

REPORT DOCUMENTATION PAGE

Form Approved
OMB No. 0704-0188

Public reporting burden for this collection of information is estimated to average 1 hour per response, including the time for reviewing instructions, searching existing data sources, gathering and maintaining the data needed, and completing and reviewing the collection of information. Send comments regarding this burden estimate or any other aspect of this collection of information, including suggestions for reducing this burden, to Washington Headquarters Services, Directorate for Information Operations and Reports, 1215 Jefferson Davis Highway, Suite 1204, Arlington, VA 22202-4302, and to the Office of Management and Budget, Paperwork Reduction Project (0704-0188), Washington, DC 20503.

1. AGENCY USE ONLY (Leave blank)			2. REPORT DATE	3. REPORT TYPE AND DATES COVERED
			26 Nov 96	Final Technical Report 10/1/95 - 9/30/96
4. TITLE AND SUBTITLE			5. FUNDING NUMBERS	
Fundamental Issues in the Coalescence-Based Processing of Polymer Powders and Colloids			F49620-95-C-0008	
6. AUTHOR(S)			7. PERFORMING ORGANIZATION NAME(S) AND ADDRESS(ES)	
Claudio Argento Anand Jagota Stephen Mazur			E. I. Dupont de Nemours & Co. P. O. Box 80356 Wilmington, DE 19880-0356	
			AFOSR-TR-97 	
9. SPONSORING/MONITORING AGENCY NAME(S) AND ADDRESS(ES)			10. SPONSORING/MONITORING AGENCY REPORT NUMBER	
AFOSR/NA 110 Duncan Avenue, Suite B 115 Bolling AFB, DC 20332-8050			19971002 082	
11. SUPPLEMENTARY NOTES				
12a. DISTRIBUTION AVAILABILITY STATEMENT			12b. DISTRIBUTION CODE	
Approved for public release; distribution unlimited.				
13. ABSTRACT (Maximum 200 words)				
<p>The processing of polymer colloids occurs under the influence of internal surface forces and externally applied tractions. Internal surface forces result from molecular volume-to-volume and surface interactions. a formulation for the computation of surface tractions resulting from these interactions has been developed. It generalizes and replaces Derjaguin's appoximation and consistently combines curvature-based and direct van der Waals contributions. In this formulation the influence of a body on any other is described by a second order inter-surface stress tensor. Its properties and physical significance have been explored. The formulation is general and applicable to many other phenomena where surfaces forces play an important role. It has been implemented as a surface finite element which allows its use in numerical simulations of deformation. Detailed finite element simulations of viscoelastic coalescence driven by surface forces have been conducted. They confirm the experimentally observed importance of viscoelastic rheology for coalescence of polymers. The consistent treatment of surface forces has exposed and resolved inconsistencies in the current understanding of elastic adhesion and viscous sintering. Finite element simulations of deformation of soft colloidal particles under DLVO forces have also been conducted. It is found that under suitable conditions, due to large contact deformation, during drying particles can continue to be separated by a liquid film. Experimental investigation on well-characterized particles over a range of particle size have established that coalescence of soft colloids is primarily by recoverable elastic deformation, in agreement with theoretical predictions.</p>				
14. SUBJECT TERMS			15. NUMBER OF PAGES	
DTIC QUALITY INSPECTED 4			16. PRICE CODE	
17. SECURITY CLASSIFICATION OF REPORT		18. SECURITY CLASSIFICATION OF THIS PAGE	19. SECURITY CLASSIFICATION OF ABSTRACT	20. LIMITATION OF ABSTRACT
Unclassified		Unclassified	Unclassified	UL

Fundamental Issues in the Coalescence-Based Processing of Polymer Powders and Colloids

Claudio Argento, Anand Jagota, and Stephen Mazur

E.I. Dupont de Nemours & Co.
P.O. Box 80356
Wilmington, DE 19880-0356

Phone: 302-695-2003
Fax: 302-695-1664
email: jagotaa@esvax.dnet.dupont.com
smazur@esvax.dnet.dupont.com

Final Technical Report
for period
10/1/95 - 9/30/96

26 November, 1996
AFOSR F49620-95-C-0008

Abstract

The processing of polymer colloids occurs under the influence of internal surface forces and externally applied tractions. Internal surface forces result from molecular volume-to-volume and surface interactions. A formulation for the computation of surface tractions resulting from these interactions has been developed. It generalizes and replaces Derjaguin's approximation and consistently combines curvature-based and direct van der Waals contributions. In this formulation the influence of a body on any other is described by a second order inter-surface stress tensor. Its properties and physical significance have been explored. The formulation is general and applicable to many other phenomena where surface forces play an important role. It has been implemented as a surface finite element which allows its use in numerical simulations of deformation. Detailed finite element simulations of viscoelastic coalescence driven by surface forces have been conducted. They confirm the experimentally observed importance of viscoelastic rheology for coalescence of polymers. The consistent treatment of surface forces has exposed and resolved inconsistencies in the current understanding of elastic adhesion and viscous sintering. Finite element simulations of deformation of soft colloidal particles under DLVO forces have also been conducted. It is found that under suitable conditions, due to large contact deformation, during drying particles can continue to be separated by a liquid film. Experimental investigations on well-characterized particles over a range of particle size have established that coalescence of soft colloids is primarily by recoverable elastic deformation, in agreement with theoretical predictions. The new surface formulation has also been used to develop a technique by which Hamaker constants may be measured using atomic force microscopy. Contact constitutive relations for deformation by externally applied forces have been developed. These will form the basis for discrete computational methods and continuum constitutive modeling.

1. Introduction

The overall objective of this project has been to develop a quantitative understanding of the mechanics governing coalescence of a particulate polymer precursor into a homogeneous dense product such as a coating, compression molded part, or extrudate. We have focused our attention particularly on the coalescence of polymer particles driven by surface forces.

Surface forces deriving from molecular interactions control the deformations of small particles. Early in the project it was realized that a consistent formulation for such surface forces did not exist. The classical curvature formulation works well for large isolated bodies but was shown to be completely unable to model the early stages of coalescence of two particles. The only available formulation for direct attraction across a small gap, Derjaguin's approximation, is limited to special geometries and had not been improved upon since its development in 1934. Moreover, there was no formulation that would consistently combine these two surface manifestations of molecular interactions. We also discovered that handling interactions between particles as body forces was computationally intractable.

A new surface formulation has been developed that prescribes how effective surface tractions can be computed for any short-range inter-molecular potential. The formulation combines, in a consistent fashion, tractions due to interactions within a particle and between particles. In the new formulation, the effect of a particle on any other particle is expressed in terms of a second-order tensor field: the *inter-surface stress tensor*. This new quantity is like the internal stress tensor in many ways, *e.g.*, upon an inner product with the normal of any surface introduced in the vicinity of the particle, it yields the traction vector on that surface. The new surface formulation also provides new formulae for the computation of the total force and total energy of interaction between particulates in terms of surface integrals instead of the usual volume integrals resulting in analytical and computational simplification. The surface formulation has been implemented as a general surface finite element. By this means the surface formulation has been combined with the analysis of deformation, without being restricted by material or geometric nonlinearities. It can be applied to the study of several other problems, *e.g.*, fracture mechanics and AFM tip/material interactions.

Adhesive contact between elastic and viscoelastic spheres has been studied via finite element analysis. The results of the elastic analysis are in good agreement with approximate analytical results; no exact results are available. Simulations of viscoelastic coalescence have rationalized several experimental findings and have exposed certain inadequacies in the current understanding of sintering processes. The interaction of particles while still separated by a liquid prior to drying is also of great importance. An analytical and computational study of deformation of colloidal particles by DLVO and van der Waals forces has been conducted. It is shown that as particles are brought together during drying, they deform under the influence of long-range electrostatic repulsion. The extent of the deformation depends critically on the repulsive forces and a parameter that includes the shear stiffness. If the particle is soft compared to the repulsive forces, large deformations of the particles are predicted even when the global energy minimum would indicate a flocculated state. This has important consequences for the processing of polymer colloids.

Studies of neck growth between acrylic polymer spheres show clear evidence for the viscoelastic character of this process and indicate that the early stage of neck growth is controlled entirely by recoverable (delayed-elastic) deformation. For polymers at temperatures near T_g the

recoverable compliance grows rapidly to a plateau value which is independent of molecular weight but varies substantially with molecular structure. These considerations lead to the prediction that for suitably small particles (corresponding to large surface tractions) an aggregate of polymer particles should sinter to full density by delayed elastic deformation alone requiring no contribution from viscous flow.

This final technical report is organized as follows. Sections 2 to 8 summarize the main accomplishments. Details for each section, where not available in published form, are provided in Appendices 3 to 7. Appendix 1 contains a list of publications and presentations based on this work. Appendix 2 contains information regarding transitions and connections resulting from this work.

Section 2 contains a description of the new surface formulation. Section 3 discusses the new quantity, the inter-surface stress tensor, that in the new formulation describes the influence of any body. Its implementation as a surface finite element is described in Section 4. Results of simulations of viscoelastic coalescence and of deformation under DLVO forces are summarized in Section 5. Experimental results are discussed in Section 6. Section 7 presents the use of the new formulation in extracting Hamaker constants from force measurements during atomic force microscopy. Section 8 describes ongoing work on the development of contact constitutive equations, discrete computational models, and continuum constitutive equations, and the direction in which we believe this work will lead.

2. Surface Formulation for Molecular Interactions of Macroscopic Bodies.

It was realized early in this work that the analysis of coalescence of particles requires a mathematical formulation for surface forces. This subject has a long history and has been approached in different ways, *e.g.*, at the discrete level of many atoms (Landman *et al.*, 1990; Harrison *et al.*, 1992, Rowlinson and Widom, 1982), or the continuous level, applicable to macroscopic problems (Hamaker, 1937; Herring, 1953; Orowan, 1970). Existing work on this problem was found to be inadequate and sometimes inconsistent. A description of molecular interactions as body forces or surface tractions is necessary for the construction of predictive models for processes such as sintering (Hiram & Nir, 1983; Jagota & Dawson, 1990), adhesion (Israelachvili, 1991; Johnson *et al.*, 1971; Derjaguin *et al.*, 1975), crack-tip deformations (Lawn, 1993; Chan *et al.* 1987), colloidal interactions, and atomic force microscopy (Landman *et al.*, 1990; Hartmann, 1991, Argento and French, 1996). There are two important macroscopic manifestations of molecular interactions. Interactions within a body manifest as surface tension (*self-interactions*); interactions between bodies (*other-body interactions*) influence phenomena such as adhesion and the behavior of colloids. In certain problems, such as sintering, both manifestations play an important role. Our goal is to develop a continuum formulation for surface forces that combines these two manifestations. Self-interactions are treated using the classical concept of surface tension. For the other-body interactions we present a new surface formulation.

Consider first other-body interactions. Let the potential energy of interaction between two molecules as a function of distance s be $w(s)$. The potential energy of interaction $e(s)$ between two elemental volumes dV_1 and dV_2 then is

$$e(s) = \rho_1 \rho_2 w(s) dV_1 dV_2, \quad (1)$$

where ρ_1 and ρ_2 are the number densities of molecules. These infinitesimal volumes interact, each with every other, and it is assumed that the total energy of the system is the sum of individual interaction energies. The interaction energy between two bodies defined by the volumes V_1 and V_2 is then given by the double volume integral

$$E = \iint_{V_2 V_1} \rho_1 \rho_2 w(s) dV_1 dV_2. \quad (2)$$

In like fashion, the total force of interaction between two bodies can be computed. The force of interaction between two molecules is the gradient of the potential energy

$$\mathbf{f} = -\nabla w. \quad (3)$$

The total force between two bodies is then given by

$$\mathbf{A} = \iint_{V_2 V_1} \rho_1 \rho_2 \mathbf{f}(s) dV_1 dV_2. \quad (4)$$

Interactions handled in this manner have been used to study adhesion of solids (Israelachvili, 1991; Derjaguin *et al.*, 1975), atomic force microscopy (Hartmann, 1991; Argento and French, 1996), and fracture (Chan *et al.*, 1987). The analytical integration of the pair potential to obtain the macroscopic interaction potential was done by Bradley (1932), de Boer (1936), and Hamaker (1937) for the specific case of van der Waals interactions. A compilation of their results can be found in Israelachvili (1991). This approach assumes: a) additivity: the total force can be obtained by the pairwise summation of individual contributions; b) continuous medium: the summation is replaced by an integration over the volume; c) constant material properties: the number densities ρ and the interaction constants do not vary over the volume of the bodies. The last assumption implies a step definition of the surface. The double-volume integrations are difficult to execute, both analytically and numerically, which has limited the application of this theory to simple geometries such as planar half-spaces and spheres. Because the potential $w(s)$ typically decays rapidly with distance s , the interaction forces are usually concentrated near the surface of the body. This fact makes it very difficult to integrate expressions (2) and (4) numerically. Much would be gained if the volume integral could be replaced by surface integrals.

Consider the case of two smooth bodies separated by a distance S , which is small compared to the radii of curvature. Derjaguin (1934) (see also Israelachvili, 1991) introduced an approximation that allows the double volume integral (4) to be replaced by a double surface integral. In its original form, the approximation was used to compute the total force between the bodies. It was shown that the interaction force equals the interaction energy of two half spaces separated by a distance S and multiplied by a geometrical factor that depends on the radii of curvature. The approximation has subsequently been adapted to impose distributed surface tractions for the analysis of deformation under surface forces (Muller *et al.*, 1980; Hughes and White, 1979; Chan *et al.*, 1987). The first step in the computation of tractions involves the determination of the interaction force $f(s)$ (per unit area) between two half-spaces as a function of the distance of separation s . The second step involves defining a symmetry direction (with unit vector \mathbf{E}) along which all tractions are assumed to act. Derjaguin's approximation does not specify if and how such a direction can be chosen in general. The traction \mathbf{T} at any point on the surface is then assumed to be:

$$\mathbf{T} = f(s)(\mathbf{E} \cdot \mathbf{n})\mathbf{E}, \quad (5)$$

where s is measured along \mathbf{E} .

Even when the total interaction force predicted by Derjaguin's approximation is accurate, the distribution of surface tractions can be very different from the actual field of distributed body forces. Analysis of local deformation may therefore be inaccurate. When the conditions under which Derjaguin's approximation is valid are not met, it is difficult even to define \mathbf{E} uniquely.

We have developed a new surface formulation for arbitrarily shaped bodies, without the geometrical limitations associated with Derjaguin's approximation. In this scheme the influence of a body is represented by a second order tensor: the *inter-surface stress tensor*. This tensor field depends on the shape of the body and the basic intermolecular potential. Upon an inner product with the surface normal of another body, it produces a surface traction.

Consider now interactions within an isolated body (self-interactions). As a result of unmatched molecular interactions near a free surface, the surface has an excess energy. This is the surface energy and is defined as the work required to create a new surface of unit area (Herring, 1953; Orowan, 1970; Rowlinson and Widom, 1982). It provides, for example, the driving force for shape change and the concept of equilibrium shapes of bodies. Closely associated with the surface energy is the surface stress which is distinguished from the surface energy as being the work required to stretch the surface. The surface stress can also be obtained directly in terms of the unbalanced interaction forces (Orowan, 1970; Defay *et al.* 1966). For an isotropic liquid, the surface stress is isotropic and tensile (a surface tension) and is numerically equal to the surface energy (Herring, 1953, Blakely 1973). The driving force for deformation in this case can be written as an effective surface traction proportional to the product of surface energy and surface mean curvature: the Young-Laplace equation (Adamson, 1976, Herring 1953). The Young-Laplace equation can also be derived directly in terms of unbalanced interaction forces (Rowlinson and Widom, 1982). This approach has been used widely to study deformation of fluids under the influence of surface energy (Batchelor, 1967; Jagota & Dawson, 1990; van de Vorst 1993). For an isolated body, this classical formulation is sufficient to describe the driving forces for deformation as long as the radii of curvature of the surface are large relative to the length scale of molecular interactions. For solid bodies, the relationship between surface stress and surface energy is more complex.

The surface formulation has been implemented as a surface finite element. In cases where the curvature formulation is invalid even for the self terms, for example at a cusp as in a sharp sintering neck, part of the body can be treated as another body. The surface formulation replaces the Derjaguin approximation and at the same time offers great advantages over full volume integration to obtain body forces. It is shown that full volume integration quickly becomes computationally intractable whereas it is possible, using the surface formulation, to analyze problems of macroscopic scale. We have applied it successfully to solve several problems: adhesion of elastic spheres, and the calculation of force-displacement laws for several body geometries.

Two types of problems can be addressed using the surface formulation presented here: the determination of the total interaction force/energy between several bodies and the computation of equivalent surface tractions to study their deformations. As has been described, the results for the total interaction force/energy are exact for any interaction potential. The surface formulation does not have the geometrical restrictions associated with Derjaguin's approximation. All this, of course, within the basic limitations of Hamaker's approach. The use of the surface formulation to calculate effective surface tractions on a body and to study its deformation may have some practical limitations. This is related to the fact that there is no unique way to distribute the integrated body force over the surface of the bodies. However, the scheme

presented here is very efficient for most important geometries. As has been shown, it produces a field of tractions on the body that is a very good approximation of the local body force field. This is specially true for potentials which decays rapidly with distance.

The surface formulation is able to handle dissimilar materials but is limited in its present form to isotropic and piecewise homogeneous materials. We have not explicitly considered here other surface forces such as electrostatic attraction or repulsion, steric repulsion, and hydration forces that often play a role in physical phenomena where the inter-molecular forces are important. Because these forces are, to begin with, expressed as surface forces, their inclusion in the expression for the total surface traction at a point poses no additional difficulty if their influence is additive.

This part of the work is described in detail in Argento, Jagota, and Carter (1996) which is attached as Appendix 3.

3. The Inter Surface Stress Tensor

The work described in the previous section resulted in the definition of a fundamental new quantity we term the *inter-surface stress tensor* \mathbf{h} . This tensor field depends on the shape of the body and the basic inter-molecular potential. Upon an inner product with the surface normal of another body, it produces a surface traction. The total energy of interaction between two bodies is obtained in a similar fashion in terms of surface integrals alone. The formulation is applicable to arbitrarily shaped bodies and offers major computational simplification.

This part of the work is devoted to a discussion of the new quantity that has emerged from the surface formulation: the inter-surface stress tensor. A new derivation of the surface formulation is developed that highlights some the properties of the inter-surface stress tensor. General properties such as symmetry, lack of positive definiteness, and reduction to Derjaguin's approximation are derived. This is a symmetric tensor which, like the internal stress tensor, yields a traction upon an inner product with the normal to a surface. The trace of the tensor represents the effective hydrostatic stress in an elemental volume and equals the volume integral of the molecular potential. Actual components of the tensor are computed for several geometries: a plane half-space, a quadrant, a sphere, and a cylinder. Although in general the two are different, it is shown that the new formulation and Derjaguin's approximation coincide for the case of a half-space. The new surface formulation yields the correct total force and energy of interaction; errors in Derjaguin's approximation can be quantified in other cases. The formulation can be used to analyze deformations driven by surface forces without restrictions on the geometry, large deformations, etc.

Details of this part of the work can be found in Jagota and Argento (1996) which is attached as Appendix 4.

4. Numerical Implementation

The new surface formulation leads naturally to the definition of a surface element for use with finite element methods. It has been implemented for planar, axisymmetric, and three-

dimensional geometries as a surface element in a commercial finite element code (ABAQUS®). This section describes the implementation briefly. The elements can be attached to any appropriate elements. They serve to transmit tractions due to surface forces to the discretized body and have not stiffness of their own. However, because surface forces depend strongly on the location of surface nodes, in a nonlinear solution procedure they contribute to the Jacobian matrix.

We describe here how a surface element is implemented to compute the surface tractions produced by the surface formulation of the molecular interactions. This element has no stiffness and, by virtue of being attached to volume elements, transmits surface tractions to the material. For further details on the general principles of implementing such an element in a finite element code refer to any text book on the finite element method, *e.g.*, Zienkiewicz (1989).

The surface of the structure is discretized into linear elements. The finite element method requires the computation of an element force matrix:

$$\mathbf{F} = \int_{S_e} \mathbf{N}^T \mathbf{T} dS, \quad (6)$$

where \mathbf{N} is the matrix of element shape functions and \mathbf{T} is the vector of tractions imposed on the element and the integral is done over the surface S_e of the element. In the following, details of the evaluation of this integral in the case of 2 and 3 dimensional elements are presented. The tractions \mathbf{T} are solution dependent since, as it is shown below, they are function of the curvature of the body and of the distance between the different surfaces. Therefore, in a non-linear finite element algorithm, such as the Newton-Raphson algorithm, it is necessary to take into account the surface tractions in the evaluation of the tangent (or Jacobian) matrix. The tangent matrix is defined as the derivative of the residual vector with regards to the solution variable, in this case the displacements. The residual vector is defined as:

$$\mathbf{R} = \mathbf{KU} - \mathbf{F}, \quad (7)$$

where \mathbf{K} is the nonlinear stiffness matrix, \mathbf{U} is the solution variable vector and \mathbf{F} is the force vector defined above. The component ij of the tangent matrix is defined as the derivative of the i component of the residual vector with regards to the j component of the solution variable vector:

$$J_{ij} = \frac{\partial R_i}{\partial U_j}. \quad (8)$$

Since our element has no stiffness ($\mathbf{K} = \mathbf{0}$), the components of the tangent matrix for these elements are simply

$$J_{ij} = -\frac{\partial F_i}{\partial U_j}. \quad (9)$$

The evaluation of the tangent matrix is done numerically and its details are presented below for each type of element.

The total traction consists of two parts: \mathbf{T}_o and \mathbf{T}_s corresponding to interactions with other bodies and self interactions respectively. Separate procedures are followed to compute these two contributions to the total traction. Consistency between the two is established by ensuring that the energy released by annihilation of surfaces due to contact equals the energy due to surface stretching. This implies that the surface tension equals the surface energy, an assumption that is strictly valid only for liquid-like materials.

4.1 Self force

It is known that an excess energy is associated with a free surface: the surface energy, which manifests itself as the surface tension. If the distance between a point inside a body and the nearest free surface is much larger than the typical range of the interaction forces, the point is equally surrounded by the material and the net force on it is zero. However, as this distance decreases, there is a net body force on the point and this is what we wish to compute.

It can be shown that the stress state at every point in a body, originating from all pair interactions within the body, can be identically reproduced when effective tractions are applied to the surface of this body. These effective tractions are computed using the Young-Laplace equation (Adamson, 1976), which gives a traction proportional to the product of the surface energy and the surface mean curvature:

$$\mathbf{T} = -\gamma \operatorname{tr}(\mathbf{k})\mathbf{n}, \quad (10)$$

where γ is the surface energy, \mathbf{k} is the surface curvature and \mathbf{n} is the surface normal. This formulation has been widely used to study the deformation of fluids under the influence of surface tension as, for example, in viscous sintering (Jagota and Dawson, 1990). It has the advantage of bypassing the singularity problem inherent to the self term (Argento et al. 1996). However, this expression cannot be applied directly to a body that has been discretized in linear elements, since the curvature is zero inside the element and indeterminate at the nodes. An exception to this situation is the axisymmetric element, which is detailed below. The force on the nodes of a linear element is obtained by an equivalent approach. The surface energy is written as a function of the coordinates of the nodes of the element. The force on the node along the different coordinates is then obtained by taking the derivative of the surface energy of the element with regards to the coordinate of the node. With this simple and straightforward scheme, the force vector for the element is obtained without the need of numerical integration of expression.

4.2 Plane elements

Considering first a 2-d plane stress element. The surface energy contained within the element is

$$E_\gamma = \gamma t \sqrt{(x_A - x_B)^2 + (y_A - y_B)^2}, \quad (11)$$

where t is the thickness of the element. The force on node A along direction x is given by

$$F_{xA} = -\frac{\partial E_\gamma}{\partial x_A}, \quad (12)$$

or

$$F_{xA} = \frac{\gamma t (x_B - x_A)}{\sqrt{(x_B - x_A)^2 + (y_B - y_A)^2}}. \quad (13)$$

The expression for the nodal forces in a plane strain element can be found in a similar fashion.

4.3 Axisymmetric elements

For the axisymmetric case each element represents the surface of a truncated cone. The surface energy associated with this geometry is obtained by multiplying the surface of the cone and the surface energy:

$$E_\gamma = \gamma \pi (r_B + r_A) \sqrt{(r_B - r_A)^2 + (z_B - z_A)^2}. \quad (14)$$

The force along the radial direction is defined as the negative of the derivative of the surface energy with regards to the radius, and on the node A is given by

$$F_{rA} = \gamma \pi \left[\frac{(r_B^2 - r_A^2)}{\sqrt{(r_B - r_A)^2 + (z_B - z_A)^2}} - \sqrt{(r_B - r_A)^2 + (z_B - z_A)^2} \right]. \quad (15)$$

The force along the z direction is given by

$$F_{zA} = \gamma \pi \frac{(r_B + r_A)(z_B - z_A)}{\sqrt{(r_B - r_A)^2 + (z_B - z_A)^2}}. \quad (16)$$

Both these expressions represent the total force that is distributed over the circumference $2\pi r_A$.

4.4 3-D Triangle

Consider now a triangular element with nodes A , B and C and sides a , b and c . The area of the triangle is

$$A_\Delta = \frac{1}{4} \sqrt{-a^4 + 2a^2b^2 - b^4 + 2a^2c^2 + 2b^2c^2 - c^4}, \quad (17)$$

which multiplied by the surface energy γ gives the total energy contained within the element.

As an example, the force on node A in the direction of the component x is obtained by taking the negative of the derivative of the total surface energy with regards to this component at the node, namely

$$F_{xA} = -\frac{\partial \gamma A_\Delta}{\partial x_A}, \quad (18)$$

or

$$F_{xA} = \gamma \frac{2a^2 x_A + (-a^2 - b^2 + c^2)x_B + (-a^2 + b^2 - c^2)x_C}{8 A_\Delta}. \quad (19)$$

4.4 Other-body force

This term represent the interactions between physically distinct bodies or, in the case of a single convex body, interactions between different regions of the body separated by a gap. The expression for the other-body traction developed in Argento et al. (1996) are in terms of surface integrals over interacting bodies. That is, to compute the traction at a point A on surface S_1 of body 1, one must integrate over the surface of all other bodies. Specifically, if only one other body is present:

$$\mathbf{T}_s = \rho_1 \rho_2 \int_{S_2} \mathbf{n}_2 \mathbf{G} dS_2, \quad (20)$$

where \mathbf{n}_2 is the normal to surface 2, and \mathbf{G} is a vector function of distance between two surface points. This quantity has to be computed at all surface quadrature points. In general, therefore, one must compute a surface integral for each quadrature point. This is accomplished by scanning over all the surface quadrature points of surface 2 to compute the traction on a quadrature point at surface 1. Because the kernel \mathbf{G} is typically decays rapidly with distance, only a few of the closest points on surface 2 contribute to any given point on surface 1. Some simplification can be

achieved by taking this into account. In the special case when surface 2 is a plane bounding a half-space one can make use of the fact that the surface formulation reduces to Derjaguin's approximation. In that case, equation (20) can be integrated analytically, obviating the need for one of the numerical integrations.

Details of the numerical implementation will be the subject of a forthcoming publication (Appendix 1). Fortran subroutines that contain the coding for the surface elements are available from the authors.

5. Growth of Adhesive Contacts for Viscoelastic Spheres

The new mathematical formulation for tractions based on surface forces has been applied to study the coalescence of viscoelastic spheres. The ability of surface tension to alter the shapes and increase the contact area of contacting particles is fundamental both to adhesion and sintering phenomena. Analyses of adhesive contacts (Johnson et al. 1971; Derjaguin et al. 1975; Muller et al 1980) have generally treated the particles as perfectly elastic. Analyses of sintering kinetics assume either a single mechanism for mass transport such as viscous flow (Kuczynski 1949; Frenkel 1945; Hiram & Nir 1983; Jagota & Dawson 1988) or some temperature-dependent superposition of such mechanisms (Ashby 1974; Swinkels & Ashby 1981). These models successfully account for experimental measurements within restricted regimes of time, particle size, and material parameters. However, they cannot be expected to fully account for the behavior of real materials whose mechanical response is inevitably more complex. For example, when two liquid droplets come into contact they deform immediately to an extent dictated by their instantaneous elastic compliance regardless of their viscosity. Thus the true initial condition for viscous sintering is a consequence of short-time viscoelastic character. Viscous sintering models customarily assume an arbitrarily small initial contact size, but the limitations of that approximation have never been systematically examined. Viscoelastic effects are especially prominent for polymer particles. Viscoelastic relaxations in polymer melts commonly span several decades in time and are manifest in experimental measurements of both adhesion (Johnson et al. 1971) and sintering (Lontz 1964; Mazur & Plazek 1994; Mazur 1995; Lin & Meier 1996).

In addition to the issue of material response, there remain unresolved questions concerning the proper representation surface forces. Existing models for elastic adhesion and viscous sintering have relied respectively on very different formulations of the surface tractions. Adhesive contact models invoke only the attractive forces operating across the gap between opposing surface elements when they approach within range of molecular van der Waals interactions. These forces "zip" the surfaces together, increasing contact area until elastic strain energy balances the decrease in surface energy. In contrast, models for viscous sintering invoke only forces associated with surface curvature which tend to "stretch" the circumference of the neck bounding the contact. Our objective herein is to develop a model for the evolution of particle shape, contact area, and stress distribution under intrinsic surface forces for contacting spheres with the properties of viscoelastic liquids. It turns out that both zipping and stretching modes are important in this problem. Consequently, the self-consistent prescription for both kinds of surface tractions developed as part of this work is crucial.

Calculations were performed for a Maxwell viscoelastic sphere of colloidal dimensions in contact with a smooth, rigid plane. In the limits of very short and very long times, the results agree well with the simple models for elastic and Newtonian materials respectively. However, the calculations reveal some unanticipated effects. The first stages of contact growth prove to be dominated by the zipping mode. Throughout this period the growth kinetics differs significantly from earlier viscous sintering models which neglect van der Waals forces. Moreover kinetics in the zipping regime do not scale with particle size, as do all the idealized models for sintering kinetics (Kuczynski 1949; Ashby 1974; Mazur 1995). The fraction of contact area contributed by zipping does, however, increases with decreasing particle size such that sufficiently small particles may sinter completely by this mechanism.

Coalescence of spherical particles begins with the formation of an initial elastic contact and proceeds by time-dependent contact growth. An initial elastic contact is formed which is in good agreement with the JKR model. There is a viscoelastic transition into viscous contact growth by a zipping mechanism. This stage of the mechanism is insensitive to the value of the initial elastic contact radius and is a mode of viscous deformation driven mainly by attractive forces outside the contact region. It is not found in existing models for viscous sintering. There is a second transition to a mode of contact growth governed by curvature-based tractions and characterized by a stretching mode of contact growth. The contact radius at which the second transition occurs depends primarily on the particle size. It decreases from a value as high as 0.6 to about 0.1 as one increases the sphere radius from 100 nm to 10 μm . For large spheres, the stretching mode of contact growth dominates over the entire range of contact radius; the converse is true for small spheres. However, for the range of particle sizes and material properties commonly used, both modes of contact growth are important.

Zipping and stretching are both viscous sintering; kinetics are governed by a characteristic time scale for a given particle size. However, it is shown that due to the fact of an additional length scale associated with van der Waals forces, there is no unique scaling with respect to particle size during the zipping mode of contact growth. When only Laplace-Young tractions are applied, the boundary conditions for a sphere on a rigid plane are identical to those for two identical spheres. However, the van der Waals forces for the case of two spheres are different. Because these tractions vary approximately as the cube of distance between surfaces, their influence compared to Young-Laplace tractions is smaller for two spheres versus a sphere on a rigid plane by a factor of eight. We have restricted our attention to sintering by viscoelastic deformation; accounting for direct attractive forces may influence models for sintering by other mechanisms as well.

The interaction of particles while still separated by a liquid prior to drying is also of great importance. An analytical and computational study of deformation of colloidal particles by DLVO and van der Waals forces has been conducted. It is shown that as particles are brought together as the body of which they form a part dries, they deform under the influence of long-range electrostatic repulsion. The extent of the deformation depends critically on the repulsive forces and a parameter that includes the shear stiffness. If the particle is soft compared to the repulsive forces, large deformations of the particles are predicted even when the global energy minimum would indicate a flocculated state. This has important consequences for the processing of polymer colloids.

A draft manuscript describing this part of the work in detail can be found in Appendix 5. We expect to publish further results of simulations on viscoelastic coalescence (Appendix 1).

6. Experimental Studies of Viscoelastic Coalescence

Our earlier studies of neck growth between acrylic polymer spheres showed clear evidence for the viscoelastic character of this process and indicated that the early stage of neck growth is controlled entirely by recoverable (delayed-elastic) deformation. For polymers at temperatures near T_g the recoverable compliance grows rapidly to a plateau value which is independent of molecular weight but varies substantially with molecular structure. These considerations led to the prediction that for suitably small particles (corresponding to large surface tractions) an aggregate of polymer particles should sinter to full density by delayed elastic deformation alone requiring no contribution from viscous flow. This expectation has been justified and quantified by the theoretical work presented in previous sections. The magnitude of the limiting particle size was estimated from the plateau compliance and surface tension for a number of common polymers. The size predicted for poly(tetrafluorethylene) is very close to that of the dispersion particles produced under commercial polymerization conditions. A more rigorous test was provided by experiments on a series of acrylic latex particles with diameters ranging from 0.14 to 1.55 μm . Consistent with expectations, for particles smaller than the limiting size (ca. 0.25 μm) the aggregates sintered rapidly to full density at temperatures just above T_g (78 °C) even when the polymer was a lightly cross-linked gel with essentially infinite viscosity. By contrast, for larger particles the final stage of densification required temperatures as high as 150 °C corresponding to Newtonian flow in the terminal regime.

Part of the work has been reported in Mazur (1995). A draft manuscript containing further details can be found in Appendix 6.

7. AFM Tip - Material Interactions

The surface formulation developed as part of this work promises to be a powerful tool for analyzing other phenomena controlled by surface forces. We have employed it to explore the possibility of extracting fundamental material properties from AFM measurements. The van der Waals force, which arises from the interaction of oscillating dipoles, has a role in controlling many aspects of the behavior of materials. It controls or influences macroscopic phenomena such as surface tension, wetting behavior, colloidal stability, fracture and adhesion. The van der Waals interactions can be quantified through the Hamaker constant (Israelachvili 1992), which is a material property, and through an appropriate force-distance relation, which is dependent on the system geometry.

The determination of the Hamaker constant is an important field of research. Ackler *et al.* (1996) provide a description of the different methods available to obtain the Hamaker constant for different materials and configurations. One technique is the observation of the manifestation of these interactions on a macroscopic scale, in a phenomenological approach. For example, the surface force apparatus (Tabor & Winterton 1969) has been used to determine the interaction force between crossed cylinders with surfaces of cleaved mica. Through an analysis such as the one presented by Hamaker (1937), the expression for the total interaction force for the specific

geometry and material configuration can be calculated. Following a fit of the force-distance relation obtained experimentally, the Hamaker constant is obtained. A similar and promising new approach is the use of atomic force microscopy (AFM), due to its intrinsic capability of measuring very small forces ($\sim nN$) at very small separations ($\sim nm$).

Atomic force microscopy is based on the determination of the interaction force between a probe and the substrate-sample. Different kinds of interactions may be present including electrostatic (Stern *et al.* 1988), magnetostatic (Martin *et al.* 1987), and van der Waals (Weisenhorn *et al.* 1989). The van der Waals interactions are omnipresent and, for a clean, uncharged and non-magnetic system, it can be the only force field present. In a procedure similar to the one described for the surface force apparatus, the Hamaker constant can be determined. So far, due to the difficulty involved in the integration to obtain the interaction force, the probe has been erroneously modeled with simple geometries, such as a sphere. The use of such models has prevented the accurate determination of the Hamaker constant for systems of interest.

The problem to be resolved can be stated as one of integrating the interaction force over the volumes of an arbitrary probe and the sample and obtaining a correct force-distance relation. The surface formulation developed in this work has proved useful in obtaining such a relation. We use a parametric model for a typical AFM probe. The interaction of this probe with a planar halfspace is obtained using the surface formulation. We then show that the traditional power-law relation used to describe the force-distance dependence of the interaction force is inadequate since the AFM tip-substrate force-distance relation (FDR) can not be approximated by a power-law. We then demonstrate that the parametric tip-substrate force-distance relation (PT/FDR) that we develop can be used to fit (non-linear fit) experimental data and to determine both the tip parameters and the Hamaker constant for the material configuration.

A study on numerically generated data set shows that, in the more common cases when the tip radius is large, the determination of Hamaker constant from the non-linear fitting routine is compromised by the fact that the Hamaker constant and the tip radius are redundant parameters. In these cases, the angle of the conical part of the probe is irrelevant, especially when the data has a high noise to signal ratio at large separations. However, the same analysis shows that all the three parameters can be accurately extracted from the data if the tip radius is small. This is specially interesting since, in these cases, the sphere model is completely invalid. The non-linear fitting routine is very efficient when there is no redundancy of parameters in the PT/FDR, as in the small radius regime.

A manuscript containing details of this part of the work can be found in Appendix 7.

8. Discrete Numerical Methods and Continuum Modeling

To develop a micro-mechanical constitutive model for viscoelastic granular materials one needs additionally to consider viscoelastic contact problems driven by external tractions. Detailed numerical computations of viscoelastic contact problems under forces along the contact normal have been conducted (Paliwal 1995). These confirm the validity of analytical results (Lee & Radok 1960; Ting 1968) upto large contacts. One-dimensional contact constitutive equations for contacting spheres deformed in shear and torsion have been developed using the viscoelastic correspondence principle and Mindlin's (1949) solutions for the corresponding elastic problems.

Contact constitutive relations when a pair of particles deforms simultaneously in the different modes of deformation have been developed but remain to be tested by numerical simulation. These form the basis both for the development of continuum constitutive relations and for discrete numerical tools for the simulation of viscoelastic deformation of sets of particles. A discrete formulation for the simulation of the deformation of many-particle systems is under development. It is an extension of a previously developed *quasi*-static formulation for elastic and viscous materials to visco-elastic contacts (Jagota & Scherer 1995).

9. References

ABAQUS (TM), Hibbit, Karlsson & Sorensen, Inc., Tel: (401) 727 4200.

H.D. Ackler, R.H. French and Y.-M. Chiang., *J. Coll. Int. Sci.* **179**, 460 (1996).

Adamson, A.W. (1976) *Physical Chemistry of Surfaces*, 3rd Ed., John Wiley and Sons.

Argento, C. and French R.H. (1996), Parametric tip model and force-distance relation for Hamaker constant determination from AFM, *Journal of Applied Physics*, in press.

Argento C. and Jagota A. (1996), A surface finite element for molecular interactions, in preparation.

Ashby M.F. (1974), A first report on sintering diagrams, *Acta Metallurgica*, **22**, 275-289.;
Swinkels F.B., Ashby M.F., (1981) A second report on sintering diagrams, *Acta Metallurgica*, **29**, 259-281.

Batchelor G.K. (1967), *An introduction to fluid dynamics*, Cambridge University Press, Cambridge, U.K.

Bradley R.S. (1932), The cohesive force between solid surfaces and the surface energy of solids, *Phil. Mag.*, **13** 853-862.

Chan, D.Y.C., Hughes, B.D. and L.R. White (1987) A physically consistent theory of fracture in a brittle solid, *J. Colloid Interface Sci.*, **115** [1] 240-259.

de Boer, J.H. (1936), The influence of van der Waals' forces and primary bonds on binding energy, strength and orientation, with special reference to some artificial resins, *Trans. Faraday Soc.*, **32** 10-38.

Defay R., Prigogine I., Bellemans A., (1966), *Surface Tension and Adsorption*, D.H. Everett (translator), Longmans, Green, & Co., London.

Derjaguin, B.V. (1934) Untersuchungen über die Reibung und Adhäsion, IV, (Investigations concerning friction and adhesion IV), *Kolloid Z.*, **69** 155-164.

Derjaguin, B.V., Muller, V.M. and Toporov, Y.P. (1975) Effect of contact deformations on the adhesion of particles, *J. Colloid Interface Sci.*, **53** [2] 314-326.

Frenkel J., (1945) Viscous flow of crystalline bodies under the action of surface tension, *J. Phys (Moscow)*, **9** [5] 385-391.; J.D. Eshelby, *Met. Trans.*,), Discussion of a paper by A.J. Shaler, "Seminar on the kinetics of sintering" **185**, 796, (1949).

Hamaker, H.C. (1937) The London-van der Waals attraction between spherical particles, *Physica*, **4** 1058-1072.

Hartmann, U. (1991) Theory of van der Waals microscopy, *J. Vac. Sci. Technol. B*, **9** [2] 465-469.

Herring C., (1953), The use of classical macroscopic concepts in surface-energy problems, in *Structure and Properties of Solid Surfaces*, R. Gomer and C.S. Smith (eds.), University of Chicago Press.

Hiram, Y. and Nir, A. (1983) A Simulation of surface tension drive coalescence, *J. Colloid Interface Sci.*, **95** [2] 462-470.

Hughes B.D., White L.R. (1979), Soft contact problems in linear elasticity, *Q. J. Mech. App. Math.*, **32** [4] 445-471.

Israelachvili, J. (1991) {lit Intermolecular and Surface Forces}, second edition, Academic Press, San Diego (USA).

Jagota A., Dawson P.R. , (1988) Micromechanical modelling of powder compacts - I. Unit problems for sintering and traction induced deformation, *Acta Metallurgica*, **36** [9] 2551-2561.

Jagota A., Scherer G.W., Viscosities and sintering rates of composite packings of spheres, *Journal of the American Ceramic Society*, **78** [3] 521-528 (1995).

Jagota A. and Dawson, P.R. (1983) Simulation of viscous sintering of two particles, *J. Am. Ceram. Soc.*, **73** [1] 173-177.

Johnson, K.L., Kendall K. and Roberts A.D. (1971) Surface energy and the contact of elastic solids, *Proc. R. Soc. Lond. A*, **324** 301-313.

Kuczynski G., *J. Met. (Met. Trans.)*, **1**, 169, (1949).

Landman, U., Luedtke, W.D., Burnham, N.A. and Colton, R.J. (1990) Atomistic mechanism and dynamics of adhesion, nanoidentation and fracture, *Science*, **248** 454-461.

Lawn, B.R. (1993) *Fracture of Brittle Solids*, Second edition, Cambridge University, New York.

Lee E.H. & Radok J.R.M., The contact problem for viscoelastic bodies, *Journal of Applied Mechanics*, 438-444 (1960).

Lin & D.J. Meier, *Langmuir*, **12**, 2774, (1996).

Lontz J.J., in *Fundamental Phenomena in Materials Sciences*, (eds. L.J. Bonis & H.H. Hausner), Vol. 1, pp.25-47, Plenum , 1964.

Martin Y. and Wickramasinghe K.K., *Appl. Phys. Lett.* **50**, 1455 (1987).

Mazur S. & Plazek D.J., *Prog. Org. Coatings*, **24**, 225, (1994).

Mazur S., (1995), Coalescence of Polymer Particles, Chap. 8, in *Polymer Powder Technology*, M. Narkis, N. Rosenzweig (editors), John Wiley & Sons, New York.

Mindlin R.D. (1949), "Compliance of elastic bodies in contact" *Journal of Applied Mechanics*, 259-268.

Muller V.M., Yushchenko V.S., Derjaguin B.V. (1980), *Journal of Colloid and Interface Science*, **77** [1] 91-101.

Orowan E., (1970), Surface energy and surface tension in solids and liquids, *Proc. R. Soc. Lond. A*, **316** 473-491.

Paliwal M., (1995), Numerical Simulation of Viscoelastic Contact Problems, *Master of Technology Thesis*, Indian Institute of Technology, Delhi.

Stern J.E., Terris B.D., Mamin H.J. and Rugar D., *Appl. Phys. Lett.* **53**, 2717 (1988).

Tabor D. and Winterton R.H.S., *Proc. Roy. Soc.* **312**, 435 (1969).

Ting T.C.T. (1968) "Contact problems in the linear theory of viscoelasticity", *Journal of Applied Mechanics*, 248-254.

Weisenhorn A.L., Hansma P.K., Albrecht T.R., and Quate C.F., *Appl. Phys. Lett.* **54**, 2651 (1989).

Zienkiewicz O.C., Taylor R.L., *The Finite Element Method*, Fourth Edition, McGraw-Hill (London) (1989).

Appendix 1

Publications and Presentations

1. C. Argento, S. Mazur, & A. Jagota, "Problems in Viscoelastic Neck Growth", in *Sintering Technology*, proceedings of *Sintering 1995 - An international Conference on the Science, Technology, and Applications of Sintering*, held at Pennsylvania State University, Sept. 24-27, 1995.
2. S. Mazur, "Coalescence of Polymer Particles", Chap. 8 in *Polymer Powder Technology*, edited by M. Narkis & N. Rosenzweig, John Wiley & Sons Ltd., 1995.
3. C. Argento, A. Jagota & W.C. Carter, "Surface Formulation for Molecular Interactions of Macroscopic Bodies", accepted for publication in the *Journal of the Mechanics and Physics of Solids*, (1996).
4. C. Argento, R.H. French, "Parametric tip model and force-distance relation for Hamaker constant determination from AFM", *Journal of Applied Physics*, in press (1996).
5. A. Jagota, C. Argento, "An Inter-Surface Stress Tensor", submitted to the *Journal of Colloid and Interface Science*, (1996).
6. S. Mazur & C. Argento, "Mechanical Forces and Material Response in the Coalescence of Polymer Particles", proceedings of American Chemical Society (Division of Polymeric Materials Science & Engineering), Symposium Series volume on Film Formation v. 73, p. 47 (1995).
7. S. Mazur, "Paste Extrusion of Polytetrafluoroethylene Fine Powders", Chap. 15 in *Polymer Powder Technology*, edited by M. Narkis & N. Rosenzweig, John Wiley & Sons Ltd., 1995.
8. S. Mazur, A. Jagota, "Non-contact deformation of elastic particles by DLVO forces", poster presented at the *Gordon Conference on Colloidal, Macromolecular, and Polyelectrolyte Solutions*, February 1996.
9. S. Mazur, R. Beckerbauer, "Sintering of Polymer Colloids", poster presented at the *Symposium of Liquid Crystals, Colloids, and Emulsions*, University of Pennsylvania, May 1996.
10. C. Argento & R. French, "Force Displacement Curves for AFM Tips", presented at the American Ceramic Society Basic Science Fall Meeting, November 1995.

In preparation

- 1 C. Argento, A. Jagota, "A Surface Finite Element for Molecular Interactions", to be submitted to *Computational Materials Science* (1996).

2. S. Mazur, A. Jagota, "Non-contact deformation of spherical particles under DLVO forces", to be submitted to the *Journal of Colloid and Interface Science* (1996).
- 3 C. Argento, A. Jagota, S. Mazur, "Viscoelastic coalescence of spherical particles", to be presented at *Powders and Grains '97*, an International Conference on Granular Materials, May 1997.
- 4 A. Jagota, C. Argento, "An Inter-Surface Stress Tensor", to be presented at the *SIAM Conference on Mathematical Aspects of Materials Science*, May 1997.
- 5 S. Mazur, R. Beckerbauer, J Buckholz, "Particle size limits for viscous sintering of polymer particles".
6. C. Argento, A. Jagota, S. Mazur, "Growth of Adhesive Contacts for Maxwell Viscoelastic Spheres", to be submitted to *Journal of Applied Physics* (1996).

Appendix 2

Interactions/Transitions

A - Meetings

1 - AFOSR Workshop on Environmental Effects on High Performance Polymers and Composites, May 25, '95, Fairborn, Ohio. (A copy of transparencies used in the program review are included in the Appendix

2 - National Meeting of the American Chemical Society, Aug. 21, '95, Chicago, Ill. The paper (see V-2 above) was presented by Dr. Mazur in the Polymeric Materials Symposium on Film Formation.

3 - "Sintering 1995 - An international Conference on the Science, Technology, and Applications of Sintering", Sept. 24. The paper (see V-1 above) to be presented by Dr. Argento.

4 - American Ceramic Society Basic Science Fall Meeting , November, 1995. The paper (see V-4 above) was presented by Dr. Argento.

5 - Annual meeting of the American Ceramic Society, April 1996.

6 - SIAM meeting on Mathematics in Materials Sciences, Philadelphia PA, May 1997.

7 - Powders and Grains '97, Durham NC, May 1997.

B - New Directions and Collaborations

1 - The surface formulation was developed in collaboration with Dr. W.C Carter, NIST, Ceramics Division.

2 - Applications of the surface forces analysis to AFM measurements was done in collaboration with Dr. Roger French (Dupont - CR&D).

3 - Applications of the surface force analysis to study crack tip profile in brittle fracture, is being pursued in collaboration with Dr. Stephen Bennison (Dupont - CR&D).

4 - The role of particle size, polymer rheology, and colloidal interactions in particle deformation during drying and sintering of polymer colloids is a subject of continuing experimental investigations. This study makes use of a series of well-characterized acrylic co-polymer latex particles with narrow size distributions prepared by Dr. R. Beckerbauer (DuPont - CR&D).

5 - Small angle X-ray and neutron scattering studies are in progress to determine the changes in internal surface area and evolution of morphology in aggregates of polymer colloids and

films obtained from the coalescence of latex dispersions. These studies are in collaboration with Drs. G.D. Andrews and A. Biswas (DuPont), and C. Glinka (NIST).

6 - A collaboration has been established with Professor D. Weitz's group at the University of Pennsylvania (Physics Department) to investigate the evolution of structure and mechanical properties during drying of polymer latex dispersions. Using materials prepared at DuPont (see item 4) a combination of different methods will be employed to characterize highly concentrated dispersions and the drying process itself. We plan to exploit theory and modelling capabilities developed over the past two years in this study.

Appendix 3

1. "Problems in Viscoelastic Neck Growth", C. Argento, S. Mazur, A. Jagota, in *Sintering Technology*, R.M. German, G.L. Messing, R.G. Cornwall (editors), 21-28, Marcel Dekker (New York), 1996.
2. "Surface formulation for Molecular Interactions of Macroscopic Bodies", C. Argento, A. Jagota, W.C. Carter, *Journal of the Mechanics and Physics of Solids*, in press (1996).

Appendix 4

“An Inter Surface Stress Tensor”, A. Jagota, C. Argento, submitted to the *Journal of Colloid and Interface Science* (1996).

Appendix 5

1. "Growth of Adhesive Contacts for Maxwell Viscoelastic Spheres", A. Jagota, C. Argento, S. Mazur, to be submitted to *Journal of Applied Physics* (1996).
2. "Non-contact deformation of elastic particles by DLVO forces," S. Mazur, A. Jagota, poster presented at the *Gordon Conference on Colloidal, Macromolecular and Polyelectrolyte Solutions* (1996).
3. "Mechanical forces and material response in the coalescence of polymer particles", *American Chemical Society Symposium series of Film Formation* (Division of Polymeric Materials Science and Engineering) (1996).

Appendix 6

1. “Sintering of Polymer Colloids,” S. Mazur & R. Beckerbauer, poster presented at the *Symposium of Liquid Crystals, Colloids, and Emulsions*, University of Pennsylvania (1996).
2. “Particle size limits for viscous sintering of polymer particles”, S. Mazur R. Beckerbauer, J. Buckholz.

Appendix 7

“Parametric tip model and force-distance relation for Hamaker constant determination from Atomic Force Microscopy”, C. Argento, R.H. French, *Journal of Applied Physics*, in press (1996).



Sintering Technology

edited by

Randall M. German
Gary L. Messing
Robert G. Cornwall

*The Pennsylvania State University
University Park, Pennsylvania*

Marcel Dekker, Inc.

New York • Basel • Hong Kong

Library of Congress Cataloging-in-Publication Data

Sintering technology / edited by Randall M. German, Gary L. Messing, Robert G. Cornwall.

p. cm.

Includes index.

ISBN 0-8247-9775-2 (hardcover : alk. paper)

1. Sintering—Congresses. I. German, Randall M. II. Messing, Gary L. III. Cornwall, Robert G.

TN695.S594 1996

671.3'73—dc20

96-26522

CIP

The publisher offers discounts on this book when ordered in bulk quantities. For more information, write to Special Sales/Professional Marketing at the address below.

This book is printed on acid-free paper.

Copyright © 1996 by MARCEL DEKKER, INC. All Rights Reserved.

Neither this book nor any part may be reproduced or transmitted in any form or by any means, electronic or mechanical, including photocopying, microfilming, and recording, or by any information storage and retrieval system, without permission in writing from the publisher.

MARCEL DEKKER, INC.
270 Madison Avenue, New York, New York 10016

Current printing (last digit):

10 9 8 7 6 5 4 3 2 1

PRINTED IN THE UNITED STATES OF AMERICA

Problems in Viscoelastic Neck Growth

C. Argento, S. Mazur, and A. Jagota

Central Research & Development Division
E.I. Dupont de Nemours & Co. Inc. - P.O. Box 0356
Wilmington, DE 19880-0356

Abstract

Particle coalescence is central to many industrial fabrication processes for organic polymers. While formally analogous to the sintering of inorganic materials, the mechanics and kinetics which govern polymer coalescence are fundamentally different, in large part because of the viscoelastic rheology of high molecular weight polymers. These issues are reviewed in relation to neck growth between spheres. Our objective is to develop physically rigorous computational models for visco-elastic coalescence of polymer particles based on realistic rheology, particle size, and force fields.

I- Viscoelastic Response of Amorphous Polymers

Coalescence of an aggregate into a uniformly dense body requires deformation of the component particles into space-filling shapes. A sufficient description of the time-dependent response to deviatoric stresses for an isotropic material is provided by the shear compliance $J(t)$ and Poisson's ratio ν (which may also be time-dependent). $J(t)$ equals the ratio of strain at time t to a constant stress imposed on the fully relaxed sample at $t=0$. The stress-strain relation is defined using the Boltzman superposition principle:

$$\mathbf{e}(t) = \int_{-\infty}^t J(t-t') \frac{d\mathbf{s}(t')}{dt'} dt' \quad (1)$$

where \mathbf{e} is the deviatoric strain and \mathbf{s} is the deviatoric stress. An analogous expression applies for the bulk compliance.

For linear high molecular weight polymers, $J(t)$ reflects kinetic processes which span several decades in time (Plazek, 1980) and can be partitioned into recoverable and Newtonian viscous contributions:

$$J(t) = J_r(t) + t / \eta_0 \quad (2)$$

The recoverable compliance $J(t)$ represents that part of the time-dependent strain which will spontaneously recover if the stress is removed at time t .

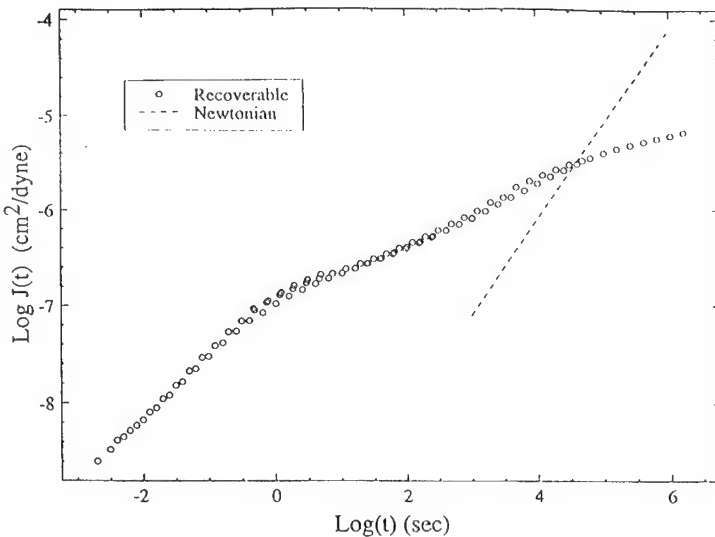


Figure 1: Shear creep compliance for poly(methyl methacrylate co ethyl acrylate), molecular weight 101,000. Data at four different temperatures has been reduced to 133°C (Mazur & Plazek, 1994).

Figure 1 illustrates typical behavior for an acrylic copolymer with broad molecular weight distribution at 20°C above its glass temperature T_g . $J(t)$ increases from the glassy value ($J(0) < 1\text{GPa}^{-1}$) to about 2 MPa^{-1} in the "plateau" regime. It is noteworthy that viscous flow remains negligible relative to $J_r(t)$ for more than three hours. Since η_0 increases strongly with polymer molecular weight while the growth in $J_r(t)$ through the plateau regime is relatively insensitive, it is not uncommon to find even greater temporal separation of the two deformation mechanisms. Moreover, the principle of time/temperature super-position (Ferry, 1980) (thermo-rheological simplicity) dictates that retardation times for the growth of $J_r(t)$ and t / η_0 respectively will decrease by the same factors with increasing temperature. Thus even at much higher temperatures, recoverable viscoelastic deformation is always several orders of magnitude faster than viscous flow.

For times and temperatures corresponding to the plateau regime, polymer melts resemble an ideal elastic material with time-invariant

compliance J_n , ($J_n \sim 2 \text{ MPa}^{-1}$ in Fig. 1). A logical starting point for analyzing deformation of viscoelastic particles is the corresponding mechanics for elastic materials.

II - Elastic Deformation for Various Forces

Particle deformation and the growth of interparticle contacts may be driven by different kinds of forces depending upon processing conditions. Analytic results for equilibrium elastic contacts under applied loads or surface tension provide some insights relevant to actual processing conditions for polymers.

In compression molding a polymer powder is heated above T_g and subjected to applied load. For a pair of elastic spheres of radius r and compliance J_n pressed together by an axial force F , the radius of the contact x may be calculated at small contacts according to Hertz (Timoshenko & Goodier, 1955):

$$\frac{x}{r} = \left[\frac{3(1-\nu)J_n F}{8r^2} \right]^{\frac{1}{3}} = \left[\frac{3\pi(1-\nu)J_n P}{8} \right]^{\frac{1}{3}} \quad (3)$$

where P is the mean interparticle pressure. Starting from a regular packing of spheres, the extent of densification can be related to growth of the dimensionless contact radius x/r . For realistic packing densities complete densification is achieved at $x/r \approx 0.58$ (Mazur, 1995). According to Eq. 3 this limit corresponds to $P \approx 1/(3J_n)$ and is independent of particle size (r). For the acrylic polymer of Fig. 1, Eq. 3 predicts that full density should be achieved with pressures of order 200 KPa. In the absence of other processes, elastic densification is perfectly reversible so that the sample would return to its initial density upon removing the load. In practice irreversibility is a consequence of the relaxation of the elastic stresses and diffusion of polymer chains across the particle interfaces. These processes require times comparable to the terminal relaxation time $\tau_n = J_n \eta_0$ (Mazur, 1995). Thus compression molding times are primarily governed by internal relaxation which has little to do with densification *per se*.

In the absence of external loads, neck growth and particle deformation may be driven by interfacial tension γ between the polymer and surrounding medium (for example, air). By assuming that the surface forces operate only across the contact, Johnson, Kendall, & Roberts (1971) (JKR theory) extended Hertz's analysis to obtain the following expression:

$$\frac{x}{r} = \left[\frac{9\pi(1-\nu)J_n \gamma}{8r} \right]^{\frac{1}{3}} \quad (4)$$

Unlike the simple Hertz case, here x/r depends explicitly on r . For a given material such that J_n , v , and γ are constants, the extent of deformation may be increased by decreasing r . Thus to achieve $x/r=0.58$ requires $r \geq 9\gamma J_n$.

These models for elastic materials reveal the importance of $J_r(t)$ for neck growth in the plateau regime, but they are of limited predictive value. Firstly, equations (3) and (4) are derived in the limit of small contact area with uncertain reliability for $x/r \sim 0.5$. Secondly, the relationship between an equilibrium elastic contact and the kinetics of viscoelastic growth of a contact is non-trivial. Substitution of $J_r(t)$ for J_n in eq.(4), which is inconsistent with Boltzmann's superposition principle, predicts neck growth kinetics in qualitative agreement with experiment (Mazur & Plazek, 1994) but results in large quantitative error in the time scale. A more sophisticated approximation (Lee & Radok, 1960) (still limited to small contacts) requires independent knowledge of the stress history and is therefore inapplicable to neck growth driven by surface tension.

III- Interfacial Driving Forces

A rigorous analysis of neck growth requires accurate description of the interfacial forces originating from deviation in molecular interactions near a surface relative to those in the bulk. These forces may be manifest in continuum mechanics in three different ways depending upon the size and structure of volume elements over which the molecular interactions are formally integrated.

The least detailed manifestation of surface forces (the thermodynamic approach) corresponds to the integration of molecular interactions over the entire body. Thus the interfacial force associated with a change in some linear dimension of an object equals the corresponding derivative of the surface energy (surface area times γ). This isotropic average force reveals nothing about the local deviatoric stress field responsible for specific changes of shape. A more localized manifestation of surface forces corresponds to integration of molecular interactions along the "immediate continuous vicinity" of a local volume element. The driving force for deformation of the volume element may be obtained from the Young-Laplace equation (Adamson, 1976), which gives an effective surface traction proportional to the product of surface energy and surface curvature. The tractions acting on a curved surface is then:

$$\mathbf{t} = -\gamma \mathbf{tr}(\mathbf{k})\mathbf{n} \quad (5)$$

where \mathbf{t} is the surface traction from the excess free energy, γ is the surface free energy, \mathbf{k} is the surface curvature and \mathbf{n} is the surface normal. This approach has been successfully used to study fluid deformation, as in viscous sintering (Jagota & Dawson, 1990; Hiram & Nir, 1983). However, preliminary

calculations showed that it fails when the material is elastic or viscoelastic. The main contribution of this term is the expansion of the contact area, not the creation of new contact, which is qualitatively different from what is observed in experiments.

None of these manifestations can describe the interactions of molecules operating across a gap of a second medium. In this case, the complete description of the interaction potential is necessary. For non-polar polymer molecules, it is assumed that the interactions are of Van der Waals type and can be described by a Lennard-Jones potential. Continuum mechanics assumes a uniform density distribution which is a valid approximation only for intermolecular distances larger than the minimum in this potential (the nearest neighbor separation). For this purpose only the attractive part of the potential is important and it will be necessary to truncate integrations at some cut-off distance, which is large compared to the minimum in the true molecular potential.

The attractive potential is expressed by:

$$w = -A / (\pi^2 d^n) \quad (6)$$

where A is the Hamaker constant for the given material configuration and d is the distance between the two molecules. For the case of Van der Waals interactions, in the non retarded regime, $n=6$ (Israelachvili, 1994). This contribution has been widely studied under the scope of elastic adhesion (Derjaguin, Muller & Toporov, 1975) (DMT theory). In the DMT model, the adhesion is presumed to result entirely from Van der Waals attraction outside of the area of contact. In contrast, in the JKR model, the adhesive forces are derived from the thermodynamic approach and assumed to be entirely restricted to within the contact area.

The force acting on a point of body V_1 due to another volume V_2 is given by the volume integration:

$$\mathbf{f} = \int_{V_2} \nabla w dV_2 \quad (7)$$

This volume integration is very time consuming and extremely sensitive to the mesh coarseness. Since these forces are concentrated near the surface (Tabor, 1981), it would be useful to express them in terms of a surface force resulting from a surface integration. Therefore, the approach adopted was the one derived by Argento, Jagota & Carter (in preparation). It consists of a new integration method for inverse power law body forces of high order ($n>3$) that allows the reduction of the three dimension volume integration to a two dimension surface integration. The body force field \mathbf{f} is replaced by a surface stress tensor \mathbf{h} , of the form:

$$\mathbf{h} = \int_{S_2} \mathbf{G} dS_2 \quad (8)$$

where S represents the surface of bodies 1 and 2. The kernel \mathbf{G} has the following form:

$$\mathbf{G} = \frac{x_i \mathbf{e}_i}{(3-n)(\mathbf{x} \cdot \mathbf{x})^{\frac{n}{2}}} \quad (9)$$

where \mathbf{x} is the vector linking the point on the surface of 1 to a point on the surface of 2, x_i is the component of \mathbf{x} on the direction \mathbf{e}_i , which is the coordinate system unitary base vector. In the case of near parallel surfaces, like the region near the contact zone between two large spheres, this scheme reduces to the well known "Derjaguin approximation" (Derjaguin, 1934).

IV- Numerical Study

Since no adequate analytical model exists to describe the kinetics of viscoelastic neck growth under the conditions described beforehand, it seems convenient to study this problem with the help of a numerical tool such as the finite element method. Therefore, the method described in the previous section was implemented in the ABAQUSTM finite element code (Hibbit, Karlsson & Sorensen, Inc.). Calculations were made of contacts of elastic spheres where surface forces were represented by a combination of Young-Laplace and van der Waals contributions.

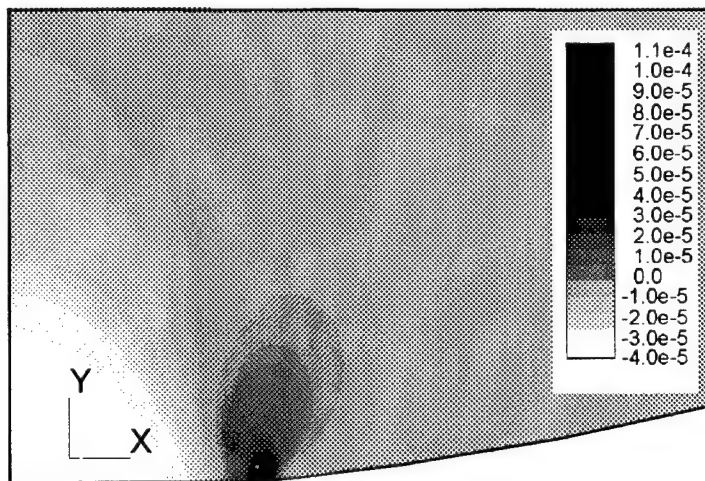


Figure 2: Vertical stresses near the contact between a deformed viscoelastic sphere and a plane.

In preliminary calculations the results were found to be sensitive to the cut-off distance. For an appropriate choice of the cut-off (by trial and error), we obtained a good agreement with the JKR analytical model. Figure 2 shows the vertical stresses in a close-up around the contact between a deformed viscoelastic sphere and a rigid plane. It can be seen that the stress profile is close to the one predicted by the JKR theory, the external ring of the contact is under high tensile stresses while the core of the contact is under compressive stresses.

Some preliminary viscoelastic calculations have also shown that, in agreement with experimental results (Mazur & Plazek, 1994) the time scale of relaxation of the contact radius is orders of magnitude greater than the time scale the time scale of relaxation of the material.

V- Conclusion

A numerical model to describe elastic and viscoelastic neck growth under interfacial forces was implemented in a finite element code and some preliminary calculations were performed. So far, the following can be concluded:

- the curvature formulation based on the surface energy alone is not sufficient to describe the kinetics observed.
- the choice of the cut-off distance for the integration of the attractive potential is very important, a rational criterion for this choice is being worked out.
- qualitative agreement between numerical calculations and experiments has been obtained for viscoelastic sintering, showing the difference of many orders of magnitude between the relaxation time of the radius of contact and the relaxation time of the material.

Acknowledgment

This work has been supported by the Air Force Office of Scientific Research under Grant F49620-95-C-0008

References

D.J. Plazek, in "Methods of Experimental Physics", Vol. 16c, Chap. 11, Academic Press, (1980).

J.D. Ferry, "Viscoelastic Properties of Polymers", 3rd Ed., John Wiley & Sons, (1980).

H. Hertz, as summarized in S.P. Timoshenko & J.N. Goodier, "Theory of Elasticity", 3rd Ed., McGraw-Hill, London, (1955).

S. Mazur, Chap. 8 in "Polymer Powder Technology", M. Narkis & N. Rosenzweig, Ed's., John Wiley & Sons, (1995).

K.L. Johnson, K. Kendall, & A.D. Roberts, "Surface Energy and the Contact of Elastic Solids", *Proc. Roy. Soc. Lond.*, A., 324 301-313 (1971).

S. Mazur & D.J. Plazek, "Viscoelastic Effects in the Coalescence of Polymer Particles", *Prog. Org. Coat.*, 24 225-236 (1994).

E.H. Lee & J.R.M. Radok, "The Contact Problem for Viscoelastic Bodies", *Trans. ASME, J. Appl. Mech.*, 438-444 (1960).

C. Herring, "Effect of Change of Scale on Sintering Phenomena", *J. Appl. Phys.*, 21 301-303 (1950).

A.W. Adamson, "Physical Chemistry of Surfaces", pp 4-6, 3rd Ed., John Wiley & Sons, (1976).

A. Jagota and P.R. Dawson, "Simulation of viscous sintering of two particles", *J. Am. Ceram. Soc.*, 73 [1] 173-177 (1990).

Y. Hiran & A. Nir, "A Simulation of Surface Tension Drive Coalescence", *J. Colloid Interface Sci.*, 95 [2] 462-470 (1983).

J. Israelachvili, "Intermolecular & Surface Forces", pp. 155-159, 2nd edition, Academic Press, New York, (1994).

B.V. Derjaguin, V.M. Muller & Y.P. Toporov, "Effect of Contact Deformations on the Adhesion of Particles", *J. Colloid Interface Sci.*, 53 [2] 314-326 (1975).

D. Tabor, "Surface Forces and Surface Interactions", *J. Colloid Interface Sci.*, 58 [1] 2-13 (1977).

C. Argento, A. Jagota & C. Carter, "Surface Formulation for Body Forces", in progress.

B.V. Derjaguin, "Untersuchungen über die Reibung und Adhäsion, IV", *Kolloid Z.*, 69 155-164 (1934).

Hibbit, Karlsson & Sorensen, Inc., Tel.: (401) 727 4200.

Surface Formulation for Molecular Interactions of Macroscopic Bodies

C. Argento

Central Research and Development, The DuPont Company

Wilmington, DE 19880-0356, USA

A. Jagota

Department of Applied Mechanics, Indian Institute of Technology (Delhi)

Hauz Khas, New Delhi 110016, INDIA

W.C. Carter

National Institute of Standards & Technology, Ceramics Division

Gaithersburg, MD 20899, USA

submitted to the *Journal of the Mechanics and Physics of Solids*

Paper No.: 96/511

Abstract

The determination of forces resulting from molecular interactions between macroscopic bodies is important for the analysis of a variety of processes such as sintering, adhesion, and fracture. Body forces resulting from these interactions are usually concentrated near the surfaces of the bodies and are responsible for phenomena such as surface tension and surface energy. In the formulation presented here, the volume integrated intermolecular force between bodies is partitioned to obtain a distribution of effective surface tractions. This new surface formulation eliminates the geometrical restrictions associated with the commonly used Derjaguin approximation. The influence of each body on the surface of any other body is represented by a new quantity: the *inter-surface stress tensor*. Additional forces resulting from interactions within the body, the surface tension, have been considered for liquid-like materials. These *self* interactions are modeled by the classical Young-Laplace equation relating the effective traction on a surface to the energy of the surface and its curvature. The surface formulation offers considerable reduction in computational complexity compared to a formulation based on body forces. The efficacy of the technique is demonstrated using several examples.

1. Introduction

A description of molecular interactions as body forces or surface tractions is necessary for the construction of predictive models for processes such as sintering (Hiram & Nir, 1983; Jagota & Dawson, 1990), adhesion (Israelachvili, 1991; Johnson *et al.*, 1971; Derjaguin *et al.*, 1975), crack-tip deformations (Lawn, 1993; Chan *et al.* 1987), colloidal interactions, and atomic force microscopy (Landman *et al.*, 1990; Hartmann, 1991, Argento and French, 1996). This subject has a long history and has been approached in different ways, *e.g.*, at the discrete level of many atoms (Landman *et al.*, 1990; Harrison *et al.*, 1992, Rowlinson and Widom, 1982), or the continuous level, applicable to macroscopic problems (Hamaker, 1937; Herring, 1953; Orowan, 1970). There are two important macroscopic manifestations of molecular interactions. Interactions within a body manifest as surface tension (*self-interactions*); interactions between bodies (*other-body interactions*) influence phenomena such as adhesion and the behavior of colloids. In certain problems, such as sintering, both manifestations play an important role. Our goal is to develop a continuum formulation for surface forces that combines these two manifestations. Self-interactions are treated using the classical concept of surface tension. For the other-body interactions we present a new surface formulation.

Consider first other-body interactions. Let the potential energy of interaction between two molecules as a function of distance s be $w(s)$. The potential energy of interaction $e(s)$ between two elemental volumes dV_1 and dV_2 then is

$$e(s) = \rho_1 \rho_2 w(s) dV_1 dV_2, \quad (1)$$

where ρ_1 and ρ_2 are the number densities of molecules. These infinitesimal volumes interact, each with every other, and it is assumed that the total energy of the system is the sum of individual interaction energies. The interaction energy between two bodies defined by the volumes V_1 and V_2 is then given by the double volume integral

$$E = \iint_{V_2 V_1} \rho_1 \rho_2 w(s) dV_1 dV_2. \quad (2)$$

In like fashion, the total force of interaction between two bodies can be computed. The force of interaction between two molecules is the gradient of the potential energy

$$\mathbf{f} = -\nabla w. \quad (3)$$

The total force between two bodies is then given by

$$\mathbf{A} = \iint_{V_2 V_1} \rho_1 \rho_2 \mathbf{f}(s) dV_1 dV_2. \quad (4)$$

Interactions handled in this manner have been used to study adhesion of solids (Israelachvili, 1991; Derjaguin *et al.*, 1975), atomic force microscopy (Hartmann, 1991; Argento and French, 1996), and fracture (Chan *et al.*, 1987). The analytical integration of the pair potential to obtain the macroscopic interaction potential was done by Bradley (1932), de Boer (1936), and Hamaker (1937) for the specific case of van der Waals interactions. A compilation of their results can be found in Israelachvili (1991). This approach assumes: a) additivity: the total force can be obtained by the pairwise summation of individual contributions; b) continuous medium: the summation is replaced by an integration over the volume; c) constant material properties: the number densities ρ and the interaction constants do not vary over the volume of the bodies. The last assumption implies a step definition of the surface. The double-volume integrations are

difficult to execute, both analytically and numerically, which has limited the application of this theory to simple geometries such as planar half-spaces and spheres. Because the potential $w(s)$ typically decays rapidly with distance s , the interaction forces are usually concentrated near the surface of the body. This fact makes it very difficult to integrate expressions (2) and (4) numerically, as is discussed in Section 2. Much would be gained if the volume integral could be replaced by surface integrals.

Consider the case of two smooth bodies separated by a distance S , which is small compared to the radii of curvature. Derjaguin (1934) (see also Israelachvili, 1991) introduced an approximation that allows the double volume integral (4) to be replaced by a double surface integral. In its original form, the approximation was used to compute the total force between the bodies. It was shown that the interaction force equals the interaction energy of two half spaces separated by a distance S and multiplied by a geometrical factor that depends on the radii of curvature. The approximation has subsequently been adapted to impose distributed surface tractions for the analysis of deformation under surface forces (Muller *et al.*, 1980; Hughes and White, 1979; Chan *et al.*, 1987). The first step in the computation of tractions involves the determination of the interaction force $f(s)$ (per unit area) between two half-spaces as a function of the distance of separation s . The second step involves defining a symmetry direction (with unit vector \mathbf{E}) along which all tractions are assumed to act. Derjaguin's approximation does not specify if and how such a direction can be chosen in general. The traction \mathbf{T} at any point on the surface is then assumed to be:

$$\mathbf{T} = f(s)(\mathbf{E} \cdot \mathbf{n})\mathbf{E}, \quad (5)$$

where s is measured along \mathbf{E} .

Even when the total interaction force predicted by Derjaguin's approximation is accurate, the distribution of surface tractions can be very different from the actual field of distributed body forces. Analysis of local deformation may therefore be inaccurate. When the conditions under which Derjaguin's approximation is valid are not met, it is difficult even to define \mathbf{E} uniquely.

In this paper we present a new surface formulation for arbitrarily shaped bodies, without the geometrical limitations associated with Derjaguin's approximation. In this scheme the influence of a body is represented by a second order tensor: the *inter-surface stress tensor*. This tensor field depends on the shape of the body and the basic intermolecular potential. Upon an inner product with the surface normal of another body, it produces a surface traction. This formulation is developed in detail in Section 3.

Consider now interactions within an isolated body (self-interactions). As a result of unmatched molecular interactions near a free surface, the surface has an excess energy. This is the surface energy and is defined as the work required to create a new surface of unit area (Herring, 1953; Orowan, 1970; Rowlinson and Widom, 1982). It provides, for example, the driving force for shape change and the concept of equilibrium shapes of bodies. Closely associated with the surface energy is the surface stress which is distinguished from the surface energy as being the work required to stretch the surface. The surface stress can also be obtained directly in terms of the unbalanced interaction forces (Orowan, 1970; Defay *et al.* 1966). For an isotropic liquid, the surface stress is isotropic and tensile (a surface tension) and is numerically equal to the surface energy (Herring, 1953, Blakely 1973). The driving force for deformation in this case can be

written as an effective surface traction proportional to the product of surface energy and surface mean curvature: the Young-Laplace equation (Adamson, 1976, Herring 1953). The Young-Laplace equation can also be derived directly in terms of unbalanced interaction forces (Rowlinson and Widom, 1982). This approach has been used widely to study deformation of fluids under the influence of surface energy (Batchelor, 1967; Jagota & Dawson, 1990; van de Vorst 1993). For an isolated body, this classical formulation is sufficient to describe the driving forces for deformation as long as the radii of curvature of the surface are large relative to the length scale of molecular interactions. For solid bodies, the relationship between surface stress and surface energy is more complex and is discussed briefly in Section 3 along with our implementation of self terms in the surface formulation.

The surface formulation has been implemented as a surface finite element. A brief account of the implementation is presented in Section 4 along with several analytical and numerical examples of the use of the formulation. We conclude the paper with a discussion of the salient results in Section 5.

2. Problems of full volume integration

Due to the complexity of the integration of the total interaction force (4), it is evident that, in most cases, it has to be done numerically. In this section we present a comparison between a typical numerical integration scheme and the analytical integration of expression (4), for the case of a cube interacting with a plane half-space, as shown in

Figure 1. For the sake of simplicity, only one dimension of the integration is done numerically. The interactions considered are of the van der Waals type.

In a numerical integration scheme, the value of the integrand is evaluated at quadrature points inside the integration volume. We are interested in evaluating the errors generated in such scheme as a function of the density of integration points. If the density necessary to achieve an accurate solution is too high, then the method is intractable.

Consider the van der Waals pair potential (London, 1937; Israelachvili, 1991):

$$w(s) = -A/s^6, \quad (6)$$

where A is the interaction coefficient. The pair-force \mathbf{f} is given by (3)

$$\mathbf{f}(s) = -\frac{6A}{s^7}. \quad (7)$$

For the geometry shown in Figure 1, the interaction force per unit area on an infinitesimal transversal layer of the cube with thickness ds , due to the planar half-space, is the volume integral of the pair-force over the half-space:

$$d\mathbf{F} = -\frac{\pi\rho^2 A}{2s^4} \mathbf{e} ds, \quad (8)$$

where \mathbf{e} is the unit vector normal to the plane. Expression (8) has to be integrated in the direction normal to the plane to obtain the total force between the cubic element and the planar half-space. This integral can be solved analytically and yields (per unit area):

$$\mathbf{F} = \int_{s_0}^{s_0+l} d\mathbf{F} = -\frac{\pi\rho^2 A}{6} \left(\frac{1}{s_0^3} - \frac{1}{(l+s_0)^3} \right) \mathbf{e}. \quad (9)$$

The force per unit area can also be obtained numerically using a Gaussian quadrature (Press *et al.*, 1986):

$$\mathbf{F}_N = \sum_i \left[\frac{\pi \rho^2 A}{2s_i^4} W_i \right] \mathbf{e}, \quad (10)$$

where W_i are the Gauss weights and the summation is done over the quadrature points i .

Figure 1 shows the relative error $(|\mathbf{F} - \mathbf{F}_N|/|\mathbf{F}|)$ on one dimension of integration for the numerical scheme. This error is plotted as a function of the size of the integration element, which contains five quadrature points. The separation was fixed at $s_0 = 0.2 \text{ nm}$, which is a typical value for contacting solids. It is clear from Figure 1 that full volume integration requires elements on the order of one nm in size. This would make numerical evaluation of the force on macroscopic bodies -- anything more than tens of nm in size--intractable. Note that this example involved numerical integration in only one dimension. To obtain the interaction between arbitrarily shaped bodies, the integration would involve discretization of the volume of each body in three dimensions, resulting in a six dimensional integration and, consequently, a much larger cumulative error. Great computational advantage is gained by reducing the dimension of the integration (and simultaneously the degree of the potential). Replacing a double volume integral with a double surface integral reduces the integration problem from an N^6 to an N^4 one. For this it is useful to express the interaction forces in terms of surfaces forces resulting from a surface integration, as has been done by Derjaguin (1934).

3. Surface formulation

Consider Figure 2. If the distance between a point p inside a body and the nearest free surface is much larger than the typical range of the interaction forces, the point is equally surrounded and the net force on it is zero. However, as this distance decreases, there is a net body force on the point and this is what we wish to compute. The force between two elemental volumes dV_1 and dV_2 is

$$d\mathbf{F} = -\rho_1 \rho_2 \nabla w \, dV_1 dV_2. \quad (11)$$

The body force (per unit volume) at any point p then is

$$\mathbf{b} = -\rho_1 \int_V \rho_2 \nabla w \, dV, \quad (12)$$

where ρ_1 is the number density at point p , and the integration is over all the bodies in the system including the body to which the point belongs. We write the integral as a sum of integrals over the different particles:

$$-\rho_1 \int_V \rho \nabla w dV = -\rho_1 \int_{V_1} \rho_1 \nabla w dV - \rho_1 \sum_{i=2}^{n_p} \int_{V_i} \rho_i \nabla w dV = \mathbf{b}_s + \mathbf{b}_o, \quad (13)$$

where '1' is the label of the particle that contains the point p ; $2, \dots, n_p$ are other particles.

The total body force on a point p has been partitioned into two terms \mathbf{b}_s and \mathbf{b}_o representing the self and other-body contributions. In the case of two or more distinct particles the volumes V_1 and V_2 etc. are conveniently identified as the volumes of the individual particles. The integral over the volume that contains the point p gives the self-contribution to the body force, while the remaining integrals represent other-body contributions. On physical grounds, the self contribution is finite (Orowan, 1970; DeFay *et*

et al., 1966). However its actual computation for a given potential, *e.g.*, the van der Waals potential, is problematic because the kernel is highly singular and a cut-off distance is usually introduced (Israelachvili, 1991). Here we handle the self contribution by following the classical approach of replacing its contribution to the body force distribution by an effective surface stress, resulting in effective surface tractions \mathbf{T}_s . The other-body contributions to the body force are also replaced by effective surface tractions \mathbf{T}_o , as detailed in the following sections.

As noted in the Introduction, the surface stress formulation is restricted by the assumption that the surface curvature is smooth compared to the characteristic range of interaction forces. For example, the surface of a single body resulting from the contact of two previously separate bodies may have a sharp cusp. In such cases, it is often necessary to further decompose the self-volume into two parts as illustrated in Figure 2b. The contribution to effective surface tractions from the integral over V_{1a} may be estimated by the surface stress formulation. Physically, it represents the forces that would be present if the volume V_{1b} were not present. The contribution to effective surface tractions from the integral over V_{1b} is not accounted for by the surface stress formulation. By treating this volume as a separate body, its contribution can then be computed by the surface integrals to be presented in following sections.

3.1 Other-body interaction

Consider the simpler case of bodies 1 and 2 as shown in Figure 2. These may be two physically distinct objects or one body, part of which is being treated as the other body. Clearly, any number of other bodies can be treated additively once the results for two

bodies are established. The coordinates of points in the two bodies are \mathbf{x}_1 and \mathbf{x}_2 respectively. Let $w(s)$ be the pair potential between molecules in the two bodies. The force on an element of volume dV_1 in body 1 due to an element of volume dV_2 in body two is

$$\mathbf{f}(s) = -\rho_1 \rho_2 \nabla_1 (w(s)) dV_1 dV_2 = \rho_1 \rho_2 \nabla_2 (w(s)) dV_1 dV_2 \quad (14)$$

$$s = ((\mathbf{x}_2 - \mathbf{x}_1) \cdot (\mathbf{x}_2 - \mathbf{x}_1))^{\frac{1}{2}},$$

where ∇_1 and ∇_2 represent the gradients with respect to \mathbf{x}_1 and \mathbf{x}_2 , respectively. If ρ_1 and ρ_2 are constant over the volumes, then the other-body force (per unit volume) in body 1 is

$$\mathbf{b}_o = \rho_1 \rho_2 \int_{V_2} \nabla_2 (w(s)) dV_2 = \rho_1 \rho_2 \int_{S_2} w(s) \mathbf{n}_2 dS_2, \quad (15)$$

where the second equality follows by an application of the divergence theorem. The orientation of the body force at a point in body 1 is an average of the normal to surface 2 \mathbf{n}_2 , weighted by the function $w(s)$. For short-range inter-molecular forces, the other-body force distribution has significant magnitude only near free surfaces. The body force distribution is replaced by a distribution of effective surface tractions as described below.

Consider now Figure 3. The contribution to the body force in 1 due to an element of area dS_2 centered around point P on surface 2 is

$$d\mathbf{b}_o = \rho_1 \rho_2 w(s) \mathbf{n}_2 dS_2. \quad (16)$$

Construct a cone of infinitesimal solid angle $d\alpha$ emanating from the point P and piercing surface 1 at points Q_i , where for odd i the axis enters the surface while for even i

it leaves the surface. Let the unit vector along the cone axis be \mathbf{e} , defined as pointing from Q_1 towards P . The force on body 1 due to dS_2 , integrated in the cone, is

$$d\mathbf{F} = \int_{V_{\text{cone}}} d\mathbf{b}_o dV_1. \quad (17)$$

By making $dV_1 = s^2 d\alpha ds$ in the cone, where s measures distance along the cone axis, this integral can be expressed in terms of a one-dimensional integral. The domain of integration is piecewise continuous; it consists of parts of the cone axis that are contained within the body 1. If this domain is called s_{cone} , the integral can be written as

$$\begin{aligned} d\mathbf{F} &= \left(\rho_1 \rho_2 \mathbf{n}_2 d\alpha \int_{s_{\text{cone}}} w(t) t^2 dt \right) dS_2 \\ &= \left(\rho_1 \rho_2 \mathbf{n}_2 d\alpha \left[\int_{s_1}^{s_2} w(t) t^2 dt + \int_{s_3}^{s_4} w(t) t^2 dt + \dots \right] \right) dS_2, \end{aligned} \quad (18)$$

where s_1, s_2, \dots are distances from point P to points Q_1, Q_2, \dots , respectively. The integral over each interval can be written as a sum of two integrals, as for example for the first interval:

$$\int_{s_1}^{s_2} w(t) t^2 dt = \int_{s_1}^{\infty} w(t) t^2 dt - \int_{s_2}^{\infty} w(t) t^2 dt. \quad (19)$$

Equation (17) can now be written as a sum of the following integrals:

$$d\mathbf{F} = dS_2 \left(\rho_1 \rho_2 \mathbf{n}_2 d\alpha \sum_i (-1)^{i+1} \int_{s_i}^{\infty} w(t) t^2 dt \right) = \sum_i d\mathbf{F}_i. \quad (20)$$

We propose to use this partitioning of the force to assign each successive term $d\mathbf{F}_i$ of the above expression to surface points Q_i respectively. For example, the force on point Q_1 is

$$d\mathbf{F}_1 = dS_2 \left(\rho_1 \rho_2 \mathbf{n}_2 d\alpha \int_{s_1}^{\infty} w(t) t^2 dt \right). \quad (21)$$

It is assumed that $w(s)$ decreases faster than $1/s^3$, which makes the integrals finite. The solid angle $d\alpha$ can be expressed as:

$$s_i^2 d\alpha = (-1)^{i+1} (\mathbf{e} \cdot \mathbf{n}_1) dS_1. \quad (22)$$

Substituting (22) into (20), $d\mathbf{F}_i$ is:

$$d\mathbf{F}_i = dS_1 dS_2 \left(\rho_1 \rho_2 \frac{1}{s_i^2} (\mathbf{e} \cdot \mathbf{n}_1) \int_{s_i}^{\infty} w(t) t^2 dt \right) \mathbf{n}_2. \quad (23)$$

The quantity in brackets represents the force on a unit area of body 1 due to a unit area on body 2. Note that the contribution to the traction at Q_i from the point P does not equal the contribution to the traction at P from the point Q_i , which is consistent with the fact that the body force vectors at P and Q_i are different as well.

Because S_1 and S_2 are independent, the traction \mathbf{T}_o on point Q_i (force per unit area of surface 1) is an integral of expression (23) over surface S_2 :

$$\mathbf{T}_o = \left(\rho_1 \rho_2 \int_{S_2} \mathbf{n}_2 \cdot \mathbf{G} dS_2 \right) \cdot \mathbf{n}_1, \quad (24)$$

where, using the substitution $\mathbf{e} = (\mathbf{x}_2 - \mathbf{x}_1)/s$,

$$\mathbf{G} = (\mathbf{x}_2 - \mathbf{x}_1)v(s) \quad (25)$$

and

$$v(s) = \frac{1}{s^3} \int_s^\infty w(t) t^2 dt. \quad (26)$$

The subscript i , no longer required, has been omitted. The scalar function of distance between the two surfaces, $v(s)$, has units of energy per molecule per molecule. The direction of the traction, like the body force distribution, is an average of the normal to S_2 weighted by $v(s)$. The quantity:

$$\mathbf{h} = \rho_1 \rho_2 \int_{S_2} \mathbf{n}_2 \cdot \mathbf{G} dS_2 \quad (27)$$

is a second-order tensor field which we shall call the *inter-surface stress tensor*. The tensor field exists outside any body and upon an inner product with the surface of another body produces an effective surface traction like the internal stress tensor, $\mathbf{T}_o = \mathbf{h} \cdot \mathbf{n}_1$. The vector function \mathbf{G} is termed the *inter-surface force kernel* and has units of force per unit area (of S_1) per unit area (of S_2).

The procedure described above has accomplished a partitioning of distributed body forces into distributed surface tractions. The proposed partitioning is not unique but fully accounts for all the body forces. Indeed, by formally enforcing this condition one obtains

an alternate method by which \mathbf{G} may be related to the pair potential w . The total force on body 1 due to body 2, \mathbf{A} , may be written as a double volume integral of the body force field:

$$\mathbf{A} = \rho_1 \rho_2 \int_{V_2} \int_{V_1} \nabla_2 w dV_1 dV_2 = \rho_1 \rho_2 \int_{S_2} \mathbf{n}_2 \left(\int_{V_1} w dV_1 \right) dS_2, \quad (28)$$

or as a double surface integral using the effective tractions:

$$\mathbf{A} = \rho_1 \rho_2 \int_{S_2} \int_{S_1} \mathbf{n}_2 (\mathbf{G} \cdot \mathbf{n}_1) dS_1 dS_2 = \rho_1 \rho_2 \int_{S_2} \mathbf{n}_2 \left(\int_{V_1} \nabla_1 \cdot \mathbf{G} dV_1 \right) dS_2, \quad (29)$$

where the last equality follows from the divergence theorem. For expressions (28) and (29) to be identical for arbitrary bodies:

$$\nabla_1 \cdot \mathbf{G} = w. \quad (30)$$

Substituting equation (25) into this equation yields an ordinary differential equation for the scalar function $v(s)$:

$$s \frac{d v(s)}{ds} + 3v(s) = -w(s). \quad (31)$$

The particular solution for this differential equation,

$$v(s) = -\frac{1}{s^3} \int w(s) s^2 ds, \quad (32)$$

is identical to the result found directly (26) if the integral vanishes as $s \rightarrow \infty$. However (32) can be used to obtain an expression for $v(s)$ even if $w(s)$ decays slower than $1/s^3$. Although there is little physical justification for effective surface tractions for such long-range forces, the formulation can still be used to compute the total force of attraction between bodies in terms of surface integrals.

Converting from the body force distribution to surface tractions therefore has been reduced to the problem of determining $v(s)$ in terms of the molecular pair potential via equation (32), a few examples of which are discussed in the following. For several types of molecular interactions, $w(s)$ varies as an inverse power of distance (Israelachvili, 1991):

$$w(s) = \frac{B}{s^m}, \quad (33)$$

where B is an interaction constant. Then, from (26),

$$v(s) = \frac{B}{(m-3)s^m}, \quad (m > 3). \quad (34)$$

A particular case of the inverse power potential is the van der Waals potential for which $m = 6$ and B is a negative number. A generalization of the van der Waals potential has been proposed by Anandrajah and Chen (1995):

$$w(s) = \frac{Bc}{s^6(s+c)}, \quad (35)$$

where c is a characteristic decay distance, and B is a negative number. In this case $v(s)$ is given by:

$$v(s) = \frac{B}{3s^6} - \frac{B}{2cs^5} + \frac{B}{c^2s^4} + \frac{B \ln s}{c^3s^3} - \frac{B \ln(c+s)}{c^3s^3}. \quad (36)$$

Short-range repulsion can be characterized by (de Boer, 1936):

$$w(s) = B e^{-s/c}, \quad (37)$$

for which,

$$v(s) = B e^{-s/c} \frac{c^3}{s^3} \left(2 + 2 \frac{s}{c} + \frac{s^2}{c^2} \right). \quad (38)$$

The total interaction energy E between two particles is another quantity of interest. It can be calculated in terms of surface integrals in a similar way. The interaction energy between two bodies (1) with constant number densities is:

$$E = \rho_1 \rho_2 \int_{V_2} \int_{V_1} w dV_1 dV_2. \quad (39)$$

Writing w in terms of \mathbf{G} using (30) and using the divergence theorem to convert the integral over the volume of body 2 into a surface integral:

$$E = \rho_1 \rho_2 \int_{S_1} \left(\int_{V_2} \mathbf{G} dV_2 \right) \cdot \mathbf{n}_1 dS_1. \quad (40)$$

Define a scalar function, the *inter-surface potential*, $u(s)$, such that its gradient is the *inter-surface force kernel*:

$$\nabla_2 u = -\mathbf{G}. \quad (41)$$

Using (41),

$$\int_{V_2} \mathbf{G} dV_2 = - \int_{S_2} u \mathbf{n}_2 dS_2, \quad (42)$$

and the total energy is

$$E = \rho_1 \rho_2 \int_{S_1} \int_{S_2} u (-\mathbf{n}_1 \cdot \mathbf{n}_2) dS_2 dS_1. \quad (43)$$

Note that (41) determines $u(s)$ and therefore E to within a constant. Since \mathbf{G} has a particular form given by (25), $u(s)$ can be obtained in terms of $v(s)$ as:

$$u(s) = - \int s v(s) ds. \quad (44)$$

It can be verified that (44) satisfies condition (41). For the inverse power law (33), for example,

$$u(s) = \frac{B}{(m-2)(m-3)s^{m-2}}. \quad (45)$$

3.2 Self-interaction

Consider now body 1 in Figure 3. As discussed in the Introduction, the classical formulation of self-interactions as a surface stress is used here. The surface stress \mathbf{g} , a second order tensor, and the surface energy γ are related by (Herring, 1953; Blakely, 1973):

$$\mathbf{g} = \gamma \mathbf{I} + \left(\frac{\partial \gamma}{\partial \boldsymbol{\varepsilon}} \right), \quad (46)$$

where $\boldsymbol{\varepsilon}$ is an appropriate strain measure and \mathbf{I} is the identity tensor. Note that \mathbf{g} has units of force per unit length and is defined on the surface of a three-dimensional body. The surface stress may therefore be a function of strain at the surface. It may additionally depend on the orientation of the surface. If, as for a liquid, the structure of the surface does not change upon straining, the surface stress is tensile and isotropic, and equals the surface energy in magnitude. For solids the structure of the surface generally changes upon straining and the surface stress is a difficult quantity to define and measure. In general the surface stress is anisotropic and may even be compressive (Orowan, 1970; Blakely, 1973). When the deformation is dominated by irreversible mechanisms such as plastic slip, diffusion, creep, or viscoelasticity (Orowan, 1970; Woodruff, 1973) it can

often be assumed that the surface tension equals the surface energy. Indeed, all analyses involving surface forces and large deformations of adhesive contact problems, sintering, and shape evolution of particles are based on this assumption.

If it can be assumed that the surface stress is tensile and isotropic and equals the surface energy in magnitude, the surface tractions required to analyze deformation can be obtained using the Young-Laplace equation. These tractions are proportional to the product of the surface energy and the surface mean curvature and act along the surface normal:

$$\mathbf{T}_s = -\gamma \operatorname{tr}(\mathbf{k}) \mathbf{n}_1, \quad (47)$$

where \mathbf{T}_s is the surface traction, \mathbf{k} is the surface curvature tensor, $\operatorname{tr}()$ refers to the trace, and \mathbf{n}_1 is the surface normal. In terms of the principal radii of curvature R_1 and R_2 :

$$\operatorname{tr}(\mathbf{k}) = \frac{1}{R_1} + \frac{1}{R_2}. \quad (48)$$

The implementation of the surface formulation presented in this paper is restricted to cases where equation (47) applies and is described briefly in the Section 4. The other limiting case of fully faceted crystalline solids can also be handled; the driving force for deformation is the *weighted mean curvature* (Carter et al., 1995). The main restriction to computations using the general expression for surface stress (46) is the uncertainty regarding its actual dependence on surface strain.

3.3 Consistency between other-body forces and surface energy

Both the self forces and the other-body forces arise due to the same fundamental intermolecular force field. In our formulation, the self-forces are represented by the surface energy γ , whereas the other-body forces are characterized principally by the interaction coefficients as in equations (33), (35), and (37).

Consistency between surface energy and other-body forces is established by ensuring that the total work done by the other-body forces in bringing two surfaces to contact from infinite separation equals the surface energy. The procedure varies a little depending on the particular form of the potential $w(s)$ used. Here we illustrate it by showing the consistency condition for the inverse power law potential (33). The interaction energy per unit area of two identical half planes separated by a distance S is (Israelachvili, 1991):

$$W(S) = \frac{2\pi B\rho^2}{(m-2)(m-3)(m-4)S^{m-4}}. \quad (49)$$

When such a potential is used, a cut-off distance $S = \varepsilon$ is usually introduced which represents the interfacial contact separation. Equating $W(\varepsilon)$ to -2γ one obtains:

$$B = \frac{-\gamma(m-2)(m-3)(m-4)\varepsilon^{m-4}}{\pi\rho^2}. \quad (50)$$

If γ and B are experimentally measured quantities, equation (50) fixes the value of ε . For a variety of materials it is found that $\varepsilon \approx 0.16\text{nm}$ (Israelachvili, 1991). Similar consistency conditions can be established for other potentials such as the Lennard-Jones potential, and for dissimilar materials.

4. Examples

The efficacy of the surface formulation is demonstrated in this section by the aid of a few examples. In the first set of examples we compute the distributed and total force between rigid bodies. The use of the surface formulation to compute deformations is illustrated by analyzing the adhesion of an elastic sphere to a half-space. For this purpose the surface formulation has been implemented as a surface element in a finite element code.

4.1 Total force and surface tractions between rigid bodies

Consider two plane half-spaces 1 and 2 separated by S along the axis z , and with normals $\mathbf{n}_1 = \{0,0,1\}$ and $\mathbf{n}_2 = \{0,0,-1\}$. Assume that the interaction potential is given by an inverse power law (33). By symmetry, the only component of \mathbf{h} that does not vanish identically is h_{33} , which is given by

$$h_{33} = B \rho_1 \rho_2 \frac{1}{(m-3)} \int_{S_2} \frac{z}{(x^2 + y^2 + z^2)^{m/2}} dS_2. \quad (51)$$

The surface tractions on half-space 1 are then

$$\mathbf{T}_{\text{plane}} = h_{33} \mathbf{n}_2. \quad (52)$$

The integration over S_2 can be easily performed by replacing $y^2 + x^2 = r^2$ and $dS_2 = r d\theta dr$, and integrating over r from $0 \rightarrow \infty$ and over θ from $0 \rightarrow 2\pi$, which yields

$$h_{33} = \frac{2\pi B \rho_1 \rho_2}{(m-3)(m-2) S^{m-3}}. \quad (53)$$

This is the known expression for plane-plane interaction force (Israelachvili, 1991) and is the result that is used in Derjaguin's approximation, $f(S)$ in equation (5). Consider now the case of the interaction of a half-space (body 2) with an arbitrary body (body 1). Clearly, if the direction \mathbf{E} of Derjaguin's approximation is chosen to be \mathbf{n}_2 , the distribution of tractions on body 1 as given by Derjaguin's approximation and the new surface formulation are identical. This shows that the new surface formulation reduces to Derjaguin's approximation for the computation of surface tractions on any body due to a half-space. However, the distribution of tractions on the half-space due to body 1 given by the two approaches differ, as will be illustrated in the next example. It is also evident that the Derjaguin approximation produces the exact total force between the bodies when one of them is a plane half-space.

In Figure 4 the distribution of effective surface tractions for the interaction of a sphere and a half-space is compared to the distributed body force field. The vectors in this figure represent force per unit volume in the case of the body force field and force per unit area in the case of the surface formulation and of the Derjaguin approximation. The length of the vector is proportional to the logarithm of the magnitude of the force. The interaction potential considered here is the inverse power law with an exponent 6, which is characteristic of van der Waals interactions. The sphere radius is fixed at 5 times the minimum separation. Note that the body forces are highly localized near the surface, which indicates the validity of using the surface formulation. On the sphere, both surface fields are almost identical to the body force field on its outermost layer, since they are all directed along \mathbf{E} (outward normal to the plane). This is due to the symmetry of the half-

space and the constant value of its normal. However, this is not the case for the fields on the half-space. It is easy to show that the body force field points towards the center of the sphere, since this is the direction of minimum separation between the point being considered and the surface of the sphere. The field obtained by the surface formulation mimics this effect because of the averaging of \mathbf{n}_2 (outward normal to the surface of the sphere) present in equation (27). The field obtained by Derjaguin's approximation is always directed along \mathbf{E} . As it has been discussed above, the two surface fields produce the exact total force between the bodies.

The same example can be used to examine the computational efficiency of the surface formulation. We are interested in obtaining the total interaction force on the sphere by numerical integration of the body force field over its volume and by integration of the surface field over its surface. The sphere would physically represent a particle with diameter $125\mu\text{m}$. The force was calculated for separations going from $S = 0.165\text{nm}$, representing a contact situation, up to $S = 500\text{nm}$. For the evaluation of the volume integral, the first volume integral in equation (4) is done analytically, producing the interaction force between an infinitesimal volume in the sphere and the whole half-space. Only the integration over the volume of the sphere is done numerically, resulting in a 3 dimensional gain in the total integration effort. The same approach is adopted for the surface formulation: the surface integral in equation (24), which represents the plane surface of the half-space, is done analytically, producing the interaction force between an infinitesimal area on the surface of the sphere and the plane. This represents a 2 dimensional gain in efficiency in the total integration effort. In both cases, the forces are

integrated analytically in the axisymmetric direction reducing the numerical integration by one extra dimension. As it has been described in section 2, in the numerical integration scheme the interaction force is evaluated at quadrature points distributed over the integration domain. The precision of such an integration scheme is proportional to the density of integration points. For this example two integration densities were used: 11 and 28 integration points / μm . Note that in the volume integration, this corresponds to 121 and 784 integration points / μm^2 .

The results of the numerical integration are compared to the analytical solution for the force distance relation for this geometry in Figure 5. There is a large quantitative error in the volume integration schemes. It is evident that the mesh density adopted is insufficient to capture the strong variations in the force field experienced by the material, even with the very fine integration mesh. It must be noted here that, in the case of a complex geometry, where the order of the numerical integration cannot be reduced analytically, the disagreement would be even greater. With increasing separation between the sphere and the plane the force gradient reduces and is consequently easier to integrate, therefore the results of the volume integration converge to the correct solution. This illustrates again the advantage in accuracy obtained by using the surface formulation, which produces accurate results at all separations. It is expected that, for most macroscopic problems, full volume integration would be intractable.

Consider now the interaction between two quadrants, as shown in Figure 6. The figure shows the force fields obtained with the three different approaches and was constructed in a similar way as the sphere-plane example presented above. Notice that the

surface formulation produces a surface field which is slightly different than the outermost layer of the body force field. Also, due to the discontinuity of the normal \mathbf{n}_2 in equation (27), the surface tractions are discontinuous on the sharp corner. This is not the case in Derjaguin's approximation, since the direction of the tractions is constant.

Orowan (1970) showed that the total interaction force per unit of length between opposite quadrants, resolved in a direction normal to one of the quadrant faces, equals the surface energy, as defined by the consistency relation (50). Since it has been proved that the surface formulation presented here produces the exact total interaction force, it is interesting to compute this force using Derjaguin's approximation. This is easily achieved by integrating expression (5) over the surface of the quadrant, assuming that they are separated by ε , which yields

$$F = \frac{B\pi\rho_1\rho_2}{6\sqrt{2}\varepsilon^2}. \quad (54)$$

When compared to γ as given by relation (50), the above expression is incorrect by a factor of $2\sqrt{2}$. This then represents a case where Derjaguin's approximation does not yield the correct total interaction force. Note that if the two quadrants were misaligned, it would not be possible even to identify a unique direction \mathbf{E} along which the distance between the two surfaces is computed for use in the Derjaguin approximation.

4.2 Adhesive contact between an elastic sphere and a half-space

The new surface formulation has been used to prescribe surface tractions on a finite element model of a body. Specifically, a 2-node axisymmetric surface element has been

developed. This element computes surface tractions based on equation (24) for the other body term and on equation (47) for the surface tension term. By virtue of being attached to volume elements, the surface element transmits the tractions to the material. This element has been implemented in a commercial finite element code (Abaqus(TM), HKS), which has been used to compute the results presented below. A full description of this implementation is under preparation and will be the object of a forthcoming publication.

In the finite element example discussed here, we consider the contact of elastic spheres under the influence of interaction forces. For elastic materials, the phenomenon is dominated by other-body forces but for viscoelastic and viscous materials only the early stages of deformation are controlled by other-body forces. The later stages of deformation or sintering are controlled by the self-forces. This stage has been widely studied. Jagota & Dawson (1990) used a simplified version of the surface finite element, including only the surface tension term, to model the viscous sintering of two particles. It is the desire to model the entire sintering process, from two spheres at point contact to the final equilibrium shape, that motivated much of the work presented in this paper.

The contact and coalescence of spheres is a problem in which both the self-terms and other-body terms play a crucial role, albeit at different stages of the process. A full study of this problem will be presented elsewhere. Here we present an analysis of the adhesive contact of elastic spheres, which is dominated by the other-body terms in the surface traction. The problem of adhesive contact of elastic spheres has a long history. An important work in this area is by Johnson, Kendall and Roberts (1971) (JKR theory). However, there is a long discussion in the literature about the domain of validity of this

theory. Essentially, the JKR theory is an extension of Hertz (1896) contact theory that takes into account the adhesion between spheres. Elastic spheres brought into contact attain an equilibrium contact area even in the absence of external applied forces. In the JKR theory this process has been modeled in terms of minimization of total potential energy. Equivalently, it may be seen as the equilibrium response of an elastic sphere to surface forces as will be done here. According to the JKR theory, in the absence of any external driving force, the contact radius between a sphere and a rigid plane is given by:

$$\frac{r_c}{R} = \left(\frac{9\gamma \pi (1 - \nu^2)}{E R} \right)^{1/3}, \quad (55)$$

where R is the undeformed particle radius, ν is the Poisson's ratio and E is the elastic modulus. Here we show that the surface formulation developed in the present work is able to model the same problem. Moreover, it is more general, being applicable to inelastic materials and arbitrarily large deformations.

The mesh and boundary conditions used for the simulation are shown on Figure 7. The sphere was modeled as an elastic solid while the half-space was assumed to be rigid. Surface interaction elements were attached to the surface of the sphere. Because stress gradients are concentrated near the contact, only part of the sphere was modeled. The curvature term on the sphere would cause a hydrostatic state of stress far from the contact. To compensate for this effect, an external pressure was imposed on the surfaces created by the cutting around the contact (top and right-hand side faces of the mesh on figure 7). The value of this pressure is consistent with equation (47) and has very little effect on the final contact area.

Since we consider a rigid half-space, the interactions of an element of the surface of the sphere with an element of the plane were analytically integrated over the plane, yielding the interaction of the element on the sphere with the entire plane. Therefore, the numerical integration is reduced by 2 dimensions.

Figure 8 shows the traction on the sphere surface normal to the contact plane obtained with the finite element model and the predictions from the JKR model. The numerical simulations predict that the inner part of the contact is under compression while the outer part is under tension, consistent with the JKR theory. In the JKR theory surface forces are neglected outside the contact area which lead to the unphysical prediction of an infinite stress at the edge of the contact. The numerical calculation, based on surface forces consistent with the surface energy γ , does not suffer from these singularities in the stress at the edge of the contact. Figure 9 shows the variation of the normalized contact radius as a function of a non-dimensional number that is the kernel of expression (55). For large values on the horizontal axis, the numerical solution approaches the predictions of the JKR theory. We have not been able to compute accurate values of the equilibrium contact radius for larger values on the horizontal axis due to computational problems in the contact algorithm not associated with the surface formulation that we wish to focus on in this paper. Nevertheless, it can be seen that there is good quantitative agreement with the JKR theory, knowing that it is increasingly accurate for large contacts (Tabor, 1977).

5. Summary and Conclusions

A new surface formulation for molecular interactions as distributed tractions has been developed. The surface formulation deals separately with tractions resulting from interactions within a body and between bodies. The former are modeled using the classical concept of surface stress; our implementation uses the Laplace-Young equation relating surface traction to surface energy and curvature. In cases where the curvature formulation is invalid even for the self terms, for example at a cusp as in a sharp sintering neck, part of the body can be treated as another body. Body forces due to other bodies are written as effective surface tractions by converting the double volume integral defining the total force between two bodies into a double surface integral. This leads to the definition of an inter-surface stress tensor which depends on the fundamental molecular potential, and on the geometry of the bodies. Its inner product with the surface normal yields the effective surface traction. The surface formulation replaces the Derjaguin approximation and at the same time offers great advantages over full volume integration to obtain body forces. It is shown that full volume integration quickly becomes computationally intractable whereas it is possible, using the surface formulation, to analyze problems of macroscopic scale. We have applied it successfully to solve several problems: adhesion of elastic spheres, and the calculation of force-displacement laws for several body geometries.

Two types of problems can be addressed using the surface formulation presented here: the determination of the total interaction force/energy between several bodies and the computation of equivalent surface tractions to study their deformations. As has been described, the results for the total interaction force/energy are exact for any interaction

potential. The surface formulation does not have the geometrical restrictions associated with Derjaguin's approximation. All this, of course, within the basic limitations of Hamaker's approach. The use of the surface formulation to calculate effective surface tractions on a body and to study its deformation may have some practical limitations. This is related to the fact that there is no unique way to distribute the integrated body force over the surface of the bodies. However, the scheme presented here is very efficient for most important geometries. As has been shown, it produces a field of tractions on the body that is a very good approximation of the local body force field. This is specially true for potentials which decays rapidly with distance.

The surface formulation is able to handle dissimilar materials but is limited in its present form to isotropic and piecewise homogeneous materials. We have not explicitly considered here other surface forces such as electrostatic attraction or repulsion, steric repulsion, and hydration forces that often play a role in physical phenomena where the inter-molecular forces are important. Because these forces are, to begin with, expressed as surface forces, their inclusion in the expression for the total surface traction at a point poses no additional difficulty if their influence is additive.

Acknowledgments

This work has been supported by the Air Office of Scientific Research, USAF, under contract number F49620-95-C-0008. The views and conclusions herein are those of the authors and should not be interpreted as necessarily representing the official policies or endorsements, either expressed or implied, of the Air Force Office of Scientific Research

or the U.S. Government. The authors would like to acknowledge helpful discussion and encouragement from Stephen Mazur and the suggestions of the reviewers. In addition WCC acknowledges helpful discussions with Ken Brakke.

References

ABAQUS (TM), Hibbit, Karlsson & Sorensen, Inc., Tel: (401) 727 4200.

Anandrajah A., Chen J. (1995), Single correction function for computing retarded van der Waals attraction, *J. Colloid Interface Sci.*, **176**, 293-300.

Adamson, A.W. (1976) *Physical Chemistry of Surfaces*, 3rd Ed., John Wiley and Sons.

Argento, C. and French R.H. (1996), Parametric tip model and force-distance relation for Hamaker constant determination from AFM, *Journal of Applied Physics*, in press.

Argento C. and Jagota A. (1996), A surface finite element for molecular interactions, in preparation.

Batchelor G.K. (1967), *An introduction to fluid dynamics*, Cambridge University Press, Cambridge, U.K..

Bradley R.S. (1932), The cohesive force between solid surfaces and the surface energy of solids, *Phil. Mag.*, **13** 853-862.

Carter W.C., Roosen A.R., Cahn J.W., Taylor J.E. (1995), Shape evolution by surface diffusion and surface attachment limited kinetics on completely faceted surfaces, *Acta Met. Mat.*, **43** [12] 4309-4323.

Chan, D.Y.C., Hughes, B.D. and L.R. White (1987) A physically consistent theory of fracture in a brittle solid, *J. Colloid Interface Sci.*, **115** [1] 240-259.

de Boer, J.H. (1936), The influence of van der Waals' forces and primary bonds on binding energy, strength and orientation, with special reference to some artificial resins, *Trans. Faraday Soc.*, **32** 10-38.

Defay R., Prigogine I., Bellemans A., (1966), *Surface Tension and Adsorption*, D.H. Everett (translator), Longmans, Green, & Co., London.

Derjaguin, B.V. (1934) Untersuchungen über die Reibung und Adhäsion, IV, (Investigations concerning friction and adhesion IV), *Kolloid Z.*, **69** 155-164.

Derjaguin, B.V., Muller, V.M. and Toporov, Y.P. (1975) Effect of contact deformations on the adhesion of particles, *J. Colloid Interface Sci.*, **53** [2] 314-326.

Hamaker, H.C. (1937) The London-van der Waals attraction between spherical particles, *Physica*, **4** 1058-1072.

Hartmann, U. (1991) Theory of van der Waals microscopy, *J. Vac. Sci. Technol. B*, **9** [2] 465-469.

Herring C., (1953), The use of classical macroscopic concepts in surface-energy problems, in *Structure and Properties of Solid Surfaces*, R. Gomer and C.S. Smith (eds.), University of Chicago Press.

Hertz H. (1896) *Miscellaneous Papers*, Macmillan, London.

Hiram, Y. and Nir, A. (1983) A Simulation of surface tension drive coalescence, *J. Colloid Interface Sci.*, **95** [2] 462-470.

Hughes B.D., White L.R. (1979), Soft contact problems in linear elasticity, *Q. J. Mech. App. Math.*, **32** [4] 445-471.

Israelachvili, J. (1991) {*Intermolecular and Surface Forces*}, second edition, Academic Press, San Diego (USA).

Jagota A. and Dawson, P.R. (1983) Simulation of viscous sintering of two particles, *J. Am. Ceram. Soc.*, **73** [1] 173-177.

Johnson, K.L., Kendall K. and Roberts A.D. (1971) Surface energy and the contact of elastic solids, *Proc. R. Soc. Lond. A*, **324** 301-313.

Landman, U., Luedtke, W.D., Burnham, N.A. and Colton, R.J. (1990) Atomistic mechanism and dynamics of adhesion, nanindentation and fracture, *Science*, **248** 454-461.

Lawn, B.R. (1993) *Fracture of Brittle Solids*, Second edition, Cambridge University, New York.

London F. (1937), The general theory of molecular forces, *Trans. Faraday Soc.*, **33** 9-26.

Muller V.M., Yushchenko V.S., Derjaguin B.V. (1980), *Journal of Colloid and Interface Science*, **77** [1] 91-101.

Orowan E., (1970), Surface energy and surface tension in solids and liquids, *Proc. R. Soc. Lond. A*, **316** 473-491.

Press, W.H., Flannery, B.P. (1986) Teukolsky, S.A. and Vetterling, S.A., *Numerical Recipes*, Cambridge University Press.

Rowlinson J.S., Widom B. (1982), *Molecular Theory of Capillarity*, Oxford University Press, New York.

Tabor, D. (1977) Surface forces and surface interactions, *J. Colloid Interface Sci.*, **58** [1] 2-13.

van de Vorst, G.A.L. (1993), Integral method for a two-dimensional Stokes flow with shrinking holes applied to viscous sintering, *J. Fluid Mech.*, **257** 667-689.

Woodruff D.P. (1973), *The Solid-Liquid Interface*, Cambridge University Press, Cambridge UK.

Figure captions

Figure 1: Relative error as a function of element size for the interaction between a cube and a plane half-space obtained by numerical integration. Five integration points were used with the minimum distance $s_0 = 0.2 \text{ nm}$.

Figure 2: Interactions within and between arbitrarily shaped bodies; \mathbf{b}_o is the other-body term and \mathbf{b}_s is the self-interaction term.

Figure 3: Scheme for the derivation of the other-body surface traction between two arbitrarily shaped bodies.

Figure 4: Body force field and surface fields obtained by the new surface formulation and by Derjaguin's approximation for the interaction between a sphere and a half-space. The vectors are plotted on a logarithmic scale, represented on the right hand side of the figure. The potential considered is an inverse power law with exponent 6.

Figure 5: Interaction force between a sphere and a plane half-space: comparison between the volume integration scheme and the surface formulation. The potential considered is an inverse power law with exponent 6.

Figure 6: Body force field and surface fields obtained by the new surface formulation and by Derjaguin's approximation for the interaction between two opposite quadrants. The vectors are plotted on a logarithmic scale, represented on the right hand side of the figure. The potential considered is an inverse power law with exponent 6.

Figure 7: Finite element mesh and boundary conditions used for the simulation of the adhesive contact between an elastic sphere and a rigid half-space.

Figure 8: Surface traction as a function of radial position for the adhesion of an elastic sphere and a rigid half-space. The radial distance is normalized by the JKR contact radius.

The surface traction is normalized by the quantity $-\left(8E^2\gamma / \left(3(1-v^2)R\pi^2\right)\right)^{1/3}$.

Figure 9: Normalized contact radius as a function of dimensionless parameter $(9\gamma\pi(1-v^2)/ER)$ for the adhesive contact between the elastic sphere and a rigid half-space.

figure 1

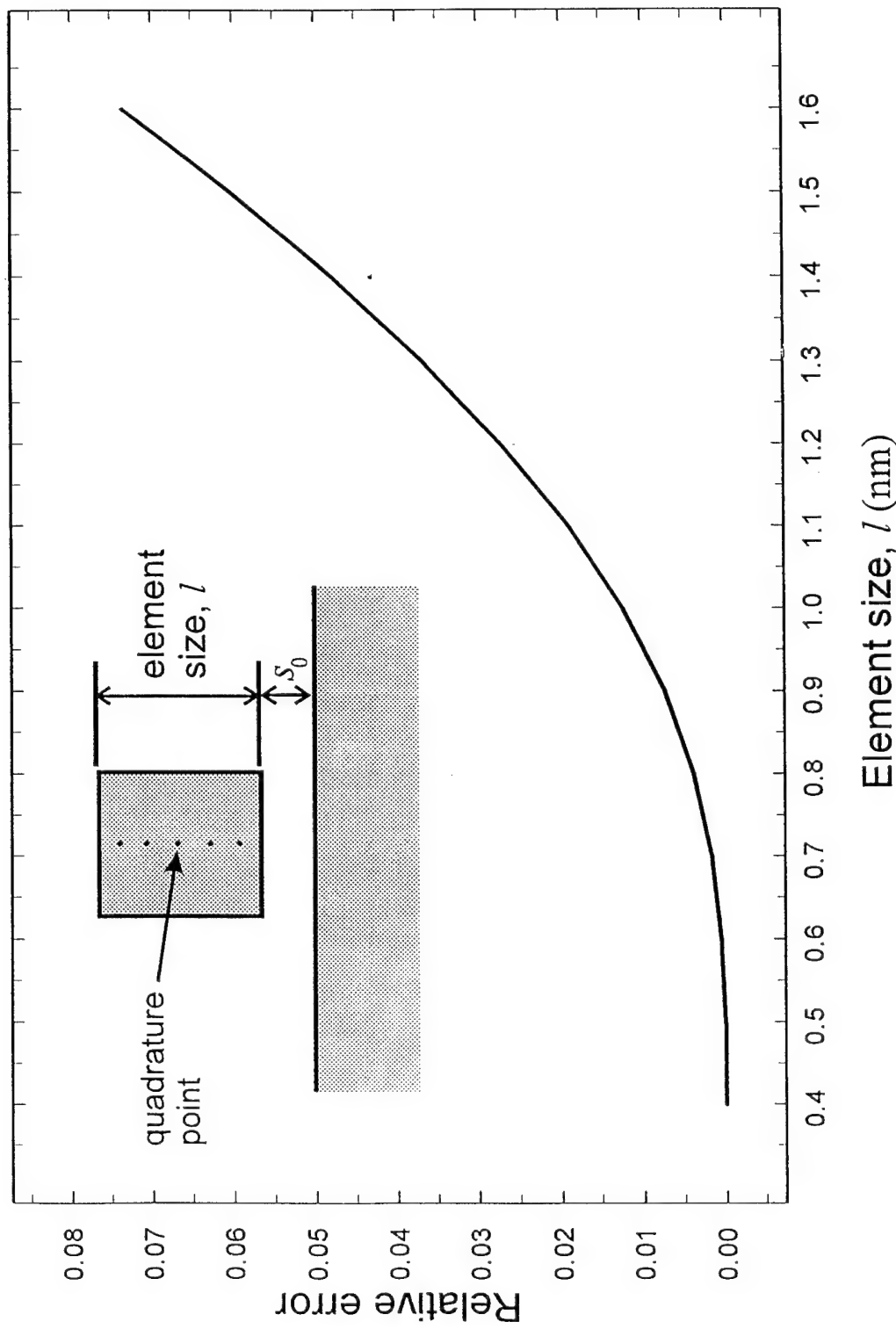
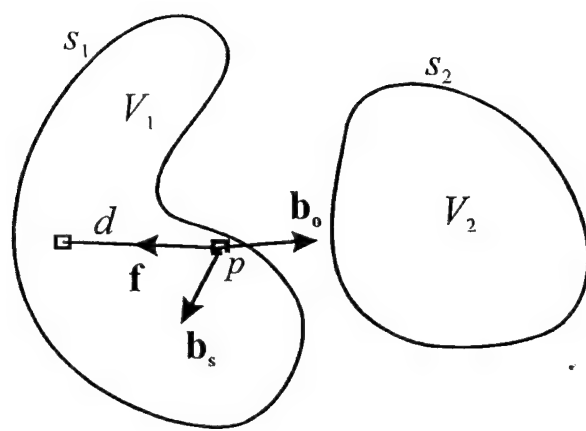


FIGURE 1

a)



b)

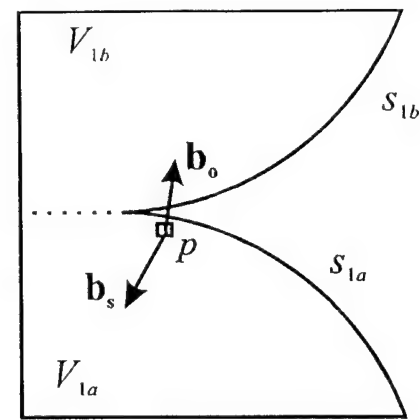


Figure 2.

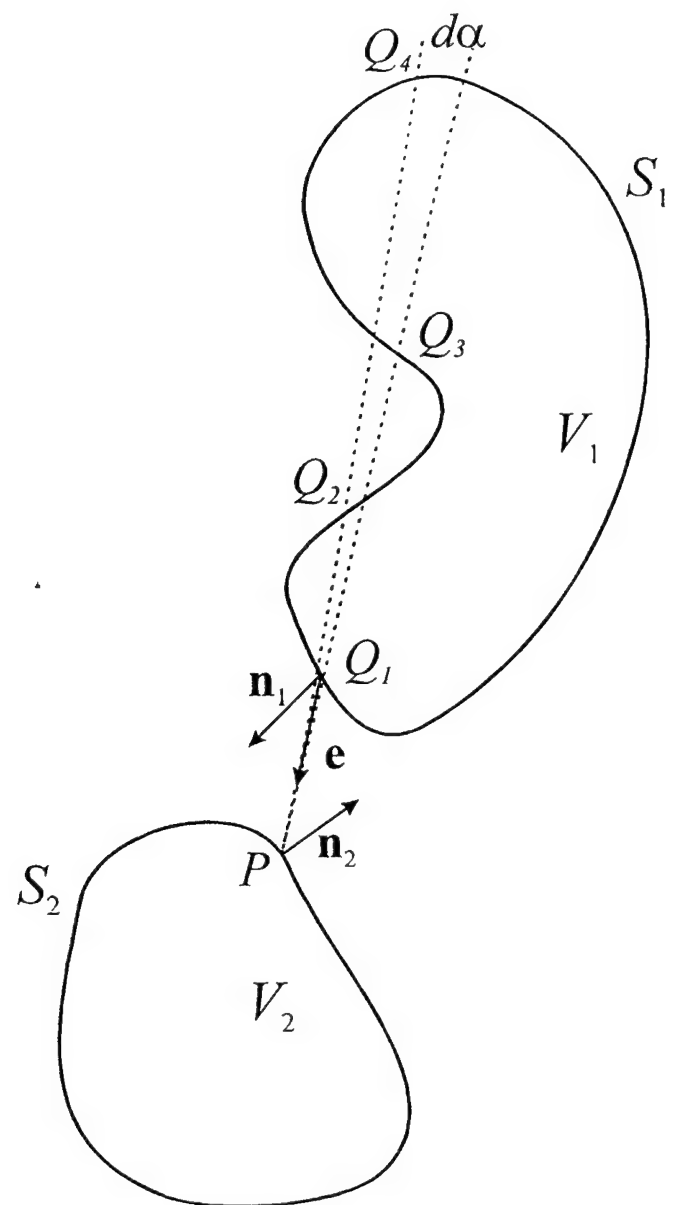


Figure 3.

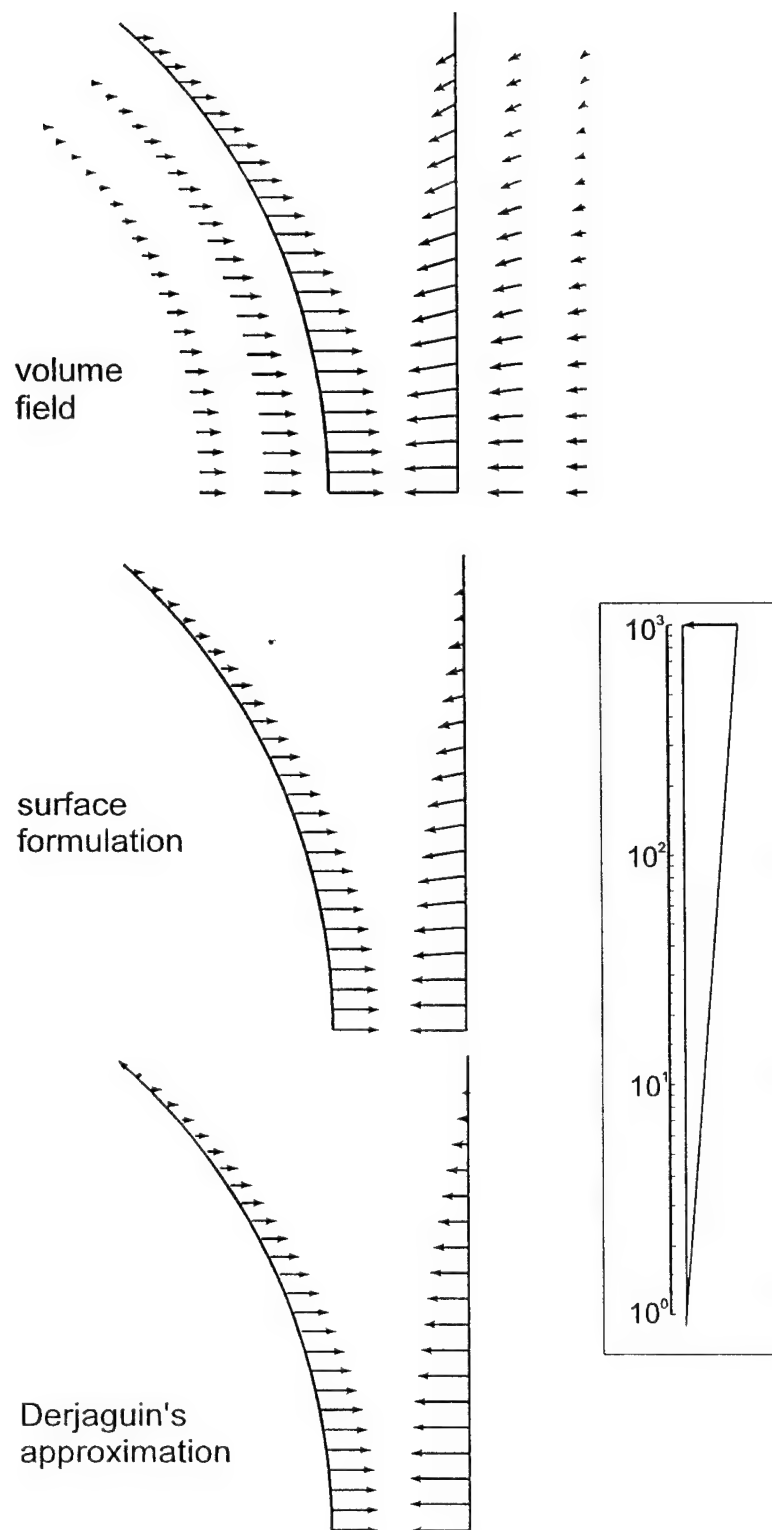


Figure 4.

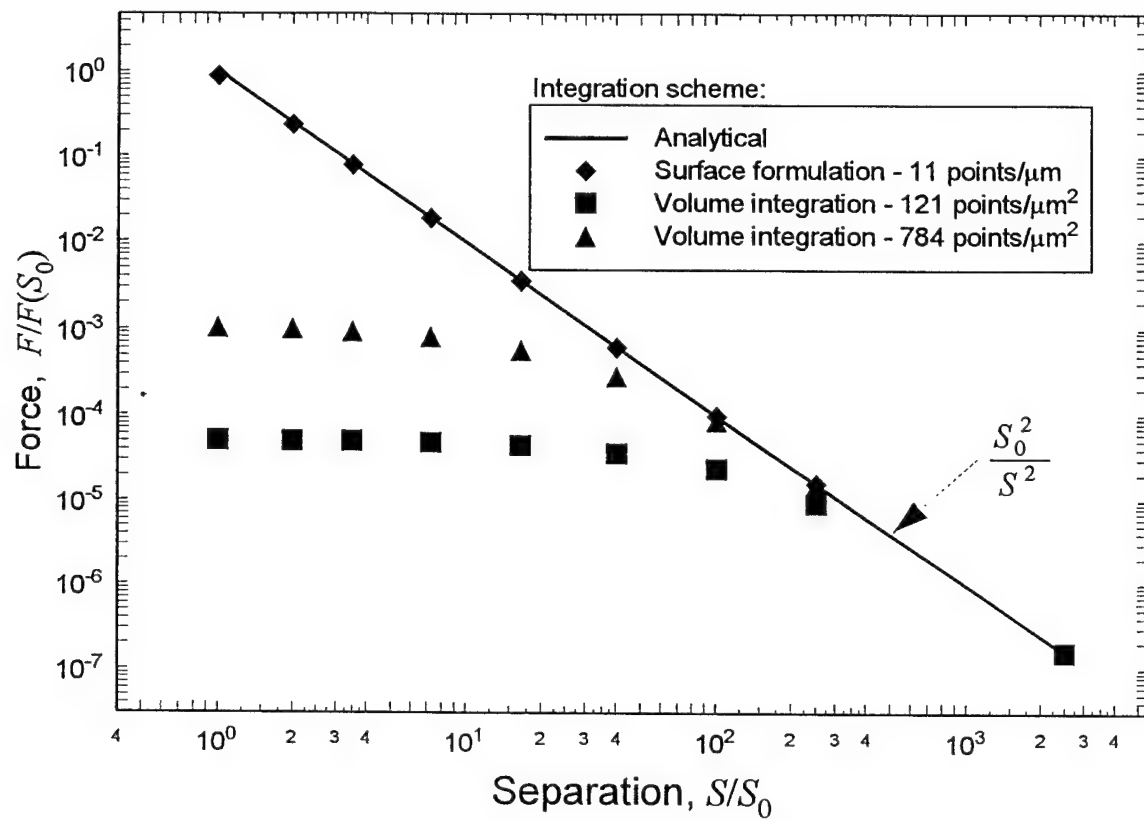


Figure 5.

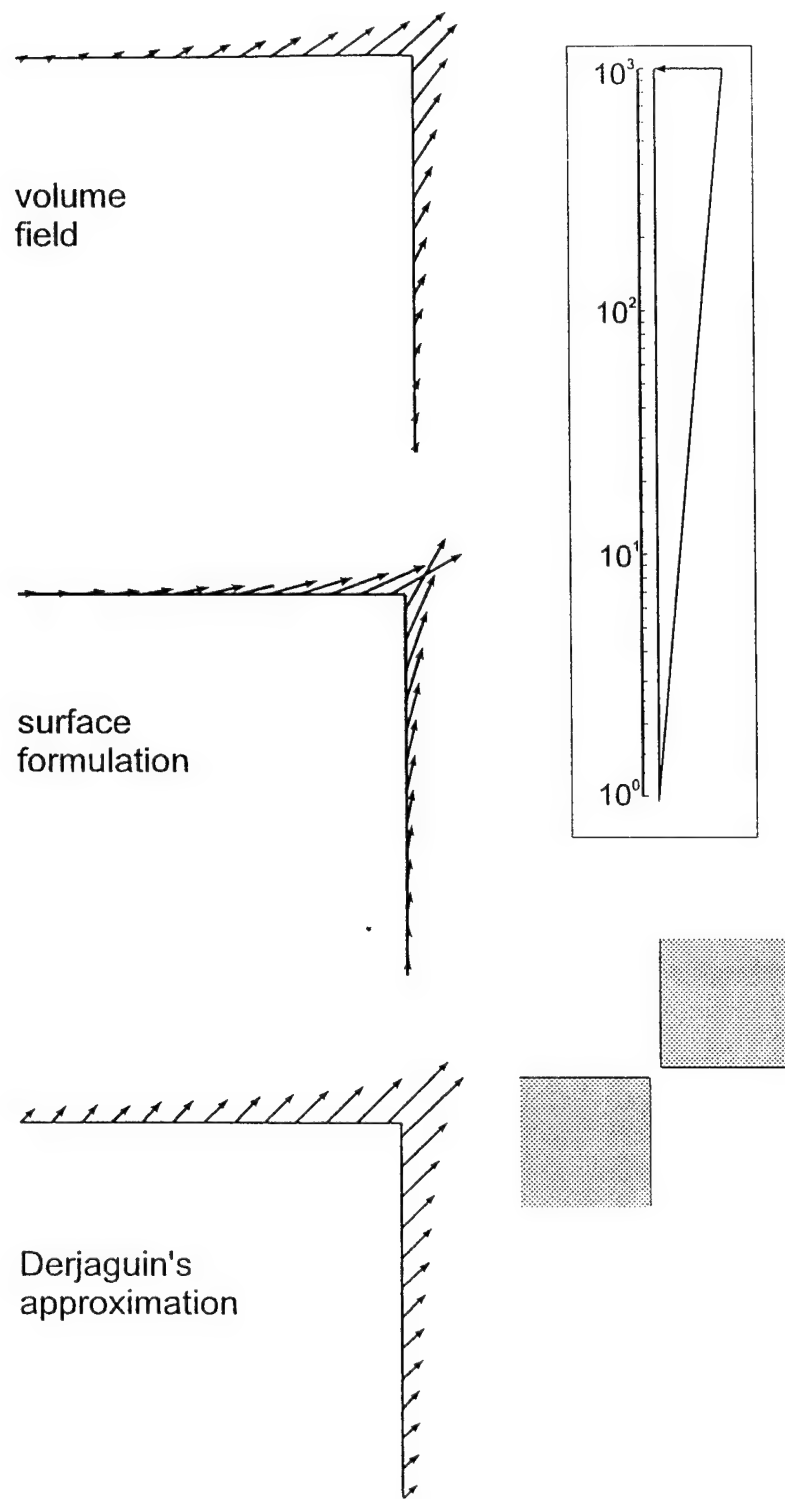


Figure 6.

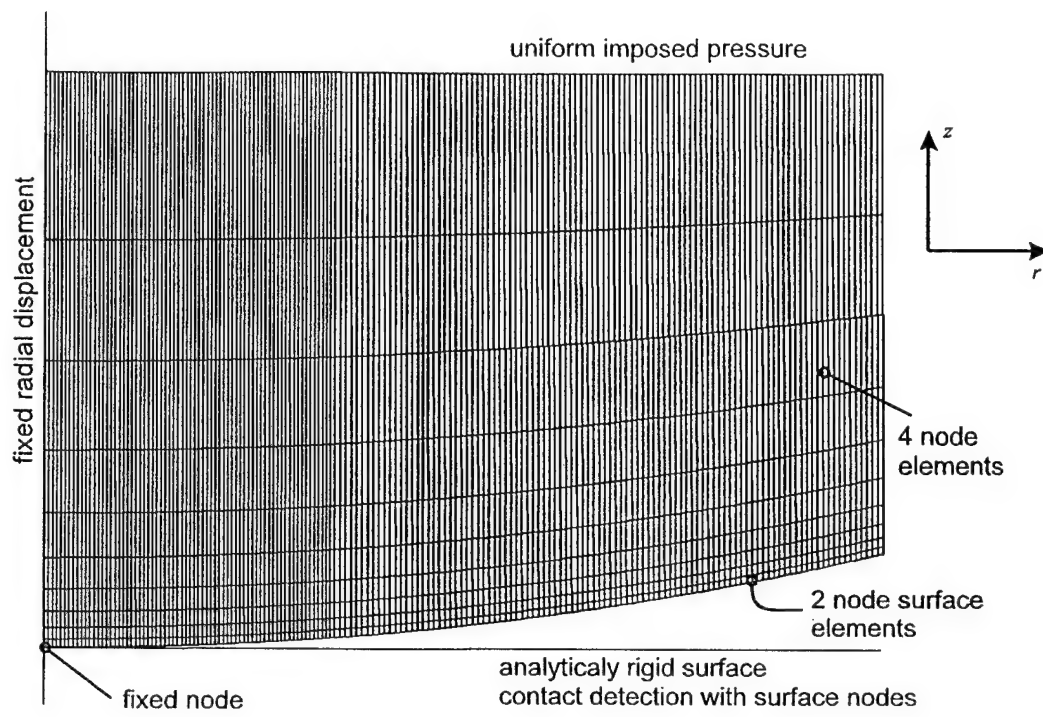


Figure 7.

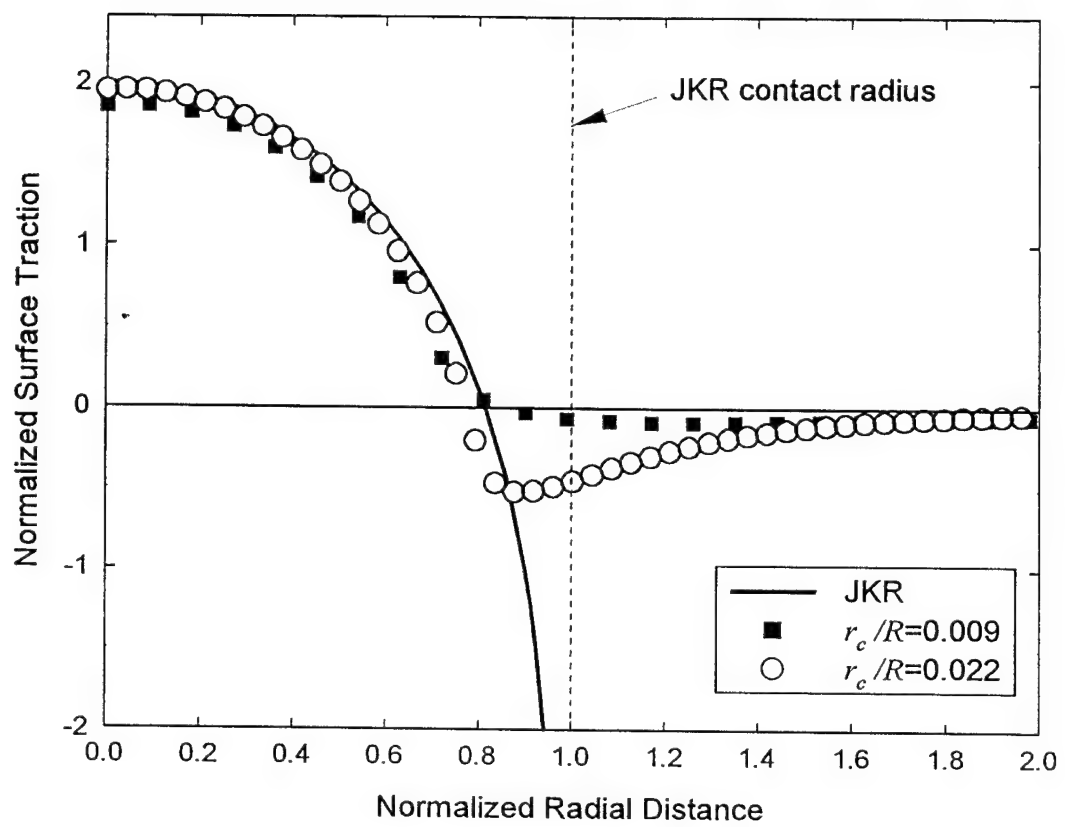


Figure 8.

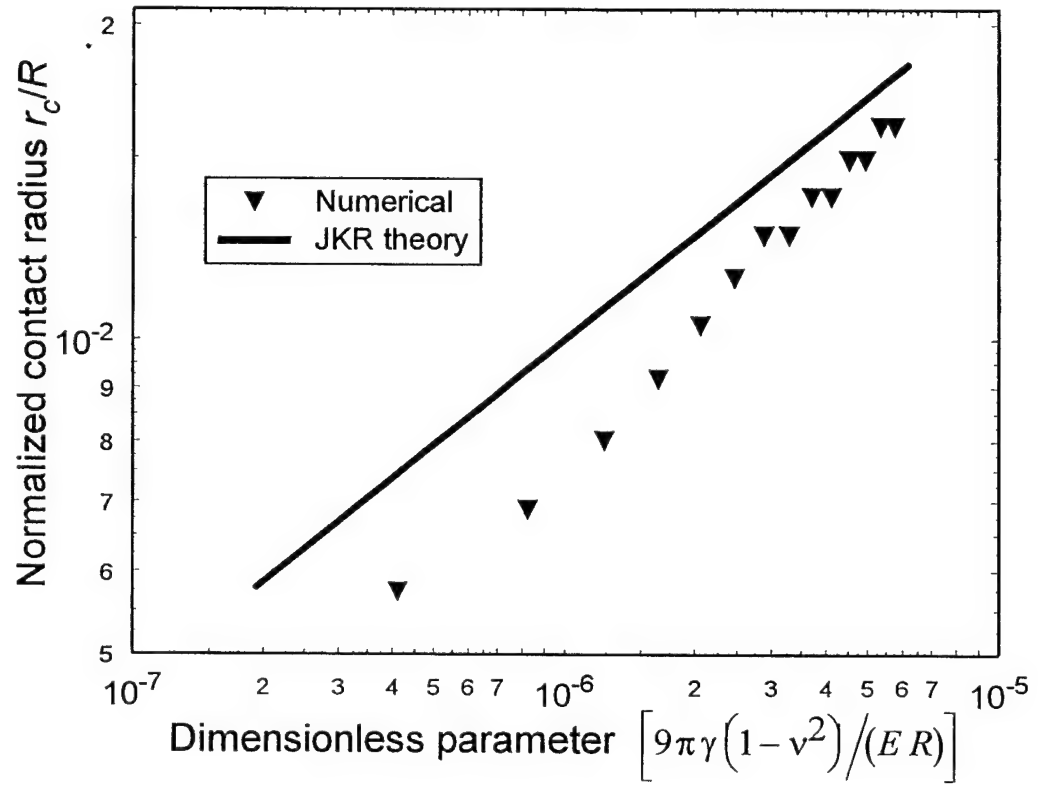


Figure 9

An Inter-Surface Stress Tensor

A. Jagota, C. Argento

Central Research and Development, The DuPont Company

Wilmington, DE 19880-0356, USA

submitted to the *Journal of Colloid and Interface Science*

Abstract

Distributed forces resulting from molecular interactions between macroscopic bodies are usually concentrated near surfaces. A new formulation that replaces these distributed body forces by effective surface tractions and is not limited by the geometrical restrictions of Derjaguin's approximation has been developed. It offers great computational simplification over the use of the body force distribution. The body force distribution is integrated and partitioned to various surface elements. The resulting expressions for surface traction involve a second-order tensor termed the *inter-surface stress tensor*. It is a symmetric tensor defined for any body in terms of the intermolecular potential and the shape of the body. It acts much like the internal stress tensor; the surface traction vector on a surface introduced into its field is the inner product of the tensor and the surface normal. The new surface formulation reduces to Derjaguin's approximation for the case of a half-space with a plane surface. Properties of the new tensor are explored along with their physical significance. Actual components are derived for several geometries.

Key Words: surface formulation; surface forces; effective tractions, molecular interactions

Introduction

The continuum description of the effects of molecular interactions between bodies is important for the analysis of a variety of processes such as sintering (1,2), adhesion (3-5), crack-tip deformations (6,7), colloidal interactions, and atomic force microscopy (8,9). If $w(s)$ is the potential function between a pair of molecules as a function of separation s , one of the basic problems is the determination of total force or energy of interaction between macroscopic bodies. The analytical integration of the pair potential to obtain the macroscopic interaction potential was done by Bradley (10), de Boer (11), and Hamaker (12) for the specific case of van der Waals interactions. A compilation of their results can be found in (3). This approach assumes: a) additivity: the total force can be obtained by the pairwise summation of individual contributions; b) continuous medium: the summation is replaced by an integration over the volume; c) constant material properties: the number densities of molecules, ρ , and interaction constants do not vary over the volume of the bodies. Specifically, the interaction energy E between two bodies defined by the volumes V_1 and V_2 is given by the double volume integral:

$$E = \rho_1 \rho_2 \int_{V_2} \int_{V_1} w(s) dV_1 dV_2. \quad [1]$$

where ρ_1 and ρ_2 are the number densities of molecules in the two bodies. Similarly, the total force of interaction between two bodies, \mathbf{A} , is

$$\mathbf{A} = -\rho_1 \rho_2 \int_{V_2} \int_{V_1} \nabla w dV_1 dV_2. \quad [2]$$

Because the double-volume integrations are difficult to execute analytically, the application of this theory has been limited to simple geometries such as planar half-spaces and spheres (3). Numerical integration is also difficult because the forces are usually concentrated near the surface of the body (13). Much would be gained if the volume integral could be replaced by surface integrals.

Another problem, important for the analysis of deformation of bodies under the influence of these forces, is the determination of effective surface tractions. A simple and powerful method that uses surface tractions and addresses both these problems is the Derjaguin approximation (14). In its original form, Derjaguin's approximation was used to compute total forces and energies of interactions between particles. The approximation has also been used to specify distributed surface tractions on bodies to analyze deformation (5,7). Let the interaction force per unit area between two planar half-spaces be $f(s)$, where s is the distance separating the half-spaces. For two given bodies, choose a direction with unit vector \mathbf{E} , for example as the line connecting the centers of two spheres. Then, according to Derjaguin's approximation the traction \mathbf{T} at any point on the surfaces of the two bodies is assumed to be:

$$\mathbf{T} = f(s) (\mathbf{E} \cdot \mathbf{n}) \mathbf{E}, \quad [3]$$

where \mathbf{n} is the normal to the surface and s measures distance along \mathbf{E} . Derjaguin's approximation is accurate for smooth convex surfaces with small curvature compared to the separation between the bodies. For many simple geometries, symmetry provides an obvious choice of \mathbf{E} . In general, however, Derjaguin's approximation does not indicate how and if \mathbf{E} can be chosen.

A new method for the computation of effective surface tractions resulting from molecular interactions has recently been developed (13). The body force distribution in one body due to another is integrated and partitioned to obtain distributed surface tractions. In this scheme the influence of a body is represented by a second order tensor: the *inter-surface stress tensor*. This tensor field depends on the shape of the body and the basic inter-molecular potential. Upon an inner product with the surface normal of another body, it produces a surface traction. The total energy of interaction between two bodies is obtained in a similar fashion in terms of surface integrals alone. The formulation is applicable to arbitrarily shaped bodies and offers major computational simplification. It has been implemented as a surface finite element (13,15) which also includes terms due

to self-interactions (the surface tension). The effectiveness of the new formulation has been demonstrated by its application to several problems: computation of the force between bodies and adhesion between spheres (13), viscoelastic coalescence (16), and tip-material interactions in atomic force microscopy (17).

This paper is devoted to a discussion of the new quantity that has emerged from the surface formulation: the inter-surface stress tensor. We begin in Section 2 with a new derivation of the surface formulation that highlights some the properties of the inter-surface stress tensor. Its properties and their physical significance are discussed in Section 3. Actual components of the tensor are computed in Section 4 for several geometries: a plane half-space, a quadrant, a sphere, and a cylinder. Although in general the two are different, it is shown that the new formulation and Derjaguin's approximation coincide for the case of a half-space. The new surface formulation yields the correct total force and energy of interaction; errors in Derjaguin's approximation can be quantified in other cases.

Surface formulation

Consider two bodies 1 and 2 as shown in figure 1. The coordinates of points in the two bodies are \mathbf{x}_1 and \mathbf{x}_2 respectively. Let $w(s)$ be the pair potential between molecules in the two bodies. If ρ_1 and ρ_2 are the (uniform) number density of molecules, the force on an element of volume dV_1 in body 1 due to an element of volume dV_2 in body two is¹:

$$\mathbf{f}(s) = -\rho_1 \rho_2 \nabla_1 (w(s)) dV_1 dV_2 = \rho_1 \rho_2 \nabla_2 (w(s)) dV_1 dV_2, \quad [4]$$

$$s = ((\mathbf{x}_2 - \mathbf{x}_1) \cdot (\mathbf{x}_2 - \mathbf{x}_1))^{\frac{1}{2}},$$

where ∇_1 and ∇_2 represents the gradient with respect to \mathbf{x}_1 and \mathbf{x}_2 , respectively. The body force distribution in body 1 due to body 2, \mathbf{b} , is²:

$$\mathbf{b} = \rho_1 \rho_2 \int_{V_2} \nabla_2 w dV_2 = \rho_1 \rho_2 \int_{S_2} w \mathbf{n}_2 dS_2, \quad [5]$$

where the last equality follows from the divergence theorem. For short-range intermolecular forces, the body forces decay rapidly with distance from the free surface. These are replaced by a distribution of effective surface tractions as discussed below.

Consider a cone of infinitesimal solid angle $d\alpha$ emanating from a point P in body 2 and piercing surface 1 at points Q_i , where for odd i the cone axis enters the surface while for even i it leaves the surface. Let the unit vector along the cone axis be \mathbf{e} oriented from the Q_i towards P . The integrated force in this cone per unit volume of body 2 is:

$$\frac{d\mathbf{F}}{dV_2} = \rho_1 \rho_2 \int_{V_{\text{cone}}} \nabla_2 w \, dV_1. \quad [6]$$

This integral may be written as a sum of line integrals along the cone axis, each from s_i to ∞ , where s_i is the distance from P to Q_i . By making $dV_1 = t^2 d\alpha \, dt$ in the cone, where t measures distance along the cone axis, and noting that the gradient operator can be extracted out of the integral, we obtain

$$\frac{d\mathbf{F}}{dV_2} = \rho_1 \rho_2 \nabla_2 \left(d\alpha \sum_i (-1)^{i+1} \int_{s_i}^{\infty} w(t) t^2 \, dt \right) = \sum_i \frac{d\mathbf{F}_i}{dV_2}, \quad [7]$$

where $d\mathbf{F}_i$ is the force assigned to the various points Q_i . It is assumed that $w(t)$ decreases faster than $1/t^3$, quickly enough for the integrals to be finite. We propose to use this partitioning of the force to assign to surface points Q_i each successive term of the above expression, e.g., the force on point Q_1 is

$$\frac{d\mathbf{F}_1}{dV_2} = \rho_1 \rho_2 \nabla_2 \left(d\alpha \int_{s_1}^{\infty} w(t) t^2 \, dt \right). \quad [8]$$

The solid angle can be expressed as:

$$s_i^2 d\alpha = (-1)^{i+1} (\mathbf{e} \cdot \mathbf{n}_1) dS_1, \quad [9]$$

Substituting [9] into [7], the effective force on point Q_i may be written as:

$$\frac{d\mathbf{F}_i}{dV_2} = \rho_1 \rho_2 \nabla_2 \left((\mathbf{e} \bullet \mathbf{n}_1) dS_1 \frac{1}{s_i^2} \int_s^\infty w(t) t^2 dt \right). \quad [10]$$

This procedure partitions the integrated effect of a volume element in body 2 on the conical volume element in body 1 into terms that can then be assigned to the surface S_1 .

Note that we now have an expression that is valid for any point on the surface of body 1.

Define a vector function \mathbf{G} , termed the *inter-surface force kernel*, as:

$$\begin{aligned} \mathbf{G} &= (\mathbf{x}_2 - \mathbf{x}_1) v(s) \\ v(s) &= -\frac{1}{s^3} \int_s^\infty w(t) t^2 dt \end{aligned} \quad [11]$$

The scalar function of distance $v(s)$ has units of energy per molecule per molecule while $\rho_1 \rho_2 \mathbf{G}$ has units of force per unit area of 1 per unit area of 2. Note that $\mathbf{e} = (\mathbf{x}_2 - \mathbf{x}_1) / s$ and substitute [11] into [10]. The total effective traction \mathbf{T} at any point on the surface of body 1 (per unit area dS_1) is now obtained by integrating the resulting expression over the volume of body 2:

$$\mathbf{T} = \left(\rho_1 \rho_2 \int_{V_2} [\nabla_2 \mathbf{G}]^T dV_2 \right) \cdot \mathbf{n}_1 = \left(\rho_1 \rho_2 \int_{S_2} \mathbf{n}_2 \mathbf{G} dS_2 \right) \cdot \mathbf{n}_1 \quad [12]$$

where the last equality follows from an application of the divergence theorem. This is a formula that computes an effective traction on the surface of body 1. Like the body force [5], the orientation of the traction vector at any point on surface 1 is an average of the normal to the surface 2, weighted by a function of distance. The quantity

$$\mathbf{h} = \rho_1 \rho_2 \int_{V_2} [\nabla_2 \mathbf{G}]^T dV_2 = \rho_1 \rho_2 \int_{S_2} \mathbf{n}_2 \mathbf{G} dS_2 \quad [13]$$

is a second-order tensor field which we call the *inter-surface stress tensor*. The tensor field exists outside any body and upon an inner product with the surface of another body produces an effective surface traction like the internal stress tensor. Its dependence on the pair potential is captured by the inter-surface force kernel [11]. Through the volume or surface integral, it depends on the shape of the body. Specific forms for a few different

potentials have been given in (13); here we shall use the case of an inverse power-law potential to illustrate the properties of the inter-surface stress tensor:

$$w(s) = \frac{B}{s^m}, \quad [14]$$

Then, from [11],

$$v(s) = \frac{1}{s^3} \int_s^\infty w(t)t^2 dt = \frac{B}{(m-3)s^m}, \quad (m > 3). \quad [15]$$

The *inter-surface force kernel* for this potential is

$$\mathbf{G} = (\mathbf{x}_2 - \mathbf{x}_1) \frac{B}{(m-3)s^m}. \quad [16]$$

In the following sections we shall explore the significance of the inter-surface stress tensor. It is worth mentioning at this point, however, that converting the distributed body-force field into a field of effective surface tractions also affords great computational simplification. It has been shown (13) that the total force between two bodies, \mathbf{A} , and the total interaction energy, E , can now be computed in terms of double surface integrals:

$$\mathbf{A} = \rho_1 \rho_2 \int_{S_1} \mathbf{h} \cdot \mathbf{n}_1 dS_1 = \rho_1 \rho_2 \int_{S_1} \int_{S_2} \mathbf{n}_2 (\mathbf{G} \cdot \mathbf{n}_1) dS_1 dS_2 \quad [17]$$

$$E = \rho_1 \rho_2 \int_{S_2} \int_{S_1} u(s) (-\mathbf{n}_1 \cdot \mathbf{n}_2) dS_1 dS_2 \quad [18]$$

The scalar function $u(s)$ is termed the *inter-surface potential* and is defined by:

$$u(s) = - \int s v(s) ds. \quad [19]$$

For the inverse power-law potential, it is:

$$u(s) = \frac{B}{(m-2)(m-3)s^{m-2}}. \quad [20]$$

The replacement of distributed body forces by effective surface tractions is physically valid only for potentials that decay rapidly enough for the definite integrals in [11] to be finite. However, by defining $v(s)$ via the indefinite integral:

$$v(s) = - \frac{1}{s^3} \int w(s) s^2 ds. \quad [21]$$

it is still possible to use the above formulation to compute the total force (and similarly the total energy) of interaction between two bodies in terms of a double surface integral.

The Inter-Surface Stress Tensor

Consider the specific form of the inter-surface force kernel [11] and the volume integral definition of the inter surface stress tensor [13]. Because:

$$\nabla_2 \mathbf{G} = v(s) \mathbf{I} + (\mathbf{x}_2 - \mathbf{x}_1)(\mathbf{x}_2 - \mathbf{x}_1) \frac{1}{s} \frac{dv(s)}{ds} \quad [22]$$

or

$$G_{i,2j} = \delta_{ij} v(s) + (x_{2i} - x_{1i})(x_{2j} - x_{1j}) \frac{1}{s} \frac{dv(s)}{ds}$$

the tensor \mathbf{h} (or h_{ij} in indicial notation) is real and symmetric. By its very definition it is a tensor quantity. Being real and symmetric, it has three real eigenvalues λ , given by the solution of:

$$\mathbf{h} \cdot \mathbf{n}_1 = \lambda \mathbf{n}_1. \quad [23]$$

Physically, the eigenvectors represent the three orientations of a surface for which the traction is normal to the surface.

Like the internal stress tensor, \mathbf{h} can be decomposed into a spherical and a deviatoric part

$$\mathbf{h} = Tr(\mathbf{h})\mathbf{I} + \mathbf{h}_d. \quad [24]$$

where $Tr(\mathbf{h})$ is the trace of \mathbf{h} , and \mathbf{h}_d is its deviatoric part. The trace of \mathbf{h} is:

$$Tr(\mathbf{h}) = \rho_1 \rho_2 \int_{V_2} Tr[\nabla_2 \mathbf{G}]^T dV_2 = \rho_1 \rho_2 \int_{V_2} \nabla_2 \bullet \mathbf{G} dV_2 = -\rho_1 \rho_2 \int_{V_2} w dV_2. \quad [25]$$

To establish the last equality we have used a previously established result (13):

$$\nabla_1 \bullet \mathbf{G} = -\nabla_2 \bullet \mathbf{G} = w. \quad [26]$$

This implies that the trace of the tensor depends only on the volume integral of the pair potential. If $w(s)$, as in the case of the attractive van der Waals potential, is always negative, the trace of \mathbf{h} is always positive. To explore the physical significance of this fact, consider a cubic test volume brought near the surface of body 2 under the influence of an

attractive potential. Furthermore, let the orientation of its normals coincide with the principal orientations of \mathbf{h} at that point. Then the three diagonal elements of \mathbf{h} are the three tractions normal to the faces of the cube. The trace of \mathbf{h} , the first invariant of the tensor is the effective pressure (positive when tensile) inside the test volume. It equals the work done in bringing a unit volume from infinity to the given location near body 2. The above result implies, as expected, that the pressure will be tensile if $w(s)$ is negative everywhere. In most such cases all the eigenvalues are positive; the tensor is positive definite:

$$\mathbf{n}_1 \cdot \mathbf{h} \cdot \mathbf{n}_1 > 0 \quad [27]$$

implying that the traction vector points away from the surface. However, this is not always true even for an attractive potential. Using the same test volume one can attach a physical significance to the second invariant of the deviatoric part of \mathbf{h} , \mathbf{h}_d ; it represents the effective shear stress in a test volume.

Consider also the divergence in body 1 of \mathbf{h} due to body 2. Using, successively, equations [13], [26], and [5],

$$\nabla_1 \cdot \mathbf{h} = \rho_1 \rho_2 \int_{S_2} \mathbf{n}_2 \nabla_1 \cdot \mathbf{G} dS_2 = \rho_1 \rho_2 \int_{S_2} w \mathbf{n}_2 dS_2 = \mathbf{b}, \quad [28]$$

i.e., the divergence of \mathbf{h} equals the body force. By comparison with the governing equation for stresses σ in elastostatics, $\nabla_1 \cdot \sigma + \mathbf{b} = 0$, which is based on the divergence of stresses equilibrating the body forces, equation [28] is another way of stating that the tensor \mathbf{h} replaces the body force distribution.

Examples

The nature of the inter-surface stress tensor is explored further in this section by computing its components for a few specific geometries. These geometries are important in themselves. The results for simple geometries can also be used to construct \mathbf{h} for more

complicated bodies by superposition. Determination of individual components of \mathbf{h} involves evaluation of the surface or volume integrals given by equation [13]. Here we present closed-form expressions for a few simple cases. A general numerical formulation can be found in (15). The numerical examples are for the case of the van der Waals potential which is an inverse power law with $m = 6$. It is apparent from the surface integral definition of \mathbf{h} (equation [13]) that results for any given geometry can immediately be used for the corresponding inverted geometry. For example, the expressions for components of \mathbf{h} outside a solid sphere apply equally well for a spherical cavity inside an infinite medium with a change in sign to account for the inversion of the surface.

Consider first the case of a half-space bounded by a plane (Figure 2). Fix a cartesian coordinate system on the surface of the plane with the x and y axes in the surface of the plane and the z axis normal to the plane and pointing out of it. Then the normal to the surface is

$$(n_x, n_y, n_z) = (0, 0, 1). \quad [29]$$

Consider a point located a distance a on the z axis above the surface. Because only n_x and n_y are both zero, the only components of \mathbf{h} that do not vanish identically are h_{xz} , h_{yz} , and h_{zz} . By symmetry, h_{xz} and h_{yz} also vanish after the surface integration because of cancelling contributions (equations [13] and [16]). The component h_{zz} is:

$$h_{zz} = \rho_1 \rho_2 \int_{S_2} (-a) v(s) dS_2 = -2\pi a \rho_1 \rho_2 \int_0^\infty v(s) r dr. \quad [30]$$

Changing the integration variable to s and using $s^2 = a^2 + r^2$ one obtains:

$$h_{zz} = -2\pi a \rho_1 \rho_2 \int_a^\infty v(s) s ds = 2\pi a \rho_1 \rho_2 u(a), \quad [31]$$

assuming that $u(s)$ vanishes as $s \rightarrow \infty$. The traction on a body brought near the half-space will be oriented along the z axis with magnitude

$$T_z = h_{zz} n_z = 2\pi a \rho_1 \rho_2 u(a) n_z. \quad [32]$$

The force of interaction between two planar half-spaces per unit area, $f(a)$, is given by:

$$f(a) = -\rho_1 \rho_2 \int_{V_2} \int_a^\infty (\nabla_2 w \cdot \mathbf{e}_z) dz_1 dV_2 = -\rho_1 \rho_2 \int_{V_2} \int_a^\infty w'(s) \frac{(z_2 - z_1)}{s} dz_1 dV_2, \quad [33]$$

where (x_1, y_1, z_1) and (x_2, y_2, z_2) measure the location of points in the two half spaces.

Writing $s^2 = r^2 + (z_1 - z_2)^2$, and replacing the integration variable z_1 by s :

$$f(a) = \rho_1 \rho_2 \int_{V_2} w(s) dV_2. \quad [34]$$

By the definition of \mathbf{G} , this is also:

$$f(a) = \rho_1 \rho_2 \int_{V_2} \nabla_2 \mathbf{G} dV_2 = \rho_1 \rho_2 \int_{S_2} \mathbf{G} \cdot \mathbf{n}_2 dS_2 = -\rho_1 \rho_2 \int_{S_2} (a) v(s) dS_2. \quad [35]$$

This is identical to the expression for h_{zz} (equation [30]). Consider now the use of Derjaguin's approximation to compute effective tractions on any body due to the half-space. If the direction \mathbf{E} of equation [3] is chosen to be \mathbf{n}_2 , it is evident that the tractions on any body due to a half-space are the same whether computed by the new surface formulation or Derjaguin's approximation. In this sense, the new surface formulation may be said to reduce to Derjaguin's approximation for a plane half-space. It also follows that in this case Derjaguin's approximation gives the correct total force between the half-space and any other body. However, the distribution of tractions on a half-space as computed by Derjaguin's approximation or the surface formulation will be different. In general, the use of Derjaguin's approximation may introduce errors even for the total force.

Consider next a quadrant as drawn in Figure 3. We shall compute the components of \mathbf{h} at a point $(0, y_1, z_1)$. As mentioned earlier, the result for a point in the exterior of a quadrant can also be used to determine \mathbf{h} near a re-entrant corner because one uses only a surface integration. Because the normal to the surface is always in the y - z plane, only components h_{yy} , h_{zz} and h_{yz} need be determined. Only the vertical part of the surface of

the quadrant, A , contributes to h_{yy} because the surface normal over the horizontal part of the surface, B , is oriented along the z direction. Then, for the inverse power law potential,

$$h_{yy} = \rho_1 \rho_2 y_1 \int_{z_2=0}^{-\infty} \int_{x_2=-\infty}^{+\infty} \frac{B}{(m-3)(x_2^2 + y_1^2 + (z_2 - z_1)^2)^{m/2}} dx_2 dz_2. \quad [36]$$

For the case of the van der Waals potential, $m = 6$, one obtains:

$$h_{yy} = -B \rho_1 \rho_2 \pi \left(\frac{1}{12 y_1^3} - \frac{z_1 (2z_1^2 + 3y_1^2)}{24 y_1^3 (y_1^2 + z_1^2)^{3/2}} \right). \quad [37]$$

This expression is valid everywhere except at $y_1 = 0$, where $h_{yy} = 0$ identically. By symmetry, $h_{zz}(y_1, z_1) = h_{yy}(-z_1, -y_1)$, which yields:

$$h_{zz} = -B \rho_1 \rho_2 \pi \left(\frac{1}{12 z_1^3} + \frac{y_1 (2y_1^2 + 3z_1^2)}{24 z_1^3 (y_1^2 + z_1^2)^{3/2}} \right) \quad [38]$$

By a similar integration:

$$h_{yz} = h_{zy} = -\rho_1 \rho_2 \int_{z_2=0}^{-\infty} \int_{x_2=-\infty}^{+\infty} \frac{(z_2 - z_1) B}{(m-3)(x_2^2 + y_1^2 + (z_2 - z_1)^2)^{m/2}} dx_2 dz_2 \quad [39]$$

which yields

$$h_{yz} = \frac{B \rho_1 \rho_2 \pi}{24 (y_1^2 + z_1^2)^{3/2}} \quad [40]$$

The variation of the three components with normalized distance along the y axis, y_1 / z_1 , is shown in Figure 4. The components are normalized by the value of h_{zz} for large y_1 / z_1 , equation [31]. As seen in Figure 4 (and can be shown exactly), far from the edge of the quadrant along the positive y axis the tensor \mathbf{h} reverts back to the value expected for a half-space bounded by a plane. As one approaches the edge, h_{zz} decreases in magnitude and vanishes at larger distances along the negative y axis. The other components of \mathbf{h} are present in the vicinity of the edge only. Clearly, the presence of the edge in the quadrant is felt upto distances y_1 on the order of z_1 .

Consider now a quadrant near a half-space as shown in Figure 5. The figure compares the body force vector on the surface of the quadrant and the half-space to the traction vectors given by the surface formulation and Derjaguin's approximation. Note that the tractions and the body-force vectors are different physical quantities; and not comparable

quantitatively. The comparison between the two tractions is quantitative. The purpose of this figure is more to compare the distributions of the different fields qualitatively. The body force on the quadrant is oriented along the normal to the half-space as are the surface tractions. Also, the tractions as given by the surface formulation and Derjaguin's approximation are identical. The body forces on the half-space due to the quadrant can be determined using the surface integral [5]. Specifically,:

$$b_y = \rho_1 \rho_2 \int_{z_2=0}^{\infty} \int_{x_2=-\infty}^{+\infty} \frac{B}{(m-3)(x_2^2 + y_1^2 + (z_2 - z_1)^2)^{m/2}} dx_2 dz_2. \quad [41]$$

which, for $m = 6$, yields:

$$b_y = -B \rho_1 \rho_2 \pi \left(\frac{1}{12 y_1^4} - \frac{z_1 (2z_1^2 + 3y_1^2)}{24 y_1^4 (y_1^2 + z_1^2)^{3/2}} \right). \quad [42]$$

By symmetry, $b_z(y_1, z_1) = b_y(-z_1, -y_1)$. The tractions, as given by the surface formulation, are:

$$\begin{Bmatrix} T_y \\ T_z \end{Bmatrix} = \begin{bmatrix} h_{yy} & h_{yz} \\ h_{zy} & h_{zz} \end{bmatrix} \begin{Bmatrix} 0 \\ -1 \end{Bmatrix} = - \begin{Bmatrix} h_{yz} \\ h_{zz} \end{Bmatrix}. \quad [43]$$

Derjaguin's approximation, using the normal to the half-plane as \mathbf{E} , gives tractions on the half-space that are equal and opposite to the tractions on the quadrant surface. The comparison of the three force distributions in Figure 5 shows that the effective surface tractions given by the surface formulation are very similar to the distribution of body forces. Derjaguin's approximation, applicable in this case because a unique direction \mathbf{E} is identifiable, does not capture the decrease in surface tractions near the edge of the quadrant.

A knowledge of \mathbf{h} for the quadrant makes it possible to compute tractions on any other surface brought in the vicinity of the quadrant. An example is the interaction of two quadrants as shown in Figure 6. Again, we display the body force field and the tractions as given by the two formulations. To compute tractions using Derjaguin's approximation, the direction \mathbf{E} has been chosen as the symmetry axis $y=z$. Note that for general alignment of the two quadrants, the choice of \mathbf{E} is not clear. Consequently the

application of Derjaguin's approximation is problematic. Body force and traction vectors on the surface are computed in a manner similar to that shown above. The body force vectors on the surface increase in magnitude as one approaches the corner and change orientation, making an angle of $\pi/4$ with the vertical at the corner. Interestingly, at distances remote from the corner, there is a finite limiting angle of the vectors with the vertical direction ($\cos^{-1}(8/\sqrt{73}) \approx 20.6^\circ$ for van der Waals forces). Tensions given by the Derjaguin's approximation maintain a constant angle of $\pi/4$ with the vertical. Surface tractions given by the surface formulation also change orientation as one approaches the corner. However, far from the corner they align with the vertical direction. Also, at the corner, the tractions are discontinuous; there is an abrupt change in orientation. The limiting angle with the vertical direction when one approaches along the horizontal face of the quadrant is $\cos^{-1}\left(1/\sqrt{1+\left(1/\left(4\sqrt{2}-5\right)^2\right)}\right) \approx 56.7^\circ$. The total force between two quadrants as given by the surface formulation is exact. The total force, as calculated by Derjaguin's approximation, is too large by a factor of $2\sqrt{2}$.

Consider now a sphere as shown in Figure 7. We shall compute the components of the tensor at a point a distance a along the z axis, as drawn. The integration is for all points on the surface of the sphere located by the radius r and angles θ and ϕ as drawn. Clearly, the same results can be used for \mathbf{h} inside a spherical cavity by multiplying by -1 to account for the change in surface normal. By symmetry, the off-diagonal components of \mathbf{h} vanish identically. For the van der Waals potential

$$h_{xx} = h_{yy} = \frac{B\rho_1\rho_2 r^3}{3} \int_{-\pi/2}^{\pi/2} d\phi \int_0^{2\pi} \frac{\cos^3(\phi) \cos^2(\theta)}{\left(r^2 + a^2 - 2ra \sin(\phi)\right)^3} d\theta, \quad [44]$$

which is

$$h_{xx} = h_{yy} = \frac{B\rho_1\rho_2 \pi}{24a^3} \left(\frac{3r^2 - 2ar + 3a^2}{2(a-r)^2} - \frac{3r^2 + 2ar + 3a^2}{2(a+r)^2} + \log\left(\frac{(a-r)^2}{(a+r)^2}\right) \right). \quad [45]$$

Similarly,

$$h_{zz} = -\frac{B\rho_1\rho_2 r^2}{6} \int_{-\pi/2}^{\pi/2} d\phi \int_0^{2\pi} \frac{(a - r \sin(\phi)) \sin(2\phi)}{(r^2 + a^2 - 2r a \sin(\phi))^3} d\theta, \quad [46]$$

which is

$$h_{zz} = \frac{B\rho_1\rho_2 \pi}{12 a^3} \left(\frac{3r^3 - 5r^2 a - r a^2 - a^3}{2(a-r)^3} + \frac{3r^3 + 5r^2 a - r a^2 + a^3}{2(a+r)^3} - \log\left(\frac{(a-r)^2}{(a+r)^2}\right) \right). \quad [47]$$

As $a \rightarrow r$, $h_{xx} \rightarrow 0$ and

$$h_{zz} \rightarrow -\frac{B\pi\rho_1\rho_2}{6(a-r)^3}, \quad [48]$$

i.e., as one approaches the surface \mathbf{h} reverts to its value for a half-space. The two components, normalized by the value for a half-space (equation [31]), are plotted as a function of distance from the sphere surface in Figure 8. The traction on a surface introduced near the sphere is dominated by h_{zz} , i.e., it approximately points towards the center of the sphere. The body force vector due to a sphere on any element of volume points exactly towards the center. Because Derjaguin's approximation uses the half-space result, it is increasingly inaccurate in terms of orientation and magnitude of the forces as one moves away from the surface of the sphere. The same results can be used for a spherical cavity in an infinite medium. A test volume at the center of the spherical cavity would experience a hydrostatic state of stress (tension for the attractive van der Waals potential). The diagonal components of \mathbf{h} are identical at the center and are:

$$h_{xx} = h_{yy} = h_{zz} = \frac{4B\pi\rho_1\rho_2}{9r^3}. \quad [49]$$

The traction on any surface is then:

$$\begin{Bmatrix} T_x \\ T_y \\ T_z \end{Bmatrix} = \begin{bmatrix} h_{xx} & 0 & 0 \\ 0 & h_{yy} & 0 \\ 0 & 0 & h_{zz} \end{bmatrix} \begin{Bmatrix} n_x \\ n_y \\ n_z \end{Bmatrix}. \quad [50]$$

Figure 9 shows body force and traction distributions for a sphere near a half-space. Again, the forces on the sphere all point along the normal to the half-space. The forces on the half-space, as given by Derjaguin's approximation all point along the normal to the half-

space. The tractions given by the surface formulation, like the body force distribution shows a variation in orientation.

Similar results can be obtained for a cylinder. To illustrate, we present the case of $m=7$ which results in far simpler integrals than the van der Waals potential. Figure 10 shows a cylinder with the x axis as the cylinder axis. We calculate the components of \mathbf{h} at a point a distance a along the z axis. By symmetry only the diagonal elements h_{yy} and h_{zz} need be considered. These are evaluated as:

$$h_{yy} = \frac{B\rho_1\rho_2 r^2}{4} \int_0^{2\pi} d\theta \int_{-\infty}^{\infty} \frac{\cos^2(\theta)}{(r^2 + x^2 + a^2 - 2ra \sin(\phi))^{7/2}} d\theta \quad [51]$$

$$= \frac{4B\pi\rho_1\rho_2 r^2}{15(a^2 - r^2)^3}$$

$$h_{zz} = -\frac{B\rho_1\rho_2 r}{4} \int_0^{2\pi} d\theta \int_{-\infty}^{\infty} \frac{\sin(\theta) a - r \sin(\theta)}{(r^2 + x^2 + a^2 - 2ra \sin(\phi))^{7/2}} d\theta \quad [52]$$

$$= -\frac{4\pi B\rho_1\rho_2 r^2 (r^2 + 5a^2)}{15(a^2 - r^2)^4}$$

In the limit $a \rightarrow r$, as the point approaches the surface of the cylinder, $h_{yy} \rightarrow 0$ and h_{zz} approaches the value for a half-space (equation [31]). The variation of the two components, normalized by the half-space expression for h_{zz} are plotted in Figure 11. The results are qualitatively similar to those for the sphere, but the variation with increasing distance from the surface of the cylinder is more gradual. Again, with a change in sign these results apply to a point inside the cylinder as well. At the center of the cylinder:

$$h_{yy} = h_{zz} = -\frac{4B\pi\rho_1\rho_2}{15r^4} \quad [53]$$

Summary

The distributed body forces resulting from molecular interactions between bodies has been integrated and partitioned to obtain a distribution of effective surface tractions. The procedure is general and reduces to Derjaguin's approximation for the computation of tractions on any body due to a half-space. In this scheme, the effect of a body on the space

surrounding it can be written as a second order tensor field termed the inter-surface stress tensor \mathbf{h} . This is a symmetric tensor which, like the internal stress tensor, yields a traction upon an inner product with the normal to a surface. The trace of the tensor represents the effective hydrostatic stress in an elemental volume and equals the volume integral of the molecular potential. The new surface formulation removes the geometric restrictions of Derjaguin's approximation. It always yields the correct total force and total energy of interaction between bodies and offers considerable computational simplification over the use of the body force distribution. The formulation can be used also to analyze deformations driven by surface forces without restrictions on the geometry, large deformations, etc. A few simple geometries have been studied to illustrate the properties of the new tensor: a half-space, quadrant, sphere, and cylinder.

Acknowledgment

This work has been supported in part by the Air Office Office of Scientific Research, USAF, under contract number F49620-95-C-0008. The views and conclusions herein are those of the authors and should not be interpreted as necessarily representing the official policies or endorsements, either expressed or implied, of the Air Force Office of Scientific Research or the U.S. Government. The authors are indebted to Dr. S. Mazur and Dr. W.C. Carter for several helpful discussions.

References

1. Hiram, Y. and Nir, A. A Simulation of surface tension drive coalescence, *J. Colloid Interface Sci.*, **95** [2] 462-470 (1983).
2. Jagota A., Dawson P.R., Simulation of viscous sintering of two particles, *Journal of the American Ceramic Society*, **73** [1] 173-177 (1989).
3. Israelachvili, J. *Intermolecular and Surface Forces*, second edition, Academic Press, San Diego (1991).
4. Johnson K.L., Kendall K., Roberts A.D. Surface energy and the contact of elastic solids, *Proceedings of the Royal Society, London, A* **324** 301-313 (1971).
5. Derjaguin, B.V., Muller, V.M. and Toporov, Y.P. Effect of contact deformations on the adhesion of particles, *J. Colloid Interface Sci.*, **53** [2] 314-326 (1975).
6. Lawn B.R. *Fracture of Brittle Solids*, Cambridge University Press, Second Edition, Cambridge (UK) (1993).
7. Chan, D.Y.C., Hughes, B.D. and L.R. White A physically consistent theory of fracture in a brittle solid, *J. Colloid Interface Sci.*, **115** [1] 240-259 (1987).
8. Landman, U., Luedtke, W.D., Burnham, N.A. and Colton, R.J. Atomistic mechanism and dynamics of adhesion, nanoidentation and fracture, *Science*, **248** 454-461 (1990).

9. Hartmann, U. Theory of van der Waals microscopy, *J. Vac. Sci. Technol. B*, **9** [2] 465-469 (1991).
10. Bradley R.S., The cohesive force between solid surfaces and the surface energy of solids, *Philosophical Magazine* **13** 853-862 (1932).
11. de Boer, J.H., The influence of van der Waals'forces and primary bonds on binding energy, strength and orientation, with special reference to some artificial resins, *Transactions of the Faraday Society*, **32**, 10-38 (1936).
12. Hamaker, H.C. The London-van der Waals attraction between spherical particles, *Physica*, **4** , 1058-1072 (1937).
13. Argento C., Jagota A., Carter W.C., Surface formulation for molecular interaction of macroscopic bodies, *Journal of the Mechanics and Physics of Solids*, submitted (1996).
14. Derjaguin, B.V., Untersuchungen über die Reibung und Adhäsion, IV, (Investigations concerning friction and adhesion IV), *Kolloid Z.*, **69** 155-164 (1934).
15. Argento C., Jagota A., A surface finite element for molecular interactions, *Computational Materials Science*, in preparation (1996).
16. Argento C., Mazur S., Jagota A., Problems in viscoelastic neck growth, in *Sintering Technology*, R.M. German, G.L. Messing, R.G. Cornwall (editors) Marcel Dekker (New York) 21-28 (1995).

17. Argento, C. and French R.H., Parametric tip model and force-distance relation for Hamaker constant determination from AFM, *Journal of Applied Physics*, in press (1996).

Figure captions

Figure 1: Procedure followed to partition the integrated body force field into contributions that can be assigned to surface points. The forces on body 1 due to an element of volume at point P are integrated along rays emanating from P and assigned to surface points Q_i .

Figure 2: Coordinates used to compute components of \mathbf{h} for a half-space at a point located a distance a above the plane.

Figure 3: Coordinates used to compute components of \mathbf{h} for a point near the edge of a quadrant.

Figure 4: Components of \mathbf{h} for a quadrant, normalized by the value of h_{zz} for a half-space as a function of normalized distance from the edge for the van der Waals potential.

Figure 5: Surface force fields on a quadrant and a half-space for the van der Waals potential.

Figure 6: Surface force fields on two opposed quadrants for the van der Waals potential. The magnitude of the drawn vectors is proportional to the logarithm of the force vectors.

Figure 7: Coordinates used to compute components of \mathbf{h} for a point near a spherical surface.

Figure 8: Components of \mathbf{h} , normalized by the expression for a half-space, at a point near a spherical surface as a function of normalized distance from the sphere surface.

Figure 9: Surface force fields on a sphere and a half-plane. The magnitude of the drawn vectors is proportional to the logarithm of the force vectors.

Figure 10: Coordinates used to compute components of \mathbf{h} for a point near a cylindrical surface.

Figure 11: Components of \mathbf{h} , normalized by the expression for a half-space, at a point near a cylindrical surface as a function of normalized distance from the cylindrical surface.

FOOTNOTES

¹ Bold-face letters represent vectors or second-order tensor quantities; the two are distinguished by context.

When bold-face letters are used, subscripts refer to a particular body. Later in the paper, subscripts are used to refer to individual tensor components.

² We shall be concerned mainly with three physical quantities: (a) the body force distribution \mathbf{b} (vector) which has units of N/m^2 , (b) a distribution of effective surface tractions \mathbf{T} (vector) which has units of N/m^2 , and (c) a second order inter-surface stress tensor \mathbf{h} which has units of N/m^2 . Recall also that the surface traction vector and stress tensor are related by $\mathbf{T} = \mathbf{h} \cdot \mathbf{n}$, where \mathbf{n} is the outer surface normal.

①

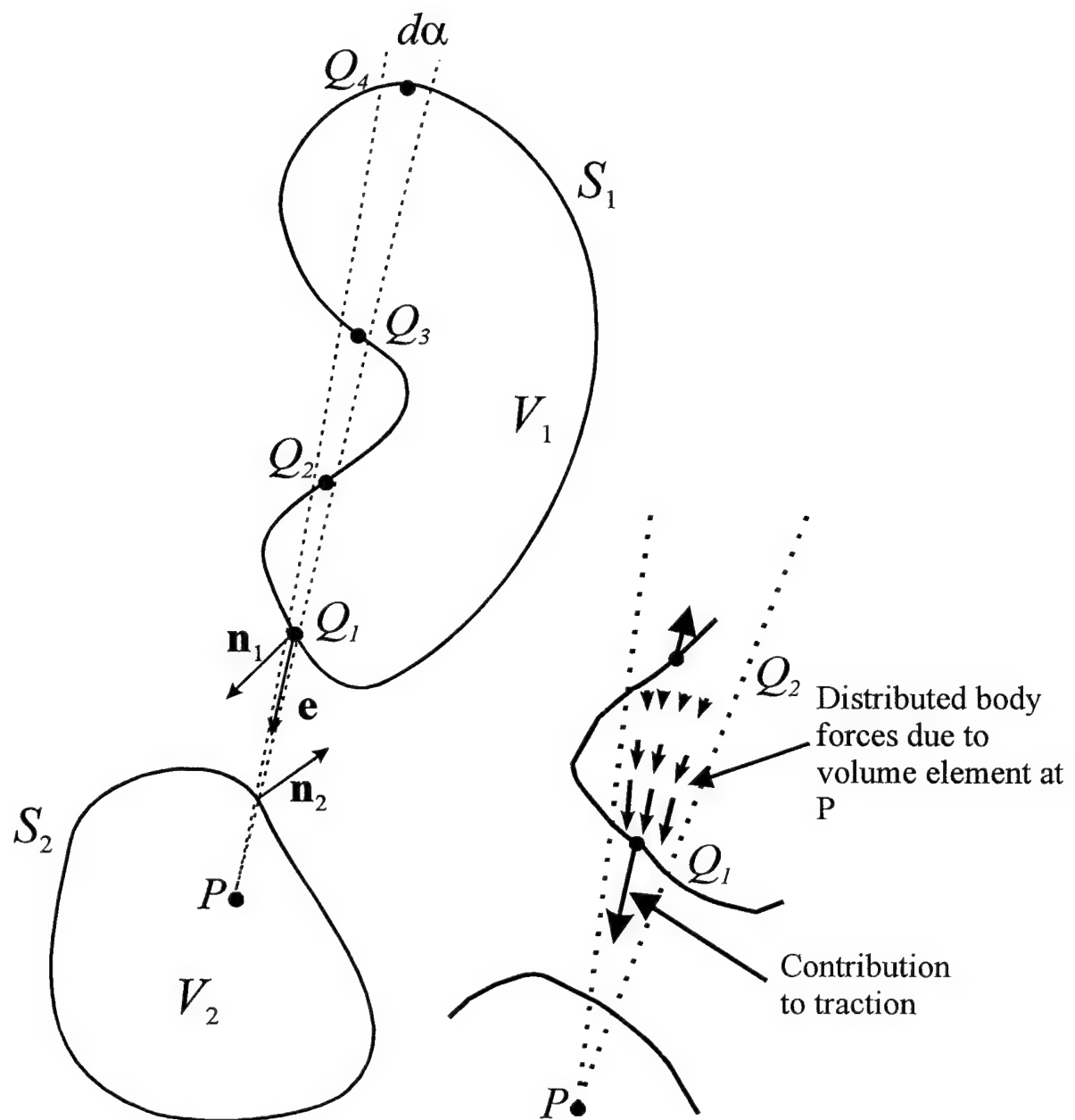


FIGURE 1

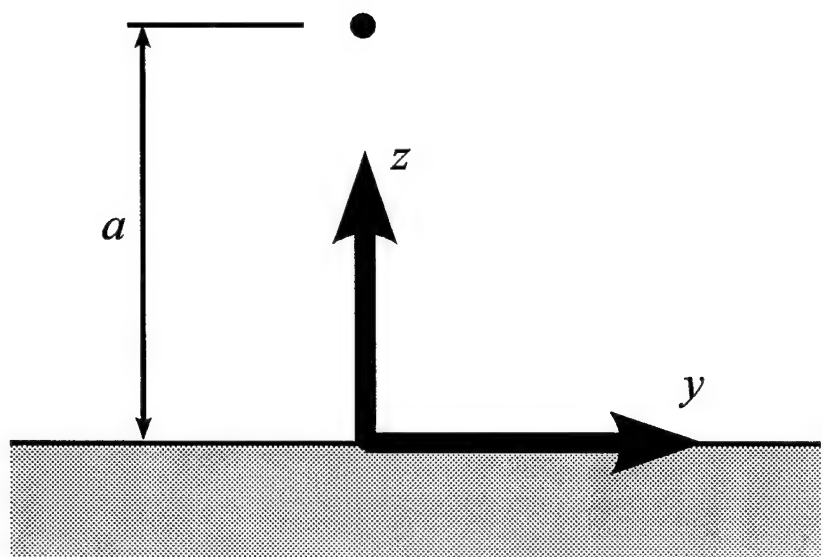


FIGURE 2

File:
c:\apaper\inter\fig2.cdr

3

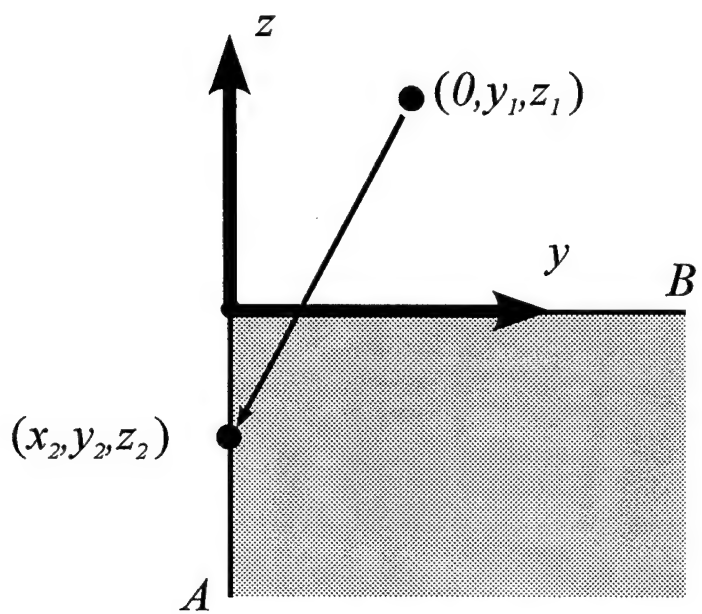


FIGURE 3

File:
c:\apaper\inter\fig3.cdr

Normalized distance (y_1/z_1)

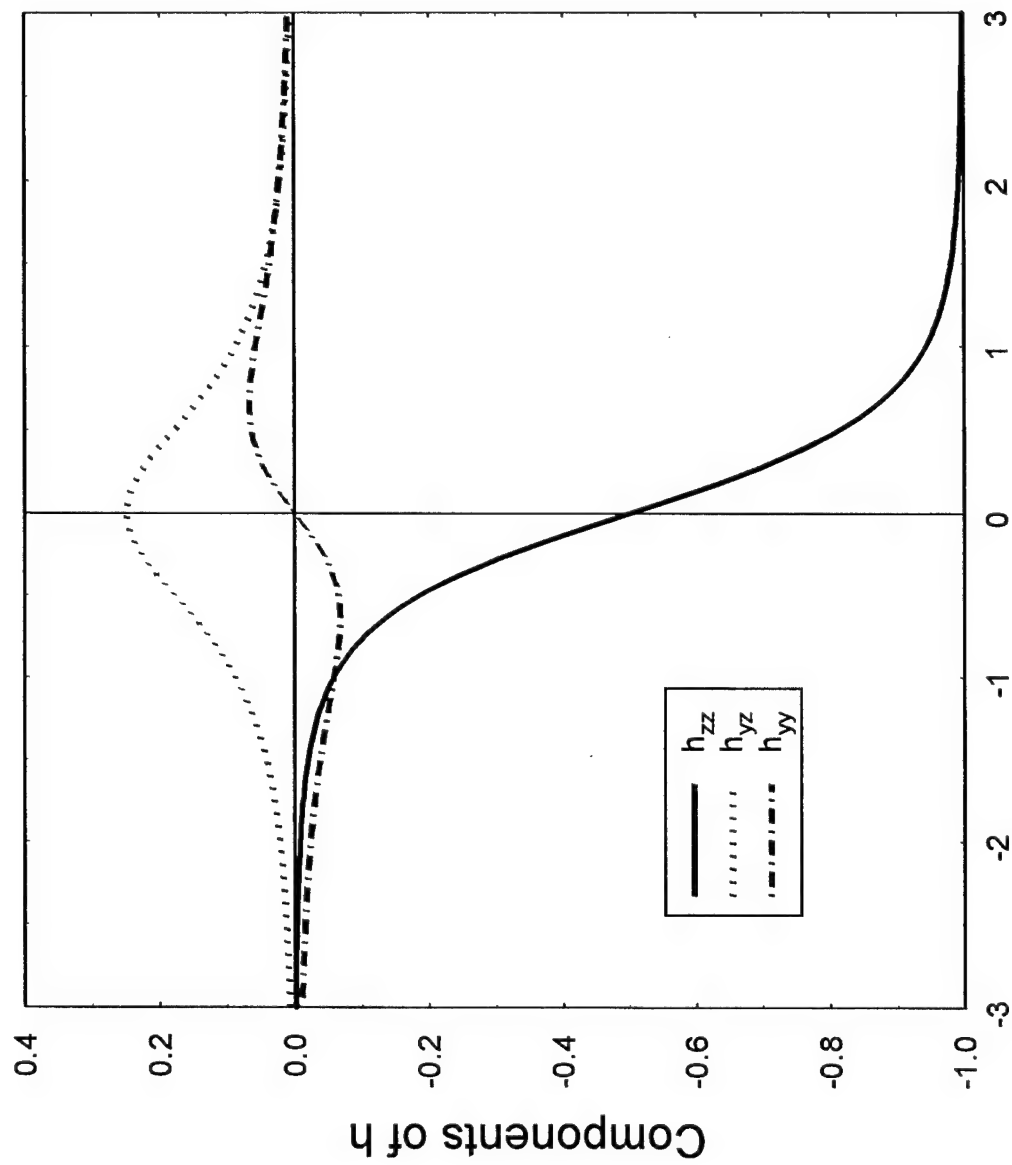
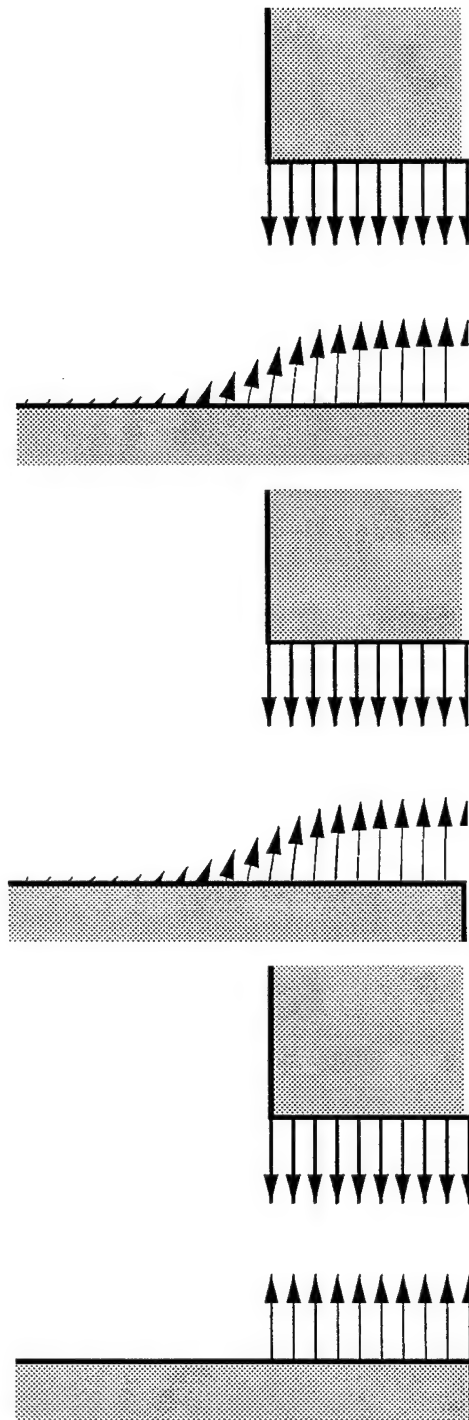


FIGURE 4



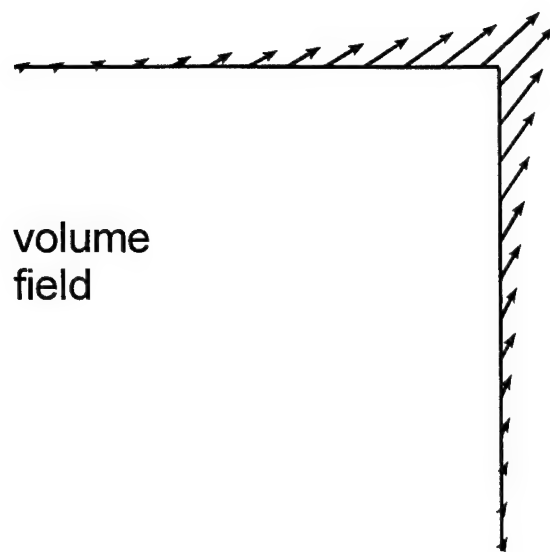
Volume field on
surface

Surface Formulation

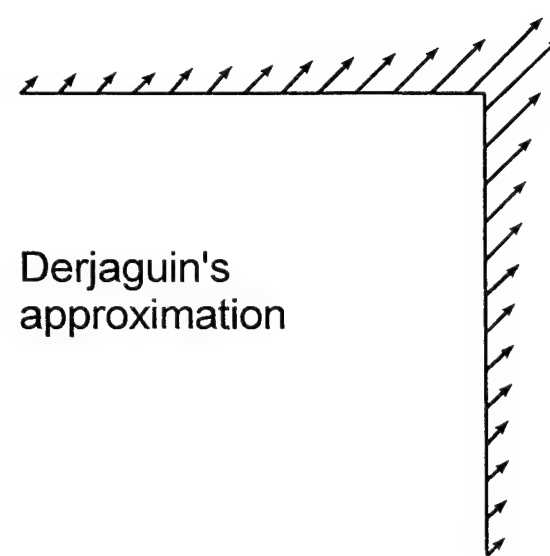
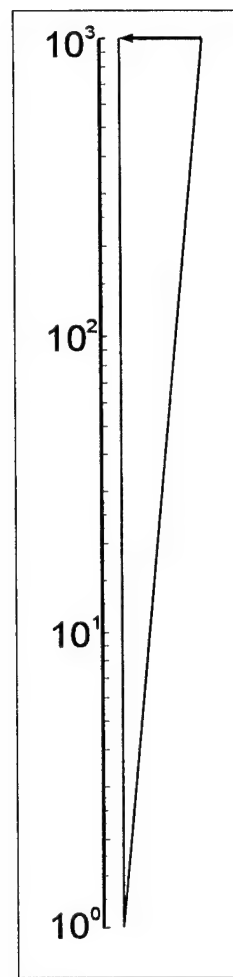
Derjaguin's
approximation

FIGURE 5

Files: intsr2.cdr, intsr2.axg, intsr2a/b/c.axd, intsr2.f, intsr2a/b/c.out, quadhij.ma



volume
field



Derjaguin's
approximation

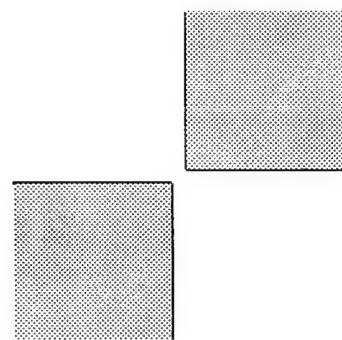
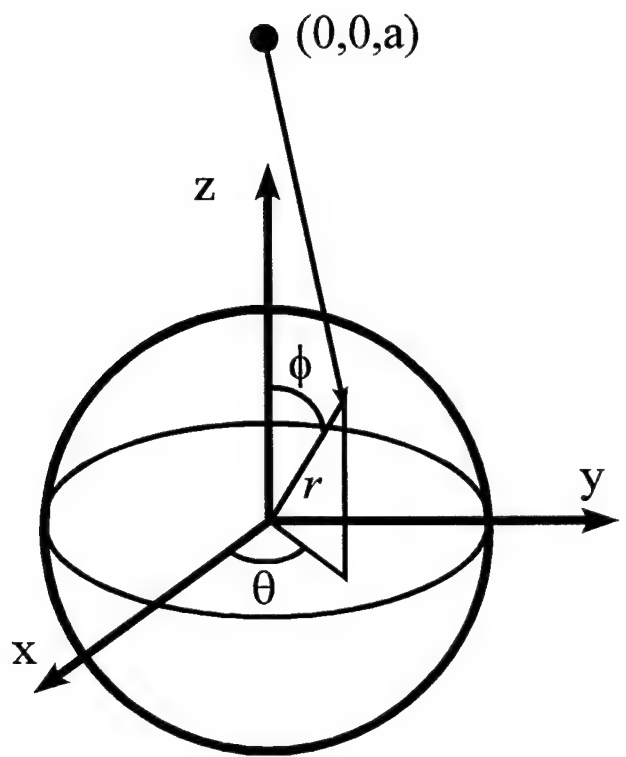


FIGURE 6



File: sphere.cdr

FIGURE 7

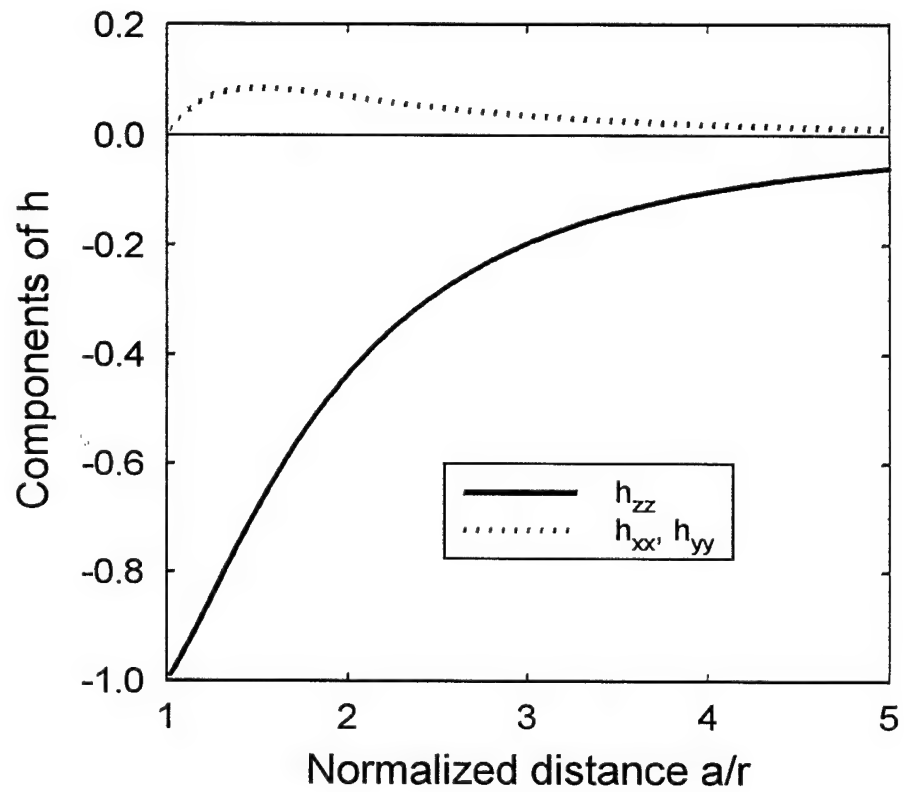


FIGURE 8

9

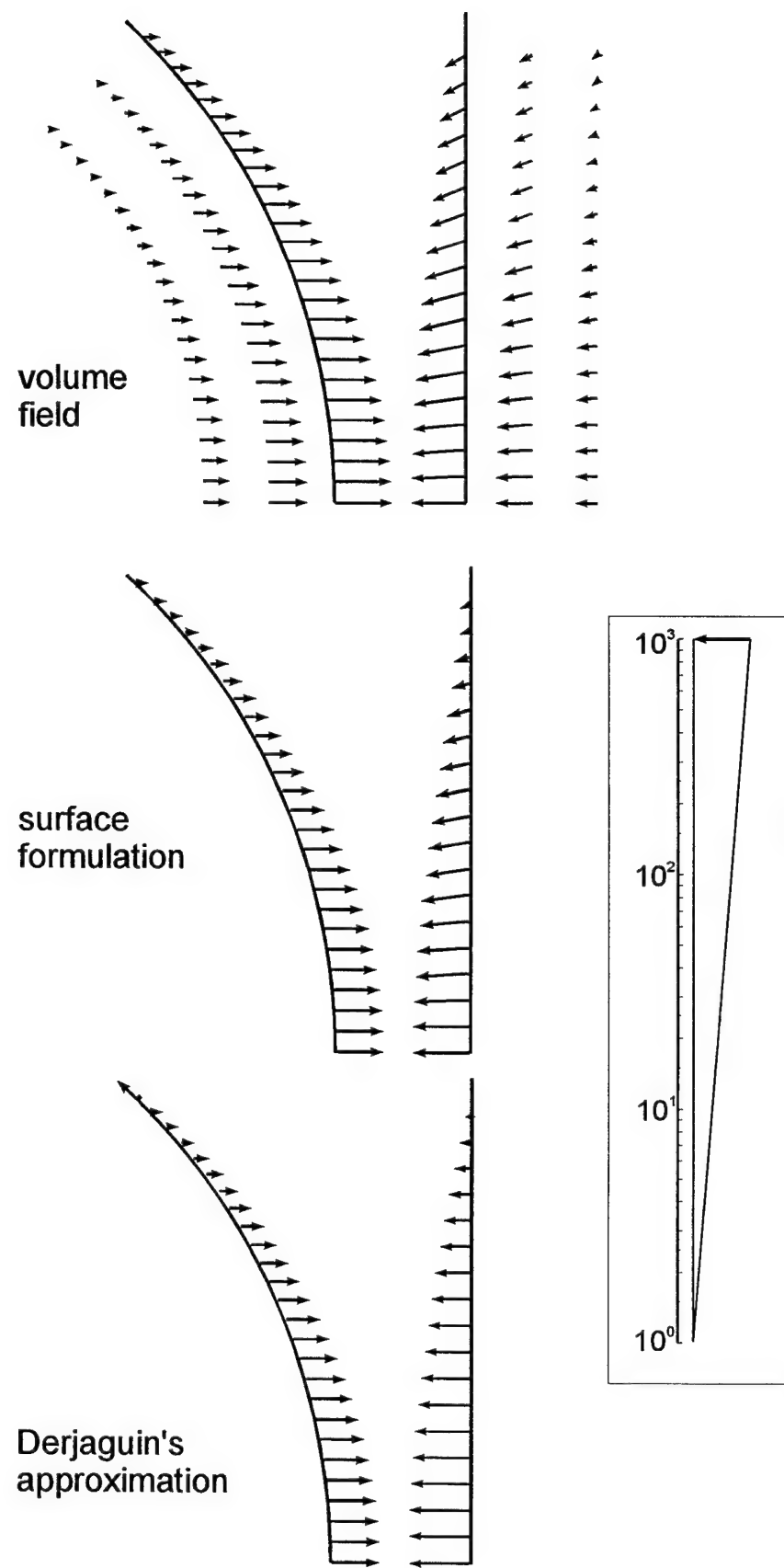
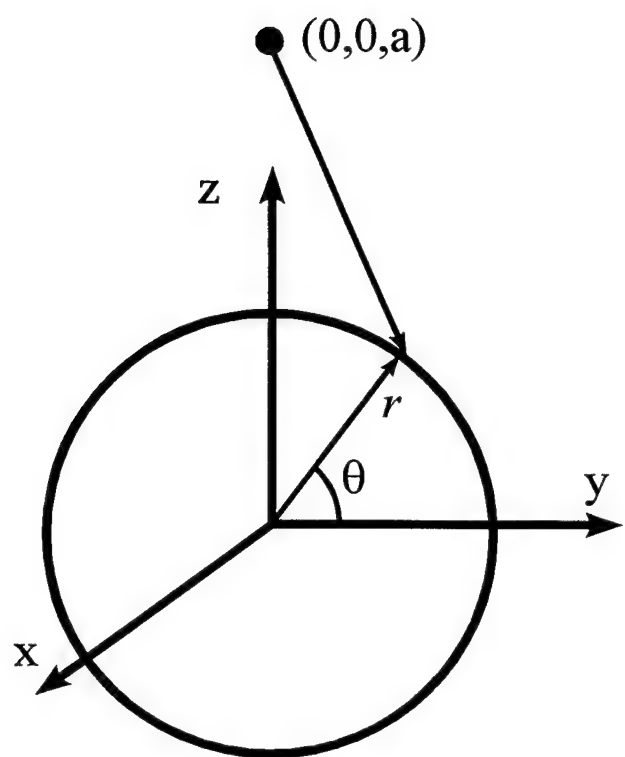


FIGURE 9



File: sphere.cdr

FIGURE 10

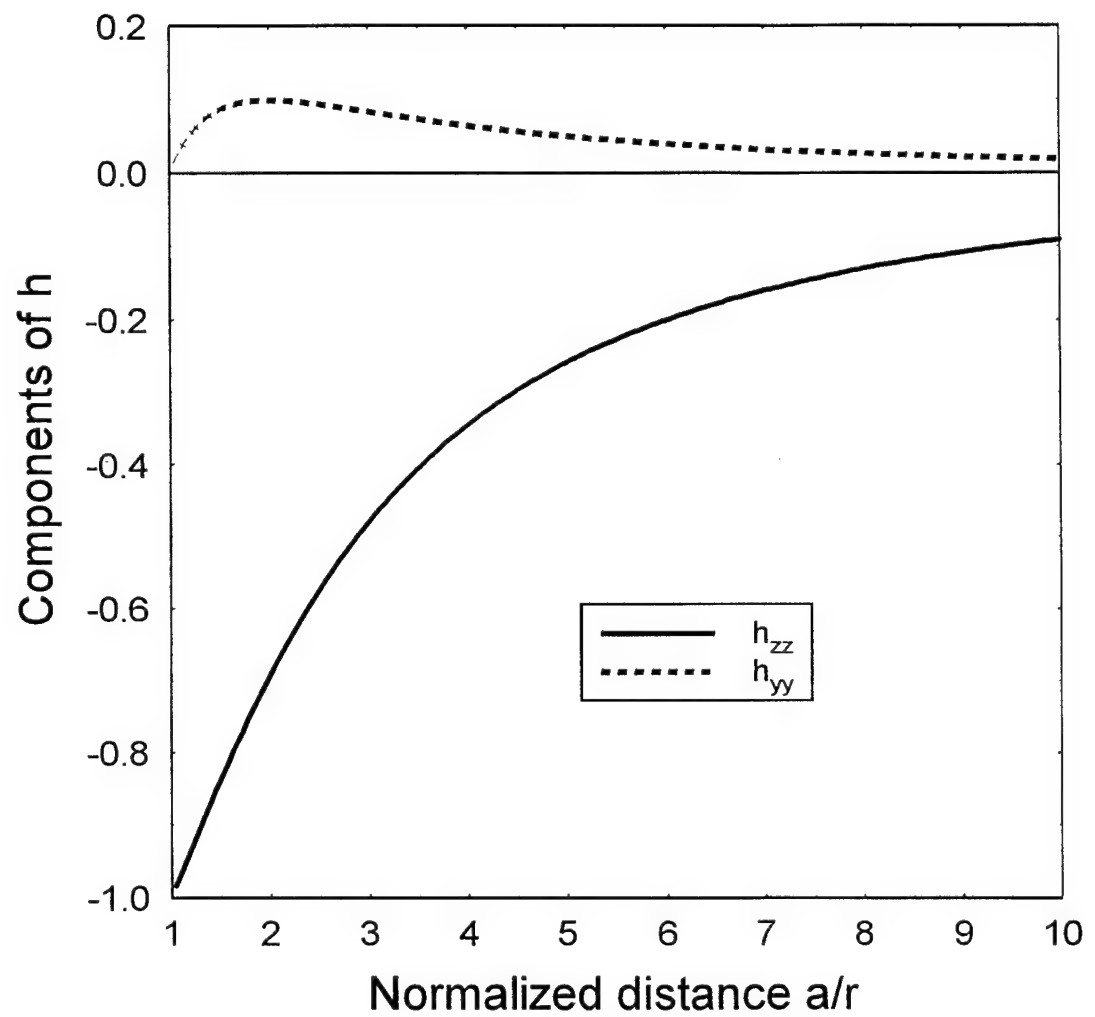


FIGURE 11

Growth of Adhesive Contacts for Maxwell Viscoelastic Spheres

A. Jagota, C. Argento, S. Mazur

Central Research and Development, The Dupont Company
Wilmington, DE 19880-0356, USA

submitted to

Journal of Applied Physics

24 November, 1996

Abstract

Coalescence of a Maxwell viscoelastic sphere to a rigid plane is analyzed to study the transition from initial elastic adhesion to viscous sintering. Deformation is driven by surface tractions due to the surface energy. The formulation for surface forces consistently combines direct van der Waals attraction across the gap ahead of the contact edge with curvature-based tractions normal to the sphere surface. These two contributions to the surface traction result in two different modes of contact growth. The initial elastic contact and the early stage of time-dependent contact growth are in a *zipping* mode of contact closure dominated by direct attractive forces. The later stage of sintering is by *stretching* of the contact and is dominated by curvature-based tractions. The transition from the initial elastic contact to the zipping mode of contact growth is viscoelastic. For a given sphere radius, kinetics of the zipping mode of contact growth scale with a characteristic viscous sintering time. However, this mode is not part of the existing sintering models because direct attractive tractions have been neglected in previous analyses of sintering. This stage of coalescence does not have unique scaling with sphere radius. The transition from the zipping to stretching mode of contact growth occurs at a contact radius that depends on sphere radius. The stretching mode of contact growth is in good agreement with previous analyses of viscous sintering.

1. Introduction

The ability of surface tension to alter the shapes and increase the contact area of contacting particles is fundamental both to adhesion and sintering phenomena. Analyses of adhesive contacts ([1]-[3]) have generally treated the particles as perfectly elastic. Analyses of sintering kinetics assume either a single mechanism for mass transport such as viscous flow ([4]- [7]) or some temperature-dependent superposition of such mechanisms [8]. These models successfully account for experimental measurements within restricted regimes of time, particle size, and material parameters. However, they cannot be expected to fully account for the behavior of real materials whose mechanical response is inevitably more complex. For example, when two liquid droplets come into contact they deform immediately to an extent dictated by their instantaneous elastic compliance regardless of their viscosity. Thus the true initial condition for viscous sintering is a consequence of short-time viscoelastic character. Viscous sintering models customarily assume an arbitrarily small initial contact size, but the limitations of that approximation have never been systematically examined. Viscoelastic effects are especially prominent for polymer particles. Viscoelastic relaxations in polymer melts commonly span several decades in time and are manifest in experimental measurements of both adhesion [1] and sintering ([9]-[12]).

In addition to the issue of material response, there remain unresolved questions concerning the proper representation surface forces. Existing models for elastic adhesion and viscous sintering have relied respectively on very different formulations of the surface tractions. The distinction is shown schematically in Figure 1. Adhesive contact models invoke only the attractive forces operating across the gap between opposing surface elements when they approach within range of molecular van der Waals interactions. These forces "zip" the surfaces together, increasing contact area until elastic strain energy balances the decrease in surface energy. In contrast, models for viscous sintering invoke only forces associated with surface curvature which tend to "stretch" the circumference of the neck bounding the contact. Our objective herein is to develop a model for the evolution of particle shape, contact area, and stress distribution under intrinsic surface forces for contacting spheres with the properties of viscoelastic liquids. It turns out that both zipping and stretching modes are important in this problem. Consequently, a self-consistent prescription for both kinds of surface tractions is required.

Calculations were performed for a Maxwell viscoelastic sphere of colloidal dimensions in contact with a smooth, rigid plane. In the limits of very short and very long times, the results agree well with the simple models for elastic and Newtonian materials respectively. However, the calculations reveal some unanticipated effects. The first stages of contact growth prove to be dominated by the zipping mode. Throughout this period the growth kinetics differs significantly from earlier viscous sintering models which neglect van der Waals forces. Moreover kinetics in the zipping regime does not scale with particle size, as do all the idealized models for sintering kinetics ([4][8][11]). The fraction of contact area contributed by zipping does, however, increases with

decreasing particle size such that sufficiently small particles may sinter completely by this mechanism.

The current state of understanding of adhesive contacts and viscous sintering is reviewed in Section 2. The viscoelastic-elastic model including generalized surface forces is described in Section 3. The numerical results are reviewed in Section 4 and compared with various analytic approximations in Section 5.

2. Background

Adhesive contact of elastic spheres was analyzed by Johnson, Kendall, and Roberts (JKR) [1]. The equilibrium contact radius r_c was solved analytically by minimizing the total energy which includes contributions from the annihilated surface, stored elastic energy, and the work done by any external force that may be present. The JKR model is exact for small strains and when the contour length just outside the contact over which the surface forces act is small compared to the particle radius R . It leads to a prediction for the contact pressure distribution which is compressive at the center of the contact, tensile as one approaches the edge, and singular at the edge. Alternate models have been developed which account for the fact that the surface force distribution outside the contact is finite [2]. The two approaches were reconciled by Maugis who related the stress distribution near the contact edge to the Dugdale model ([13], [14]) for fracture mechanics. The close relation between equilibrium adhesive contact area and equilibrium crack position has also been noted by others ([15]-[17]).

A general result of elastic adhesion models is the following scaling between geometric and material parameters:

$$\frac{r_c}{R} \propto \left(\frac{\gamma}{GR} \right)^{1/3}, \quad (1)$$

where γ is the surface tension, G is the shear modulus, r_c is the contact radius, and R is the particle radius. Relation 1 agrees well with a wide range of experimental measurements on materials ranging from mica [18] to polymers ([1][19][20]). The predicted dependence on R has been confirmed for data extending over 4 orders of magnitude and appears to remain valid for r_c/R approaching unity [19]. However, some time-dependent effects were noted for elastomeric polymers and ascribed to viscoelastic relaxation [1].

Analytic approximations have been developed to solve certain kinds of viscoelastic contact problems [21]. For example, when the viscoelastic compliance or stress relaxation modulus is known, these approximations allow the time evolution of contact area to be calculated from a known history of the total inter-particle force, or *vice versa..* This approach was used to analyze the mechanics of polymer latex deformation under idealized drying conditions [22], for which the experimental evidence is inconclusive. Their applicability to viscoelastic sintering requires some additional approximations regarding the time-evolution of the inter-particle force. As discussed in

Section 5, our calculations indicate that the total force driving coalescence varies with R and r_c in a non-trivial manner. It is therefore not surprising that significant errors were encountered when attempting [10] to relate independent experimental measurements of viscoelastic sintering kinetics and rheology based on an implicit assumption of constant force.

Current models of viscous sintering assume that the velocity fields within the particles are driven by local variations in the surface traction p which is normal to the surface and may be calculated according to the Young-Laplace equation ([23],[24]):

$$p = \gamma \left(\frac{1}{R_1} + \frac{1}{R_2} \right). \quad (2)$$

where R_1 and R_2 are the principle radii of surface curvature. Numerical solutions by finite element ([7][25]-[27]) and boundary element ([6][28]-[30]) methods have revealed some serious errors in the early approximations due to Frenkel and Eshelby [5]. In particular they show that r_c/R does not grow as a simple power law in time as predicted by Frenkel. The more complex kinetics can nevertheless be expressed in terms of a dimensionless time t/t' , where the normalization parameter t' is given by:

$$t' = \left(\frac{4\pi}{3} \right)^{1/3} \left(\frac{R\eta}{\gamma} \right). \quad (3)$$

where η is the Newtonian viscosity. Equation 3 is consistent with Herring's general argument [31] (independent of particle shape) that the time required to reach a given shape change by viscous sintering should be proportional to particle size. Within the limitation of equation (2), Hopper has obtained analytical solutions for the evolution of various two-dimensional shapes including sintering cylinders ([32],[33]). The sintering kinetics of viscous liquids has been measured experimentally ([10] [34]-[37]) by placing pairs or aggregates of amorphous solid spheres in contact with no external load and then heated them to above their glass temperature, T_g . Measurements on silicate glass spheres are in good agreement with kinetics predicted by the particle-based viscous sintering models discussed above and with intermediate and late stage models ([38][39]). A remarkable feature of these analyses is the close agreement between the various models for viscous sintering and the excellent agreement with experiments, *as far as the prediction of overall shrinkage is concerned*.

Results for polymers are more complex. Neck growth measurements on relatively large poly(styrene) and poly(methyl methacrylate) spheres ($R=250-300 \mu\text{m}$) and $r_c/R > 0.1$ agree well with the viscous sintering model [40]. However, other measurements ([10][41]) on smaller spheres of the same polymers (e.g. $R < 120 \mu\text{m}$) have shown significant contact growth at much earlier times than predicted by viscous sintering. The close relationship between this early growth kinetics and the rapid increase in the retarded elastic part of the shear compliance near T_g , suggest that the anomaly is viscoelastic in origin. Similarly, the rapid sintering of molten poly(tetrafluoro-ethylene) cylinders [9] and colloidal particles [42] with $\eta > 10^{10}$ poise has been ascribed to viscoelastic deformation. From consideration of the maximum

retarded elastic compliance of typical linear, high molecular weight polymer melts it has been proposed [11] that particles smaller than a certain critical size sinter completely by retarded elastic deformation, without any contribution from viscous flow. This critical size was estimated [11] to range from $R= 40$ nm to $R=2 \mu\text{m}$ depending upon the polymer and initial packing density. Recent experiments [43] bear out these predictions.

Existing models for both the initial elastic adhesion and for viscous sintering use internal surface energy to determine the driving force for deformation but differ in how the forces are prescribed¹. An attempt to simulate the process of viscoelastic coalescence without the direct attraction across the gap fails to model the formation of the initial elastic contact. Conversely, neglect of curvature-based tractions does not match the known viscous sintering kinetics for larger contacts. We employ a recently developed formulation for surface forces that consistently combines direct and curvature-based tractions [44] which has been implemented as a surface finite element applicable to arbitrary geometry and materials. The transition from initial elastic adhesion to viscous sintering is studied by analyzing the coalescence of a viscoelastic sphere to a rigid half-space. In this paper, we restrict our attention to a Maxwellian material which relaxes with time from a stiff solid to a Newtonian liquid. More complex kinds of viscoelasticity typical of high molecular weight or cross-linked polymers ([45],[46]) will be addressed elsewhere.

3. Formulation of the problem

3.1 Bulk constitutive behavior

Figure 2 shows a sphere in contact with a smooth, rigid plane. The sphere is discretized using 4-node axisymmetric hybrid finite elements. Isotropic viscoelastic constitutive relations are used for both the bulk and shear properties. For small strains and rotations these are:

$$\begin{aligned} \boldsymbol{\varepsilon}_{ij} &= \boldsymbol{\varepsilon}_{ij} - \frac{\varepsilon_{kk}}{3} \delta_{ij} = \int_0^t 2J(t-t') \frac{\partial s_{ij}}{\partial t'} dt' \\ \varepsilon_{kk} &= \int_0^t B(t-t') \frac{\partial \sigma_{mm}}{\partial t'} dt' \end{aligned} \quad (4)$$

where $\boldsymbol{\varepsilon}_{ij}$ is the strain tensor, ε_{ij} and ε_{kk} are its deviatoric and dilatational parts, σ_{ij} is the stress tensor, and s_{ij} and σ_{mm} are its deviatoric and spherical parts. A Maxwell model is used for both the bulk and shear compliances, $B(t)$ and $J(t)$

¹ In the thermodynamic treatment of JKR [1] and the energy balance of Frenkel [5] there is no direct assumption regarding the nature of the forces. However, an attractive force field across a gap is clearly implied by JKR in their assumed deformation modes. Frenkel's model is too simple to withstand such scrutiny; one of the enduring mysteries of this problem is why it works as well as it does.

$$J(t) = \frac{1}{G} + \frac{t}{G\tau} \quad (5)$$

$$B(t) = \frac{1}{K}$$

where G and K are the instantaneous shear and bulk moduli, and τ is the relaxation time. Note that for large times this material has a Newtonian viscosity $\eta = G\tau$. It is assumed that the bulk modulus does not change with time and the initial ratio of shear and bulk modulus corresponds to a Poisson's ratio of 0.3. As the material relaxes it becomes increasingly incompressible. The use of linear viscoelasticity implies small elastic strains and small strain rates. However, the formulation used [47] accounts for arbitrarily large strains and rotations by an appropriate geometrical transformation of the constitutive equations (4) using the deformation gradient. The formulation also allows for change in constraints applied to surface nodes as they come into contact with the rigid surface.

3.2 Surface tractions

The deformation is driven solely by tractions applied to surface elements. These tractions are computed via the surface formulation of [44] and applied via a surface finite element developed for this purpose [48]. In this formulation, there are two additive contributions to the surface traction \mathbf{T} on any element

$$\mathbf{T} = \mathbf{T}_s + \mathbf{T}_o, \quad (6)$$

where \mathbf{T}_s represents tractions due to self interactions modeled as surface tension and \mathbf{T}_o represents tractions due to the another body, in this case the rigid half-space. Self interactions are modeled using the Young-Laplace equation ([23],[24]) and are proportional to the product of the surface energy and the surface mean curvature and act along the surface normal:

$$\mathbf{T}_s = -\gamma \operatorname{tr}(\mathbf{k}) \mathbf{n}_1, \quad (7)$$

where \mathbf{k} is the surface curvature tensor, $\operatorname{tr}()$ refers to the trace, and \mathbf{n}_1 is the surface normal. In terms of the principal radii of curvature R_1 and R_2 :

$$\operatorname{tr}(\mathbf{k}) = \frac{1}{R_1} + \frac{1}{R_2}. \quad (8)$$

This formulation of self forces is strictly valid only for relaxed liquid-like surfaces and has been used in all previous analyses of viscous sintering. In the actual implementation, numerical computation of curvatures is avoided by analytically integrating equation (7) to obtain nodal forces [48].

Other-body tractions \mathbf{T}_o are related to the inter-molecular potential $w(s)$, which is taken to be the van der Waals potential ([49]-[51])

$$w(s) = \frac{A}{s^6}, \quad (9)$$

where A is an interaction constant. The tractions are then given by

$$\mathbf{T}_o = \mathbf{h} \cdot \mathbf{n}_1, \quad (10)$$

where \mathbf{n}_1 is the outer unit normal to the surface of the sphere, and \mathbf{h} is a second order tensor, the *inter-surface stress tensor* defined by

$$\mathbf{h} = \rho_1 \rho_2 \int_{S_2} \mathbf{n}_2 \mathbf{G} dS_2 \quad (11)$$

where the integration is over the rigid plane, ρ_1 and ρ_2 are number densities of molecules in the sphere and half space, \mathbf{n}_2 is the outer normal to the half space, and \mathbf{G} is a vector function of distance between the sphere and the plane

$$\mathbf{G} = (\mathbf{x}_2 - \mathbf{x}_1) v(s), \quad (12)$$

where $\mathbf{x}_2 - \mathbf{x}_1$ is vector from the sphere surface to the rigid plane, and $v(s)$ is a scalar function of distance s between points on the two surfaces defined by

$$v(s) = \frac{1}{s^3} \int_s^\infty w(s') s'^2 ds'. \quad (13)$$

For the van der Waals potential used here,

$$v(s) = \frac{A}{3s^6}. \quad (14)$$

Because one of the interacting surfaces is a plane bounding a half-space, the expression for the traction can be further simplified by carrying out the integration analytically [44]. The tractions on the sphere are oriented along the axis of the sphere, z , and are given by

$$T_z = h_{zz} n_z = \frac{\pi A \rho_1 \rho_2}{6s^3} n_z \quad (15)$$

where s now represents the distance between the sphere surface and the plane along the z axis. When one of the interacting bodies is a half-space bounded by a plane, the tractions computed by the surface formulation are identical to those given by the Derjaguin approximation ([3][44][52]).

Consistency between the two tractions \mathbf{T}_s and \mathbf{T}_o , is established by ensuring that the work done in bringing two surfaces together from infinite separation without deformation equals the surface energy, thus equating surface energy and surface tension. The interaction energy per unit area of two identical half planes separated by a distance S interacting by the van der Waals potential is [50]:

$$W(S) = \frac{\pi A \rho_1 \sigma_2}{12 S^2}. \quad (16)$$

Because we are using only an attractive potential, a cut-off distance $S = \varepsilon$ is introduced which represents the interfacial contact separation and makes the energy finite. Equating $W(\varepsilon)$ to -2γ one obtains:

$$A \rho_1 \rho_2 = \frac{-24\gamma \varepsilon^2}{\pi}. \quad (17)$$

Thus, all tractions are determined in terms of the surface energy γ . A value of $\varepsilon \approx 0.17$ nm has been found appropriate for several materials [50].

Therefore, in the computation of \mathbf{T}_o , distance is measured from a 0.17 nm below the nominal rigid surface. It introduces a fixed length scale in the problem and directly controls the size of the region outside the contact over which the van der Waals forces act.

This has an important effect on both the physics of the problem and the non-linear numerical solution. With a given number of elements in a particle, the number of elements influenced by these forces decreases as the particle size is increased. Moreover, the forces are increasingly non-linear. Because the surface forces are geometry-dependent, they introduce additional non-linearity in the computational problem. In a Newton-Raphson scheme they would provide an additional contribution to the Jacobian matrix of the system. In the implementation used here, only the direct geometry-dependent nodal forces are computed. This converts the numerical solution to a direct iteration scheme. With the mesh shown in Figure 2, we have found that it is possible to obtain reliable computational results for particle radii R no larger than $10 \mu\text{m}$. For larger particles errors are introduced due to the inaccurate numerical integration over the surface element of the van der Waals forces.

The simulation is begun by bringing the sphere into point contact with the rigid plane. The surface energy is gradually incremented over a short time step (compared to the relaxation time). During this step the contact grows, initially in a *zipping* mode. As nodes come into contact, they are constrained by the rigid surface. A surface traction corresponding to the distance ϵ is maintained over elements in contact, which allows contact tractions to be tensile. The simulation is continued with fixed surface energy, allowing the geometry to evolve. Also shown in Figure 2 is the deformed sphere after the formation of an initial, elastic, contact. In contrast to previous simulations of viscous sintering, much of the early contact growth is in the *zipping* mode which involves little element distortion. As the contact increases the effect of curvature-based tractions increases in importance with corresponding mesh distortions. The results presented here are without any mesh rezoning; simulations were halted when mesh distortions became excessive. One complete simulation typically involves 500-1000 time steps.

4. Results

The JKR result for initial elastic contact radius for a sphere on a rigid plane is

$$\frac{r_c}{R} = \left(\frac{9\pi\gamma(1-v^2)}{ER} \right)^{1/3}, \quad (18)$$

where E is the Young's modulus and v is Poisson's ratio. This may be treated as the exact result for contacts small enough for small-strain assumptions to apply but large enough for the zone over which van der Waals forces operate outside the contact is small compared to the contact radius. It has been shown in [44] that numerically computed contact radii are in good agreement with the JKR result. The distribution of contact tractions [53] corresponding to the JKR theory predicts an infinite tensile traction at the edge of the contact. Numerically computed contact tractions are limited by the cut-off value, and vary smoothly.

Figure 3 shows the evolving shape of a particle with $R = 100 \text{ nm}$, $E = 10 \text{ GPa}$, and $\gamma = 0.01 \text{ J/m}^2$. At this scale, the evolution of the shape qualitatively resembles previous results of viscous sintering simulations [27]. Figure 4 shows the difference $z'(r)$ between the deformed surface $z_d(r)$ and the initial spherical surface $z_s(r)$

$$z'(r) = z_d(r) - z_s(r). \quad (19)$$

At the larger scale, each shape now resembles the JKR or viscous sintering neck shapes. The envelope represents the contact plane where the difference is the spherical surface itself. For a particular shape, at large radial distances there is a constant difference between the surface location and the original sphere representing the displacement of the sphere center. As one approaches the contact edge, the difference increases, characteristic of usual viscous sintering neck shapes and of the JKR shape outside the contact. Very close to the contact edge the difference decreases again. This represents the region over which van der Waals forces are operative and significantly alter the shape². Within the flat contact region the difference between the deformed surface and the initial spherical surface is simply a sphere. The fact that the deformed surface has a smooth transition into the contacting region shows the presence of a cusp at the contact edge. The different regions are most pronounced when the contact radius is of modest extent. A small cusp does persist up to large contact radii, but the shape is increasingly dominated by the familiar rounded sintering neck. Contact growth in the early stages is dominated by the *zipping* mode: nodes sequentially make contact with little stretching of the contact plane. As the contact radius increases, curvature-based tractions become more important. This is manifest as increased stretching of the contact plane and squeezing of nodes along the surface outside the contact towards the edge of the contact. As the simulation proceeds in its later stages, nodes outside the contact are squeezed towards the edge of the contact. They then enter the small van der Waals zone and make contact with the rigid surface. Increasingly, however, in the interval between successive increases in contact radius by *zipping* the contact continues to grow by stretching.

The distribution of traction T_z on the surface of the sphere is shown in Figure 5 at different contact radii (and increasing time). Because deformation is driven only by surface forces, the net force corresponding to this distribution is zero. The initial distribution, characteristic of the JKR solution, is compressive in the interior of the contact, tensile just inside and outside the contact edge and decays with increasing distance outside it. The location of maximum tensile traction coincides with the position of the contact edge. With increasing contact radius, the stress field quickly changes into one with a minimum at the middle of the contact, a compressive peak just inside the contact edge and van der Waals tension outside the contact. This characteristic shape of the traction distribution is maintained through most of the simulation. The apparent decrease in the peak traction is an artifact due to the fact that in post-processing the results surface tractions have been obtained by extrapolating stresses from inside the element using linear interpolation function and averaging at nodes, for the sake of consistent treatment of nodes inside and outside the contact. The surface integration for the computation is more accurate because we use five quadrature points on the surface.

In Figure 6 the distribution of surface tractions at $t=0$ is compared with the JKR model. The agreement is very close except at the edge of the contact where the JKR

² Note a possible inconsistency in this picture: a sharp cusp implies an infinite curvature and hence infinite traction. This is resolved by the fact that the total force obtained by integrating around the cusp is finite [54] and is accounted for in the numerical analysis.

traction is unbounded. Also shown is the traction distribution at a later time, compared to a model based on the Lee and Radok solution for viscoelastic contact which is described in greater detail in the following section.

Figure 7 shows simulations of contact growth for $R=200\text{nm}$, Young's modulus $E=100\text{GPa}$ ($G=38.5\text{GPa}$), with γ varied over three orders of magnitude. The initial contact radii increase with decreasing γ . Also shown are the results for simulations where only curvature forces were included [27]. The growth kinetics are shown as a function of the normalized time t/t' , where t' is defined by equation (3). The viscoelastic time constant for the material is $\tau=\eta/G$, or in the normalized time scale:

$$\frac{\tau}{t'} = \left(\frac{3}{4\pi} \right)^{1/3} \frac{\gamma}{RG}. \quad (20)$$

We see that the viscoelastic growth for different γ eventually converge into a universal curve at $t/t' > 10^{-4}$. For each value of γ the convergence time is roughly proportional to γ , and corresponds to about $10\tau/t'$. For $t/t' > 10^{-4}$ the results in Figure 7 apparently represent Newtonian flow, free of the viscoelastic history. However, the growth kinetics derived from the combination of van der Waals and Young-Laplace forces differs substantially from the conventional viscous sintering model based on only curvature forces. That is, for t/t' between 10^{-4} and 10^{-1} the additional increment in r_c/R is a consequence of viscous flow via the zipping mode.

In order to examine the effects of particle size on contact growth by the zipping mode a series of simulation were performed with $E=100\text{GPa}$, and $R=100\text{nm}$ to $10\mu\text{m}$. (For computational reasons described earlier, it was not possible to perform reliable calculation for larger R). For the simulations with $1\mu\text{m}$ and $10\mu\text{m}$ particles, the ratio γ/R was held constant at 100Pa . As a consequence the viscoelastic relaxation time (equation 20) is also constant and very small: $\tau/t'=2.6\times 10^{-9}$. The results shown in Figure 8 represent the effects of particle size on viscous growth kinetics driven by both van der Waals and Young-Laplace forces. Results are also shown for calculations involving only Young-Laplace forces, i.e. the traditional viscous sintering model. It is apparent that early growth in the zipping mode is strongly dependent on R . With decreasing R the contact area contributed by zipping increases and convergence to the stretching mechanism is offset to longer times and larger contact areas. Thus for $R \leq 200\text{nm}$ the zipping mode provides $r_c/R \sim 0.5$, which is sufficient to fully densify a regular dense packed aggregate of spheres. On the other extreme, for $R \geq 10\mu\text{m}$ zipping accounts for less than 10% of the contact growth. It is particularly interesting to compare the behavior of the $1\mu\text{m}$ and $10\mu\text{m}$ particles. Because the ratio γ/R is the same for the two, their initial elastic contact radius is identical. Because of the same reason, the two behave in an identical manner when stretching dominates. However, in the regime of contact growth by zipping, the kinetics are markedly different, indicative of a second length scale controlling the process: the scale ε of van der Waals forces.

The fact that no significant deviations from the traditional viscous sintering model (with only curvature forces) have been detected in experiments on simple viscoelastic materials like silicate glasses may be a consequence of the relatively large

particle sizes (ca. 100 μm) used in those studies ([34]- [37]). The results in Figure 8 suggest that significant deviations should be observed for colloidal particles of the same materials. In the absence of any zipping contribution we would expect a 100-fold increase in sintering rate on going from $R=100 \mu\text{m}$ to $R=1 \mu\text{m}$ (eq. 3). However, for the latter the zipping contribution at early times should increase this by an additional factor of 10. Perhaps this will be sufficient motivation for further experimentation.

We now consider in greater detail how the present model compares with the earlier analytic approximations for viscous flow and viscoelastic contacts, especially with regards to the dependence of growth kinetics on particle size and the character of the inter-particle forces.

5. Comparison with analytical approximations

It is apparent from Figure 8 that at late times the process becomes dominated by the stretching mode, and that the growth kinetics, expressed in normalized units, become independent of R . This is explained by Herring's analysis [31], which shows that when the tractions are derived solely from Young-Laplace forces both normalization constants (t' and R) are simply proportional to R . However, at early times one or both of these proportionalities apparently breaks down since that the normalized growth rate becomes R -dependent. Since we know that in the elastic limit r_c varies as $R^{2/3}$ [1], one might expect some kind of systematic transition from elastic size scaling to viscous size scaling, but the results in Figure 8 are not consistent with that expectation. For one thing the time-scale is very long compared to the viscoelastic relaxation τ/t' . But more importantly the early time kinetics cannot be re-normalized by any power of R . Rather, we believe that these variations represent a fundamental breakdown in the principle of size scaling. This breakdown is due to the fact that van der Waals forces are themselves characterized by an intrinsic length scale which does not change with R . In other words, under conditions where van der Waals forces play an important role in contact growth, the problem cannot be reduced to a dimensionless length scale because the mechanics is governed by two, mutually independent dimensions.

Figure 9 shows the relationship between center displacement δ and the contact area. Interestingly this relationship, which is essentially a statement of volume conservation, is insensitive to the mode of contact growth and may be well approximated by:

$$\frac{\delta}{R} = C \left(\frac{r_c}{R} \right)^2, \quad (21)$$

The constant C is estimated by a fit to be 0.39, quite different from the Hertz geometric relationship for this case [55]:

$$\frac{\delta}{R} = \left(\frac{r_c}{R} \right)^2. \quad (22)$$

Returning to the issue of viscoelastic effects, we examined the utility of the general analytic formulation of viscoelastic contacts due to by Lee & Radok [21] to

predict the intrinsic growth kinetics under surface tractions. The contact deformation is driven by forces outside the contact. We replace the total force outside the contact by a work-equivalent force applied at a point remote from the contact. Because contact growth is monotonic, the Lee and Radok analysis can then be used to estimate the kinetics of contact from independent knowledge of the compliance $J(t)$. The work-equivalent force between centers F is computed by equating the work done by the force to the energy released due to contact growth:

$$F d\delta = 4\pi \gamma r_c dr_c \quad (23)$$

$$F = 4\pi \gamma r \frac{dr_c}{d\delta},$$

Invoking the geometric relationship equation (21) one obtains:

$$F = 2C\pi R \gamma, \quad (24)$$

Thus, for a contact which grows due to increase in $J(t)$ and subject to eq. (21) we might expect the interparticle force to remains constant. This conclusion is apparently independent of whether the contact grows by zipping or stretching in so far as the same geometric relation holds in both regimes (Figure 9). Accordingly, Lee & Radok's solution for contact growth kinetics yields:

$$r_c^3 = \frac{3}{16} R F J(t) \quad (25)$$

$$\frac{r_c}{R} = \left(\frac{3 \pi \gamma C J(t)}{8 R} \right)^{1/3}.$$

In Figure 10 we compare equation (25) with results of FEM calculations based on van der Waals forces, Young-Laplace forces, or both. Equation (25) deviates significantly from all of the results. To find the source of this deviation, we examined the validity of eq. (23). This equation specifies that the work-equivalent inter-particle force F remains constant during the growth process. In the simulation based on van der Waals forces, the total force was monitored as a function of contact radius. The results are shown in Figure 11. For contact radii $r_c > 0.1R$, F is seen to fall significantly below the value predicted by eq. (24). It is possible, by assuming a variation of F with contact radius, to bring the Lee and Radok solution into closer agreement with the numerical results. However, since this variation in F with contact growth is not known *a priori* it is not useful for predicting neck growth kinetics under surface tractions. This avenue for the development of analytical expressions governing the zipping mode of viscous sintering is promising and requires further work. For example, the contact tractions corresponding to the solution for fixed F , shown in Figure 6, capture the relaxation of tractions at the center of the contact and the presence of a compressive peak just inside the contact edge.

6. Summary and Conclusions

Coalescence of spherical particles begins with the formation of an initial elastic contact and proceeds by time-dependent contact growth. Existing models for surface

forces driving these two processes have some basic inconsistencies. Models for elastic adhesion neglect the influence of curvature-based tractions while sintering models neglect the influence of direct attractive forces across the gap ahead of the contact edge. A formulation for effective surface tractions due to molecular interactions that contains both types of traction has been employed to study the coalescence of a Maxwell viscoelastic sphere onto a rigid plane. The surface formulation has been implemented as a surface element which has been used to conduct finite element simulations of coalescence. An initial elastic contact is formed which is in good agreement with the JKR model. There is a viscoelastic transition into viscous contact growth by a zipping mechanism. This stage of the mechanism is insensitive to the value of the initial elastic contact radius and is a mode of viscous deformation driven mainly by attractive forces outside the contact region. It is not found in existing models for viscous sintering. There is a second transition to a mode of contact growth governed by curvature-based tractions and characterized by a stretching mode of contact growth. The contact radius at which the second transition occurs depends primarily on the particle size. It decreases from a value as high as 0.6 to about 0.1 as one increases the sphere radius from 100 nm to 10 μm . For large spheres, the stretching mode of contact growth dominates over the entire range of contact radius; the converse is true for small spheres. However, for the range of particle sizes and material properties commonly used, both modes of contact growth are important.

Zipping and stretching are both viscous sintering; kinetics are governed by a characteristic time scale for a given particle size. However, it is shown that due to the fact of an additional length scale associated with van der Waals forces, there is no unique scaling with respect to particle size during the zipping mode of contact growth. When only Laplace-Young tractions are applied, the boundary conditions for a sphere on a rigid plane are identical to those for two identical spheres. However, the van der Waals forces for the case of two spheres are different. Because these tractions approximately as the cube of distance between surfaces, their influence compared to Young-Laplace tractions is smaller for two spheres versus a sphere on a rigid plane by a factor of eight. We have restricted our attention to sintering by viscoelastic deformation; accounting for direct attractive forces may influence models for sintering by other mechanisms as well.

7. Acknowledgments

This work has been supported in part by the Air Office of Scientific Research, USAF, under contract number F49620-95-C-0008. The views and conclusions herein are those of the authors and should not be interpreted as necessarily representing the official policies or endorsements, either expressed or implied, of the Air Force Office of Scientific Research or the U.S. Government.

8. References

- [1] Johnson, K.L., Kendall K. and Roberts A.D. (1971) Surface energy and the contact of elastic solids, *Proc. R. Soc. Lond. A*, **324** 301-313.
- [2] Derjaguin, B.V., Muller, V.M. and Toporov, Y.P. (1975) Effect of contact deformations on the adhesion of particles, *J. Colloid Interface Sci.*, **53** [2] 314-326.; **67**, 378(1978); **73**, 293 (1980).
- [3] Muller V.M., Yushchenko V.S., Derjaguin B.V. (1980), *Journal of Colloid and Interface Science*, **77** [1] 91-101.
- [4] Kuczynski, *J. Met. (Met. Trans.)*, **1**, 169, (1949).
- [5] Frenkel J., (1945) Viscous flow of crystalline bodies under the action of surface tension, *J. Phys (Moscow)*, **9** [5] 385-391.; J.D. Eshelby, *Met. Trans.*,), Discussion of a paper by A.J. Shaler, ``Seminar on the kinetics of sintering" **185**, 796, (1949).
- [6] Hiram, Y. and Nir, A. (1983) A Simulation of surface tension drive coalescence, *J. Colloid Interface Sci.*, **95** [2] 462-470.
- [7] Jagota A., Dawson P.R. , (1988) Micromechanical modelling of powder compacts - I. Unit problems for sintering and traction induced deformation, *Acta Metallurgica*, **36** [9] 2551-2561.
- [8] Ashby M.F. (1974), A first report on sintering diagrams, *Acta Metallurgica*, **22**, 275-289.; Swinkels F.B., Ashby M.F., (1981) A second report on sintering diagrams, *Acta Metallurgica*, **29**, 259-281.

[9] Lontz, in *Fundamental Phenomena in Materials Sciences*, (eds. L.J. Bonis & H.H. Hausner), Vol. 1, pp.25-47, Plenum , 1964.

[10] Mazur & D.J. Plazek, *Prog. Org. Coatings*, **24**, 225, (1994).

[11] Mazur S., (1995), Coalescence of Polymer Particles, Chap. 8, in *Polymer Powder Technology*, M. Narkis, N. Rosenzweig (editors), John Wiley & Sons, New York.

[12] Lin & D.J. Meier, *Langmuir*, **12**, 2774, (1996).

[13] Maugis, *Langmuir*, **11**, 679, (1995).

[14] Maugis D. (1992), Adhesion of spheres: The JKR-DMT transition using a Dugdale model, *Journal of Colloid and Interface Science*, **150** [1] 243-269.

[15] Greenwood J.A., Johnson K.L., (1981), The mechanics of adhesion of viscoelastic solids, **43** [3] 697-711.

[16] Chan, D.Y.C., Hughes, B.D. and L.R. White (1987) A physically consistent theory of fracture in a brittle solid, *J. Colloid Interface Sci.*, **115** [1] 240-259.

[17] Hughes B.D., White L.R. (1979), Soft contact problems in linear elasticity, *Q. J. Mech. App. Math.*, **32** [4] 445-471.

[18] Horn, J.N. Israelachvili, & F. Pribac, *J. Coll. Interface Sci.*, **115**, 480, (1987).

[19] Kendall K., Padgett J.C., (1982), Latex Coalescence, *International Journal of Adhesion and Adhesives*, 149-154.

[20] Merill, A.V. Pocius, B.V. Thakker, & M. Tirrell, *Langmuir*, **7**, 1975, (1991).

- [21] Lee E.H., Radok J.R.M., (1960), The contact problem for viscoelastic bodies, *Journal of Applied Mechanics*, 438-444; G.A. C. Graham, *Int. J. Eng. Sci.*, **3**, 27 , (1965); W.H. Yang, *J. Appl. Mech., Trans. ASME*, 395, (1966).
- [22] Lamprecht, *Coll. & Polym.Sci. (Kolloide)*, **258**, 960 (1980).
- [23] Adamson, *Physical Chemistry of Surfaces*, 3rd Ed., Chap. 1, John Wiley & Sons, 1976.
- [24] Batchelor G.K. (1967), *An introduction to fluid dynamics*, Cambridge University Press, Cambridge.
- [25] Ross J.W., Miller W.A., Weatherly G.C., (1981) Dynamic computer simulation of viscous flow sintering kinetics, *Journal of Applied Physics*, **52** 3884-3888.
- [26] Martinez-Herrera J.I., Derby J.J., (1994) Viscous sintering of spherical particles via finite element analysis, *Journal of the American Ceramic Society*.
- [27] Jagota A. and Dawson, P.R. (1983) Simulation of viscous sintering of two particles, *J. Am. Ceram. Soc.*, **73** [1] 173-177; Jagota A. (1994), Simulation of the viscous sintering of coated particles, *Journal of the American Ceramic Society*, **77** [8] 2237-2239.
- [28] Kuiken H.K., (1990) Viscous sintering: the surface-tension-driven flow of a liquid form under the influence of curvature gradients at its surface", *Journal of Fluid Mechanics*, **214** 503-515.
- [29] van de Vorst, G.A.L. (1993), Integral method for a two-dimensional Stokes flow with shrinking holes applied to viscous sintering, *J. Fluid Mech.*, **257** 667-689.

[30] van de Vorst G.A.L. (1994) *Modelling and Numerical Simulation of Viscous Sintering*, Ph.D. Thesis, Eindhoven University of Technology, ISBN 90-386-0083-6.

[31] Herring C., *J. Appl. Phys.*, **21**, 301, (1950).

[32] Hopper R.W., (1990) Plane Stokes flow driven by capillarity on a free surface, *Journal of Fluid Mechanics*, **213** 349-375.

[33] Hopper R.W., (1984) Coalescence of two equal cylinders -- Exact results for creeping viscous plane flow driven by capillarity, *Journal of the American Ceramic Society*, **67** 262-264.

[34] Kuczynski, *J. Appl Phys.*, **20**, 1160 (1949).

[35] Kingery & M. Berg, *J. Appl Phys.*, **26**, 1205 (1955).

[36] Exner & G. Petzow, in *Sintering and Catalysis, Materials Science Research*, Vol. 10, (ed. G.C. Kuczynski), pp. 279-293 (1975).

[37] Jagota, K.R. Mikeska, & R.K. Bordia, *J. Am. Ceram. Soc.*, **73**, 2266 (1990).

[38] Mackenzie J.K., Shuttleworth R., (1949) Phenomenological theory of sintering, *Proceedings of the Physical Society*, London, **62**, 12-B.

[39] Scherer G.W. (1977) Sintering of low-density glasses: I, Theory, *J. Amer. Cer. Soc.*, **60**, 5-6.

[40] Rosenweig & M. Narkis, *Polymer Eng. & Sci.*, **21**, 1167 (1981); *Polym. Comm.*, **21**, 988 (1980); *J. Appl. Polym. Sci.*, **26**, 2787 (1981).

[41] Kuczynski, B. Neuville, & H.P. Toner, *J. Appl. Polym. Sci.*, **14**, 2069 (1970).

[42] Mazur in *Polymer Powder Technology*, (eds. M. Narkis & N. Rosenzweig), Chap. 15, John Wiley & Sons Ltd, 1995.

[43] Mazur, R. Beckerbauer, & J. Buckholz, in preparation.

[44] Argento, A. Jagota, & W. C. Carter, Surface formulation for molecular interaction of macroscopic bodies, *J. Mech. Phys. Sol.*, in press.

[45] Ferry, *Viscoelastic Properties of Polymers*, 3rd Ed., John Wiley & Sons, 1980.

[46] Plazek in *Methods of Experimental Physics*, Vol. 16c, Chap. 11, Academic Press, 1980.

[47] ABAQUS™, *Theory Manual*, Hibbit, Karlsson & Sorensen, Inc., 1996, (Tel: (401) 727-4200).

[48] Argento & A. Jagota, A surface finite element for molecular interactions, in preparation. Argento, C. and French R.H. (1996), Parametric tip model and force-distance relation for Hamaker constant determination from AFM, *Journal of Applied Physics*, in press. Jagota A., Argento C. (1996), An Inter-Surface Stress Tensor, *Journal of Colloid and Interface Science*, submitted.

[49] London F. (1937), The general theory of molecular forces, *Trans. Faraday Soc.*, **33** 9-26.

[50] Israelachvili, *Intermolecular Surface Forces*, 2nd Ed., Academic Press, 1992.

[51] Hamaker, H.C. (1937) The London-van der Waals attraction between spherical particles, *Physica*, **4** 1058-1072.

[52] Derjaguin, B.V. (1934) Untersuchungen über die Reibung und Adhäsion, IV, (Investigations concerning friction and adhesion IV), *Kolloid Z.*, **69** 155-164.

[53] Johnson K.L. (1958), A note on the adhesion of elastic solids, *British Journal of Applied Physics*, **9** 199-200.

[54] Hopper R.W., (1994) personal communication.

[55] Johnson K.L. (1985), *Contact Mechanics*, Cambridge University Press, Cambridge UK.

9. Figure Captions

Figure 1. Schematic illustration of contact growth modes in elastic adhesion and viscous sintering of spheres. Elastic adhesion is understood to be driven by direct attraction across the gap ahead of the contact neck. The contact grows in a *zipping* mode as material points previously separated by a gap come together. Tensions driving viscous sintering are modeled as being proportional to the surface curvature; the contact grows in a *stretching* mode.

Figure 2. Axisymmetric finite element discretization of a sphere making contact with a rigid surface. Also shown are contours of stress σ_{22} , the stress component normal to the contact, after initial elastic contact is established.

Figure 3. Evolution of the shape of the initially spherical particle ($R = 100$ nm).

Figure 4. Difference between the deformed and initial spherical shape. Inset shows the details close to the edge of the contact. Under the influence of van der Waals forces the surface joins the contact smoothly, resulting in a cusp at the neck. Further ahead of the contact edge the sintering neck is rounded.

Figure 5. Tensions T_z on the surface of the 100 nm sphere. Tensions have been normalized by peak compressive value of the JKR contact pressure distribution.

Figure 6. Tensions T_z on the surface of the 100 nm sphere. After initial elastic adhesion they closely match the JKR result except that the tensile tensions are bounded by the cut-off value of the van der Waals potential. At later times the tensions of a viscoelastic material under a constant force.

Figure 7. Normalized contact radius r_c/R as a function of time normalized by a characteristic viscous sintering time $t' = (3/4\pi)^{1/3}(\gamma / R\eta)$ for a 200 nm sphere with different surface energies, resulting in different initial contact radii. There is a rapid transition from initial elastic adhesion to viscous sintering by zipping which is identical for the different cases in terms of normalized time. The transition into viscous sintering by stretching is unaffected by the differences in initial elastic adhesion.

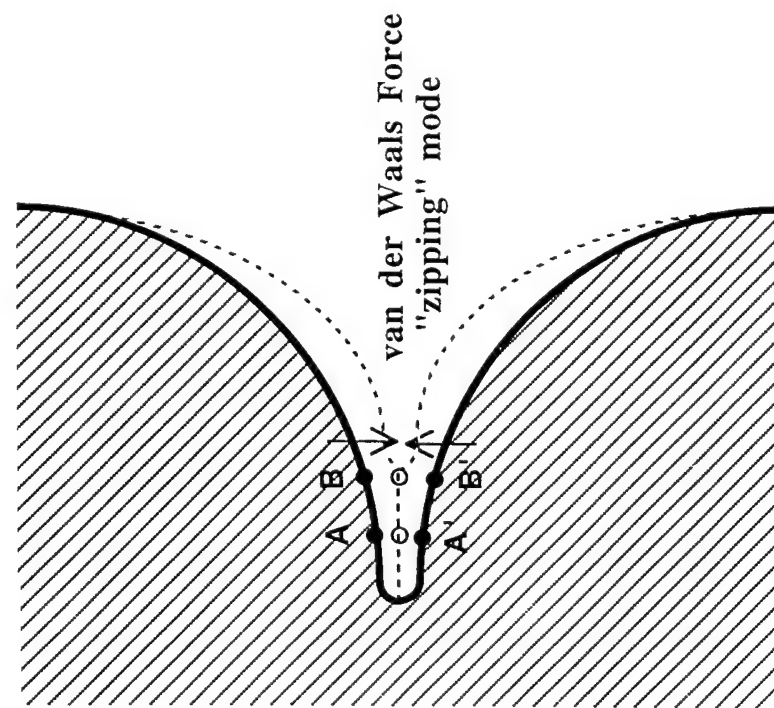
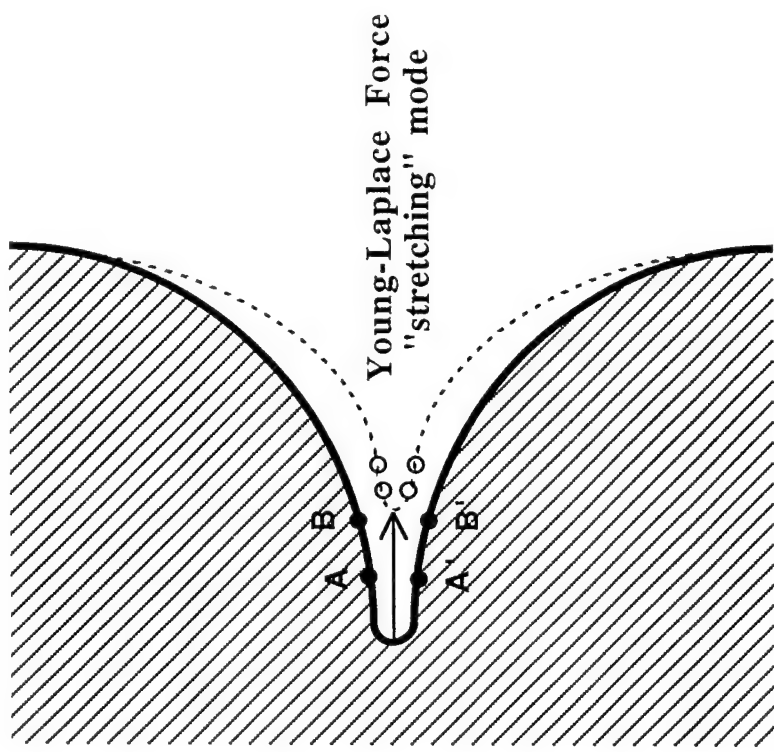
Figure 8. Normalized contact radius r_c/R as a function of time normalized by a characteristic viscous sintering time $t' = (3/4\pi)^{1/3}(\gamma / R\eta)$ for different particle sizes. The transition from the zipping to stretching mode of contact growth occurs at smaller contact radius for increasing sphere radius.

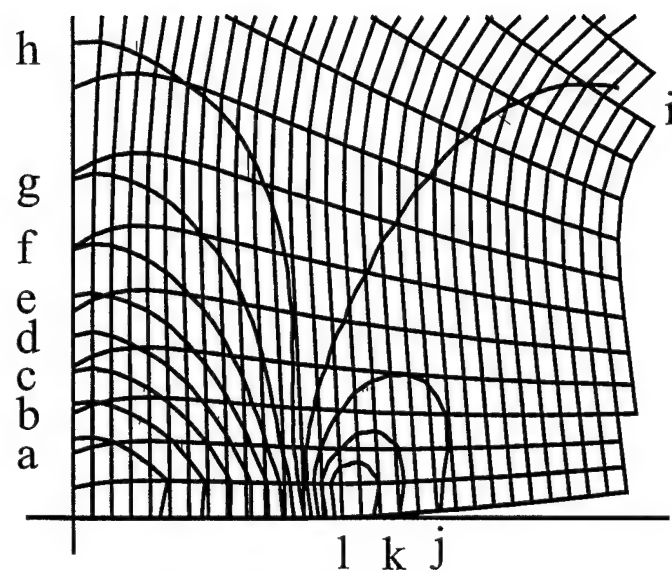
Figure 9. Motion of sphere center δ / R as a function of normalized contact area r_c^2 / R^2 . This relationship, representing volume conservation, is substantially independent of the details of growth of contact radius.

Figure 10. Normalized contact radius r_c/R as a function of time normalized by a characteristic viscous sintering time $t' = (3/4\pi)^{1/3}(\gamma / R\eta)$ for $R = 100$ nm. Simulations results under different assumptions regarding driving forces for coalescence are compared. The *zipping* and *stretching* modes of contact growth have characteristically different kinetics. There is an initial transition from elastic adhesion into viscous sintering by zipping, followed by a transition into viscous sintering by stretching.

Figure 11. Change in the total attractive van der Waals force as a function of contact radius for $R=100$ nm.

FIGURE 1

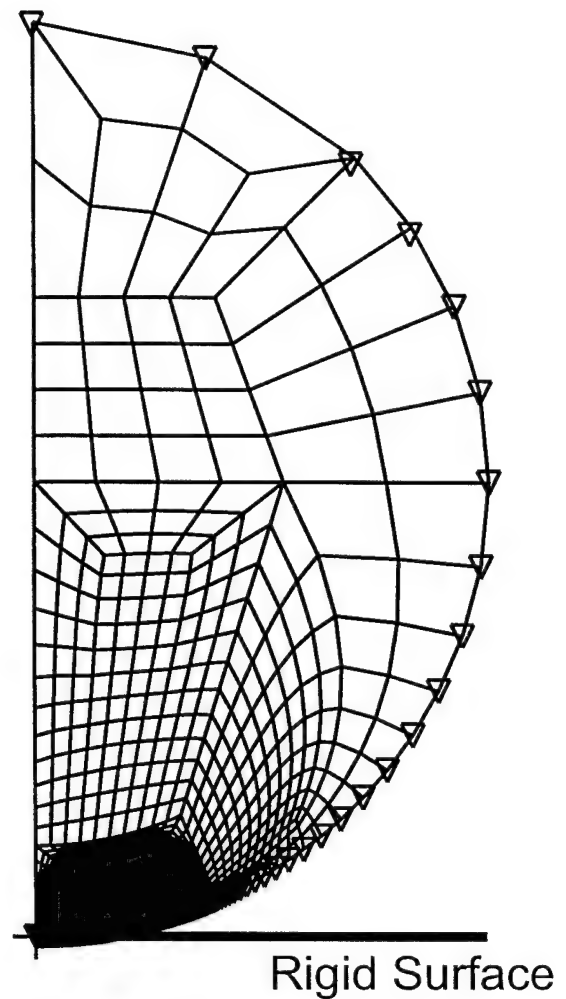




Contour levels (s22)
arb. units

a	-2.61
l	1.02
interval	0.33

2
1



▽ Surface element
nodes

Figure 2

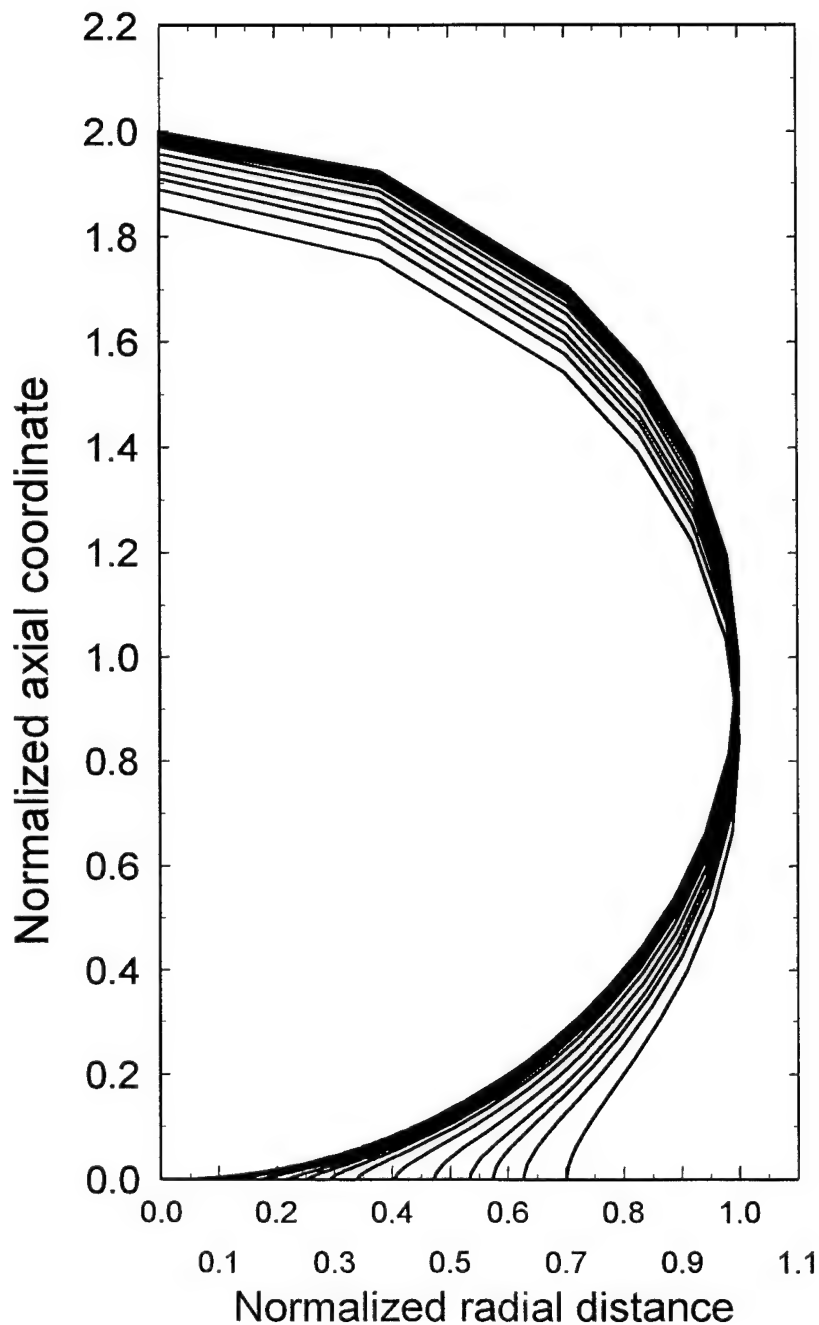


FIGURE 3

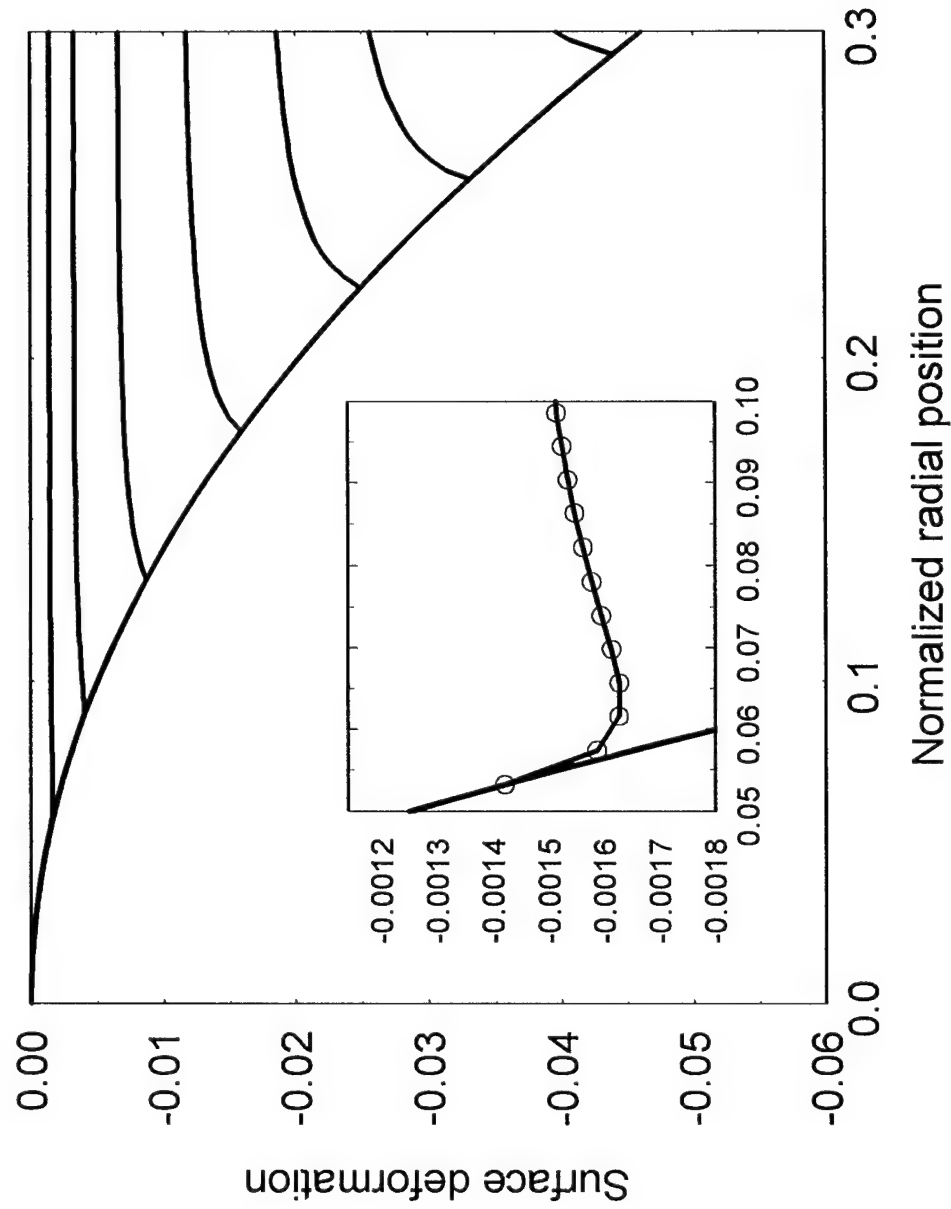


FIGURE 4

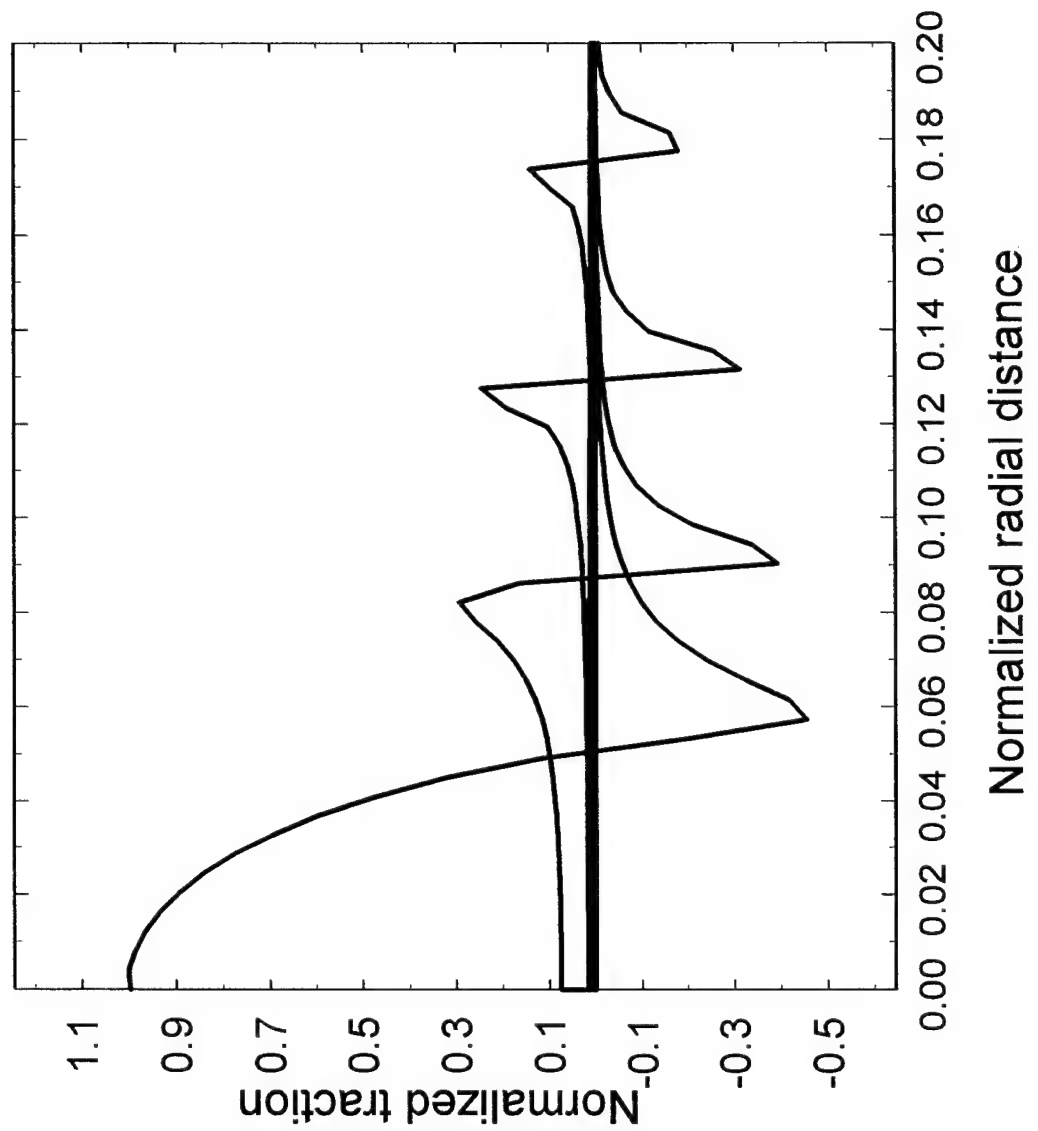


FIGURE 5

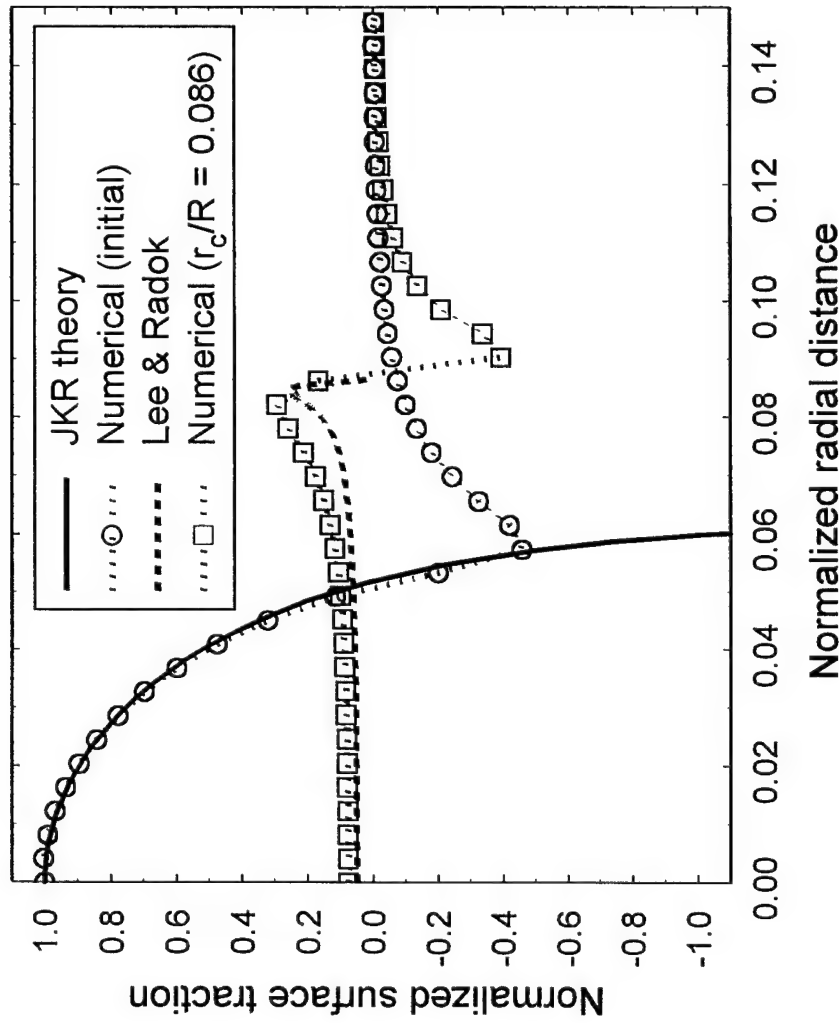


FIGURE 6

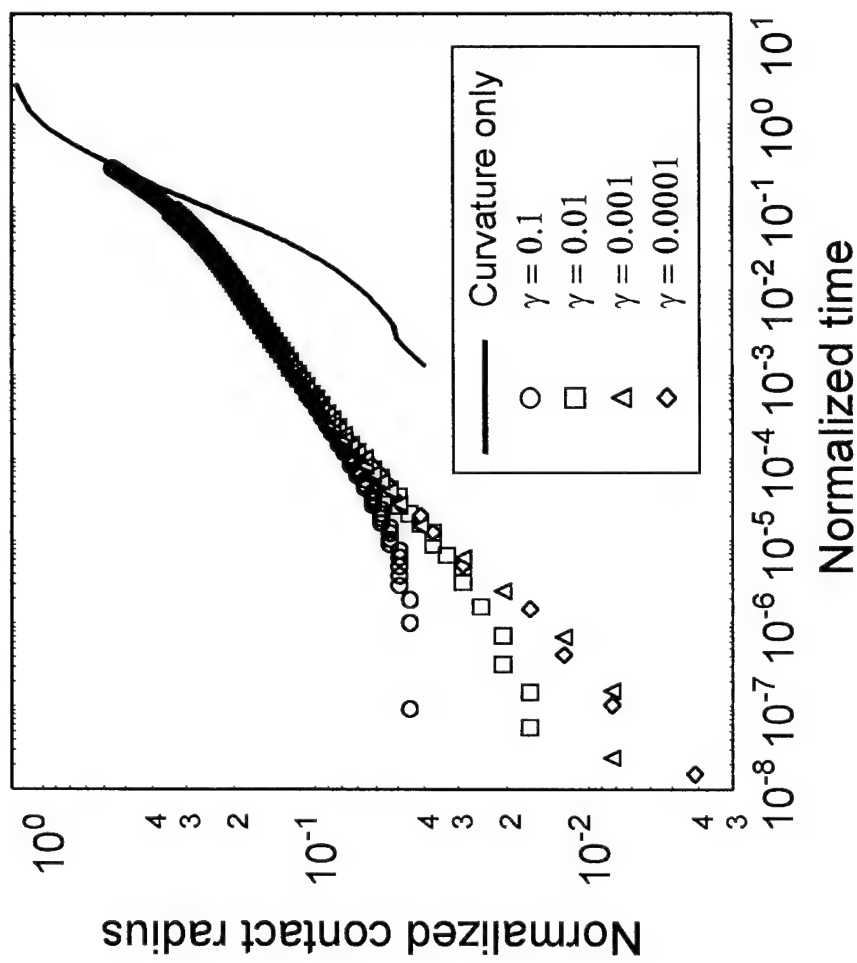


FIGURE 7

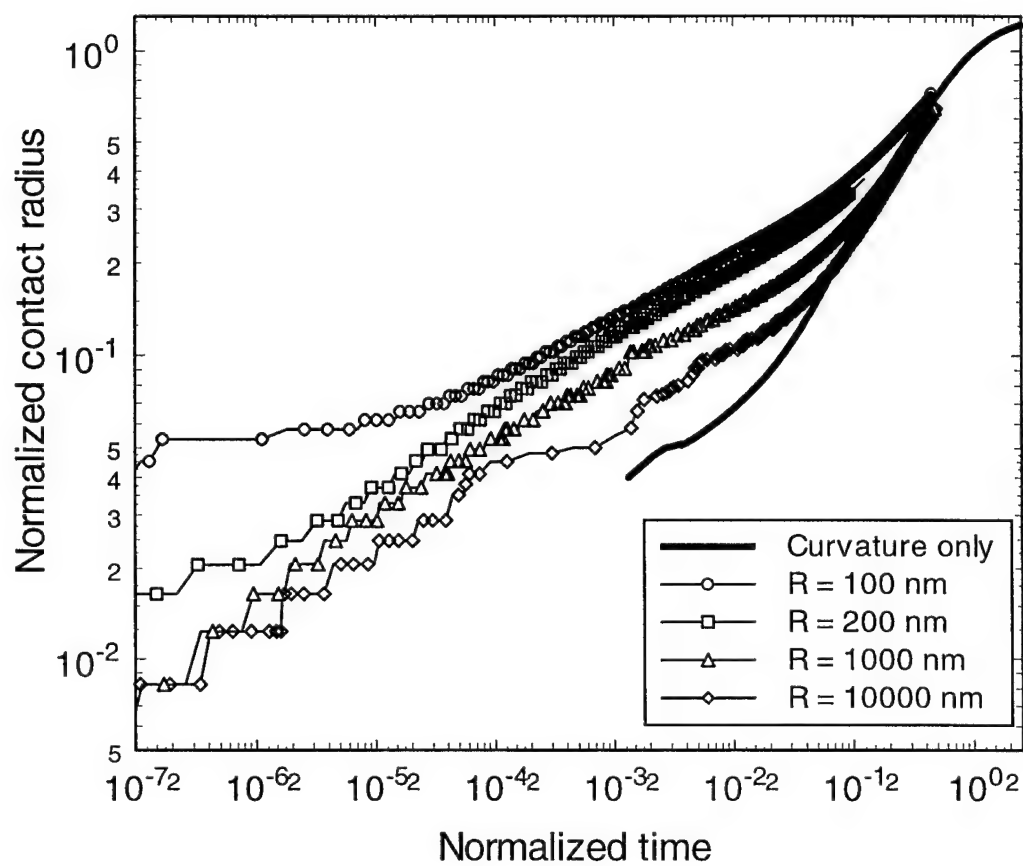


FIGURE 8

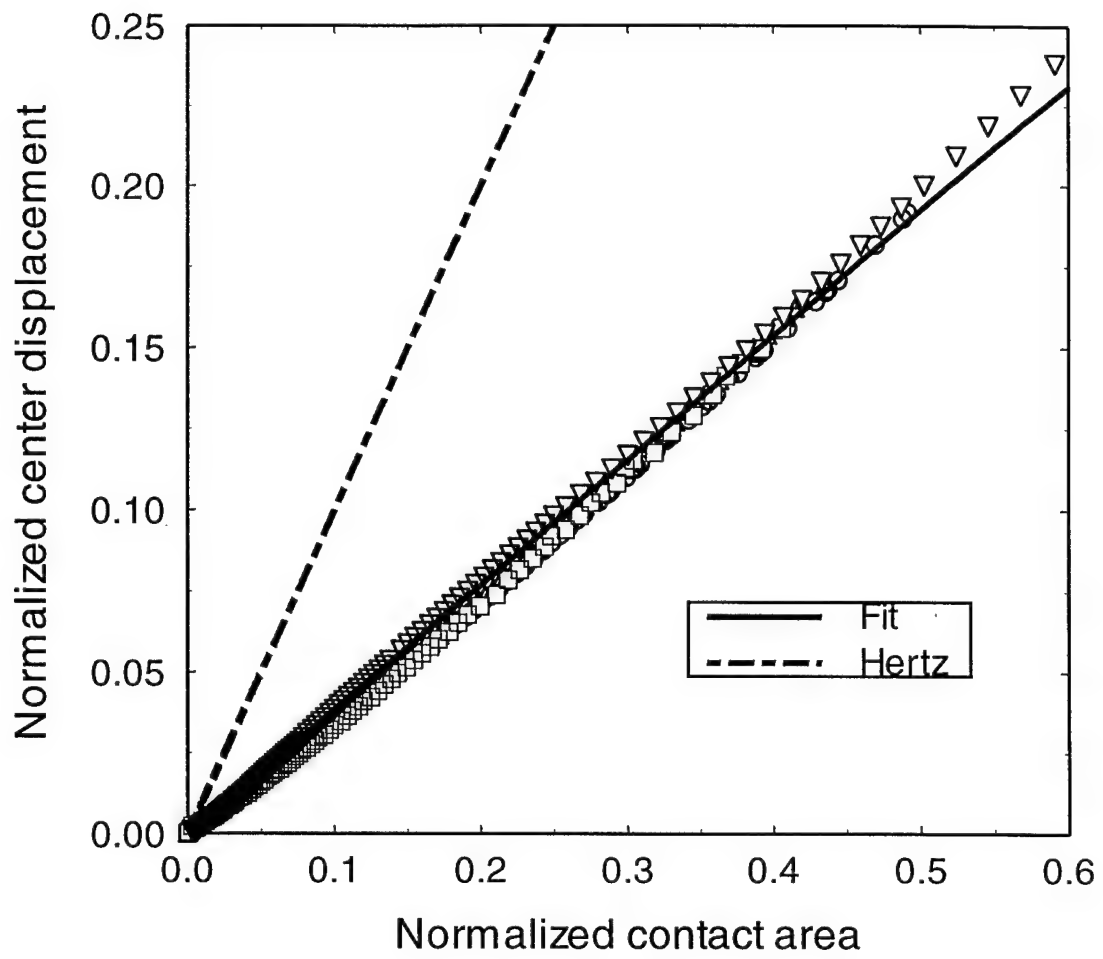


FIGURE 9

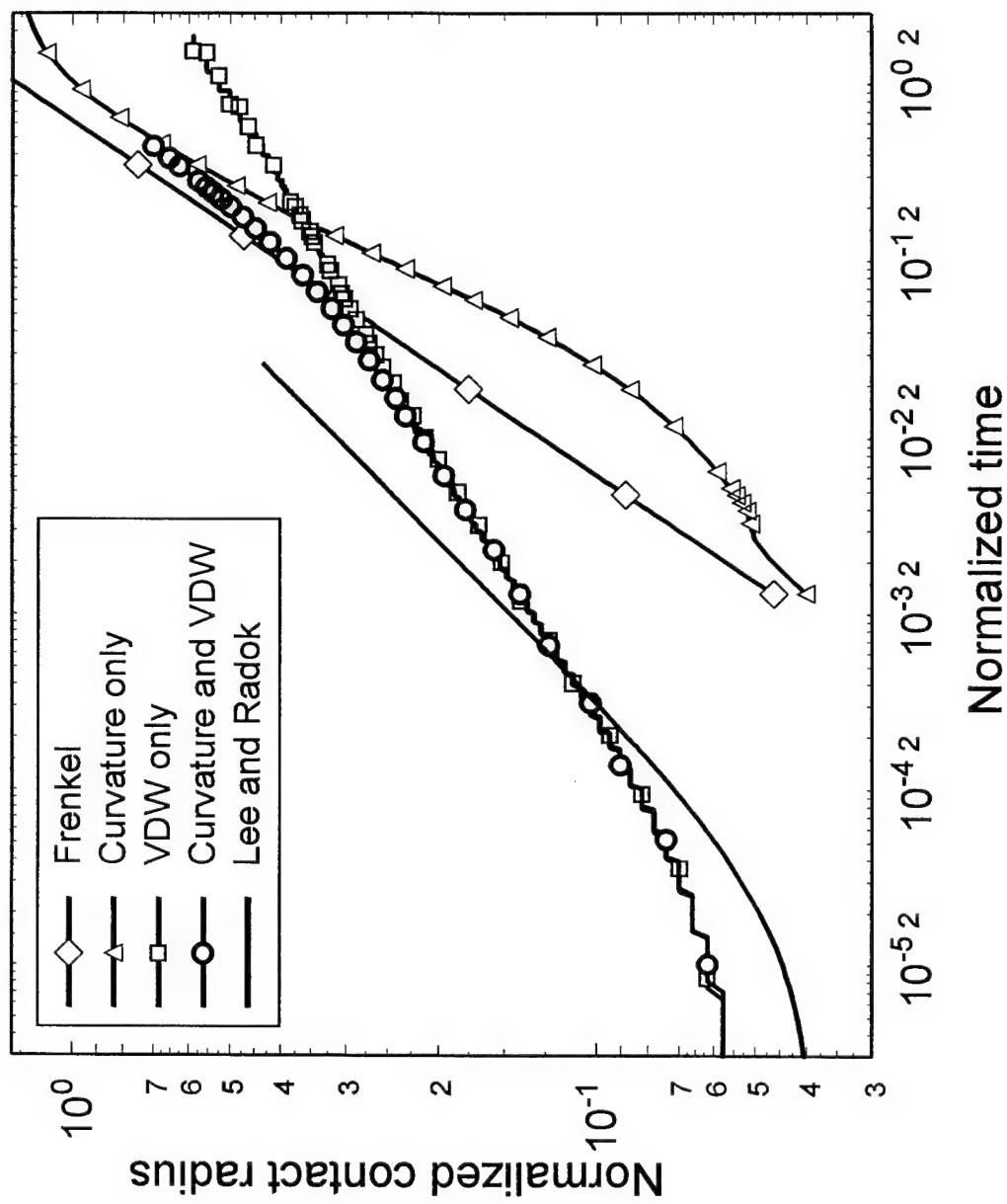


FIGURE 10

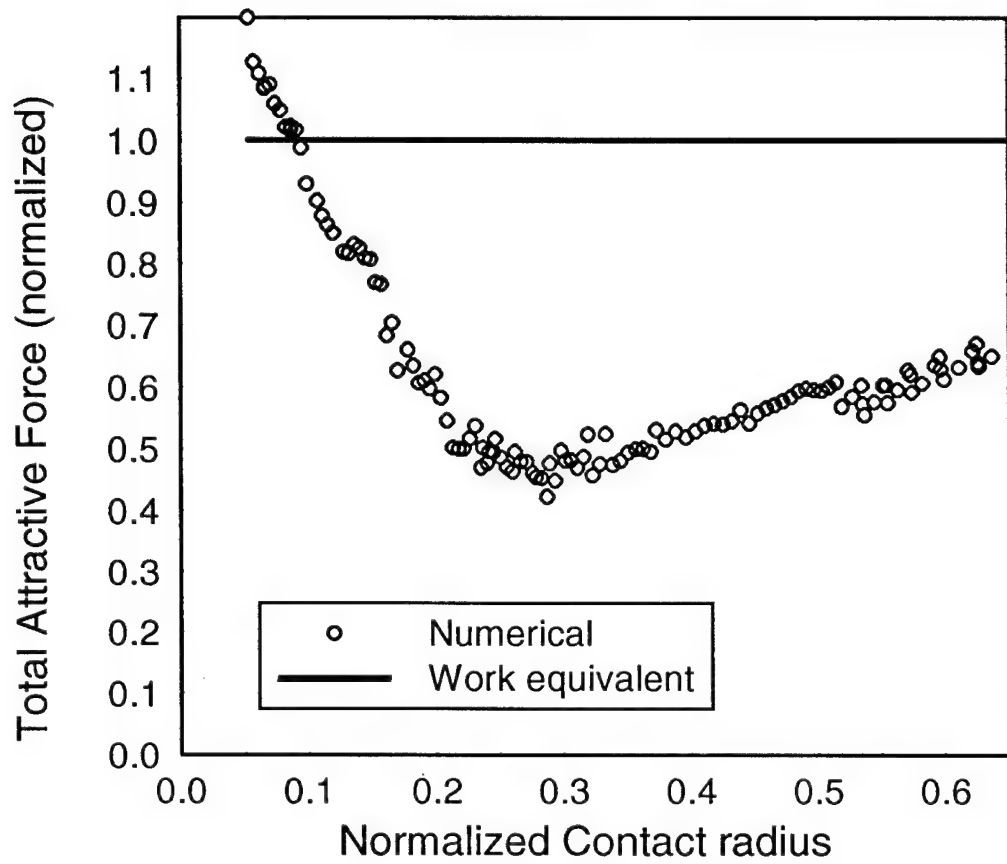
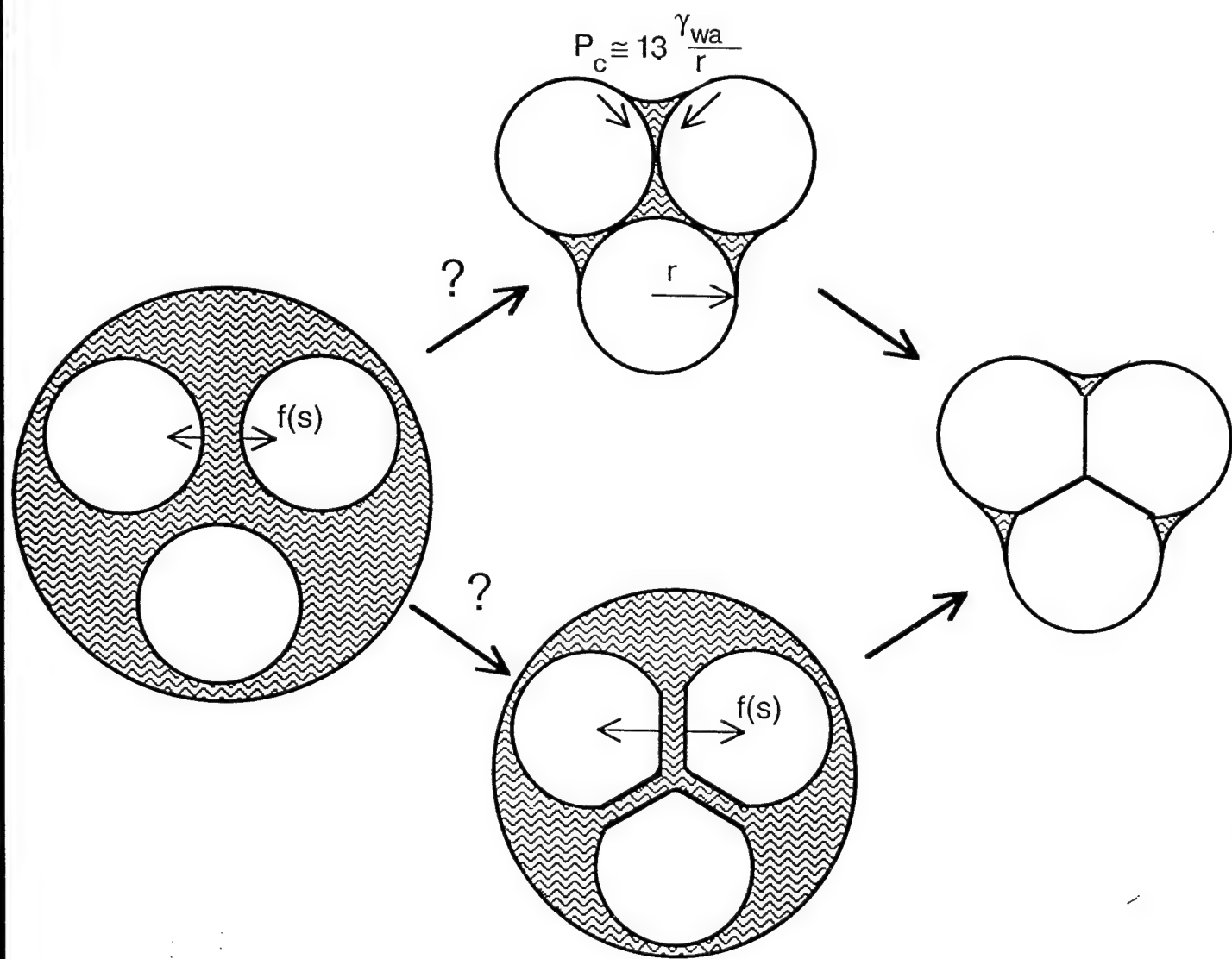


FIGURE 11

Non-Contact Deformation of Elastic Particles by DLVO Forces

Stephen Mazur & Anand Jagota
Central Research & Development Dept.
Dupont de Nemours & Co.
Wilmington, DE 19880-0356

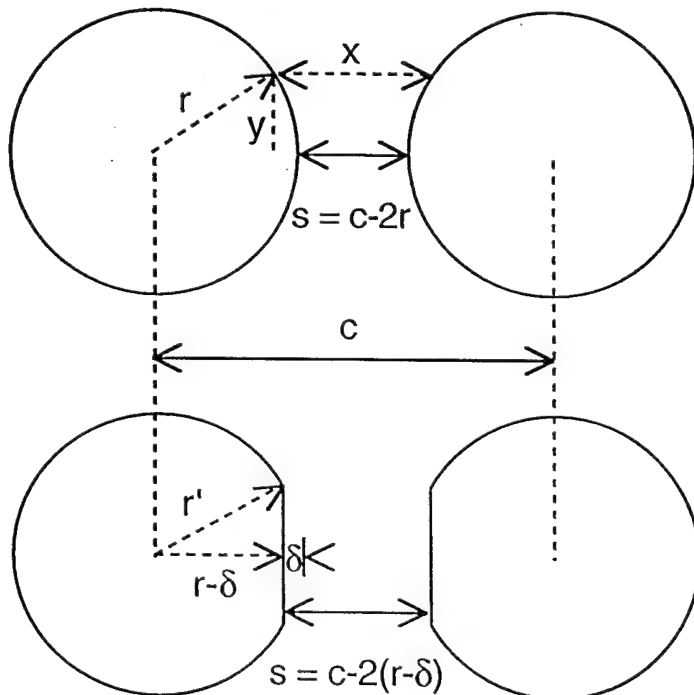


where $\epsilon\epsilon_0$ is the permittivity, $1/k$ the Debye length, and H_{eff} the effective Hamaker coefficient. In Derjaguin's approximation[7] the net force $F_o(r,c)$ between two spheres of radius r with center-to-center distance c is obtained by integrating the normal force between pairs of concentric rings over the sphere surfaces:

$$F_o(r,c) = \int_0^r dy 2\pi y f(x) \approx \pi r \int_{c-2r}^{\infty} dx f(x) = \pi r u(c-2r) \quad (2)$$

where $u(x)$ is the potential per unit area. Similarly, the pair potential is:

$$U_o(r,c) = \int_c^{\infty} dc' F_o(r,c') \quad (3)$$



Simple spheres may be converted into truncated spheres by flattening and displacing the opposing surface by δ (see diagram). This deformation increases the minimum separation s by 2δ . The interaction energy between truncated spheres $U(r,c,\delta)$ may be derived via Derjaguin's approximation. The radius of the truncated sphere r' exceeds r for the original sphere of equal volume, but this difference has a negligible effect on $U(r,c,\delta)$ (<0.5% in the regime of interest). The result simplifies as follows:

Introduction

Practical applications for polymer latex dispersions rely both on their stability against flocculation and their ability to dry into dense films. Film formation requires contact between particles (primary flocculation) and also deformation of the particles into space-filling polyhedral shapes. The sequence of these processes and the forces responsible for deformation remain controversial. Following flocculation, interfacial tension or capillary pressure often suffice to deform soft colloids[1-5], however this leaves open the possibility[6] that deformation might occur prior to contact as a consequence of long-range repulsive forces, the same forces responsible for flocculation stability. We examined the mechanics of two elastic colloidal spheres interacting according to the DLVO model for interfacial forces.

The particles were treated as incompressible elastic or viscoelastic solids with equilibrium shear modulus typical of a polymer melt. Analytic results were derived for the elastic case by restricting the deformed geometry to truncated spheres. The same approximation was elaborated earlier[7] for fluid emulsion particles. Numerical simulations based on the finite element method (FEM) were also performed to explore the consequences of unrestricted geometries and viscoelastic response. Despite differences in the equilibrium geometries, the same predictions emerge concerning surface separation in the limit of close approach. Namely, when the interaction force per unit area exceeds restoring forces from elastic and interfacial strain then the particles deform to maintain a minimum separation of several nm. In comparison with rigid colloids, the regime of flocculation stability may therefore extend to much higher volume fractions.

DLVO Model for Simple and Truncated Spheres

The DLVO model[8] represents colloidal interactions as the sum of a screened coulombic double-layer repulsion and van der Waals attraction. The force per unit area between flat half-spaces with constant surface potential Ψ_s separated by distance x in electrolyte solution may be approximated[9] by:

$$f(x) = 2\epsilon\epsilon_0\kappa^2\Psi_s^2 \frac{\exp(-\kappa x)}{\left[1+\exp(-\kappa x)\right]^2} - \frac{H_{\text{eff}}}{6\pi x^3} \quad (1)$$

$$\begin{aligned}
 U(r, c, \delta) &= \pi r' \int_{c-2r+2\delta}^c dx u(x) + \pi \left[r'^2 - (r-\delta)^2 \right] u(c-2r+2\delta) \\
 &= U_0(r, c+2\delta) + 2\delta F_0(r, c+2\delta)
 \end{aligned} \tag{4}$$

For values of c where U_0 is positive and decreases with increasing c , deformation may reduce the interaction energy: $U(r, c, \delta) < U_0(r, c)$, but the equilibrium shape depends also on the energy of deformation.

Pair Potentials and Equilibrium Shapes

Deformation entails an elastic strain energy U_e and an increase of surface free energy U_s due to increase in interfacial area. Hertz's analysis of elastic contacts[10] between truncated spheres yields :

$$U_e = \frac{16}{3} G r \delta^2 \quad G = \frac{\text{Shear modulus}}{\text{modulus}} \tag{5}$$

For $\delta \leq 0.1r$ a valid approximation[7] is:

$$U_s = 2\pi\gamma\delta^2 \tag{6}$$

where γ is the interfacial tension. The pair potential for truncated spheres is:

$$U_t = U(r, c, \delta) + U_e(r, \delta) + U_s(\delta)$$

At any value of c , the shape-dependent minima and maxima in U_t are found by taking partial derivatives with respect to δ . Solutions occur at:

$$\begin{aligned}
 \delta=0 \quad \text{and/or} \quad f(s^*) &= 8G/3\pi + \gamma/r & (7) \\
 \text{minima:} \quad \partial f(s_{\min}^*)/\partial s &< 0 \\
 \text{maxima:} \quad \partial f(s_{\max}^*)/\partial s &> 0
 \end{aligned}$$

Minima with $\delta > 0$ occur only when $f(s)$ is sufficiently large to satisfy eq. 7, such that $\delta = r + (s_{\min}^* - c)/2$.

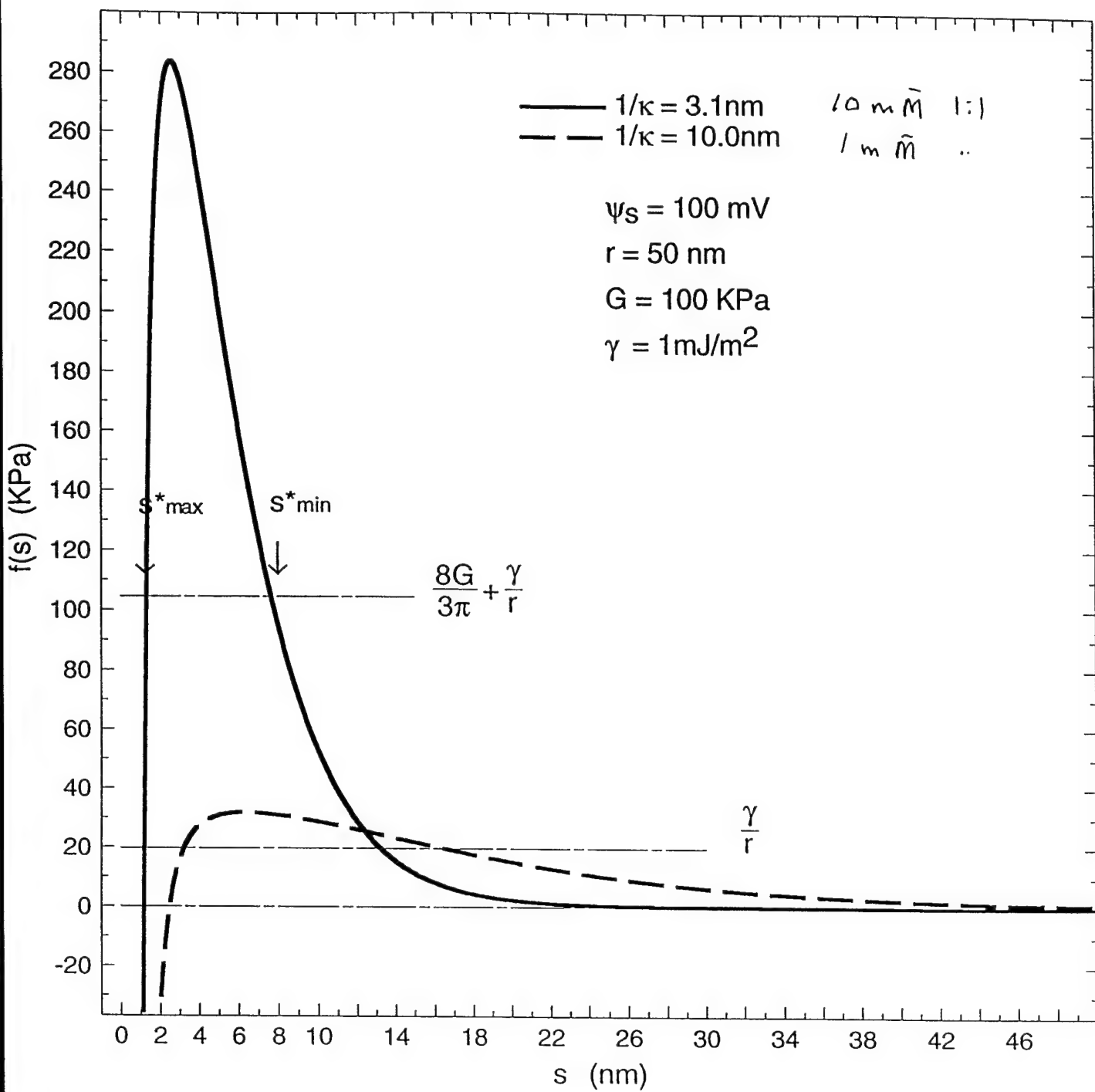


Figure 1 - Relation between $f(s)$ and restoring forces for $r=50$ nm and parameters as indicated. With $1/\kappa=10$ nm $f(s)$ remains too small to satisfy eq. 7, thus $\delta=0$ at all s . With $1/\kappa=3.1$ nm potential minima with $\delta>0$ occur at $s_{\text{min}}^* = 7.7$ nm. Results for much larger particles would be nearly the same since the only size-dependent term in eq.7 is small and varies inversely with r .

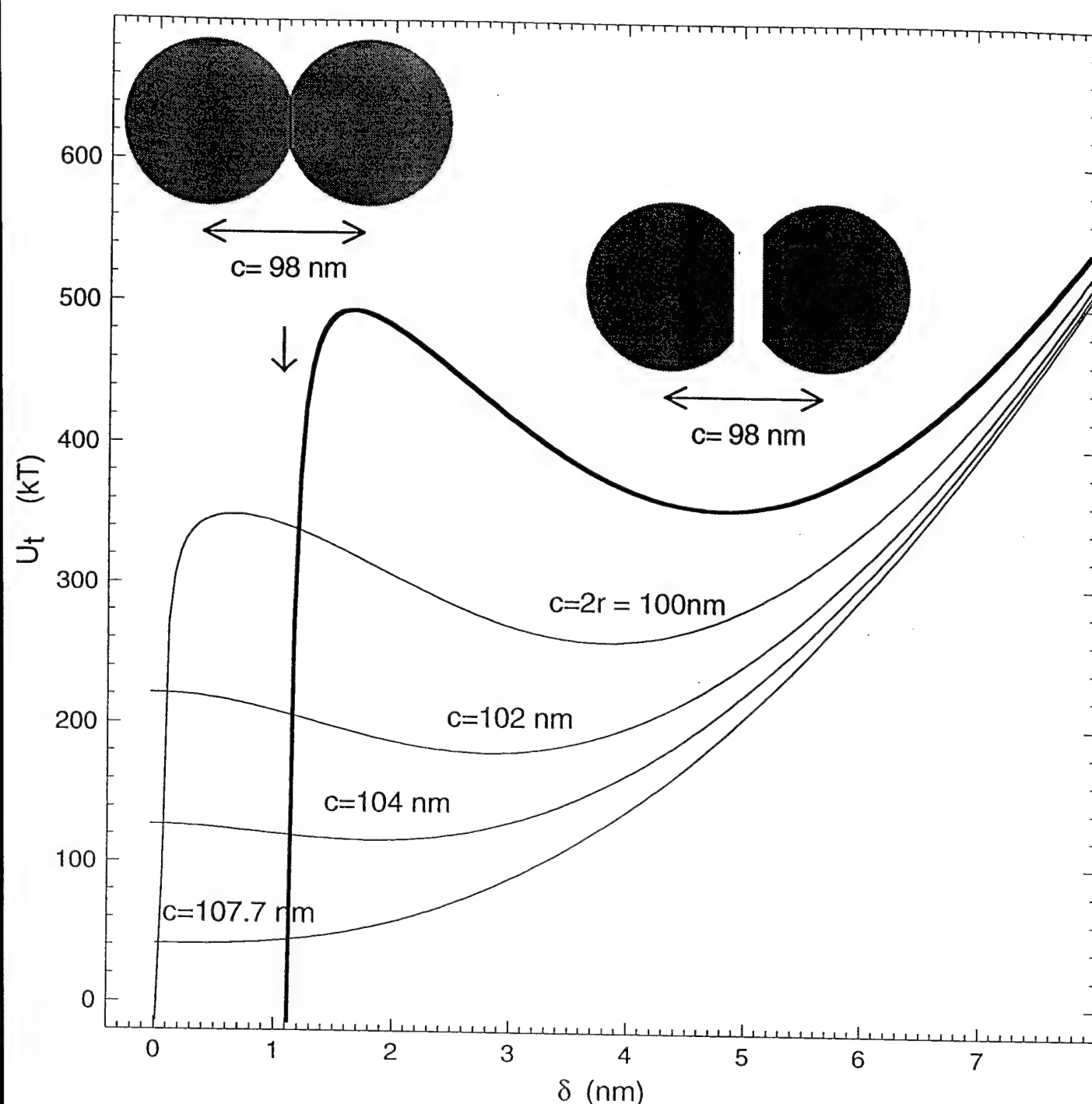


Figure 2 - Effect of deformation on the pair potential at constant c . For $2r < c < 2r + s_{\min}^*$ (100 to 107.7 nm) the global minimum occurs at $\delta > 0$ with $s = s_{\min}^*$. For $c \leq 2r$ the global minimum corresponds to primary flocculation (contact) while the non-contacting truncated shapes remain stabilized by an energy barrier at s_{\max}^* which is large enough to prevent flocculation. Accordingly, if particles were brought together from large c , adopting equilibrium shapes along the way, they would be trapped into the local minimum and remain non-contacting even for $c < 2r$.

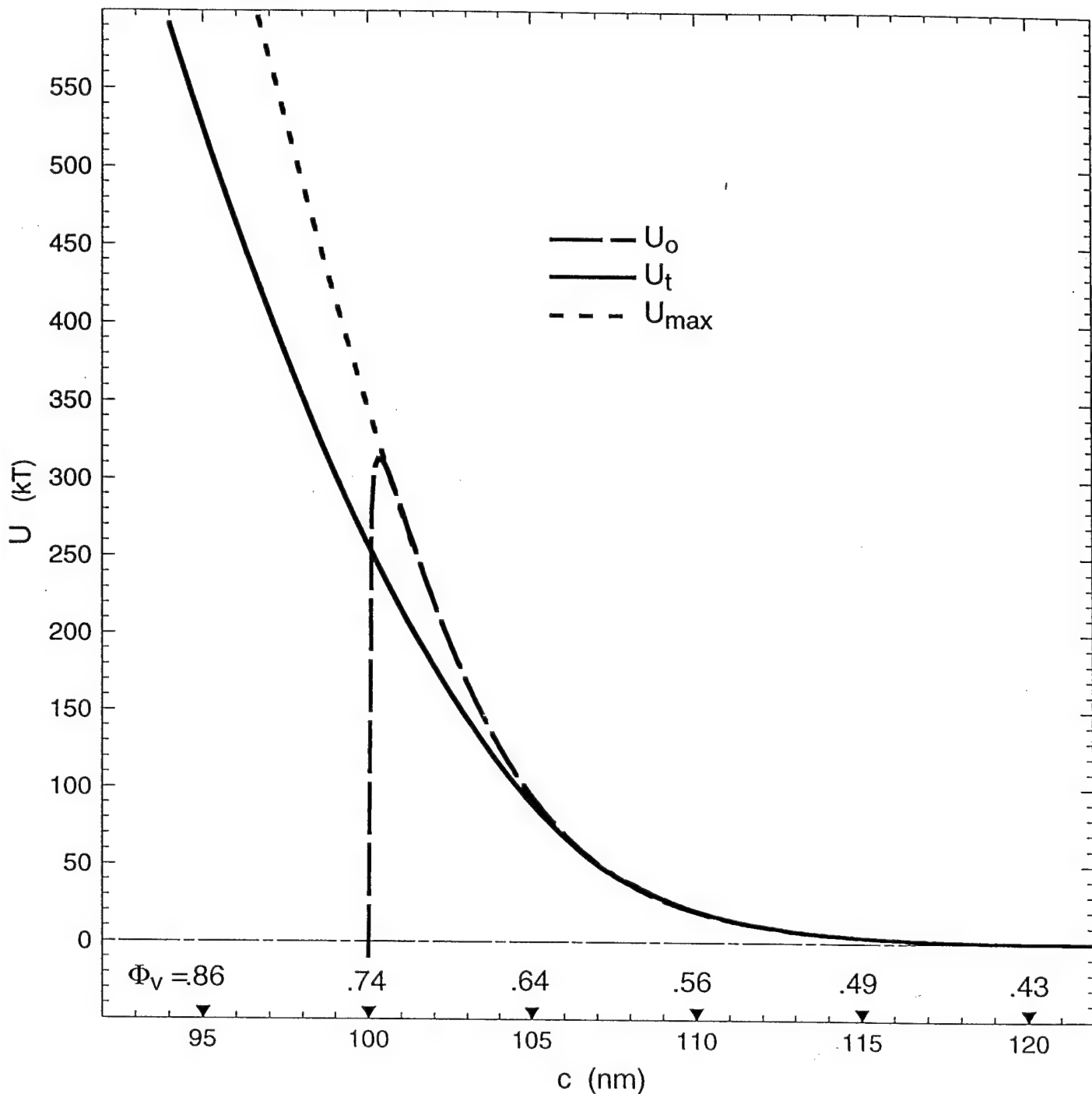


Figure 3 - Pair potentials for simple spheres (U_o), equilibrium truncated spheres (U_t), and intermediate shapes at transition state (U_{\max}) between global and local minima. Along the abscissa are indicated volume fractions for fcc ordered packings with lattice constant equal to c .

FEM Simulations

Since the analytic predictions are confined to truncated spheres, numerical simulations were performed to determine the equilibrium geometries free of constraints, and to test the generality of the predictions. These simulations begin with a pair of spheres $r=50\text{nm}$ with $1/\kappa=3.1\text{nm}$ and the remaining parameters as in Fig.1. Finite element methods (ABAQUS®) were used to determine the equilibrium geometry and stress distribution for progressively smaller values of c starting at 130nm . The boundary conditions comprised a distribution of tractions on each surface element calculated from eq. 1. The surface tractions conformed to Derjaguin's approximation in that they were calculated from the distance x between equivalent pairs of surface elements. No constraints were imposed on the surface contours.

When G was held constant at 0.1MPa with $c < 120\text{nm}$ the simulations were unstable and did not converge. The problem was overcome by allowing the shear modulus to relax exponentially from 10MPa to 0.1MPa while c was reduced linearly with time from 130nm . At each time step the stress distribution was calculated consistent with Boltzmann superposition. This simulation mimics the viscoelastic response for a polymer in the transition regime converging to its plateau modulus:

$$G(t) = [9.9\exp(-t/\tau) + 0.1]\text{MPa} \quad (7)$$

Very slow approach times $t < 1000\tau$ were required in order to obtain equilibrium results independent of t . This lag of the deformation behind the modulus is a consequence of the inhomogeneous evolution of stress fields within the particles. Similar behavior has been observed in experiments[5,11] and simulations[12] of viscoelastic sintering.

Figure 4 shows results of FEM simulations compared with analytic results for truncated spheres. Under equilibrium elastic conditions, the onset of deformation occurs at much larger c than predicted by eq. 7, but as c approaches $2r=100\text{nm}$ the value of δ converges to the analytic result. Thus the boundary layer thickness s_{\min}^* at small c is apparently insensitive to differences between realistic and idealized particle shapes. However the inter-

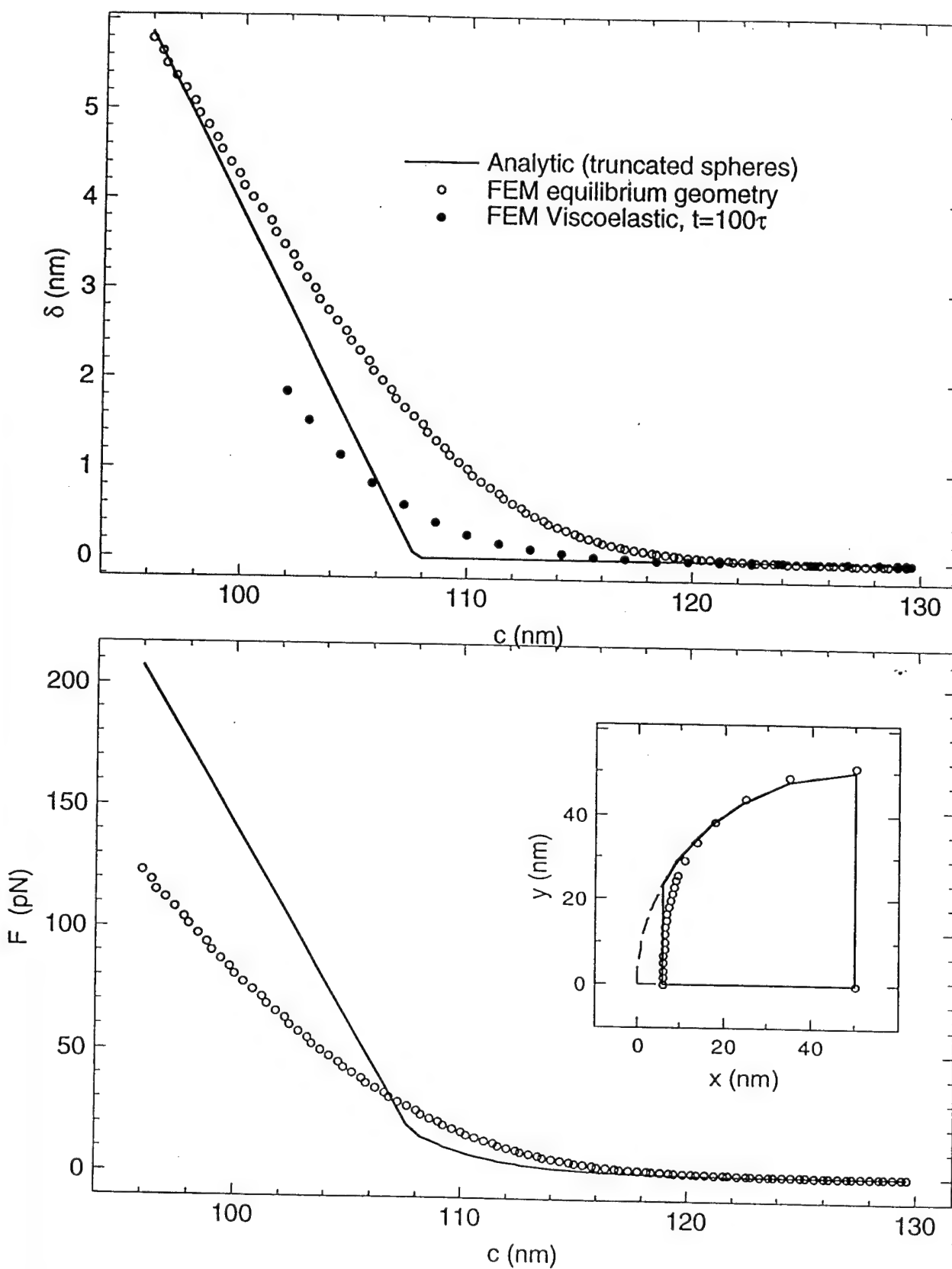


Figure 4 - Comparison between displacement (δ) and inter-particle force obtained analytically for truncated spheres and from unconstrained numerical simulations. Insert shows differences in particle profiles at $c=96$ nm.

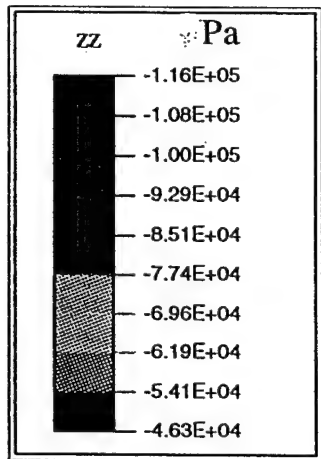
particle forces for the realistic shapes prove to be substantially lower than those for truncated spheres .

Finally, when approach times were too short to permit viscoelastic equilibration at each value of c (e.g. $t=100\tau$), then the extent of deformation was greatly reduced resulting in separations smaller than s_{\min}^* . This suggests that dynamic factors such as drying rate or rotational correlation time might influence the sequence of deformation versus flocculation in real latex dispersions.

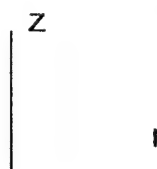
References

- 1- G.L. Brown, *J. Polm. Sci.*, **12**, 423 (1956).
- 2 - K.L. Johnson, K. Kendall, & A.D. Roberts, *Proc. Roy. Soc. Lond.*, **A**, **13**, 301 (1971).
- 3 - F. Dobler, T. Pith, M. Lambla, & Y. Holl, *J. Coll. Interfac. Sci.*, **152**, 1 (1992).
- 4 - P.R. Sperry, B.S. Snyder, M.L. O'Dowd, & P.M. Lesko, *Langmuir*, **10**, 2619 (1994).
- 5- S. Mazur, *Polymer Powder Technology*, Chap. 8, M. Narkis & N. Rosenzweig, Ed's, John Wiley & Sons, 1995.
- 6 - T.L. Crowley, A.R. Sanderson, J.S. Morrison, M.D. Barry, A.J. Morton-Jones. & A.R. Rennie, *Langmuir*, **8**, 2110 (1992).
- 7 - N.D. Denkov, D.N. Petsev, & K.D. Danov, *Phys. Rev. Lettt.*, **71**, 3226 (1993); *J. Chem. Phys.*, **99**, 7179 (1993).
- 8 - DLVO: Derjaguin, Landau, Verwey & Overbeek. See: E.J.W. Verwey & J. T.G.Overbeek, *Theory of Lyophobic Colloids*, Elsevier, 1948.
- 9 - W.B. Russel, D.A. Saville & W.R. Schowalter, *Colloidal Dispersions*, Chap. 4, Cambridge University Press, 1989.
- 10 - See K.L. Johnson, *Contact Mechanics*, Chap. 4, Cambridge Univeristy Press, 1985.
- 11 - S. Mazur & D.J. Plazek, *Prog. Org. Coat.*, **24**, 225 (1994).
- 12 - C. Argento, S. Mazur, & A. Jagota, *Proceedings of the International Conference on the Science, Technology , and Applications of Sintering*, Penn. State University, Sept. 1995.

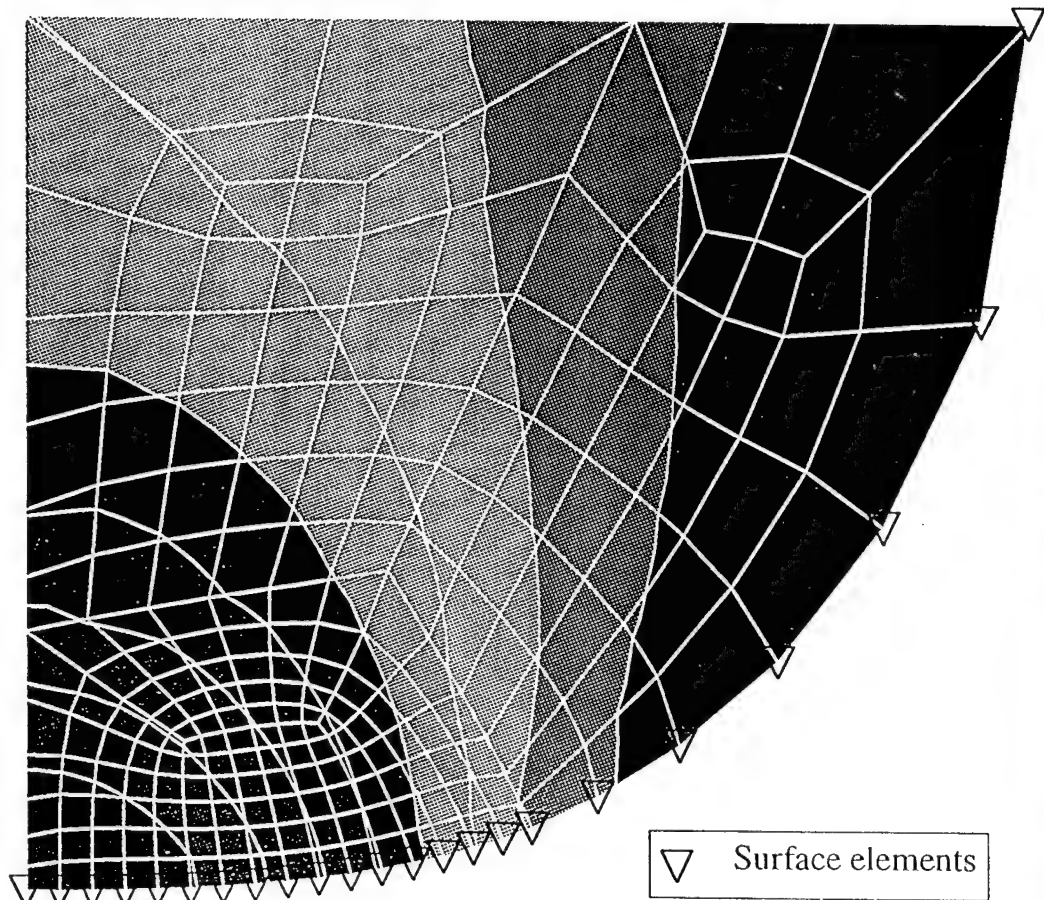
Contours of zz component of stress



$R = 50 \text{ nm}$
 $G = 100 \text{ KPa}$
 $\gamma = 1 \text{ mJ/sq.m}$
 $c/2 = 48 \text{ nm}$



symmetry plane



MECHANICAL FORCES AND MATERIAL RESPONSE IN THE COALESCENCE OF POLYMER PARTICLES*

Stephen Mazur and Claudio Argento, DuPont Central Research & Development, P.O. Box 80356, Wilmington, DE 19880-0356

Many fabrication processes require coalescence of discrete polymer particles into a dense, homogeneous body above the melting temperature T_m , and near or above the glass temperature T_g . Examples range from neat powders "free sintered" or compression molded under applied load to aqueous latex dispersions which coalesce subject to complex colloidal interactions during drying. Particle diameters may range from nm to mm. In all cases, transformation of a particulate precursor into a uniform, isotropic product requires several different kinds of physical processes including particle deformation, stress relaxation, and molecular diffusion. In contrast with recent advances in characterizing diffusion, understanding of the material mechanics remains incomplete. This presentation addresses some relationships between coalescence kinetics, inter-particle forces, particle size, and polymer visco-elastic properties (T_g , $J(t)$, η_0).

Depending upon the material properties and time interval, an aggregate of molten polymer particles may compact either by elastic deformation or viscous flow of the polymer. A universal characteristic of high polymers[1] for which M_w exceeds the entanglement weight M_e is that the shear compliance $J(t)$, which governs particle deformation, remains entirely recoverable for a considerable time following application of a load at $t=0$. Hence the initial deformation is always a quasi-elastic response dictated by the recoverable shear compliance $J_r(t)$. Because $J_r(t)$ increases roughly 1,000-fold during the glass relaxation, rheology at temperatures near T_g plays a central role in coalescence kinetics. Depending upon the magnitude of the forces and the initial packing density, quasi-elastic deformation may suffice to fully densify an aggregate at $T > T_g$ without any contribution from viscous flow. Measurements of inter-particle neck growth[2] demonstrate that viscous flow only contributes at times longer than the terminal relaxation time $\tau_n = \eta_0 J_n$. For polymers of very high M_w τ_n often exceeds the processing time.

The extent of densification due to quasi-elastic deformation should be determined by $J_r(t)$, particle size, and the inter-particle forces. Within the rubbery plateau regime where $J_r(t) \sim J_n$, analytic approximations for contact between elastic spheres may be applicable. This approach was used to estimate, for several common polymers, the minimum pressure p^* , or maximum particle radius r^* (when surface tension is the driving force) for quasi-elastic densification of monodisperse spheres in random close packing[3]. Limited experimental data on acrylics and fluoropolymers is consistent with this analysis. In order to refine such predictions and to model the detailed kinetics of visco-elastic neck growth, computer simulations have been undertaken using finite element methods. In contrast with simpler neck-growth mechanisms, such as viscous flow, the kinetics of visco-elastic neck growth should not scale in any simple way with particle size, because the visco-elastic relaxation spectrum is size-independent.

One consequence of quasi-elastic particle deformation is that residual stresses and molecular orientation may persist in the nascent product. Often these effects are not apparent because the macroscopic measurements are isotropic averages of locally anisotropic properties. Some noteworthy exceptions are illustrated by the coalescence of poly(tetrafluoroethylene) powders following cold compression molding or paste extrusion.

Coalescence during drying of aqueous latex particles is especially important in coating technology. The forces between suspended colloidal particles are complex and vary with concentration. In general, latex dispersions are stabilized by a long-range screened coulombic repulsion which overcomes the short-range Van der Waals attractions between particles. All else being equal, increasing the colloid concentration will increase inter-particle repulsion as measured, for example, by the osmotic pressure Π . But in practice drying also concentrates any soluble electrolytes which reduces the screening length, thereby destabilizing the particles with respect to flocculation. DLVO theory predicts that 100 nm polystyrene latex dispersions will flocculate when the concentration of a univalent electrolyte reaches about 0.2M[4]. Competition between these two effects may determine whether particle deformation precedes or follows inter-particle contact.

When the mean pressure exerted on each latex particle by the coulombic repulsion of its neighbors becomes comparable to p^* quasi-elastic deformation may deform the spheres into isolated polyhedra which do not contact one another but which fit together into a space-filling cellular structure as the water content goes to 0. Experimental evidence of particle deformation before contact has been reported for a number of latex systems[5,6], and recent measurements[7] of Π in surfactant-free latex dispersions at low ionic strength demonstrate that forces developed at polymer volume fractions below 0.6 can be adequate for this effect. On the other hand, if flocculation of the spherical colloid intervenes before Π reaches p^* , deformation may occur subsequently by two alternative mechanisms: The contact surfaces may grow as a consequence of polymer-water interfacial tension (similar to neck-growth in dry aggregates), or the process may be driven by further increase in Π as the drying continues. Brown originally noted[6,8] that Π will ultimately converge to a value determined by capillary surface tension when the liquid meniscus intercepts a surface of densely packed spheres. That limit corresponds to $\Pi \sim 1$ MPa for typical colloidal dimensions which exceeds p^* for any molten polymer, but is still far too small to cause deformation of the corresponding glass. The characteristic "mud-cracks" which form when a latex dispersion is dried at temperatures below T_g are presumably caused by inhomogeneous stress fields in pores which develop as liquid menisci recede into the un-deformed packing.

Such mechanistic variations have not been considered in earlier models of latex coalescence[9] and may help to explain some common variations in drying phenomenology. No experimental system has yet been adequately characterized for a quantitative analysis. A further complication is that non-uniform drying may establish osmotic gradients in the coating. The response to such gradients should depend upon the rheology of the

dispersion which is also a strong function of colloidal interactions and the water content.

References:

- * This work is supported in part by the U.S. Air Force Office of Scientific Research.
- 1. D.J. Plazek, in "Methods of Experimental Physics" Vol. 16c, Chap. 11, Academic Press, 1980.
- 2. S. Mazur & D.J. Plazek, Prog. Org. Coat., 24, 225 (1994).
- 3. S. Mazur in "Polymer Powder Technology", M. Narkis & N. Rosenzweig, Eds., John Wiley & Sons, in press.
- 4. W.B. Russel, D.A. Saville, & W.R. Schowalter, "Colloidal Dispersions", Chap. 8, Cambridge U. Press, 1989.
- 5. M. Joanicot, K. Wong, J. Maquet, Y. Chevalier, C. Pichot, C. Graillat, P. Lindner, L. Rios, & B. Cabane, Prog. Coll. Poly. Sci., 81, 175 (1990).
- 6. T.L. Crowley, A.R. Sanderson, J.D. Morrison, M.D. Barry, A.J. Morton-Jones, & A.R. Rennie, ibid, 8, 2110 (1992).
- 7. C. Bonnet-Gonnet, L. Belloni, & B. Cabane, Langmuir, 10, 4012 (1994).
- 8. G.L. Brown, J. Poly. Sci., XXII, 423 (1956).
- 9. J. Lamprecht, Colloid & Poly. Sci., 258, 960 (1980).

"Sintering" of Polymer Colloids

S. Mazur & R. Beckerbauer
Dupont Central Research & Development
Wilmington, DE

For aggregates of amorphous polymer spheres we examine the spontaneous shrinkage under surface tension at $T \geq T_g$. Analogous to sintering of inorganic powders, this process involves deformation of the component particles into space-filling shapes by local forces which vary inversely with particle size, but the viscoelastic character of polymer melts results in unique mechanistic consequences. For sufficiently small (colloidal) particles and high packing densities, the entire densification process occurs rapidly by recoverable viscoelastic creep with no contribution from viscous flow.

I - Viscoelastic growth of adhesive contacts

The creep compliance $J(t)$ measures the time-dependent strain following application of a constant stress σ_0 . For high M_w amorphous polymers, $J(t)$ can be represented[1] by the sum of a glassy elastic response $J_0 \sim 1\text{GPa}^{-1}$, a time-dependent recoverable response $J_r(t)$, and a Newtonian viscous flow:

$$J(t) = \epsilon(t)/\sigma_0 = J_0 + J_r(t) + t/\eta_0$$

Figure 1A shows data typical of an amorphous polymer with broad molecular weight distribution. During the glass relaxation ($T_g \sim 112^\circ\text{C}$) $J_r(t)$ increases rapidly to the plateau value $J_h \sim 1\text{MPa}^{-1}$. Viscous flow remains negligible until the terminal relaxation time $\tau = J_r\eta_0 \sim 5 \times 10^4$ seconds.

When two contacting polymer spheres are deformed by surface tension, the radius of the contact x_h grows in a manner similar to $J(t)$, as illustrated in Figure 1-B for 260 μm spheres. At early times neck growth is dominated by $J_r(t)$ while the viscous contribution only becomes significant at times $t > \tau$. Both contributions increase with decreasing particle size, but in multi-particle aggregates deformation proceeds only to the limit of uniform density. Thus for sufficiently small particles this limit should be reached purely via the recoverable compliance with no contribution from viscous flow.

What are the requirements to achieve uniform density within $t \ll \tau$?

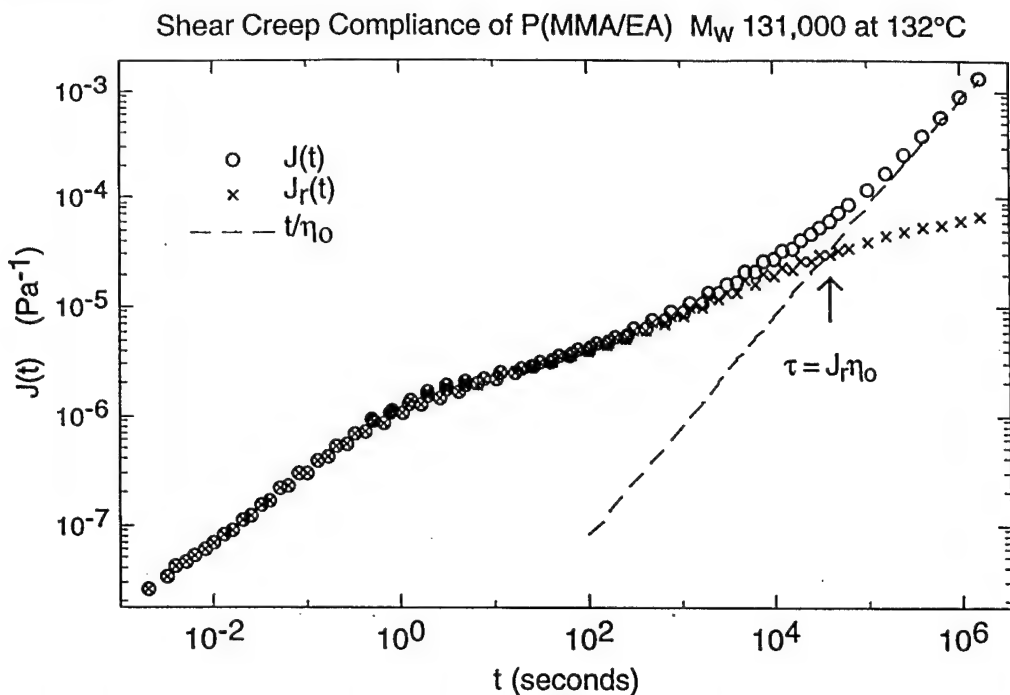


Figure 1A - Creep compliance master plot for Poly(methyl methacrylate-co-ethyl acrylate) (95/5)

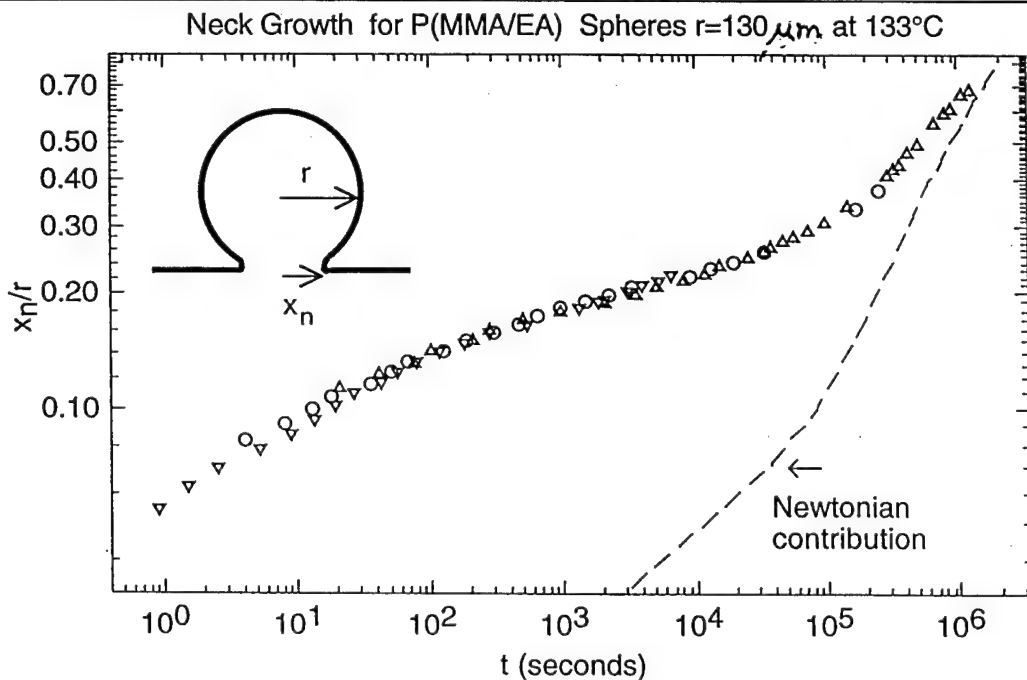


Figure 1B - Growth of contact neck radius between P(MMA/EA) sphere and film[2].

II - Predictions from theory for adhesive contacts

Consider an aggregate of identical incompressible spheres at initial packing fraction Φ_i in which each sphere contacts several of its nearest neighbors. When shrinkage occurs by uniform decrease of all interparticle distances, the particles ultimately deform into space-filling polyhedra. As Φ goes to unity the distance between closest centers goes from $2r$ to $2(r-\delta)$, such that:

$$\Phi_i/1.00 = \{2(r-\delta)/2r\}^3 \quad \text{or} \quad \delta = r(1-\Phi_i^{1/3})$$

Simulations for pairs[3] indicate the following relation between the displacement δ and contact radius x_n :

$$x_n^2 \equiv 2.42 r\delta$$

The magnitude of x_n in the plateau regime of Fig. 1-B agrees well with the value predicted by the JKR model[4] for adhesive elastic contacts. Using the last two equations to define the requisite contact radius for reaching full density, and assuming that the maximum compliance achieved for $t \ll \tau$ is just the plateau value J_n , we obtain via JKR the following approximation[5] for the maximum particle radius:

$$r_{\max} \equiv 0.47 \gamma J_n (1-\Phi_i^{1/3})^{-3/2}$$

where γ is the surface tension. Results are tabulated below for various common polymers and values of Φ_i corresponding to both disordered and ordered (e.g.hcp) packings of mono-disperse spheres.

Polymer	J_n (MPa ⁻¹)	γ (mN/m)	r_{\max} $\Phi_i = 0.58$	(nm) 0.74
Poly(ethylene)	0.44	27	83	190
Poly(tetrafluoroethylene)	0.60	10	42	97
Poly(styrene)	4.90	31	1,100	2,500
Poly(butadiene)	1.62	19	210	500
Poly(methyl methacrylate)	1.15	31	250	570

Table 1 - Maximum particle radius for full densification without viscous flow in aggregates of equi-sized spheres at the indicated packing densities.

III - Experiments on aggregates with narrow size distribution

A series of colloidal acrylic spheres was prepared by emulsion polymerization. These are co-polymers of methyl and butyl methacrylate with methacrylic acid, (48.5/48.5/3), having $M_w > 2 \times 10^5$, $T_g = 77^\circ\text{C}$ (DSC at 10°/min), and narrow size distributions. When dried at $T < T_g$, they form dense aggregates of un-deformed spheres featuring ordered (hcp or fcc) domains interspersed with less dense, disordered domains.

Shrinkage of the dried aggregates was measured as a function of temperature by minimal-load thermo-mechanical analysis (TMA-ML), and morphological changes were monitored by SEM and SAXS. TMA-ML results summarized in Figure 2 are consistent with values of r_{\max} for P(MMA) given in Table 1. For $r = 70 \text{ nm} < r_{\max}$, shrinkage to full density occurs rapidly within 15°C of T_g . Similar kinetics are observed for $r = 243 \text{ nm} \sim r_{\max}$, but at slightly higher T . Porod analysis of the SAXS data (Figure 3) shows that the internal surface area (void surface) of sample B decreases about 1000-fold in 30 minutes at 80°C. However, for the larger particles (Fig.'s 2-C,D) only a fraction of the shrinkage occurs in the transition regime. The remainder requires $T > 130^\circ\text{C}$ and is presumed to occur by viscous flow.

Figure 4 shows SEM images of samples B-D following 10 minutes at 110°C, conditions intermediate between transition and terminal creep regimes. As predicted, for $r = 770 \text{ nm} > r_{\max}$ voids persist even in ordered domains. For $r = 380 \text{ nm}$, midway between the predicted range of r_{\max} , the voids appear to be eliminated in the ordered domains but persist in the disordered domains. Finally, for $r = 243 \text{ nm}$ few, if any, voids remain in either ordered or disordered domains.

*Expert technical assistance of
J. Buckholz, R.V. Davidson, & R.G. Raty is gratefully acknowledged.*

References

- 1 - D.J. Plazek, in "Methods of Experimental Physics", Vol. 16c, pp. 1-58, Academic Press, 1980; and J. Non-Cryst. Sol., **131-133**, 836 (1991).
- 2 - S. Mazur & D. J. Plazek, *Prog. Org. Coat.*, **24**, 225 (1994).
- 3 - A. Jagota & P.R. Dawson, *J. Am. Ceram. Soc.*, **73**, 173 (1990).
- 4 - K.L. Johnson, K. Kendall, & A.D. Roberts, *Proc. Roy. Soc., Lond. A*, **13**, 301 (1971).
- 5 - S. Mazur, in "Polymer Powder Technology", Chap. 8, M.Narkis, & N. Rosenzweig, John Wiley & Sons. Ltd., Chichester, 1995.

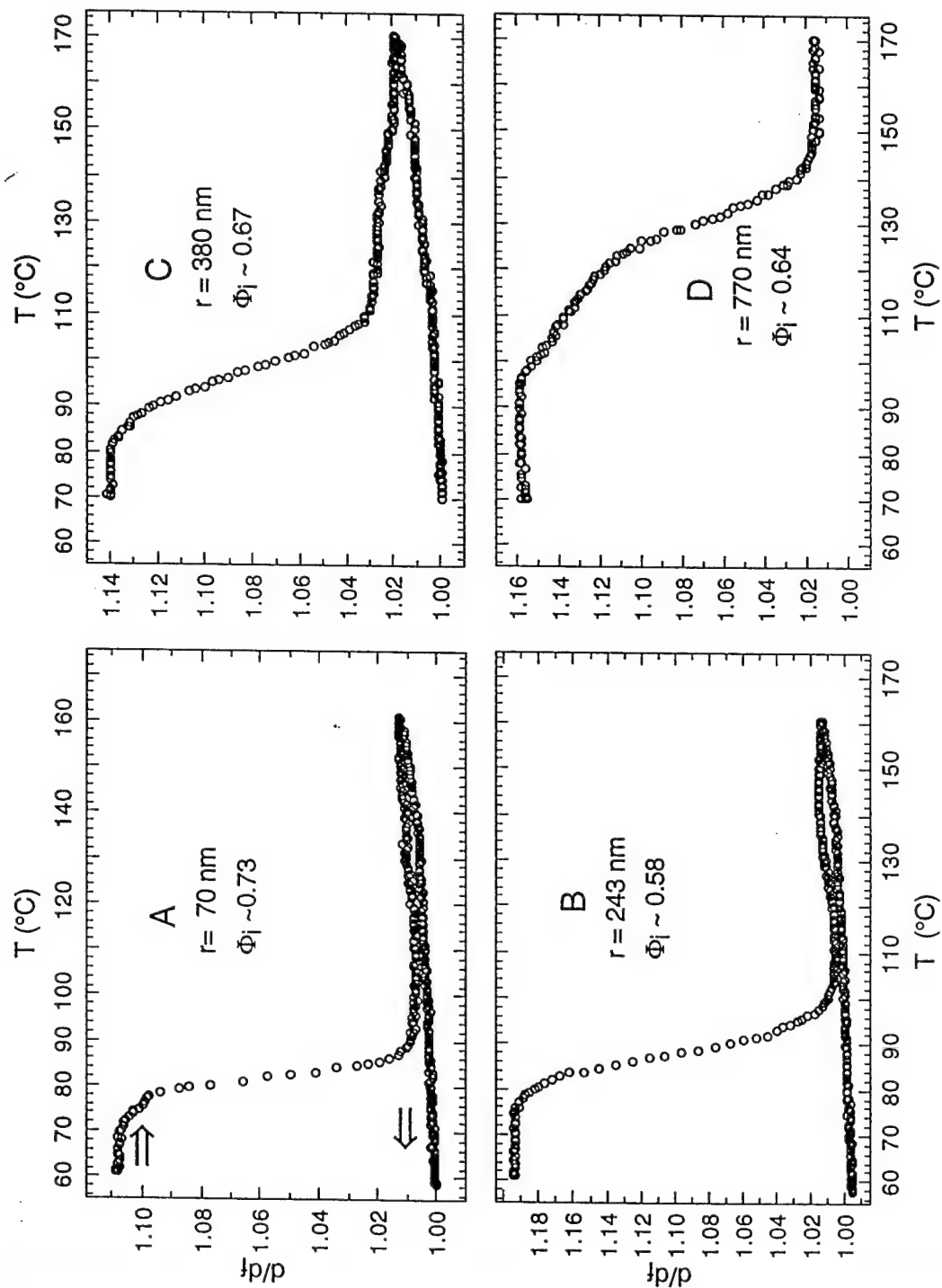
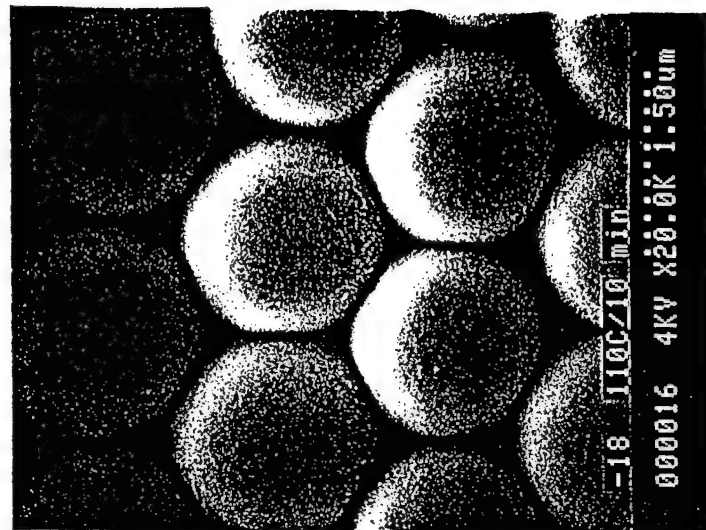
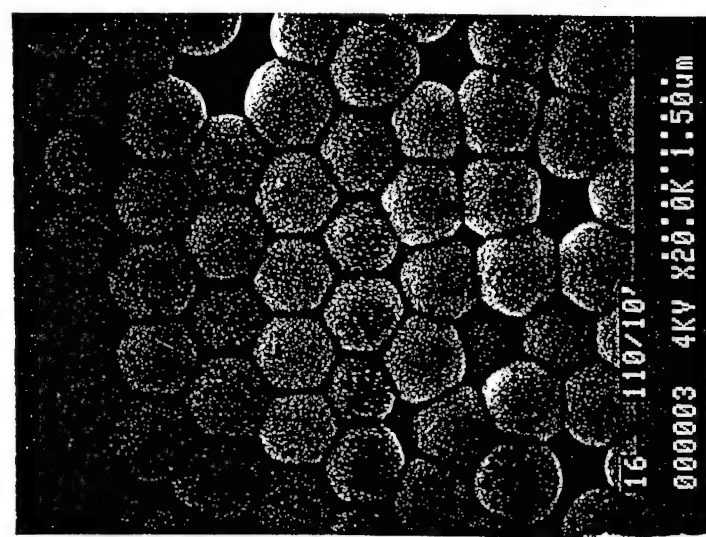


Figure 2 - Minimal-load thermomechanical analyses of colloidal acrylic aggregates heated and cooled at $10^{\circ}\text{C}/\text{min}$. $T_g = 77^{\circ}\text{C}$. Ordinate is the sample thickness normalized by final thickness of dense product.

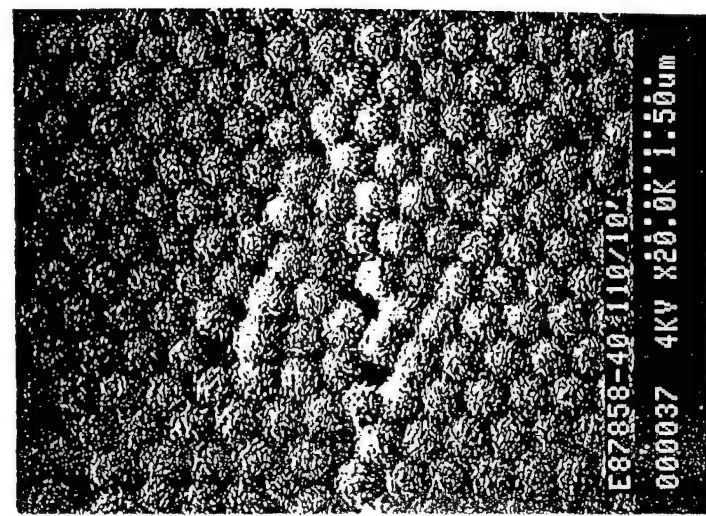
P(MMA/BMA/MAA) (48/48/4), T_g 78°C
annealed 10 minutes at 110°C



380 nm



770 nm



243 nm

Figure 4 - Scanning electron micrographs (SEM) of aggregates following conditions intermediate between transition and terminal regimes for viscoelastic creep.

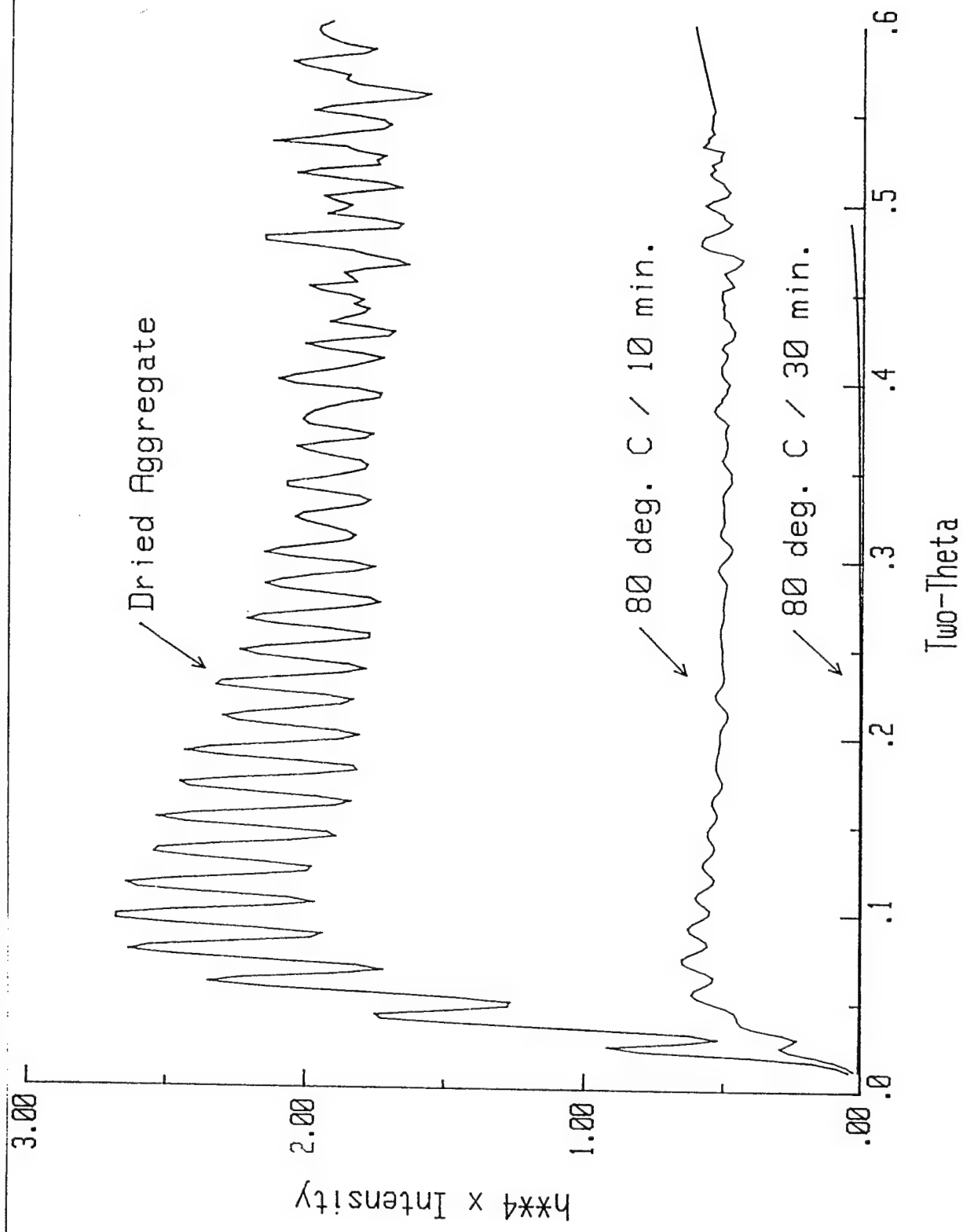


Figure 3 - Small angle X-ray scattering (SAXS) data for sample B ($r = 243\text{nm}$) before heating, and following 10 and 30 minutes at 80°C . The data have been desmeared and plotted in the Porod format, such that the magnitude at intermediate angles is proportional to internal surface area.

Parametric tip model and force-distance relation for Hamaker constant determination from atomic force microscopy

C. Argento and R. H. French

DuPont Co., Central Research, E356-317A, Experimental Station Wilmington, Delaware 19880-0356

(Received 8 July 1996; accepted for publication 14 August 1996)

Hamaker constants and dispersion forces interactions of materials are of increasing interest and the advent of atomic force microscopy (AFM) force measurements represents a new opportunity for quantitative studies of these interactions. A critical problem is the determination of a force-distance relation for realistic AFM probes. Due to the inadequacies of existing power-law sphere-plane models to describe the probe-sample system, we present a new parametric tip force-distance relation (PT/FDR). A surface integration method is developed to compute the interactions between arbitrarily shaped bodies. The method is based on the Hamaker pairwise integration in a continuous fashion, reducing the six-dimensional integration to a four-dimensional scheme. With this method, the PT/FDR is obtained and a nonlinear fitting routine is used to extract the model parameters and the Hamaker constant from AFM force-distance data. From the sensitivity analysis of the fitting of synthesized AFM force-distance data, one finds that, for large tip radius (compared to separation), the force is proportional to the product of the Hamaker constant and tip radius. Unique determination of the Hamaker constant can be achieved if a small radius tip is used in the AFM scan. By fitting to literature data, the effectiveness of the PT/FDR is shown. © 1996 American Institute of Physics. [S0021-8979(96)03422-6]

I. INTRODUCTION

The van der Waals force, which arises from the interaction of oscillating dipoles, has a role in controlling many aspects of the behavior of materials. It controls or influences macroscopic phenomena such as surface tension, wetting behavior, colloidal stability, fracture, and adhesion. The van der Waals interactions can be quantified through the Hamaker constant,¹ which is a material property, and through an appropriate force-distance relation, which is dependent on the system geometry.

The determination of the Hamaker constant is an important field of research. Ackler, French, and Chiang² provide a description of the different methods available to obtain the Hamaker constant for different materials and configurations. One technique is the observation of the manifestation of these interactions on a macroscopic scale, in a phenomenological approach. For example, the surface force apparatus³ has been used to determine the interaction force between crossed cylinders with surfaces of cleaved mica. Through an analysis such as the one presented by Hamaker,⁴ the expression for the total interaction force for the specific geometry and material configuration can be calculated. Following a fit of the force-distance relation obtained experimentally, the Hamaker constant is obtained. A similar and promising new approach is the use of atomic force microscopy (AFM), due to its intrinsic capability of measuring very small forces ($\sim nN$) at very small separations ($\sim nm$).

AFM is based on the determination of the interaction force between a probe and the substrate-sample. Different kinds of interactions may be present including electrostatic (Stern *et al.*⁵), magnetostatic (Martin and Wickramasinghe⁶), and van der Waals (Weisenhorn *et al.*⁷). The van der Waals interactions are omnipresent and, for a clean, uncharged, and nonmagnetic system, it can be the only force field present. In

a procedure similar to the one described for the surface force apparatus, the Hamaker constant can be determined. So far, due to the difficulty involved in the integration to obtain the interaction force, the probe has been erroneously modeled with simple geometries, such as a sphere. The use of such models has prevented the accurate determination of the Hamaker constant for systems of interest.

The problem to be resolved can be stated as one of integrating the interaction force over the volumes of an arbitrary probe and the sample and obtaining a correct force-distance relation. Developing such an integration scheme is the main goal of this work. Initially we present the problems involved in computing the interaction force between arbitrary bodies and discuss existing results for simple geometries. We then present a surface formulation to improve the efficiency and the precision of these calculations. Following, we present a parametric model for a typical AFM probe. The interaction of this probe with a planar half-space is obtained using the surface formulation presented. We then show that the traditional power-law relation used to describe the force-distance dependence of the interaction force is inadequate since the AFM tip-substrate force-distance relation (FDR) cannot be approximated by a power law. We then demonstrate that the parametric tip-substrate force-distance relation (PT/FDR) that we develop can be used to fit (nonlinear fit) experimental data and to determine both the tip parameters and the Hamaker constant for the material configuration.

II. INTEGRATION OF THE INTERACTION FORCE

The problem of integrating the pair interaction force to obtain the total force can be approached at many different levels: the quantum-mechanical interactions between atoms; the molecular dynamic level of many atoms; or the macro-

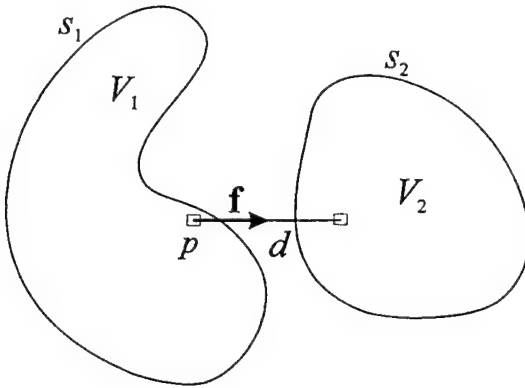


FIG. 1. Scheme for the integration of the interaction between two arbitrarily shaped bodies.

scopic (and continuous) scale. The last approach is the one used in the present work and imposes some restrictions in the dimensions of the bodies that can be considered. It is expected that it will be valid for bodies of sizes from several nanometers and larger.

Assume that the potential energy of interaction $w(d)$ is known for a pair of molecules as a function of the distance d of separation (pair potential). The interaction force between two molecules is then the gradient of the interaction potential, namely,

$$\mathbf{f} = -\nabla w. \quad (1)$$

For van der Waals interactions the potential is

$$w(d) = \frac{-C_{\text{disp}}}{d^6}, \quad (2)$$

where C_{disp} is the interaction constant as it was defined by London.⁸ In this work we adopt the usual convention that a negative force is attractive. Hamaker⁴ performed the integration of the interaction potential to compute the total interaction between macroscopic bodies. The hypotheses adopted by Hamaker were:

- additivity: the total interaction can be obtained by the pairwise summation of the individual contributions;
- continuous medium: the summation can be replaced by an integration over the volumes of the interacting bodies assuming that each "molecule" occupies a volume dV with a number density ρ ;
- constant material properties: the number density ρ and the interaction coefficient are constant over the volume of the bodies.

This latter assumption implies an atomically abrupt surface and that there is no retardation effects.¹⁹ Following this set of assumptions, the total interaction force between two arbitrarily shaped bodies, as shown in Fig. 1, is given by

$$\mathbf{F} = \rho_1 \rho_2 \int_{V_2} \int_{V_1} \mathbf{f}(d) dV_1 dV_2, \quad (3)$$

where ρ_1 and ρ_2 are the number densities of bodies 1 and 2. The Hamaker constant is then defined as

$$A = \pi^2 C_{\text{disp}} \rho_1 \rho_2. \quad (4)$$

The double volume integral (3) is very difficult to execute, both analytically and numerically. Hamaker⁴ obtained the interaction force for simple geometries (spheres and planar half-spaces). These geometries are of limited use, since they are not a good representation of the actual geometry involved in most physical problems.

A limited attempt to simplify the integration involved in this problem is the "Derjaguin approximation," developed by Derjaguin.⁹ He proposed that two general curved surfaces could be treated as two planar half-spaces, which limits its application to surfaces with small curvatures (compared to their separation). This is clearly not the case if one considers the scale involved in AFM. This fact is discussed in more detail in the following section.

III. SURFACE FORMULATION

Our approach to deal with the problem of the complexity of the six-dimensional integration is described in detail in Argento, Jagota, and Carter¹⁰ which is summarized in this section.

From Eqs. (3) and (1) one can write

$$\mathbf{F} = -\rho_1 \rho_2 \int_{V_1} \int_{V_2} \nabla w dV_1 dV_2. \quad (5)$$

Now, let \mathbf{G} be a vector field such as

$$\nabla \cdot \mathbf{G} = -w. \quad (6)$$

Then, replacing Eq. (6) into Eq. (5) and using the divergence theorem, a double-surface integral is obtained,

$$\mathbf{F} = \rho_1 \rho_2 \int_{S_1} \int_{S_2} (\mathbf{G} \cdot \mathbf{n}_1) \mathbf{n}_2 dS_2 dS_1, \quad (7)$$

where \mathbf{n}_1 and \mathbf{n}_2 represent the normals to bodies 1 and 2. This integral produces equivalent distributed tractions over the surface of body 1 that represents a weighted average of the influence of the surface of body 2. The effective tractions replaces the actual volume field resulting in the same total interaction force. The vector field \mathbf{G} is obtained from the interaction potential of two molecules (or two infinitesimal volumes in the continuous formulation). Considering the generic potential represented by a power law

$$w(d) = -C/d^m, \quad (8)$$

where $d = (\mathbf{x} \cdot \mathbf{x})^{1/2}$ and \mathbf{x} is the vector linking a point in body 2 to a point in body 1 (interacting infinitesimal volumes in the continuous formulation) and C is an interaction constant. From Eq. (6) the solution obtained for the function \mathbf{G} is

$$\mathbf{G} = \frac{C \mathbf{x}}{(3-m)(\mathbf{x} \cdot \mathbf{x})^{m/2}}. \quad (9)$$

Using the distributive property of the divergence, expression (9) can be used to represent any potential that can be described by a series of inverse powers of degree higher than 3. The major advantage of this formulation is that the volume integration (5), which is an integration over six dimensions of a potential of degree $-(m+1)$, can be reduced to Eq. (7), a four dimensions integration of a kernel of degree $-(m$

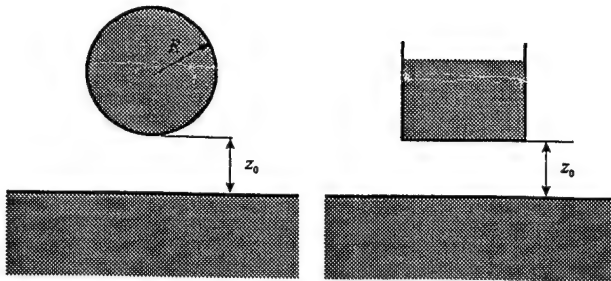


FIG. 2. Common geometrical models adopted for probe-sample system. z_0 is the separation and R is the tip radius.

– 1). This reduction in dimension and degree represents a clear advantage in analytical and numerical calculations. This surface formulation is currently being used to simulate the sintering of viscoelastic nanoparticles. It can also be used to deal with problems like adhesion, crack-tip deformations, and colloidal interactions.

IV. DEVELOPMENT OF A PARAMETRIC MODEL FOR A PROBE

Most previous work that tried to interpret the force–distance curves obtained from AFM experiments modeled the tip of the probe as a sphere or a plane surface, as shown in Fig. 2.^{2,11–14} However, the force–distance relation obtained from these models fails to describe the experimental observations. One possible reason for this fact is that the geometry proposed to describe the probe is not close to the actual one. Therefore, the force–distance relations, usually power laws, derived for these geometries are incorrect and not valid in the scale of AFM. Here we review the common sphere–plane model and present a more realistic parametric model for a typical AFM probe.

The force dependence in the case of the spherical tip and a flat sample is⁴

$$F = -\frac{2AR^3}{3z_0^2(z_0+2R)^2}, \quad (10)$$

where A is the Hamaker constant, z_0 is the separation between the sphere and the half-space surface, and R is the sphere radius. Assuming that the distance z_0 is small compared to the radius R , this relation is reduced to

$$F \approx -\frac{AR}{6z_0^2}. \quad (11)$$

This assumption is generally not valid if one considers the scale involved in AFM, where the tip radius can attain values of 5 nm and the separations are of the same order of magnitude. The use of Eq. (10) to describe the interaction is also erroneous, since it assumes that the sphere “floats” in space, by which we mean that its radius is large enough so that all the “nonspherical” parts of the probe are away from the region of strong interaction. The rate at which the transversal area of the probe increases with the distance from the sample has to be taken into account.

The model presented here is based on images of AFM probes obtained from scanning electron microscopy (SEM).

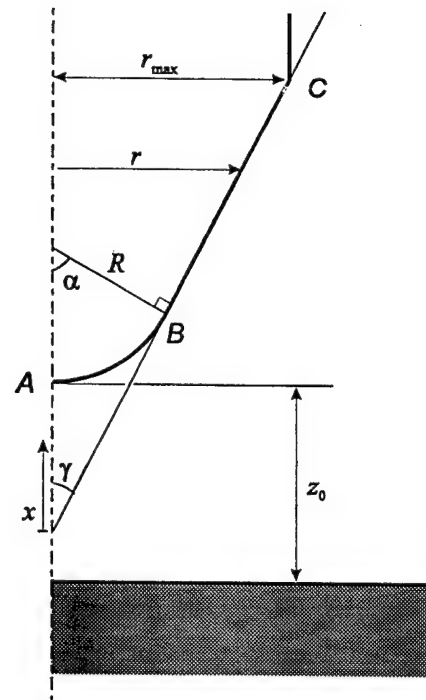


FIG. 3. Parametric tip model. R is the tip radius, r_{\max} is the radius of the cylindrical part of the probe, γ is the cone angle, $\alpha = \pi/2 - \gamma$ is the angle included in the spherical cap, z_0 is the probe–sample separation, r is the radius at any point on the surface, x is the distance from the cone apex, and A, B, and C define the spherical cap section and the conical section of the probe.

The spherical cap seems to be a good description of the tip of the probe, but the continuation of the probe should also be taken into account. Therefore, we adopt the model shown in Fig. 3. It consists of a cylinder followed by a conical section and a spherical cap. Such a model can be completely defined with three parameters: the tip radius R , the cone angle γ , and the macroscopic probe radius r_{\max} . Following we describe the integration of the interaction force for this geometry.

Let us assume that body 1 in expression (7) is the plane substrate and body 2 is the probe. We want to compute the vertical component of the interaction force, all other components being zero due to the symmetry of the problem. Therefore, $\mathbf{n}_1 = (0, 0, 1)$, and expression (7) becomes

$$\mathbf{F} = \frac{A}{\pi^2} \int_{S_2} H(z) \mathbf{n}_2 \, dS_2, \quad (12)$$

where

$$H(z) = \int_{S_1} \frac{-z}{(3-m)(x^2+y^2+z^2)^{m/2}} \, dx \, dy. \quad (13)$$

Integrating Eq. (13) over the appropriate limits for x and y , ($0 \rightarrow \infty$) yields

$$H(z) = -\frac{2\pi}{(3-m)(m-2)z^{m-3}}, \quad (14)$$

and, considering van der Waals interactions so that $m=6$,

$$H(z) = \frac{\pi}{6z^3}. \quad (15)$$

Since we are only interested in the vertical component of the force, we shall now integrate the vertical component of Eq. (12) over the surface of the probe. Integral (12) can be broken in two different contributions, as shown in Fig. 3: (1) the spherical cap and the remaining truncated cone. To obtain the contribution of the spherical cap first we write z as a function of z_0 and θ ,

$$z = z_0 + R - R \cos \theta. \quad (16)$$

From Eq. (15), $H(z)$ can be written as $H(\theta, z_0)$,

$$H^{sc}(\theta, z_0) = \frac{\pi}{6(z_0 + R - R \cos \theta)^3}, \quad (17)$$

where the superscript sc indicates the spherical cap. Since only the force along z is being considered, the component of the normal \mathbf{n}_2 along this direction is

$$n_{2z}^{sc} = -\cos \theta. \quad (18)$$

The infinitesimal element of the surface dS_2 on the spherical cap is

$$dS_2^{sc} = 2\pi r R d\theta = 2\pi R^2 \sin \theta d\theta. \quad (19)$$

The contribution of the spherical cap to the total force is

$$F_z^{sc}(z_0) = \frac{A}{\pi^2} \int H^{sc}(\theta, z_0) n_{2z}^{sc} dS_2^{sc}, \quad (20)$$

Substituting Eqs. (17), (18), and (30) into Eq. (20) and integrating over θ from 0 to α , where α is the angle included in the spherical cap, from point A to point B in Fig. 3, produces

$$F_z^{sc}(z_0) = \frac{AR^2(1-\cos \alpha)(R \cos \alpha - z_0 \cos \alpha - R - z_0)}{6z_0^2(R+z_0-R \cos \alpha)^2}. \quad (21)$$

$$F_z^{cone}(z_0) = -A \left(\frac{(r_{\max} - R \sin \alpha)[2Rr_{\max}(\cos \alpha - \cos 2\alpha) + 2r_{\max}z_0 \cos \alpha - 2R^2 \sin \alpha + R^2 \sin 2\alpha + Rz_0 \sin 2\alpha]}{12 \sin \alpha \tan \alpha (R+z_0-R \cos \alpha)^2 [r_{\max} + \cot \alpha (R+z_0-R \sec \alpha)]^2} \right). \quad (28)$$

It is generally reasonable to assume that r_{\max} is much larger than the other dimensions of the probe, therefore, taking the limit of Eq. (28) when $r_{\max} \rightarrow \infty$, we obtain

$$F_z^{cone}(z_0) = \frac{-A[z_0 \cos \alpha + R \cos \alpha - R \cos(2\alpha)]}{6 \tan \alpha \sin \alpha (z_0 + R - R \cos \alpha)^2}. \quad (29)$$

Replacing $\gamma = \pi/2 - \alpha$ we obtain

$$F_z^{cone}(z_0) = \frac{-A \tan \gamma [z_0 \sin \gamma + R \sin \gamma + R \cos(2\gamma)]}{6 \cos \gamma (z_0 + R - R \sin \gamma)^2}. \quad (30)$$

By making $R = 0$ in this expression, we obtain the expression for the force-distance relation of a sharp cone,

$$F_z^{cone}(z_0) = \frac{-A \tan^2 \gamma}{6z_0}. \quad (31)$$

By making $\alpha = \pi$ in the above expression we obtain relation Eq. (10). Replacing $\gamma = \pi/2 - \alpha$ in expression (21), we finally obtain

$$F_z^{sc}(z_0) = \frac{AR^2(1-\sin \gamma)(R \sin \gamma - z_0 \sin \gamma - R - z_0)}{6z_0^2(R+z_0-R \sin \gamma)^2}. \quad (22)$$

For the contribution of the truncated cone, first we write z as a function of r and z_0 ,

$$z = z_0 + R(1 - \cos \alpha) + \tan \alpha(r - R \sin \alpha). \quad (23)$$

From Eq. (15) and after simplification, $H(z)$ can be written as $H(r, z_0)$,

$$H^{cone}(r, z_0) = \frac{\pi \cot^3 \alpha}{6[r + \cot \alpha(R + z_0 - R \sec \alpha)]^3}. \quad (24)$$

The component of the normal \mathbf{n}_2 along z for the cone is

$$n_{2z}^{cone} = -\cos \alpha. \quad (25)$$

The infinitesimal element of the surface dS_2 on the cone is

$$dS_2^{cone} = \frac{2\pi r}{\cos \alpha} dr. \quad (26)$$

The contribution of the cone section to the total force is

$$F_z^{cone}(z_0) = \frac{A}{\pi^2} \int H^{cone}(r, z_0) n_{2z}^{cone} dS_2^{cone}. \quad (27)$$

Substituting Eqs. (30), (25), and (26) into Eq. (27) and integrating over r from $R \sin \alpha$ to r_{\max} , from point B to point C in Fig. 3, produces

V. PARAMETRIC TIP FORCE-DISTANCE RELATION (PT/FDR)

The total force on the probe, adding Eqs. (22) and (30),

$$F_z(z_0) = F_z^{cone}(z_0) + F_z^{sc}(z_0), \quad (32)$$

is

$$F_z(z_0) = \frac{AR^2(1-\sin \gamma)(R \sin \gamma - z_0 \sin \gamma - R - z_0)}{6z_0^2(R+z_0-R \sin \gamma)^2} + \frac{-A \tan \gamma [z_0 \sin \gamma + R \sin \gamma + R \cos(2\gamma)]}{6 \cos \gamma (z_0 + R - R \sin \gamma)^2}. \quad (33)$$

The assumptions made in the derivation of this expression are the same used by Hamaker (1937). Since there is no geometric assumption in this derivation, relation (33) gives exactly the force on the parametric probe if nonretarded Van

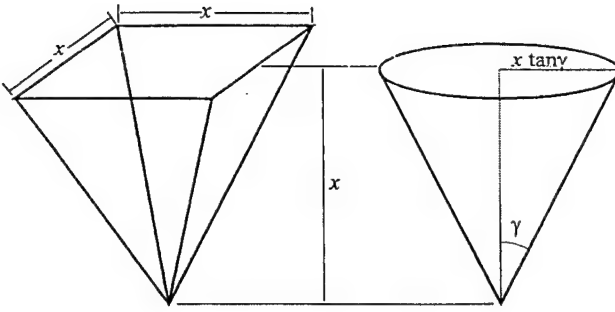


FIG. 4. Scheme for the cone with same transversal area as the pyramid probe with aspect ratio 1:1. x is the distance from the apex and γ is the cone angle.

der Waals interactions are the only interactions present. Unlike the simple power laws adopted in other works, PT/FDR does not assume that the curvature of the probe surface is small compared to the distance of separation between probe and sample. In the following section we compare PT/FDR with the traditional power-law models.

VI. ANALYSIS OF THE FORCE–DISTANCE RELATION

To determine the inadequacies of power-law models applied to AFM tips we compare them to the PT/FDR. A convenient way to do so is to analyze the force sensitivity to the distance of separation, which is the logarithmic slope of the force–distance relation. In the case of a power-law relation, the force sensitivity is identical to the exponent of the power law. The sensitivity is defined as

$$s(z_0) = \frac{\partial \ln[F_z(z_0)]}{\partial \ln(z_0)}. \quad (34)$$

The first case we are going to consider is the common pyramid probe. This probe has an aspect ratio of 1:1. The pyramidal geometry cannot be directly reproduced with the parametric model described in the previous section. To use the conical model, we should find an equivalent cone angle that will give the same transversal area for a given distance from the tip apex as for the pyramid.

In a pyramid with aspect ratio 1:1, the area of intersection of any plane parallel to the sample plane with the pyramid is simply x^2 , where x is the distance from the pyramid apex. In the cone geometry, this area is given by $\pi(x \tan \gamma)^2$, where γ is the cone angle as defined in Figs. 3 and 4. The cone angle where these two expression are equivalent is simply given by $\gamma = \arctan \sqrt{1/\pi} = 0.5137$. This geometry is shown in Fig. 4. In Fig. 5 we plot the evolution of the force sensitivity as a function of the distance z_0 from the sample plane for different tip radii and $\gamma=0.5137$. The force sensitivity of expression (10) (sphere–plane model) is also shown. Note that, except for large radii, the force sensitivity is not uniform over the distance. This implies that the power-law representation, even for the sphere–plane model, is not valid. In some extreme cases, as when the tip radius is small compared to the separation, there is strong variation in the force sensitivity. In Fig. 6 we plot the force-sensitivity as a function of the tip radius for the parametric model and for the

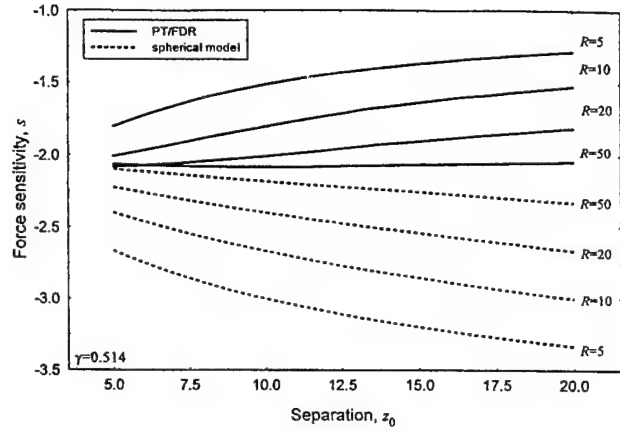


FIG. 5. Force sensitivity as a function of the separation for the PT/FDR and the spherical model for several radii R and probe angle $\gamma=0.514$. The radii and the separation are given in units of length.

sphere model for a fixed separation $z_0=10$ units of length. It is clear that for small tip radius the sphere model is completely wrong; however, there is some agreement in the large radius domain, which could be expected. These results should also be compared with the plane–plane model, with a force sensitivity of -3 , and with the sharp cone–plane model, expression (30), which has a force sensitivity of -1 . It is also clear that these models are unsuitable to describe the probe–sample interaction.

Another important aspect of this analysis is the sensitivity of the force–distance curve to each of the individual tip parameters. It is evident that the PT/FDR evolves toward the sphere model when the radius is increased, which can be verified in Figs. 5 and 6. The same is true in Fig. 7, where we plot the PT/FDR for several different tip radii and a fixed cone angle $\gamma=0.5137$. Note the near-constant slope for large radii and the varying slope for small radii. In the large radius domain, since the curves are parallel, the radius has a multiplicative effect on the PT/FDR, in the same way as the Hamaker constant. In Fig. 8 the PT/FDR is plotted for different cone angles and a fixed radius of 20 units of length. There is a slight change in the predicted force for small separations.

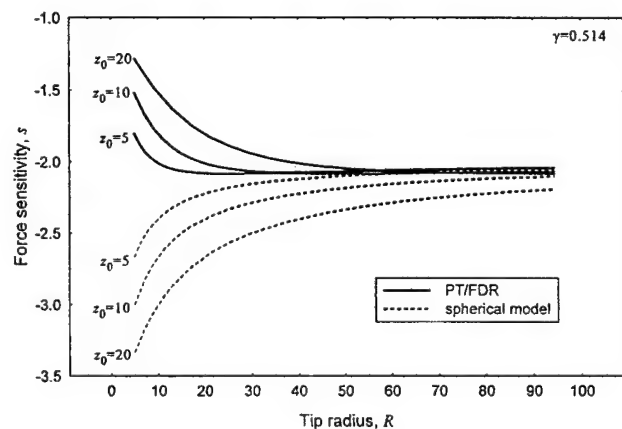


FIG. 6. Force sensitivity as a function of tip radius for the PT/FDR and the spherical model at several separations z_0 and probe angle $\gamma=0.514$. The radii and the separation are given in units of length.

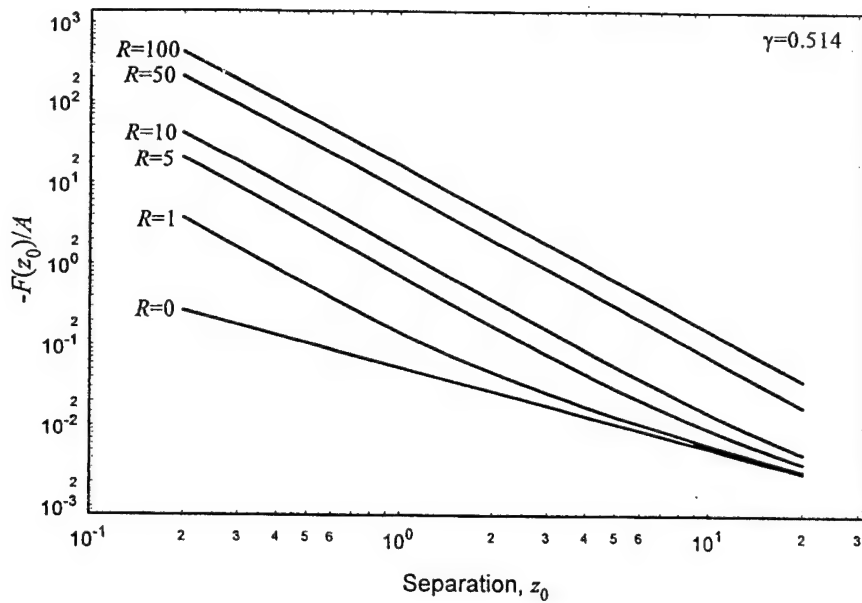


FIG. 7. Double log plot of the PT/FDR for several radii and probe angle $\gamma=0.514$. The radii and the separation are given in units of length. The vertical axis is the negative of force divided by the Hamaker constant and is given in inverse units of length.

On the other hand, at large separations, where the effect of the tip radius is diminished, the cone angle is the dominant parameter. This clearly divides the domains of importance of the parameters: close-range interaction controlled by the tip radius and long-range interaction controlled by the cone angle.

VII. NONLINEAR FITTING PROCEDURE

In this section we describe the nonlinear fitting procedure and the tests to evaluate its capability to predict the tip parameters and the Hamaker constant. Current experimental

data are inadequate to perform such evaluation since they usually contain a high noise-to-signal ratio and would lead to inconclusive results. Instead, we decide to use analytical data with artificial noise. In a first step, a number of random points is generated to represent the sampling in the distance of separation. For each of these points the force acting on the probe is calculated using the PT/FDR. The data produced this way are then perturbed by a random noise with controlled amplitude. Two cases were considered: no random noise and random noise from -10% to 10% of the maximum force on the data set. Finally, a nonlinear fitting routine is

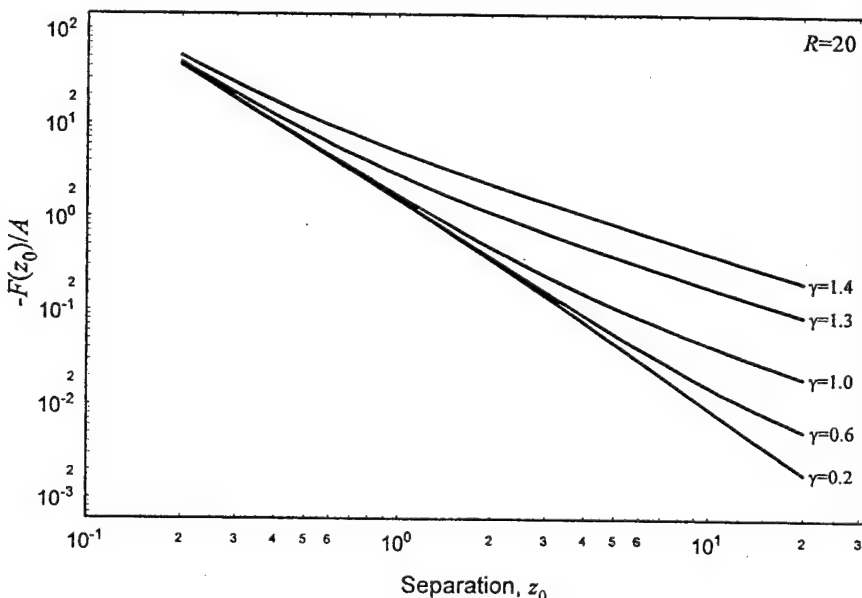


FIG. 8. Double log plot of the PT/FDR for several probe angles and tip radius $R=20$. The radii and the separation are given in units of length. The vertical axis is the negative of force divided by the Hamaker constant and is given in inverse units of length.

TABLE I. Values and errors extracted from the different fitting tests. The radius R is in units of length and the Hamaker constant A is in consistent units of energy.

	A	R	AR	γ
No noise, $R = 100$ fixed radius	$A \rightarrow 1.00$ $e = 0\%$	fixed, $R = 100$	$AR \rightarrow 100$ $e = 0\%$	$\gamma \rightarrow 0.514$ $e = 0\%$
No noise, $R = 100$ fixed angle	$A \rightarrow 0.90$ $e = -10\%$	$R \rightarrow 110.8$ $e = 10.8\%$	$AR \rightarrow 99.8$ $e = 2.5\%$	fixed, $\gamma = 0.514$
No noise, $R = 100$ all d.o.f.	$A \rightarrow 0.85$ $e = -15\%$	$R \rightarrow 118.0$ $e = 18\%$	$AR \rightarrow 99.7$ $e = -0.3\%$	$\gamma \rightarrow 0.412$ $e = -19.8\%$
10% noise $R = 100$ fixed radius	$A \rightarrow 0.99$ $e = -0.1\%$	fixed, $R = 100$	$AR \rightarrow 99.6$ $e = -0.4\%$	$\gamma \rightarrow -0.994$ $e = -293\%$
10% noise $R = 100$ fixed angle	$A \rightarrow 1.58$ $e = 58\%$	$R \rightarrow 62.82$ $e = -37.2\%$	$AR \rightarrow 99.3$ $e = -0.7\%$	fixed, $\gamma = 0.514$
10% noise, $R = 100$ all d.o.f.	$A \rightarrow 0.84$ $e = -16\%$	$R \rightarrow 117.1$ $e = 17.1\%$	$AR \rightarrow 98.0$ $e = 2.0\%$	$\gamma \rightarrow -0.324$ $e = -163\%$
No noise, $R = 5$ fixed radius	$A \rightarrow 1.00$ $e = 0\%$	fixed, $R = 5.00$	$AR \rightarrow 5.00$ $e = 0\%$	$\gamma \rightarrow 0.514$ $e = 0\%$
No noise, $R = 5$ fixed angle	$A \rightarrow 1.00$ $e = 0\%$	$R \rightarrow 5.00$ $e = 0\%$	$AR \rightarrow 5.00$ $e = 0\%$	fixed, $\gamma = 0.514$
No noise, $R = 5$ all d.o.f.	$A \rightarrow 0.98$ $e = 2\%$	$R \rightarrow 5.34$ $e = 6.7\%$	$AR \rightarrow 5.21$ $e = 4.2\%$	$\gamma \rightarrow 0.514$ $e = 0\%$
10% noise, $R = 5$ fixed radius	$A \rightarrow 0.99$ $e = -1\%$	fixed, $R = 5.00$	$AR \rightarrow 5.05$ $e = -1\%$	$\gamma \rightarrow 0.528$ $e = 2.7\%$
10% noise, $R = 5$ fixed angle	$A \rightarrow 1.03$ $e = 3\%$	$R \rightarrow 4.84$ $e = -3.3\%$	$AR \rightarrow 5.01$ $e = -0.2\%$	fixed, $\gamma = 0.514$
10% noise, $R = 5$ all d.o.f.	$A \rightarrow 1.04$ $e = 4\%$	$R \rightarrow 4.93$ $e = -1.3\%$	$AR \rightarrow 5.13$ $e = 2.6\%$	$\gamma \rightarrow 0.499$ $e = -2.7\%$

used to evaluate the parameters of the PT/FDR and these values are compared to the initial values used in the generation of the data. For the nonlinear fitting routine, we used the Levenberg–Marquardt method, as implemented in the MATHEMATICA® statistics package.¹⁵

Table I shows the results of the fitting procedure. The first set of data was constructed considering the separation from 2 to 20 units of length, a tip radius $R = 100$ units of length, the cone angle $\gamma = 0.5137$, Hamaker constant $A = 1$ unit of energy, and no random noise. Initially the tip radius was held fixed at the correct value and the Hamaker constant and the cone angle were the degrees of freedom. The fit for this case had an error of less than 0.1% for all the parameters. For the next case, where the angle was held fixed, there is a good prediction for the quantity AR . The values obtained for the Hamaker constant and the tip radius are within 10% of the correct values. When the three parameters were left as degrees of freedom, there is still a good agreement for the quantity AR , but then all the three parameters have an error of more than 10%. We notice here the effect discussed in the previous section, where the product between the Hamaker constant and tip radius is the governing parameter, when the tip radius is large. In the next set of data, a random noise going from -10% to 10% of the maximum force (calculated

at the minimum separation of 2 units of length) was added to each data point. The effect observed on the data without noise is repeated here. In all cases there is very good prediction for the quantity AR , even when all the parameters are degrees of freedom. Due to this fact, all the values for A and R that will satisfy the value for this quantity will produce good fittings. The prediction for the cone angle is very bad, even when the radius was held fixed. In the case of the large tip radius, the cone angle reflects only the information at long range and its contribution to the total force is very small, therefore being very difficult to fit. Figure 9 shows the noisy data set and the fitting for all three degrees of freedom. Notice the good fitting, even with bad predictions for A , R , and γ . This indicates that the system has redundancy, the only important parameter is the quantity AR .

The next set of data was generated under the same conditions except for the tip radius $R = 5$ units of length. The predictions for the three parameters in all cases are very good, including for the data set with noise. The contributions to the total force of the spherical and conical parts of the probe are equivalent, therefore being easier to fit. Also in this situation, the radius does not act as a multiplicative coefficient as was the case for the large radius data set. The quantity AR is not the governing parameter any more and the

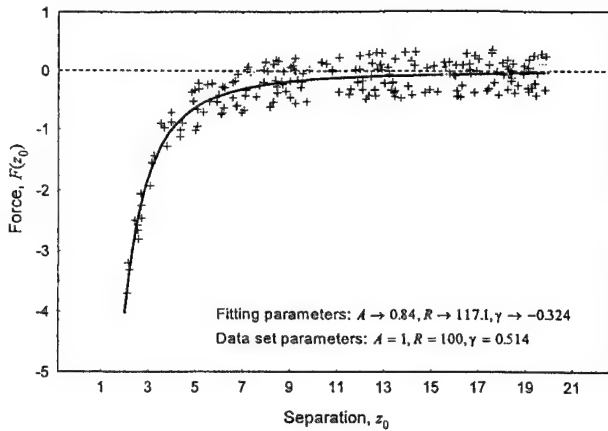


FIG. 9. Artificial data with random noise and the resulting fitting for the large radius case ($R = 100$ units of length).

individual parameters have equal importance. Figure 10 shows the noisy data set and the fitting for all three degrees of freedom. This time, a good fit and good prediction for the parameters were obtained, indicating that the system is not redundant.

From this set of tests we can conclude that the fitting procedure is very efficient to extract the parameters when the tip radius is of the same, or lower, order of magnitude as the separations where the measurements are being made. In the other case, a large tip radius, the cone angle is not an important parameter and only information on the quantity AR can be accurately extracted. This is true even for the noisy data tested.

VIII. APPLICATION OF THE FITTING PROCEDURE TO EXPERIMENTAL DATA

In this section the nonlinear fitting procedure described in the previous section is applied to two sets of experimental data. The first experiment considered was performed by Biggs and Mulvaney.¹³ They measured the force between a gold-coated AFM probe and a flat gold surface in water. The second experiment considered was performed by Ducker and

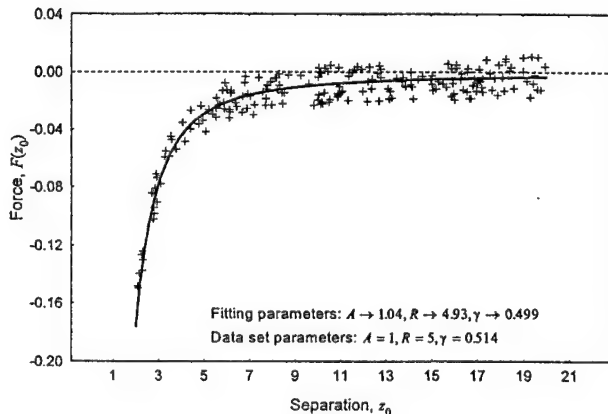


FIG. 10. Artificial data with random noise and the resulting fitting for the small radius case ($R = 5$ units of length).

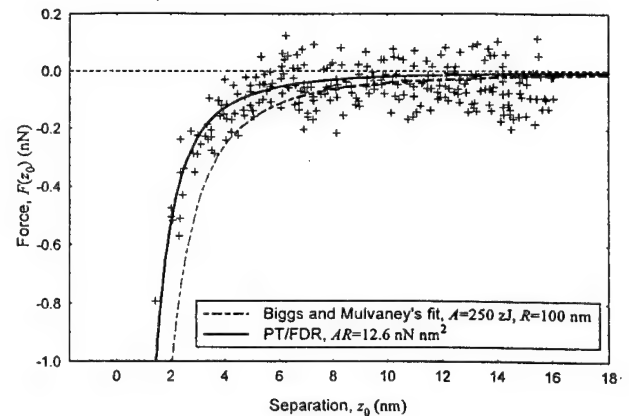


FIG. 11. Experimental data obtained by Biggs and Mulvaney (Ref. 13) and the different fittings proposed.

Clarke,^{14,16} where they obtained the force of on a silicon nitride probe interacting with a silicon nitride flat surface in water.

Biggs and Mulvaney performed two sets of experiments. In the first one, a gold-coated silica sphere was attached to the AFM cantilever. The final radius of the sphere was found to be $3.3 \pm 0.1 \mu\text{m}$. This radius places the sphere in the large radius domain and, considering the distances of separation sampled going from 9 to 100 nm, the traditional approach using the simplified power-law model can be used (except for the fact that retardation¹⁹ may be involved). The second experiment consisted of measuring the interaction force between an AFM probe coated with gold and a flat gold sample. The authors calculated an effective tip radius of 100 nm. The Hamaker constant for this configuration was obtained by Rabinovich and Churaev¹⁷ and ranges from 90 to 300 zJ, the value of 250 zJ being used by the authors as the best fit for their experimental data.

We analyzed the same experimental data under different conditions of fitting as it has been described in the previous section. The value of the force at small separations and the fact that the cone angle is a negligible parameter during the fitting indicates that the tip radius is large. Therefore, the cone angle was fixed at 0.514, which is characteristic of the cone equivalent to a pyramid with a 1:1 aspect ratio. This value had little effect on the final shape of the FDR. The values of the Hamaker constant and the tip radius fluctuated a lot under the different conditions of fitting, but we consistently extracted their product as being $12.6 \pm 0.3 \text{ nN nm}^2$. Figure 11 shows the experimental data, the fitting proposed by the authors, with a tip radius of 100 nm and a Hamaker constant of 250 zJ, and the fitting obtained with PT/FDR with $AR = 12.6 \text{ nN nm}^2$. With this value and a tip radius of 100 nm, the Hamaker constant calculated would be 126 zJ. It is clear that the curve plotted with these values is in very good agreement with the experimental data. The value of 126 zJ is within the limits obtained by Rabinovich and Churaev.¹⁷ The value of 100 nm was measured by the authors using an electrostatic method proposed by Drummond and Senden,¹⁸ where the probe is modeled as a sphere. Since the actual shape of the tip is not spherical and the value of

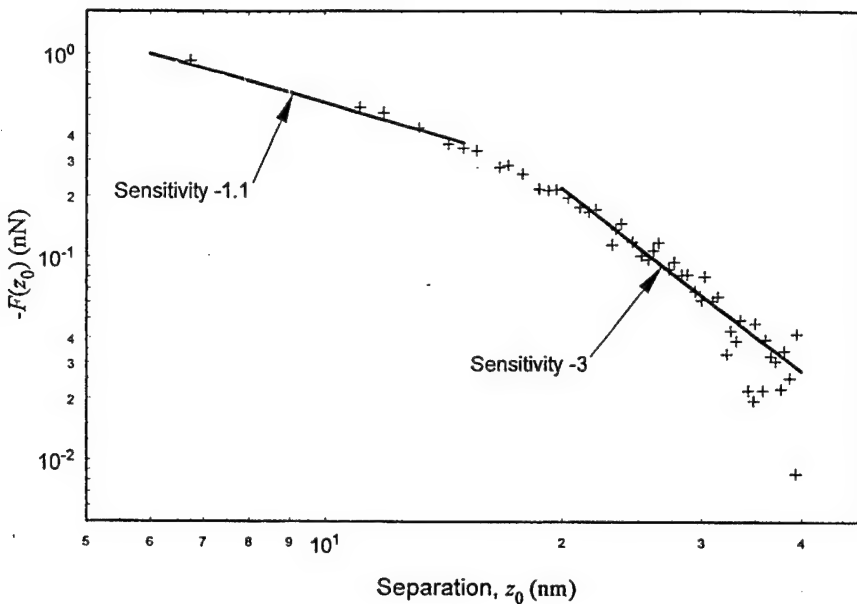


FIG. 12. Double log plot of the experimental data obtained by Ducker and Clarke (Ref. 14). The curves correspondent to force sensitivities -1.1 and -3 are also shown.

the effective tip radius given by the authors is not equivalent to the tip radius as defined in this work, some disagreement is expected.

The second set of experimental data considered here were obtained by Ducker¹⁶ as described in Ducker and Clarke.¹⁴ The data consist of force-distance points obtained with a silicon nitride probe and a flat silicon nitride sample in water, with separations ranging from 5 to 80 nm. The values for the Hamaker constant for this configuration reported in the literature range from 45 to 100 zJ.² There is no information given by the authors regarding the tip radius of the probe used; we expect it to be in the vicinity of the more common probes used today, which is 100 nm.

The first thing we notice in these data is the unusually high interaction force. With a pyramid probe and 100 nm tip radius and at the higher end of Hamaker constant for this material configuration, 100 zJ, the force calculated from PT/FDR would range from -6.37×10^{-2} nN at 5 nm to -2.20×10^{-4} nN at 80 nm. These values are far lower than the values obtained in the experiment, where the force at 5 nm is -9.26×10^{-1} nN. Another important feature of this data is its force sensitivity to distance (the log-log slope). Figure 12 shows the data in a double log plot. The sign of the force was inverted and only values representing separations from 5 to 40 nm are plotted. Notice in the figure the initial sensitivity of approximately -1.1 and its evolution to a value of -3 . This is not consistent with any of the dispersion force models described here. In the sphere model, the sensitivity ranges from -2 at close separations to -4 , which is representative of a molecule interacting with a halfspace. For the PT model the sensitivity goes from -2 at close separations to -1 at long range, which is representative of a sharp cone. There are several possible explanations for these facts. One possible cause is that the model presented here accounts only for the van der Waals forces. The model cannot repro-

duce the experiment if there is any other type of interaction present. That would be the case, for example, if other types of long-range interactions were present.

Another possible explanation for this fact is the wrong determination of the point of zero force and zero separation, what is a major problem in AFM experiments. To verify these effects, an offset was added to the distance of separation and to the total force in the PT/FDR. These two parameters were also used in the nonlinear fitting routine. In Fig. 13 the FDR thus obtained is plotted along with the data. This curve was obtained with an offset on the distance of 7.03 nm and on the force of 5.32×10^{-2} nN. As was the case with the previous example, the important parameter is the quantity AR , which was extracted as 1231 nN nm^2 . For a tip radius of 100 nm, the Hamaker constant would be 1.23×10^4 zJ, which is far greater than expected value for this material configuration.

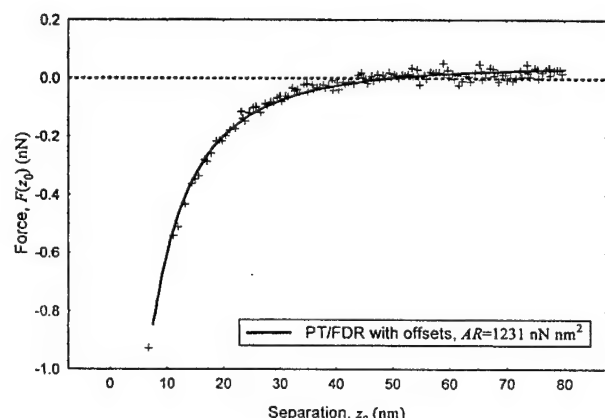


FIG. 13. Experimental data obtained by Ducker and Clarke (Ref. 14) and the fitting proposed.

IX. CONCLUSION

The main goal of this article was to introduce the force-distance relation for a realistic parametric tip, which has been successfully achieved in the form of the PT/FDR. Furthermore, the study on the numerically generated data set showed that, in the more common cases when the tip radius is large, the determination of Hamaker constant from the nonlinear fitting routine is compromised by the fact that the Hamaker constant and the tip radius are redundant parameters. In these cases, the angle of the conical part of the probe is irrelevant, especially when the data has a high noise-to-signal ratio at large separations. However, the same analysis showed that all the three parameters can be accurately extracted from the data if the tip radius is small. This is specially interesting since, in these cases, the sphere model is completely invalid. The nonlinear fitting routine is very efficient when there is no redundancy of parameters in the PT/FDR, as in the small radius regime.

The study performed on prior experimental data was not conclusive since both experiments were performed with large radius tips. In all cases we were able to produce extremely good fits to the data with the PT/FDR. The quantity AR was correctly extracted from the data set obtained by Biggs and Mulvaney¹³; however, it seems that experimental results presented by Ducker and Clarke¹⁴ cannot be accounted for by van der Waals force alone, even with the offset corrections introduced. The interaction forces in this experiment were extremely high to be described as van der Waals forces. We conclude that either there is an experimental problem or an extra attractive force.

More analysis is necessary from experiments with probes with smaller tip radius and smaller noise-to-signal

ratio. We could benefit from AFM force distance measurement in ultrahigh vacuum, where the Hamaker constant is usually large and the noise-to-signal ratio is, consequently, lower.

ACKNOWLEDGMENTS

The authors would like to acknowledge helpful discussion with D. Bonnell and W. A. Ducker. In addition, C.A. acknowledges the support of the AFOSR under Contract No. F49620-95-C-0008.

- ¹J. Israelachvili, *Intermolecular and Surface Forces*, 2nd ed. (Academic, San Diego, 1992).
- ²H. D. Ackler, R. H. French, and Y.-M. Chiang, *J. Colloid Interface Sci.* **179**, 460 (1996).
- ³D. Tabor and R. H. S. Winterton, *Proc. R. Soc. London* **312**, 435 (1969).
- ⁴H. C. Hamaker, *Physica (Amsterdam)* **4**, 1058 (1937).
- ⁵J. E. Stern, B. D. Terris, H. J. Mamin, and D. Rugar, *Appl. Phys. Lett.* **53**, 2717 (1988).
- ⁶Y. Martin and K. K. Wickramasinghe, *Appl. Phys. Lett.* **50**, 1455 (1987).
- ⁷A. L. Weisenhorn, P. K. Hansma, T. R. Albrecht, and C. F. Quate, *Appl. Phys. Lett.* **54**, 2651 (1989).
- ⁸F. London, *Trans. Faraday Soc.* **33**, 8 (1937).
- ⁹B. V. Derjaguin, *Kolloid Z.* **69**, 155 (1934).
- ¹⁰C. Argento, A. Jagota, and W. C. Carter (unpublished).
- ¹¹U. Hartmann, *J. Vac. Sci. Technol. B* **9**, 465 (1991).
- ¹²T. J. Senden, C. J. Drummond, and P. Kékicheff, *Langmuir* **10**, 358 (1994).
- ¹³S. Biggs and P. Mulvaney, *J. Chem. Phys.* **100**, 8501 (1994).
- ¹⁴W. A. Ducker and D. R. Clarke, *Colloids Surf. A* **94**, 275 (1994).
- ¹⁵MATHEMATICA®, Wolfram Research, Inc., telephone no. 1-800-441-6284.
- ¹⁶W. A. Ducker (personal communication).
- ¹⁷Ya. I. Rabinovich and N. V. Churaev, *Russ. J. Phys. Chem.* **52**, 256 (1990).
- ¹⁸C. J. Drummond and T. J. Senden (unpublished).
- ¹⁹R. H. French, R. M. Cannon, L. K. DeNoyer, and Y.-M. Chiang, *Solid State Ion.* **75**, 13 (1995).

accepted in *Journal of
The mechanics and physics
of solids*

Particle size limits for sintering polymer particles near T_g

S. Mazur, R. Beckerbauer, & J. Buckholz
DuPont Central Research & Development
Wilmington, Delaware 19880-0356

Abstract

We examine the spontaneous shrinkage of aggregates of amorphous polymer particles under surface tension as a function of temperature. The relative contributions of retarded elastic deformation and Newtonian viscous flow are considered in the context of the theory of adhesive contacts and explored in experiments on high molecular weight acrylic latex particles. The results confirm the existence of a maximum particle size and minimum packing fraction for rapid sintering at temperatures near the glass temperature T_g . Beyond these limits complete densification requires viscous flow or externally applied forces. Experimental measures of these limits for a series of acrylic copolymer colloids are in good agreement with theoretical predictions.

Draft I 11/27/96

In sintering, an aggregate of small particles spontaneously shrinks into a uniformly dense body when the intrinsic forces of surface tension deform the particles into space-filling shapes. Since these forces increase with the mean curvature of the contacting surfaces the rate of shrinkage generally increases with decreasing particle size, all other factors being equal. Herring[1] showed that for any simple mechanism of material transport, such as Newtonian flow, the sintering time should vary inversely as some characteristic power of the particle size. However, real materials often deform by more complex mechanisms[2]. For example all liquids display a viscoelastic response at very short times following application of a stress, so that the conventional Newtonian sintering model cannot describe the earliest stages of contact growth. Consideration of viscoelastic (i.e. time-dependent) mechanics is especially important for high molecular weight polymer melts because their viscoelastic compliance is large in magnitude and it remains independent of the Newtonian viscosity for many decades in time[3,4].

We examine here the particle size dependence of sintering for high molecular weight and cross-linked polymer colloid particles. We show that particle size plays is unique role as a consequence of the viscoelastic character of these materials. Specifically, for particles smaller than a certain size limit, sintering occurs entirely by retarded elastic deformation with no detectable contribution from viscous flow while for particles larger than this limit the sintering time becomes strongly dependent on viscosity. These kinetics represent dramatic deviations from Herring's scaling principle. An important practical consequence is that particles smaller than the limiting size sinter rapidly to full density at temperatures near the glass temperature T_g regardless of how high the molecular weight. Section I reviews an approximation based on the theory of adhesive contacts from which the limiting size may be predicted for several common polymers. These turn out to be in the regime of colloids generally accessible by emulsion polymerization. Experiments on both linear and cross-linked methacrylate copolymers prove to be in very good agreement with those predictions.

I - Viscoelastic growth of adhesive contacts between polymer particles

An earlier study[5] of contact growth driven by surface tension for macroscopic acrylic polymer spheres revealed the importance of viscoelastic deformation. Shown in Figure 1A are data for a sphere of radius 130 nm in contact with a flat film of the same

material. The early growth kinetics is much more rapid than predicted by numerical simulations for viscous sintering, yet it closely resembles the increase in $J(t)$, the viscoelastic shear creep compliance, measured independantly on bulk specimens of the same polymer (Figure 1B). Moreover, within the time interval corresponding to the early contact growth $J(t)$ was shown to be completely recoverable. Deformation in this time regime represents a time-dependent, retarded elastic response[3] which is completely independent of the Newtonian viscosity. The magnitude of the plateau in the growth kinetics could be predicted rather accurately from the theory of adhesive contacts due to Johnson, Kendall, & Roberts (JKR) [6] by substituting the experimentally determined recoverable compliance $J_r(t)$ for the equilibrium elastic compliance J_e in the model. (For reasons which are now understood[6] this approximation is not adequate to represent the kinetics in detail).

The rheological data in Figure 1B illustrates several features typical of amorphous, high molecular weight, linear polymers in general. At temperatures above the glass temperature T_g $J(t)$ can be generally be written as the sum of three terms[3]:

$$J(t) = J_0 + J_r(t) + t/\eta_0 \quad (1)$$

where J_0 is the elastic compliance of the glass ($<10^{-9} \text{ Pa}^{-1}$), $J_r(t)$ is the recoverable, or retarded elastic component, and t/η_0 is the contribution from Newtonian viscous flow. At temperatures near T_g $J_r(t)$ increases rapidly to the "plateau" value J_h (ca. 10^{-6} Pa^{-1} for the example shown). For polymer chains longer than the critical molecular weight M_e , J_h varies with the polymer structure but is independent of molecular weight[4]. Subsequent increases in $J(t)$ are modest until the terminal relaxation time τ when the retarded elastic response is overtaken by viscous flow, namely: $\tau = J_r \eta_0$. Since η_0 varies strongly with molecular weight (eg. $\eta_0 \propto M_w^{3.4}$) so too does τ . Consequently molecular weight has a significant effect on viscous sintering but should have no influence on the early stage of contact growth. (This expectation is consistent with experimental evidence[5]).

The surface tractions responsible for contact growth increase with decreasing particle size regardless of the deformation mechanism. But since retarded elastic deformation always precedes Newtonian flow, we expect that sufficiently small particles sintering should sinter completely (to uniform density) in times $\ll \tau$, that is with no contribution from viscous flow. As a practical matter, it is of interest to process materials

in the shortest times and lowest temperatures possible. Our objective is to identify the necessary and sufficient conditions for an aggregate of polymer particles to sinter rapidly at a temperatures near T_g . In this regime we may regard the maximum extent of deformation to be limited by the retarded elastic response of the melt which grows to the value of the plateau compliance J_N .

The extent of deformation required to fully densify an aggregate of spherical particles depends upon the initial packing fraction Φ_i . If all the particles have identical radius r and shrinkage occurs by a uniform decrease in the distances between particle centers (affine shrinkage), then the largest inter-particle contacts will develop between contacting neighbors in the original packing. The situation is illustrated in Figure 2.

As the packing fraction goes from Φ_i to 1, the center-to-center distance of these contacting pairs decreases from $2r$ to $2(r-\delta)$. This leads to the following geometric relation:

$$\frac{\Phi_i}{1} = \left(\frac{2(r-\delta)}{2r} \right)^3$$

$$\delta = r \left(1 - \Phi_i^{1/3} \right) \quad (1)$$

The relationship of the contact radius x_N to δ has been examined for a number of deformation mechanisms[7,8] and found to conform to the following empirical relation:

$$\frac{x_N}{r} \cong 1.56 \left(\frac{\delta}{r} \right)^{1/2} \quad (2)$$

Equations 1 and 2 provide an estimate of the contact radius required to achieve complete densification as a function of Φ_i , and r . For a simple elastic material we can use the classic theoretical results of contact mechanics to relate this deformation to the driving force. For example in the absence of any surface tension the required contact radius might be achieved by application of an external force F normal to each contact, and the magnitude of F may be calculated from Hertz's theory[9]. Dividing F by the cross-sectional area gives the minimum external pressure required to fully densify the packing in the absence of surface tension, namely:

$$P_{\min} = \frac{F}{\pi r^2} = 6.39 \frac{(1-\Phi_i^{1/3})^{3/2}}{J_e} \quad (3)$$

where J_e is the elastic compliance. More important for our purposes is the limiting condition where the surface tension γ provides the only driving force in the absence of any external loads ($F=0$). In that case the equilibrium contact area may be obtained from the JKR model[6] which yields the following estimate of the maximum particle radius:

$$r_{\max} = 0.47 \frac{\gamma J_e}{(1-\Phi_i^{1/3})^{3/2}} \quad (4)$$

Table 1 summarizes examples of P_{\min} and r_{\max} calculated for several common polymers where J_h has been substituted for J_e . Values of Φ_v were chose to be broadly representative of the aggregates obtained by drying un-flocculated dispersions of mono-disperse colloids. Thus $\Phi_v=0.58$ corresponds to the concentration at which particles in disordered "hard-sphere" dispersions lose mobility and develop solid-like properties[10], while $\Phi_v=0.74$ corresponds to ordered dense packings (fcc or hcp). While r_{\max} is predicted to be of colloidal dimensions in all cases, there are significant variations primarily as due to the variations in J_h .

In order to test these predictions experimentally, a series of acrylic colloids were prepared in particle sizes smaller, larger, comparable to the values of r_{\max} predicted for poly(methyl methacrylate). While the polymer used in these experiments is actually a co-polymer with butyl methacrylate and a minor fraction of methacrylic acid, the resulting differences in J_h and γ are likely to be smaller than the margin of error in the approximations.

II - Materials and Experimental Methods

The acrylic colloids were prepared by batchwise emulsion polymerization using established procedures. The larger particles were obtained by secondary growth of smaller "seed" particles. The properties are summarized in Table 1. In each case the particle size distribution was quite narrow, as reflected for example by less than 5%

non-exponential contributions to the auto-correlation function in quasi-elastic light scattering. Samples of the dispersions (25% solids) were allowed to dry on porous substrates at ambient temperatures to obtain aggregate coherent although fragile specimens about 1 cm in width, between 1 and 2 mm thick.

As shown by the scanning electron micrograph (SEM) in Figure 3, the particles remain spherical after drying and consist of both order dense domains and dis-ordered domains of a lower local density. On sintering these specimens become optically clear and mechanically tough. No bubbles are formed. Measurements before and after sintering confirmed that shrinkage in thickness and in-plane dimension were uniform. Accordingly, the difference between the initial thickness d_0 of the specimen and the thickness d_f of the fully dense sintered product may be used to estimate Φ_i :

$$\Phi_i / 1 = (d_f / d_0)^3 \quad (5)$$

Sintering kinetics was determined by thermomechanical measurements designed to minimize the effects of external forces. The sample was placed in a temperature-controlled hot stage its thickness was measured as a function of time and temperature by means of an optical displacement sensor (Fotonic Sensor, MTI instruments). The measurement requires a surface of constant reflectivity which was achieved by positioning a 2 mm sintered silver disk as optical target on the surface of the sample. The disk weighs about 2 mg, less than the mass of the sample itself. The net gravimetric pressure, ca. 16 Pa, is negligible compared to the P_{min} (Table 1) , so that the observed dimensional changes may be safely regarded as the consequence of intrinsic surface tractions.

III - Results and Discussion

Figure 4 shows thermomechanical analysis (TMA) and differential scanning calorimetry (DSC) measurements on specimens of the smallest particles ($r=70$ nm) heated at 10°C/minute. TMA results are also shown during cooling at the same rate. DSC shows the decrease in heat capacity at T_g accompanied by an overshoot typical of an aged glassy material. A very slight exothermic peak is also evident at about 82°C. The appearance of such exotherms during the first heating of a polymer colloids was first noted by Mahr[11] whose quantitative measurements supported the conclusion that they correspond to the loss of surface free-energy during sintering. Indeed the TMA

results show that densification occurs completely between 68 and 94 °C. The reversible linear changes in dimensions at higher temperatures simply reflects the coefficient of linear expansion of the melt (ca. $2 \times 10^{-4}/^{\circ}\text{C}$).

Figure 5 shows TMA results for particles for both linear and cross-linked particles with $r \sim 200\text{nm}$, just below the value of r_{\max} predicted for disordered aggregates (250 nm). Sintering again occurs in the vicinity of T_g (74-97°C), about 2°C higher than for $r=70\text{ nm}$. The most striking feature is that cross-linking has no detectable effect on the rate (or temperature regime) for sintering. This validates the conclusion that viscous flow makes no detectable contribution to sintering in this temperature regime. The role of viscous flow does becomes apparent at still larger particle sizes.

Figures 6A and 6B show respectively TMA measurements for linear polymers with $r=380\text{ nm}$ and $r=770\text{nm}$. The former is midway between values of r_{\max} predicted for disordered and ordered dense aggregates while the latter is larger than r_{\max} regardless of packing density. In both cases the TMA experiments show some shrinkage just above T_g , but a significant fraction occurs in a second stage at much higher temperature (the major fraction for $r=770\text{nm}$). We attribute this secondary sintering to viscous flow. The fact that it requires higher temperatures for the $r=380\text{nm}$ specimen is consistent with the fact that the weight average molecular weight of that sample is more than twice that of the $r=770\text{nm}$ sample. While these observations are in accord with the theoretical predictions, additional information is revealed by the morphology.

To further distinguish the high temperature sintering from that which occurs near T_g , samples were heated at 110°C for 10 minutes, intermediate between these regimes, then cooled and examined in by SEM. Figure 6 shows results for three different particle sizes of the linear (uncross-linked) polymers. At $r=243\text{ nm}$ the outline of individual particle are still distinguishable on the surface but deformation appears to be sufficient to fill space in the dense packed domains. There appear to be a few gaps remaining in the disordered domains but it is doubtful that their volume is sufficient to be detected by the TMA experiments ($\pm 1\%$). For $r=380\text{ nm}$ the distinction between fully deformed particles in the dense packed domains and open pores in disordered domains is clearly distinguished and in excellent agreement with the fact that these particles fall between the predicted values of r_{\max} (250 and 570 nm). Likewise consistent is the

observation, for $r=770$ nm that at intermediate temperatures sintering is clearly incomplete even in hexagonally close-packed domains.

In order to determine the maximum extent of elastic densification which may occur in the absence of viscous flow, aggregates of the larger cross-linked particles were annealed at much higher temperatures and examined by SEM. As shown in Figure 7, densification is nearly complete for $r=453$ nm following 10 minutes at 130°C , but remains incomplete for $r=568$ nm following 10 minutes at 170°C . It should be noted that the elastic compliance for the cross-linked particles at these temperatures may exceed J_n since $J_r(t)$ generally grows somewhat at times and/or temperatures far above the glass relaxation[3]. Nevertheless these results confirm that the simple approximations of Section I provides a reliable prediction of the limiting conditions for elastic sintering.

IV - Mixed Particle Sizes

It is well recognized particle aggregates with a wide range of particle sizes may be organized into much denser packings than those of uniform particle size. To the extent that sintering conditions depends on Φ_i (eq's. 3 & 4) this should combination of particles sizes should provide an advantage. To explore this effect, a mixed specimen was prepared from equal weights (equal volumes) of $r=70$ nm and $r=770$ nm particles. Figure 9 shows SEM results for this mixture and TMA results in comparison with the pure components. As expected, for the mixture is significantly greater than for the pure components (0.79 versus 0.64 and 0.68). SEM shows how effectively the small particles fill in the gaps between large particles. The change in sintering kinetics is striking in that the mixed specimen sinters almost entirely near T_g , as if the large particles played no role in the process.

V - Summary

An approximate analysis of sintering in aggregates of spherical particles by elastic deformation was used to predict limiting combinations of particle size and packing density within which high molecular weight polymers may sinter to full density at temperatures near T_g without any contribution from viscous flow. Experimental measurements of sintering rates and temperatures, and SEM of the resulting morphologies for linear and cross-linked acrylic colloids are in excellent agreement with

these predictions. It was shown that mixtures of large and small particles can overcome the limitations in sintering kinetics of the large particles

Acknowledgment

Particle size measurements by quasi-elastic light scattering were provided by Dr. Richard J. Flippen. Electron microscopy was performed by R. Gail Raty.

References

- 1 - C. Herring, *J. Appl. Phys.*, **21**, 301 (1950).
- 2 - F.B. Swinkels & M.F. Ashby, *Acta Metallurgica*, **29**, 259 (1981).
- 3 - D.J. Plazek, Chap. 11, in *Methods of Experimental Physics*, Vol. 16c, Academic Press, 1980.
- 4 - J.D. Ferry, *Viscoelastic Properties of Polymers*, 3rd edition, John Wiley & Sons, 1980.
- 5 - S. Mazur & D.J. Plazek, *Prog. Org. Coat.*, **24**, 225 (1994).
- 6 - C. Argento, S. Mazur, & A. Jagota, in *Sintering Technology*, pp. 21-28 edited by German, Messing, & Cornwall, Marcel Dekker, Inc., 1996.
- 7 - Jagota & Dawson
- 8 - Jagota, Argento, & Mazur
- 9 - H. Hertz, *Miscellaneous Papers* (1869), Macmillan, London.
- 10 - P.N. Pusey, Course 10 in *Liquids, Freezing, and Glass Transition*, Les Houches Session LI, 1989, edited by Hansen, Devesque, Zinn-Justin, Elsevier B.V., 1991.
- 11 - T.G. Mahr, *J. Phys. Chem.*, **74**, 2160 (1970).

Tables

Table 1 - Predictions of minimum pressure and maximum particle radius for densification of aggregates of elastic spheres respectively by externally applied force or surface tension.

Table 2 - Summary of acrylic colloids used in the study.

Figure Captions

Figure 1 - Mazur Plazek data (reference 5)

Figure 2 - Schematic illustration of the relationship deformation of contacting spheres required to achieve full density.

Figure 3 - Representative example of dried colloidal specimen before sintering.

Figure 4 - Thermo-mechanical analysis (TMA) and differential scanning calorimetry (DSC) of the smallest particles heated and cooled at 10°C/minute.

Figure 5A,B- TMA of similar sized particles for both linear and cross-linked polymer with dimensions below the predicted values for r_{max} .

Figure 6 A,B, - TMA for particles $r=380$ nm and $r=770$ nm.

Figure 7 - SEM following sintering for 10 minutes at 110°C.

Figure 8 - SEM of larger cross-linked colloids at the indicated conditions

Figure 9 - TMA for mixture of $r=70$ nm and $r=770$ nm particles (equal volumes).

Limits for Densification of Elastic Spheres

Polymer	J_n (MPa ⁻¹)	γ (mN/m)	P_{min} (MPa) $\Phi_V = 0.58 - 0.74$	r_{max} (nm) $\Phi_V = 0.58, 0.74$
Poly(ethylene)	0.44	27	0.98 - 0.43	83 - 190
Poly(tetra-fluoroethylene)	0.60	10	0.72 - 0.32	42 - 97
Poly(styrene)	4.90	31	0.09 - 0.04	1,100 - 2,500
Poly(butadiene)	1.62	19	0.27 - 0.12	210 - 500
Poly(methyl methacrylate)	1.15	31	0.37 - 0.17	250 - 570

Mono-Disperse Acrylic Lateces

R. Beckerbauer & J. Buckholz

P(MMA/BMA/MAA)
(48/48/4)

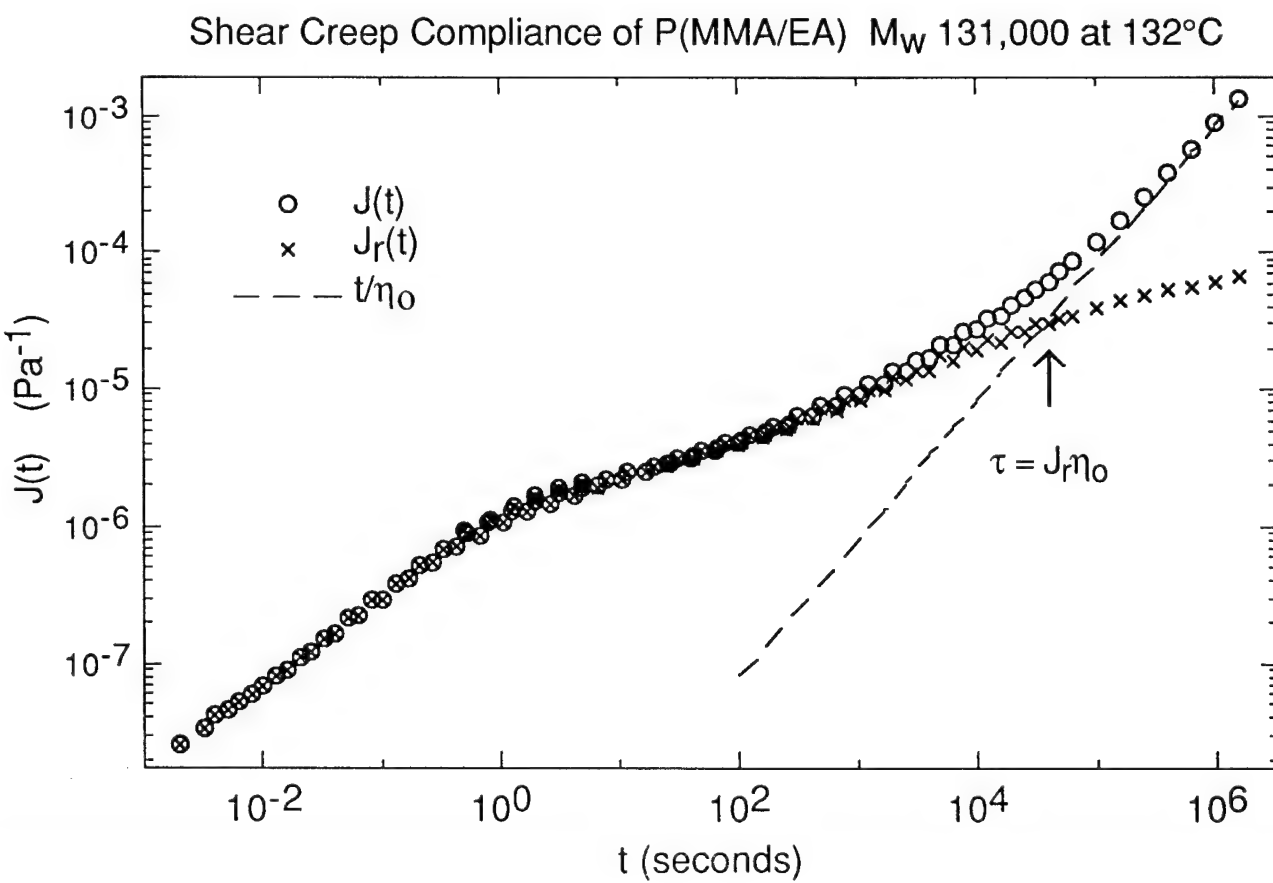
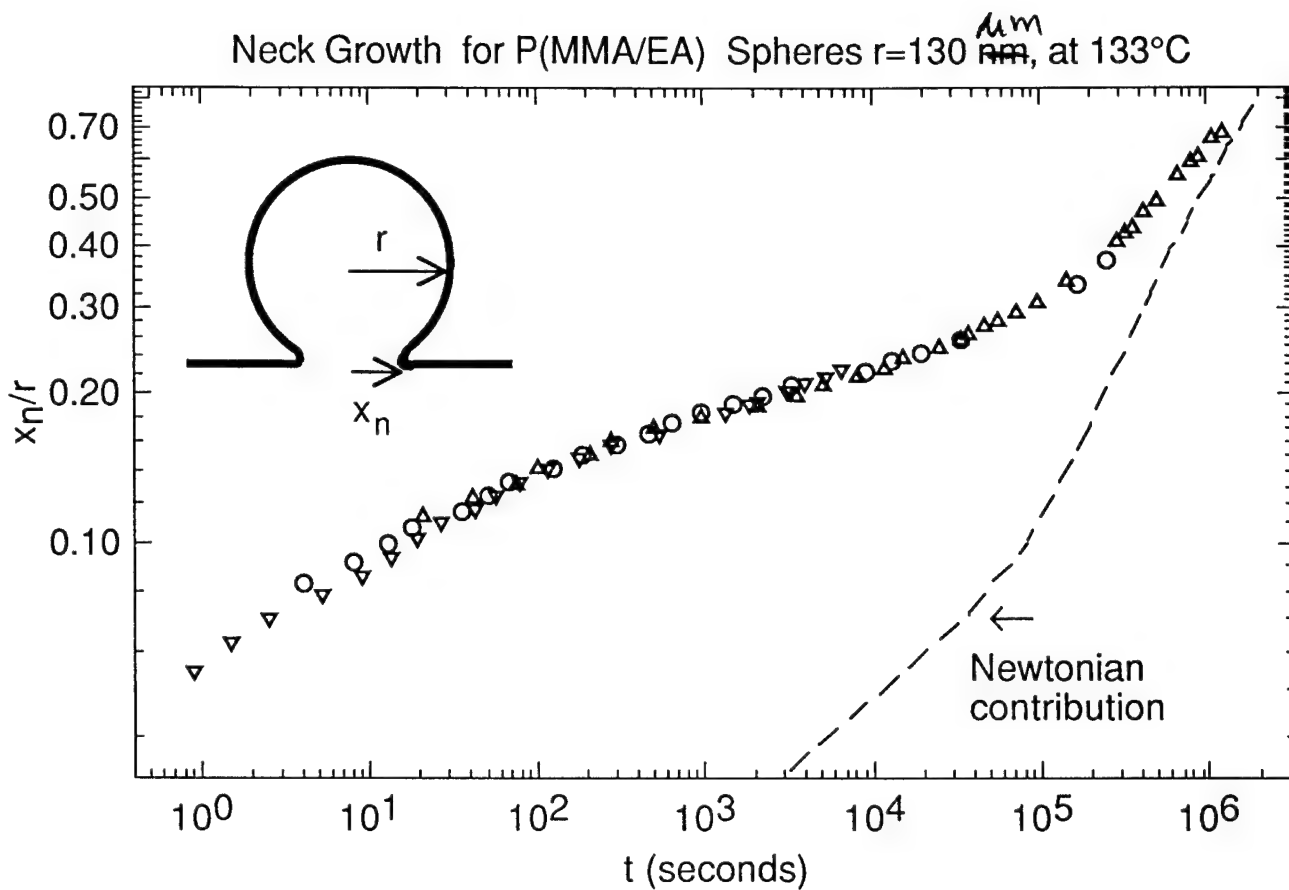
r_h nm	M_w $\times 10^{-3}$	M_n/M_w	T_g °C
70	334	5.5	79
243	356	11	77
380	695	2.9	76
770	282	2.8	74

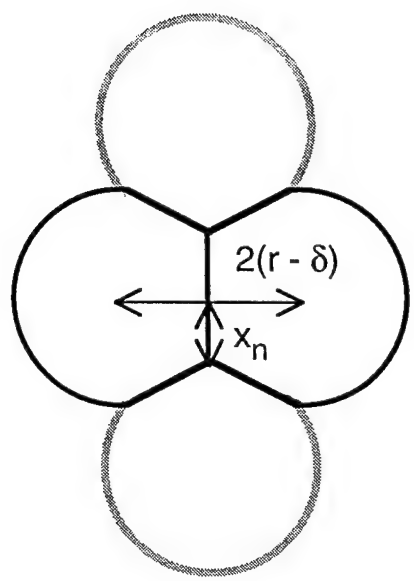
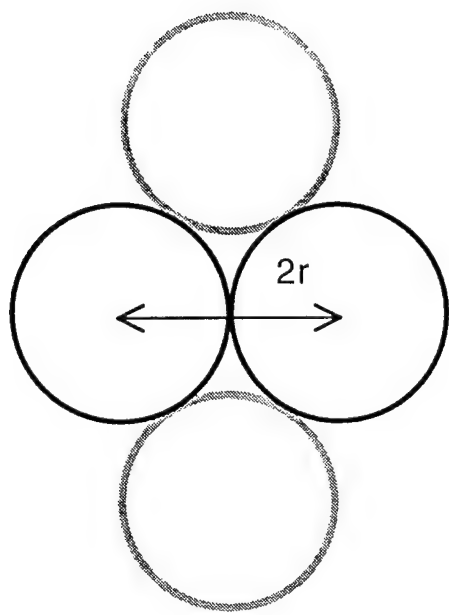
P(MMA/BMA/MAA/EGDA)
(44.6/44.6/4.7/0.5), Crosslinked

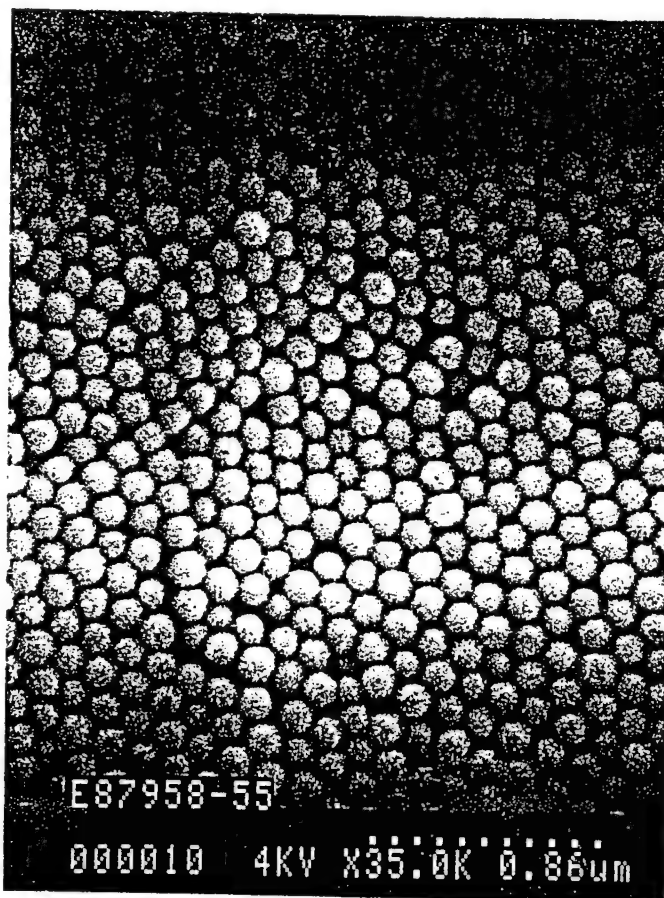
$r_h = 190$ nm

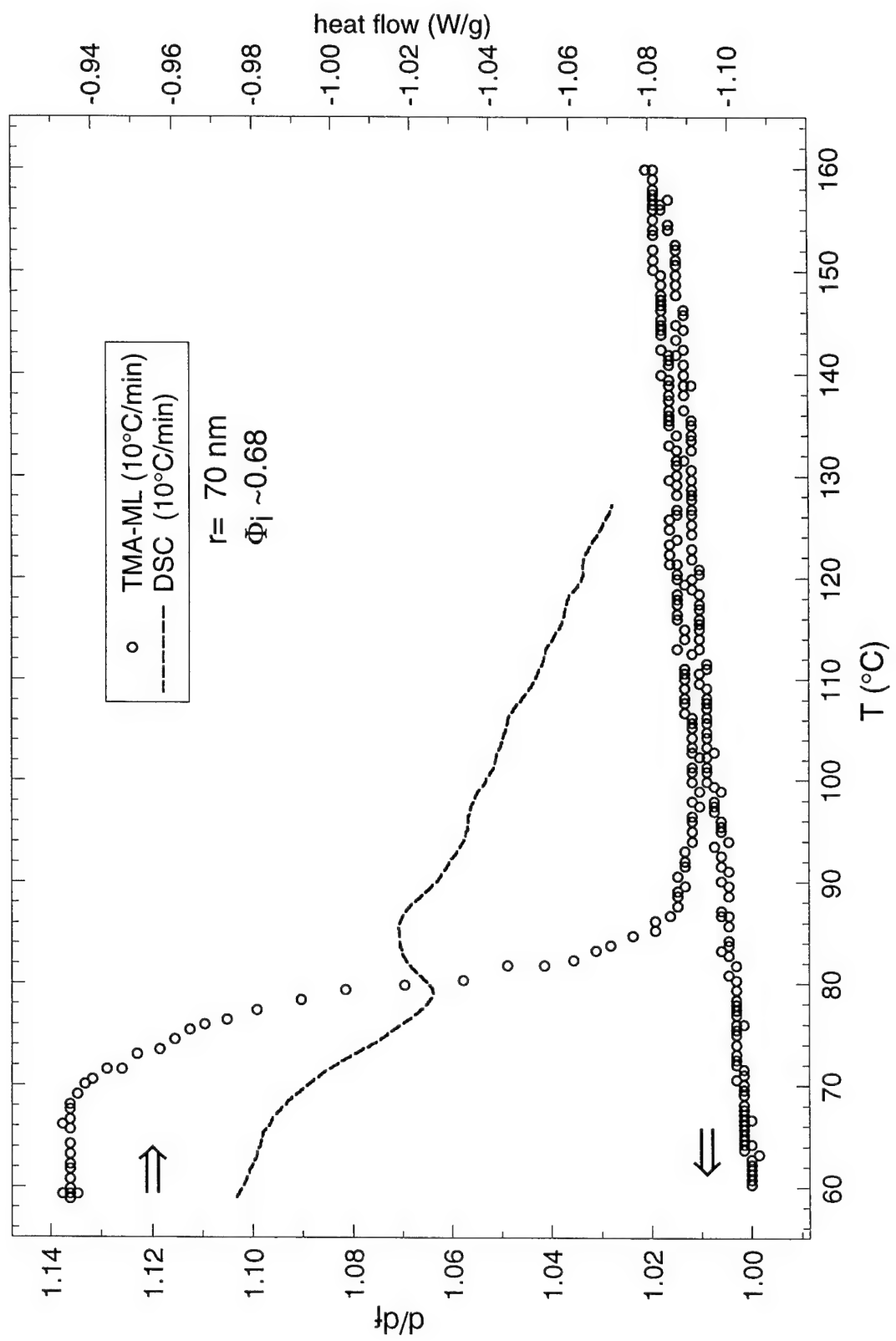
450

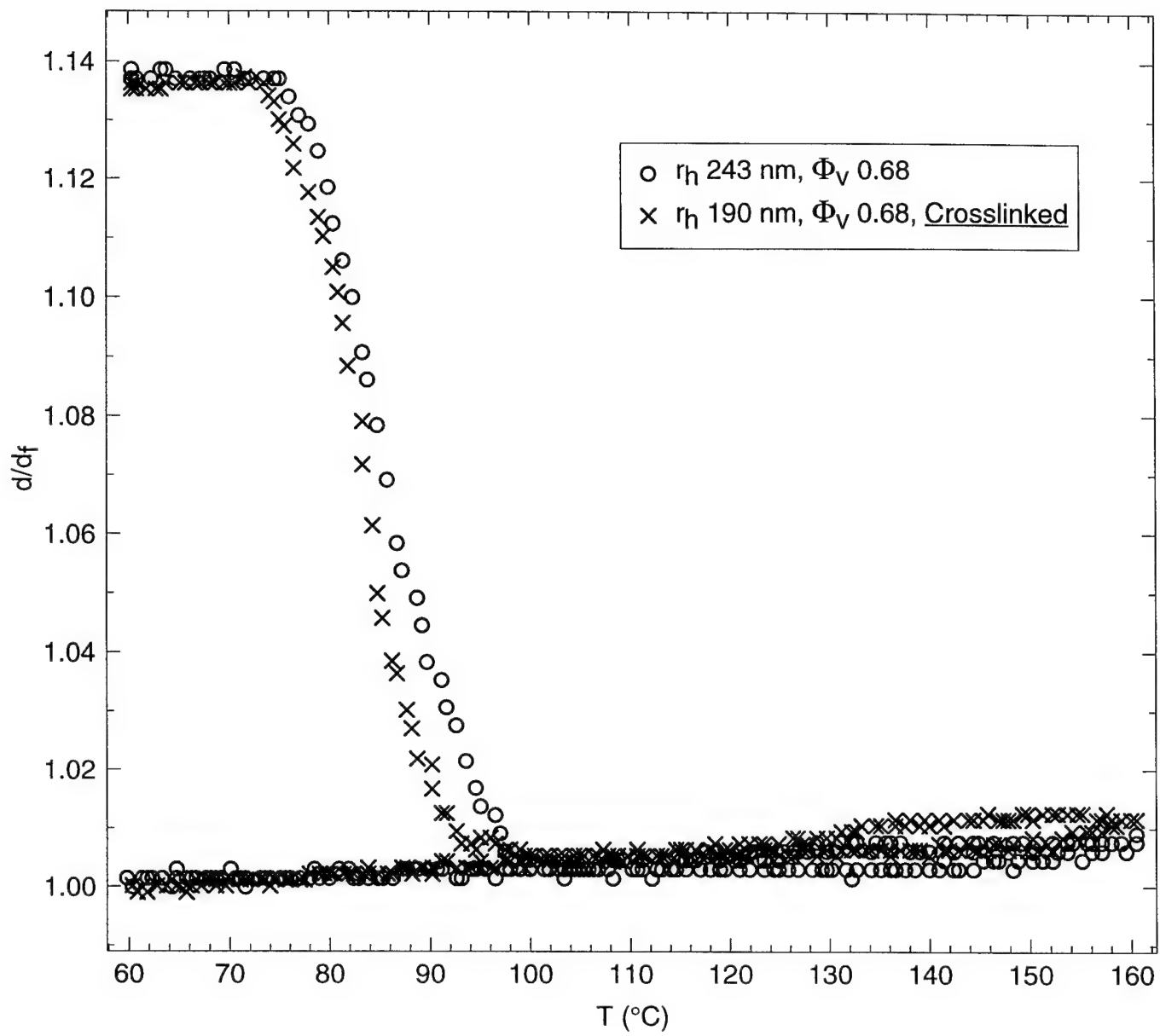
568

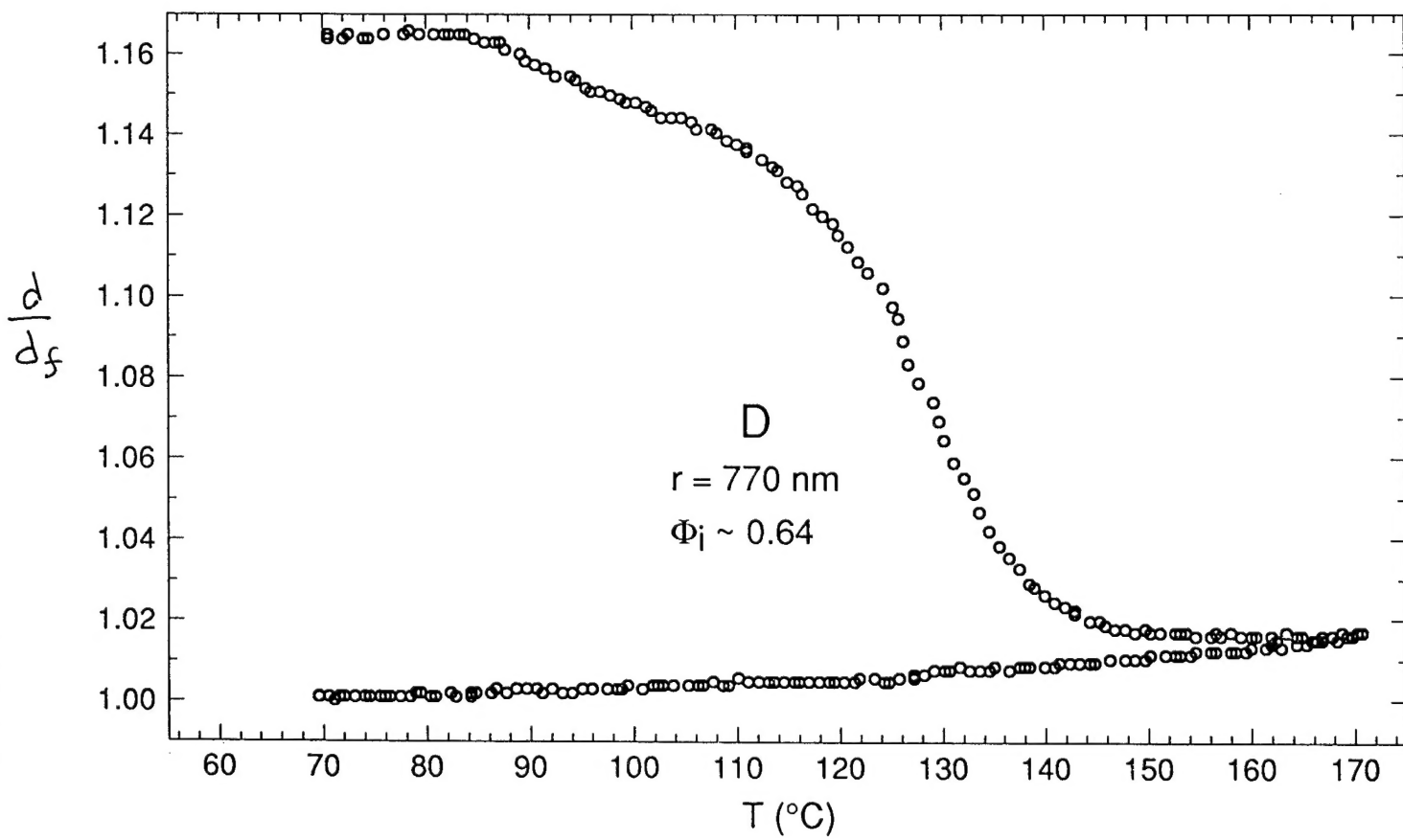
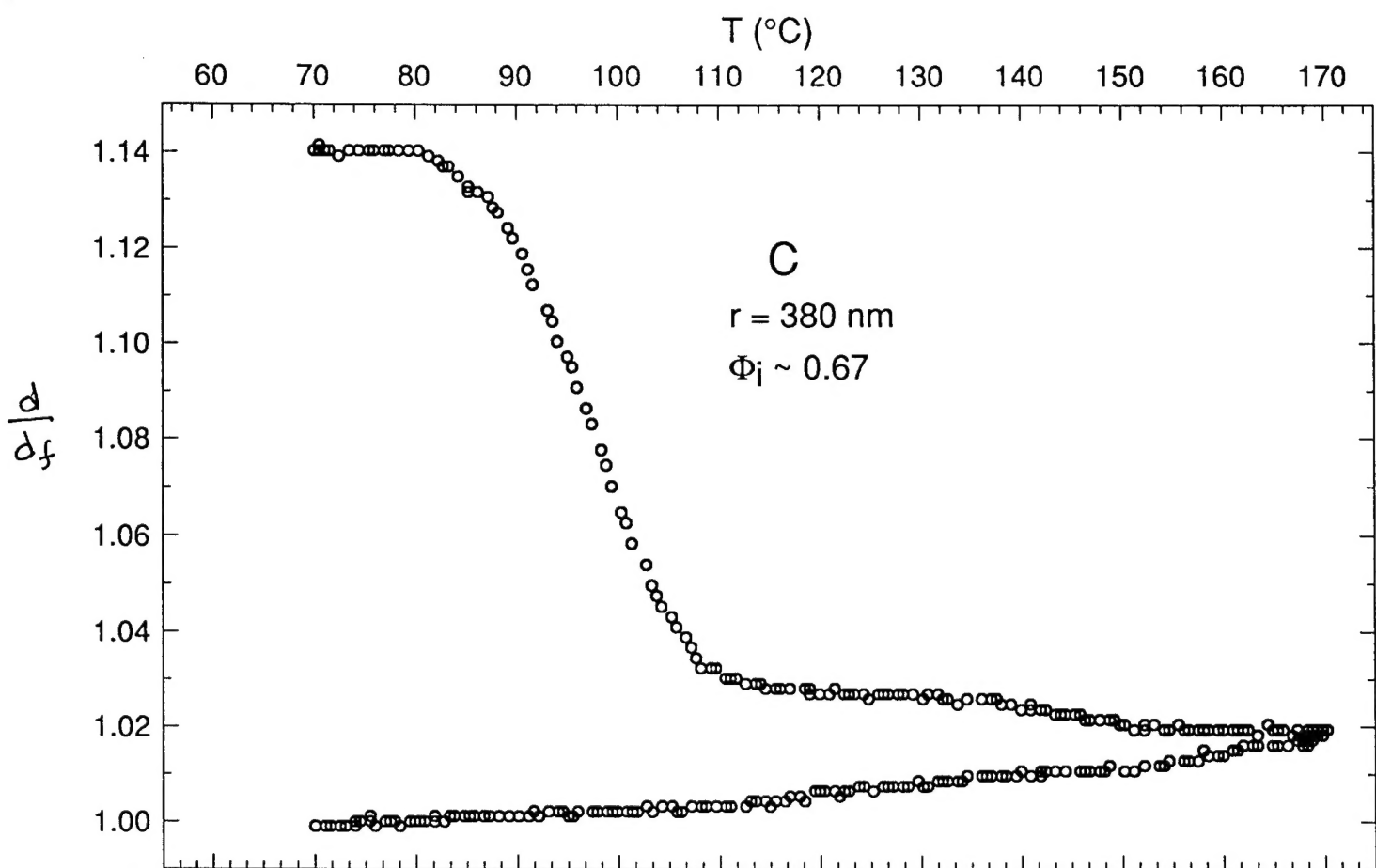




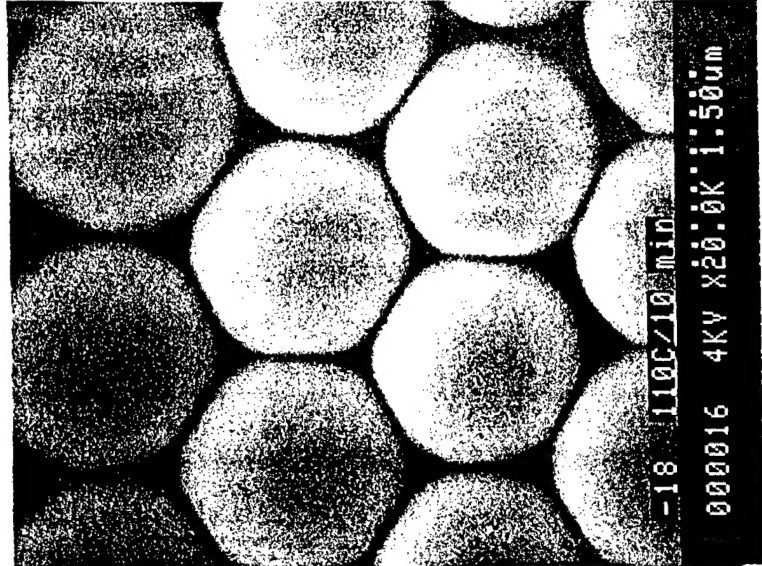




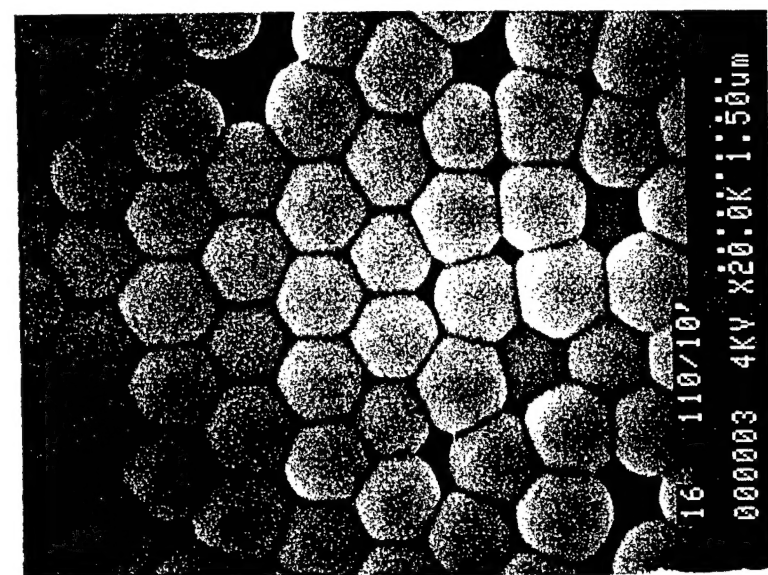




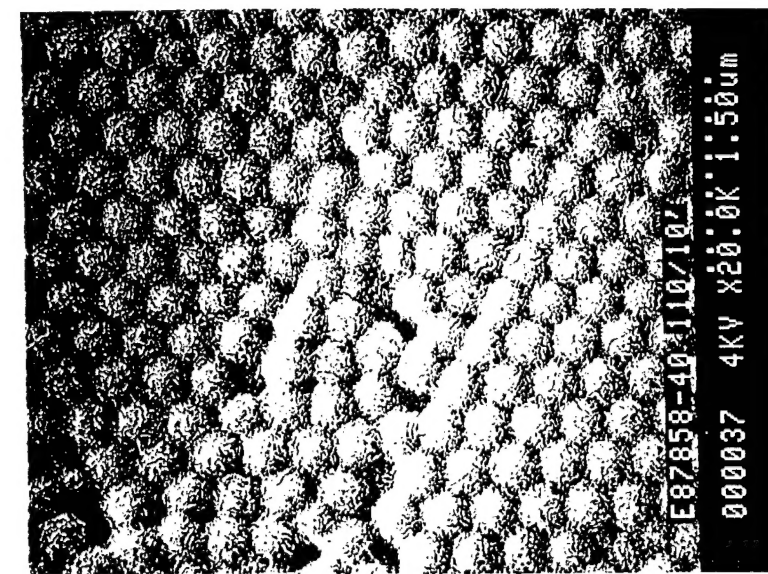
P(MMA/BMA/MAA) (48/48/4), T_g 78°C
annealed 10 minutes at 110°C



770 nm

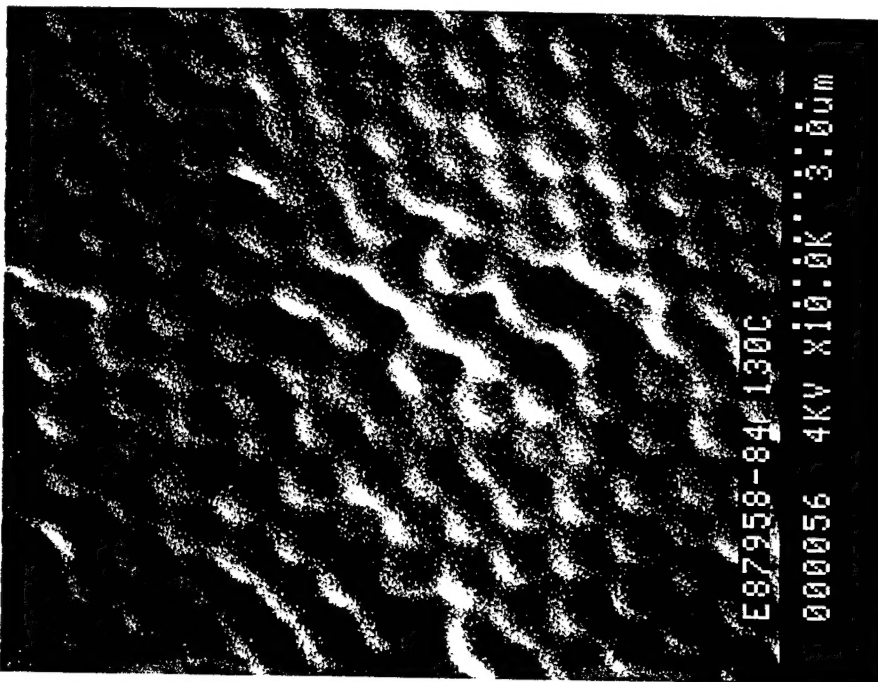


380 nm

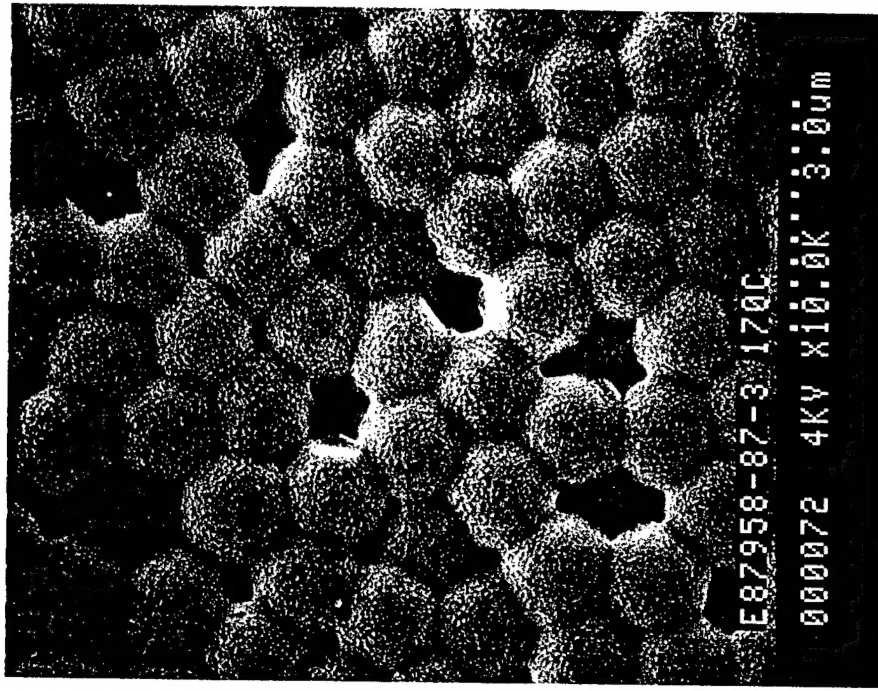


$r_h = 243$ nm

Cross-Linked Latex : P(MMA/BMA/MAA/EGDMA)
 $T_g \sim 78^\circ\text{C}$



130°C (10°/ min.)
rh 453 nm



170°C (10°/ min.)
rh 568 nm

